

Damià Gomila Villalonga

**DYNAMICS OF
SPATIAL STRUCTURES
IN NONLINEAR OPTICS**

Ph.D. Thesis

DYNAMICS OF SPATIAL STRUCTURES IN NONLINEAR OPTICS

Tesi presentada per Damià Gomila Villalonga per optar al Grau de Doctor en Física per la Universitat de les Illes Balears.

Pere Colet Rafecas, científic titular del Consejo Superior de Investigaciones Científicas,

CERTIFICA

que aquesta tesi doctoral ha estat realitzada pel Sr. *Damià Gomila Villalonga* sota la seva direcció a l'Institut Mediterrani d'Estudis Avançats i, per a què consti, firma la present

a Palma de Mallorca, 11 de Febrer de 2003.

Pere Colet Rafecas

Agraïments

Aquesta tesi ha estat realitzada a l'Institut Mediterrani d'Estudis Avançats (IMEDEA, CSIC-UIB) i finançada per una beca FPI del Ministeri de Ciència i Tecnologia associada al projecte PB97-0141-C02-02, així com per tota una sèrie de projectes d'investigació: BFM2001-0341-C02-02, BFM2000-1108, Accions integrades Hispano-Alemanes HA98-29, Accions integrades Hispano-Italianes i les xarxes europees QSTRUCT (FMRXCT960077) i PHASE.

En primer lloc vull agrair al meu director de tesi, el Dr. Pere Colet, per la seva constant ajuda al llarg d'aquests quatre anys i la seva tenacitat que tantes vegades ens ha fet arribar, de veritat, al final de les questions. També al Prof. Maxi San Miguel, tutor d'aquesta tesi, per tantes lliçons, discussions i consell, tant en el contingut físic com en altres aspectes de la ciència. Igualment vull agrair a la resta d'investigadors de l'IMEDEA que d'una manera o altre han contribuït a la meva formació al llarg d'aquests anys. En particular vull agrair al Prof. Emilio Hernández, al Dr. Oreste Piro i al Dr. Manuel Matias per tantes discussions de gran ajuda.

Most of the work about localized structures has been done in collaboration with Prof. William J. Firth and Prof. Gian-Luca Oppo from the University of Strathclyde in Glasgow. I would like to give a very special thank to them for the two very fruitful stays done during my Ph.D. I would like to thank also all the friends I meet there, and very specially to Graeme Harkness for his unvaluable lessons.

Chapter 4 has been done in collaboration with Prof. Wulfhard Lange, Dr. Thorsten Ackemann and Dr. Edgar Grosse Westhoff to whom I am very grateful for having approached me to the reality and for so many useful discussions during our intense collaborations.

Estic també molt agrait al Dr. Marco Santagiustina de la Universitat de Pàdua per tot el què m'ha ensenyat sobre collapse catastròfic i per la seva fantàstica hospitalitat durant la meva estada a Venècia.

Vull agrair, també, a Pilar Domínguez per la imatge que apareix a la portada d'aquesta tesi i a Víctor M. Eguíluz per la figura de Mallorca.

Finalment, em vull guardar un agraïment molt especial per tots els companys de l'IMEDEA i del Departament de física: aquells que són aquí, alguns que ja han marxat i d'altres que van marxar i ja tornen a ser aquí. També als meus amics de Menorca, Mallorca i Barcelona que m'han seguit animant després de tot. L'agraïment més gran és, però, per na Roberta per haver compartit el nostres doctorats.

Cover art is a computer generated picture of optical turbulence in a Kerr cavity, from the web page of the Cross-Disciplinary Physics Department of IMEDEA with permission. Optical turbulence is observed in optical Kerr cavities for large input intensities. The picture was created by Pilar Domínguez from Netconceptes.com based on a computer simulation.

Contents

Contents	xi
1 Introduction	1
1.1 Optical pattern formation	3
1.2 Localized structures in nonlinear optics	13
1.2.1 Localized structures in presence of modulation instabilities	15
1.2.2 Localized structures in presence of bistability	16
I Dynamics of extended structures	23
2 Dynamics of hexagonal patterns in a self-focusing Kerr cavity	25
2.1 Introduction	25
2.2 Model	26
2.3 Stationary hexagonal patterns	28
2.4 Secondary bifurcations of stationary hexagonal patterns	31
2.4.1 Long-wavelength instability	32
2.4.2 Amplitude instabilities	37
2.4.3 Finite wavelength Hopf instability	42
2.5 Transition to spatio-temporal chaos	46
2.5.1 Floquet analysis of oscillating hexagons	46
2.5.2 From quasiperiodicity to chaos	49
2.5.3 Transition to optical turbulence	49
2.6 Conclusions	50
3 Fluctuations and correlations in hexagonal patterns	51
3.1 Introduction	51
3.2 Description of the model	52
3.3 Linearization around a hexagonal pattern	52
3.4 Fluctuations in the near-field	56
3.5 Fluctuations and correlations in the far-field	59
3.5.1 Field fluctuations	59

3.5.2	Intensity fluctuations and correlations	59
3.5.3	Transverse momentum fluctuations	62
3.6	Conclusions	64
4	Secondary bifurcations of hexagonal patterns in sodium vapor in a single-mirror arrangement	65
4.1	Introduction	65
4.2	Experimental setup and model	66
4.3	Linear stability analysis of the homogeneous solution	67
4.4	Stationary hexagonal patterns	68
4.5	Linear stability analysis of stationary hexagonal patterns	70
4.5.1	Long-wavelength instability	72
4.5.2	$q \sim k/\sqrt{3}$ instability	76
4.5.3	$q = k/2$ instability	78
4.5.4	$q = k/4$ instability	80
4.5.5	$q \sim k/2$ instability	82
4.5.6	Discussion of the theoretical results	85
4.6	Comparison with experiment	85
4.7	Conclusions	90
II	Dynamics of localized structures	91
5	Dynamical properties of two-dimensional Kerr cavity solitons	93
5.1	Introduction	93
5.2	Kerr cavity solitons	94
5.3	Lower Kerr cavity soliton branch	97
5.4	Hopf bifurcation	98
5.5	Saddle-loop bifurcation	101
5.6	Azimuthal instabilities	106
5.7	Conclusions	107
6	Dynamics of domain walls: dark ring cavity solitons and stable droplets	109
6.1	Introduction	109
6.2	General theory of domain wall dynamics	111
6.2.1	System description	111
6.2.2	Eikonal equation	112
6.2.3	Amplitude equation for the curvature: Stable Droplets	119
6.3	Stable Droplets and Dark Ring Cavity Solitons in nonlinear optical cavities	126

6.3.1	Vectorial Kerr Resonator	126
6.3.2	Degenerate Optical Parametric Oscillator	131
6.4	Conclusions	136
7	Conclusions and Outlook	139
Appendix A:	Linear stability analysis of stationary periodic patterns	143
Appendix B:	1d fronts between two equivalent homogeneous states	147
B.1	Front symmetries	147
B.2	Front tails	148
Appendix C:	Moving reference frame	151
	Bibliography	153
	Curriculum Vitae	i

Chapter 1

Introduction

The formation of spatial structures in systems out of thermodynamical equilibrium has been the subject of a large amount of scientific research in the last quarter of the 20'th century [101, 39, 245]. Examples include patterns in hydrodynamic systems, granular media, nonlinear optics, oscillatory chemical reactions and biological systems. Definite progress has been made in the understanding of the common general theory behind the emergence and evolution of spatial structures. Methods of nonlinear dynamics and bifurcation theory such as amplitude equations, that describe the dynamics close to bifurcation points, or “phase equations”, that describe the slow distortions of patterns even far from the instability threshold, have been essential tools in the development of a universal description of pattern formation and their dynamics. However, these analytical techniques have limitations, and interesting phenomena often take place beyond their range of validity. For instance, instabilities of patterns (secondary bifurcations) may take place far away from the pattern formation instability where the dynamics of the systems is not properly reproduced by the the amplitude equations obtained at the primary instability. Furthermore, amplitude equations are usually derived using the relevant modes, in general, from a Fourier decomposition, so that they are not useful to describe states without spatial periodicity such as those containing localized structures. An alternative tool is the numerical simulation of the partial differential equations that govern the evolution of a extended system. But these numerical simulations are very time consuming and, by themselves, do not allow for a complete understanding of the dynamics of a system. For this reason, more appropriated methods of analysis have to be used and developed. Here we address this kind of problems using a powerful combination of analytical and numerical techniques.

Our approach is borrowed from dynamical system theory. The solutions of a partial differential equation can be seen as a point in a multidimensional mathematical space spanned by the dynamical variables, that is, a “phase space”. The recognition of coherent structures allows, however, to reduce the infinite degrees of freedom to a finite number of relevant variables, that is a finite-dimensional subspace. Thus, for example, a periodic pattern can be described by a finite set of Fourier modes, and a 2D localized structure by a discrete one dimensional radial

function. Thinking in a partial differential equation as being equivalent to finite sets of coupled ordinary differential equations brings powerful mathematical concepts to help on the analysis of their solutions. A Newton method can be used to find numerically stationary solutions with arbitrary precision, and continuation techniques to track them as the parameters are varied [122]. The stability of such solutions can be also determined, but here, the infinite dimensional character of the partial differential equations comes again into play. The eigenvalues of the Jacobian of the finite set of ordinary differential equation determine the stability of the solutions against perturbations that lie on the same phase sub-space. The extension of the stability analysis to arbitrary perturbations in the whole infinite phase space is a non trivial point of the analysis of partial differential equations. Finite wavelength instabilities of patterns or azimuthal instabilities of radially symmetric localized structures are examples of bifurcations that occur in directions of the phase space not parallel to the sub-space where the solution belongs to.

Even after a bifurcation the dynamics of a spatially extended systems might be understood in terms of a finite number of dynamical variables as well. This is so, due to a mathematical result known as the “center manifold theorem” [98]. When a bifurcation occurs, the associated unstable trajectories typically moves away from the original stable fixed point only with in a low dimensional sub-space of the full space. This sub-space is “attracting” in the sense that trajectories starting elsewhere converge to it, so that the degrees of freedom outside the attracting sub-space are effectively irrelevant. It is for this reason that we may need only a low-dimensional space of dynamical variables to describe some pattern-formation problems near their thresholds of instability. After the instability has produced a growing disturbance, the crucial next step is some intrinsically nonlinear mechanism by which the system moves toward a new state. In some cases they are found to saturate to finite amplitude and the new state resembles the unstable deformation of the original state. In other cases, the new pattern, that can be a stationary state or a dynamical regime including spatio-temporal chaos, looks nothing like the linearly unstable deformation from which they started. The system evolves to entirely new directions as determined by nonlinear dynamics. This nonlinear regime of the process still is one of the most challenging problems of nonlinear science [84].

This thesis is mainly devoted to the study of extended and localized spatial structures in nonlinear optics with emphasis in the generic aspects of their dynamics that are relevant for other physical systems. In the optical systems considered here, spatio-temporal phenomena arise in the structure of the electromagnetic field in the plane orthogonal to the direction of propagation as a result of the nonlinear response of the materials to intense laser beams and the spatial coupling provided by diffraction (described by the transverse Laplacian in the paraxial approximation). Particularly interesting is the case of nonlinear materials contained in optical cavities. In the mean field approximation, such systems are described by a set of partial differential equations with two spatial dimensions plus time, exactly as in the case of 2D patterns in hydrodynamics and nonlinear chemical reactions. Thus, the study of optical pattern formation share a number of aspects and techniques with general

investigations of pattern formation in other systems of scientific interest. They also have specific features such as the diffractive instead of diffusive spatial coupling or the vectorial degree of freedom associated with the polarization of the light.

Nonlinear optical systems have some advantageous properties with respect to more traditional systems. They are governed by the fundamental laws of radiation-matter interaction and their time scales are much shorter than, for example, in hydrodynamics. From an experimental point of view, large amount of data can be obtained in relatively short time. Moreover, light can be easily recorded and analyzed. A remarkable feature of optical systems is the direct access to the Fourier space by simply using lenses. Finally, optical systems are interesting from the point of view of applications to telecommunications and information technology. An already successful example is the use of solitons for the transmission in optical fibers. Recent experimental results in semiconductor microcavities also encourage the possibility of using localized structures in parallel all-optical data processing devices [16].

1.1 Optical pattern formation

There are many different configurations in nonlinear optics leading to pattern formation, going from propagation in a nonlinear medium to laser arrays [157, 12]. Some examples are:

- 1) Mirrorless configuration with unidirectional propagation.
- 2) Mirrorless configuration with counterpropagating waves.
- 3) Nonlinear medium in optical resonators.
- 4) Single feedback mirror configurations.
- 5) Nonlinear optical system with nonlocal interactions [12].
- 6) Broad area lasers [3, 153]
- 7) Laser arrays [246, 182, 112].

In the following, we give a description of the first four cases which are the most related to the contents of this thesis. Description of the other can be found in the quoted references.

A laser beam propagating through a nonlinear medium is the most simple case in which one may expect instabilities leading to the formation of spatial structures. If we assume that the electromagnetic field \tilde{E} is quasi-monochromatic, it can be described in the form

$$\tilde{E}(x, y, z, t) = E(x, y, z, t)e^{i(k_z z - \Omega t)}, \quad (1.1)$$

where the exponential term accounts for a plane wave moving in the z direction, Ω is the optical frequency, and E is the field envelope. Typically, the residual dependence in z and t of the envelope is slow ($|\partial_z E| \ll k_z |E|$, $|\partial_t E| \ll \Omega |E|$). This approximation is known as SVEA (slowly varying envelope approximation) and it has been shown to be valid even when the slow and fast scales differ by a factor less than 10, as for example in femto-second pulses [12].

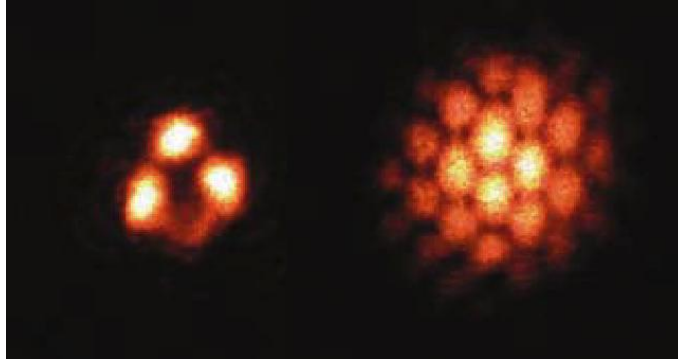


Figure 1.1: Filamentation of a near-resonant laser propagating in an atomic sodium vapor observed experimentally by Bennink et al. [20]. Left: intensity of the near field. Right: far field intensity.

Propagation in a nonlinear medium is usually studied in the framework of the nonlinear Schrödinger equation (NSE) [176, 24, 221]. This equation describes optical waves propagating through Kerr media. The optical response of these materials is characterized by a polarization with a $\xi^{(3)}$ term, $P = \xi^{(3)}EEE$. In the paraxial approximation ($|\vec{k}| \ll k_z$, where \vec{k} is the transverse wavevector) and in the reference frame moving with the group velocity of the wave, the stationary slowly varying envelope $E(x, y, z)$ of an optical wave propagating through the medium is described by the NSE

$$\partial_z E = i\nabla^2 E + i\eta|E|^2 E, \quad (1.2)$$

where $\nabla^2 \equiv \partial_x^2 + \partial_y^2$ is the transverse Laplacian and $\eta = +1(-1)$ indicates self-focusing (self-defocusing). In the self-focusing case wavetrains with uniform amplitude in the transverse plane are always unstable. Any initial perturbation originates a transport of energy from small to large wavevectors induced by the nonlinear wave mixing processes due to the Kerr effect [12, 176]. An intuitive way to understand this instability is given by geometric optics. First, in a medium with spatially dependent refractive index, light rays turn away from regions of smaller and toward regions of greater refractive index. Second, Kerr nonlinearity is associated to an intensity dependent refractive index $n = n_0 + n_2|E|^2$. Therefore, in the self-focusing case ($n_2 > 0$), there is a positive feedback because the refractive index is greater where the light is more intense. As the light propagate forward in the z direction, the light continues to focus in the regions where the intensity is greatest leading to the formation of light filaments (Fig.1.1). This instability is known as filamentation. If there is only one transverse spatial dimension, then as z increases, there is a point in which diffraction effects balance the compression due to nonlinearity. This balance leads to the formation of solitons. In the NSE with two transverse spatial dimensions the collapse is not prevented, and the light filament intensity grows to infinity in a finite time [175, 202, 221].

The analysis of counterpropagating beams in a nonlinear medium has led to the first theoretical prediction and experimental observation of hexagonal patterns in optical systems [54, 96]. For low values of the wave intensities a stationary

plane standing wave is found in the medium. However, above a certain threshold, beams propagating at a small angle with respect to the pumps are generated. Instabilities of counterpropagating waves have been observed, for instance, in atomic vapors [96, 186, 188] (Fig.1.2). The symmetry of the experimentally observed patterns is often hexagonal, though also stripes, squares and other less generic structures have been reported. For example, with a Kerr medium, hexagons have been theoretically and numerically predicted close to the instability threshold in the focusing case [38, 29, 76], while rolls or rhombi occur in the defocusing case. Despite atomic vapors are not properly described by a Kerr-like nonlinearity the pattern forming mechanisms seems to be quite independent of the details of the nonlinearity, thus allowing for comparison of models including Kerr nonlinear terms with the experiments.

Optical cavities filled with a nonlinear medium are, from the theoretical point of view, the most investigated systems in optical pattern formation. Optical resonators containing a passive nonlinear medium have been investigated in the context of optical bistability [77, 161, 151] and pattern formation [150, 12, 157]. There are two typical geometries for these systems, namely, ring and Fabry-Perot resonators. Fig. 1.3 shows schematically a ring cavity partially filled with a nonlinear medium and a Fabry-Perot resonator entirely filled with the medium. One of the most important effects of the cavity is introducing feedback. The feedback enhances nonlinear effects and induces competition among the unstable modes. But feedback is not the only effect of the cavity. While propagation in a nonlinear medium can be in some cases properly described by loss-less models, cavities are naturally dissipative due to mirror losses. Spatial structures can be, then, supported only by the presence of an external driving. While for low pump levels plane wave solutions emitted along the cavity axis are in general stable, for pump intensities above a certain threshold, they may destabilize to transverse off-axis emission leading to the formation of patterns in the transverse plane perpendicular to the propagation axis. Typically there is a further requirement in order to have such spatial instability, the existence of a detuning between the driving field and cavity frequencies. Off-axis emission is then favorable to compensate the detuning by an extra amount of diffraction. Then, the cavity reveals itself as an essential feature to observe spatial structures. In fact, spatial structures can be observed in cavities

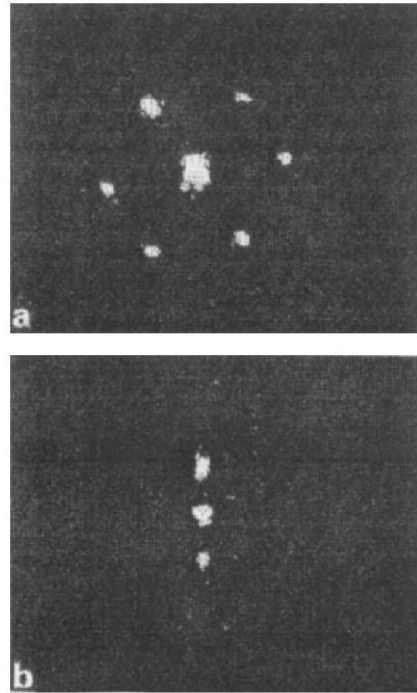


Figure 1.2: From Ref. [96]. Transmitted beam in the far field of a sodium cell pumped by counterpropagating beams. In this case the medium nonlinearity is of focusing type. In (a) the counterpropagating beams are well aligned, while in (b) they form a small angle ($\approx 5^{-3}$ rad.).

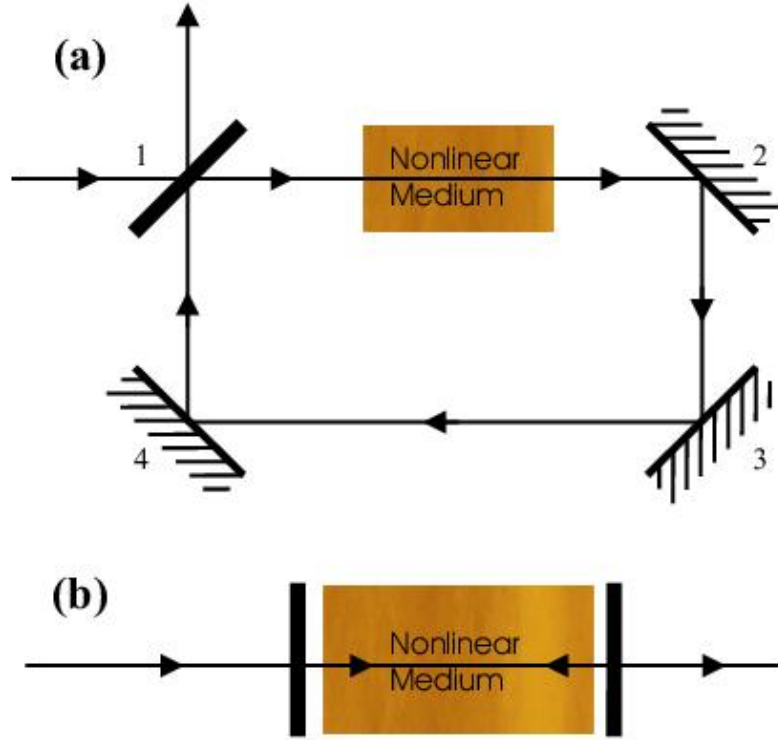


Figure 1.3: (a) Ring cavity partially filled with a nonlinear medium. Mirror 1 partially transmits the input beam. Mirrors 2,3 and 4 are completely reflecting. (b) Fabry-Perot resonator entirely filled with a nonlinear medium.

filled with nonlinear media that do not display modulation of the propagation field.

A ring cavity filled with a nonlinear Kerr medium and driven by a coherent external field E_0 is one of the most simple cavity models for pattern formation [150, 151, 154, 7, 56, 211]. In the mean field limit, the dynamics of the electric field can be described by the following equation for the scaled slowly varying amplitude $E(\vec{x}, t)$ [150]

$$\partial_t E = -(1 + i\eta\theta)E + i\nabla^2 E + E_0 + i\eta|E|^2 E \quad (1.3)$$

where E_0 is the input field (used as the frequency reference), θ is the cavity detuning, $\eta = \pm 1$ determines whether the nonlinearity is of focusing (+) or defocusing (−) type, and ∇^2 is the transverse Laplacian. Time is scaled to the cavity response time. This model is appropriated for high finesse cavities, and assumes that only one longitudinal mode is excited. The same model has been used to describe a cavity filled with two-level atoms in the limit of large detuning between the input field and the atomic line and fast atomic relaxation times [151].

The relation between the input and output homogeneous optical intensities in Eq. (1.3) shows bistability for $\theta > \sqrt{3}$. In the self-focusing case, a pattern forming instability takes always place for values of the input intensity above a certain threshold. In the self-defocusing case, however, a pattern forming instability exist only for $\theta > 2$, but it is frustrated by the bistable switching [211]. Hence, no pattern

formation takes place in the defocusing case. In the self-focusing case, a nonlinear analysis predicts a sub-critical bifurcation to hexagons [56, 211]. This is a general feature related to the existence of quadratic nonlinearities in the equation for the perturbations obtained from Eq. (1.3). Other mean field models have considered the situations in which either the medium nonlinearity is purely absorptive [57], or polarization effects are taken into account [75, 109]. In these cases, the occurrence of stripes and negative hexagons has been reported. It has been also shown that, at difference with the scalar case discussed above, polarization effects may lead to the occurrence of transverse instabilities for a defocusing Kerr nonlinearity [75, 109]. Stripe and hexagonal patterns are typical structures observed in this case. Labyrinthine patterns and localized structures have also been reported as a result of the dynamics of polarization fronts [68], and experimentally observed in degenerate four-wave mixing [224] (Fig. 1.4). The formation of these structures is studied in detail in chapter 6.

Pattern formation in cavities filled with $\chi^{(2)}$ media have been also the subject of considerable theoretical and experimental research. Two fundamentally different processes of interest in these materials are second-harmonic generation (SHG) and frequency down-conversion. SHG is a process that generates a second harmonic output at frequency 2ω from the interaction of two fundamental photons at frequency ω . The optical parametric oscillator (OPO) is based on the opposite process where the pump field at second-harmonic frequency 2ω decays through down-conversion into two, in general nondegenerate, parametric fields with frequencies ω_{\pm} such that $\omega_{+} + \omega_{-} = 2\omega$. The optical cavity, that can resonate either one, two or all of the three fields, enhances these processes. A phase-matching condition between the fundamental and second-harmonic fields is fundamental for both the SHG and frequency down-conversion processes to be efficient [21].

Pattern formation in $\chi^{(2)}$ cavities was first predicted by Oppo et al. in the degenerate optical parametric oscillator ($\omega_{+} = \omega_{-}$) [178]. In the paraxial approximation, mean field limit, and single longitudinal mode approximation for both the pump and signal fields, the following set of dynamical equations can be derived for the pump A_0 and signal A_1 slowly varying envelopes [178]

$$\begin{aligned}\partial_t A_0 &= \Gamma[-A_0 + E_0 - A_1^2] + i\frac{a}{2}\nabla^2 A_0 \\ \partial_t A_1 &= -A_1 - i\Delta_1 A_1 + A_0 A_1^* + ia\nabla^2 A_1,\end{aligned}\tag{1.4}$$



Figure 1.4: From Ref. [224]. Labyrinthine pattern observed experimentally in degenerate four-wave mixing. The transverse size is around 1 mm.

where Γ is the ratio between the pump and signal cavity decay rates, E_0 is the amplitude of the external pump field, Δ_1 is the signal detuning and a is the diffraction parameter. Eqs. (1.4) have been normalized by the signal cavity decay rate.

For positive signal detuning $\Delta_1 \geq 0$ there is no pattern formation at threshold. The zero homogeneous solution becomes unstable against zero wavenumber perturbation leading to two non-zero homogeneous solutions in a pitchfork bifurcation. Above threshold there are two equivalent solutions for the signal field that differ in a π phase difference. In this regime, fronts with oscillatory tails connecting the two equivalent homogeneous solutions are typically formed [235, 179, 181, 147, 217]. The dynamics of this kind of structures is discussed in detail in chapter 6.

For negative signal detunings $\Delta_1 < 0$, the zero homogeneous solution becomes first unstable to finite wavelength perturbation leading to the formation of a stripe pattern [178]. However, increasing further the pump, two non-zero homogeneous solutions become stable. Numerical studies in this regime find multistability between the stripe pattern, the two non-zero homogeneous solutions and irregular patterns. The latter are formed by fronts connecting the two homogeneous solutions. In systems with two spatial dimensions, there are also coexisting labyrinthine patterns as it will be discussed in chapter 6. Also for some specific values of the parameters, square patterns are found in the degenerate OPO [149, 134].

Further analytical and numerical investigations on the degenerate OPO, including a detailed derivation of amplitude equations and identification of secondary instabilities can be found in [43]. Pattern formation in non degenerate OPO have been also investigated [177, 216, 146]. In this case, a detailed nonlinear analysis shows the stability of traveling waves with respect to stripes patterns [145]. Also square patterns consisting in the superposition of four traveling waves have been reported [144].

The models for intracavity SHG and the degenerate OPO differ only by the position of the pump term in Eq. (1.4). While in the OPO the input field E_0 is in the first equation, for the field at frequency 2ω , in SHG it is located in the second equation, the one for the amplitude of the fundamental field. In spite of the similarities, SHG and OPO have very different properties. We remark the existence of a threshold for parametric down-conversion in the OPO, while in SHG frequency up-conversion is found at an arbitrarily low pump level. In doubly resonant intracavity SHG, the homogeneous solution shows four different types of instabilities leading to bistability and self-pulsing [48], and to both stationary and oscillatory transverse instabilities. Stripes, hexagons [51], and solitary structures [52] are examples of structures reported in doubly resonant SHG models. In singly resonant SHG a rich variety of spatial structures including periodic patterns and localized states have been also reported [142].

Despite the simplicity of these models and the large amount of theoretical and numerical studies about nonlinear passive cavities, there are only few experimental results in this field. Experiments involving Fabry-Perot resonators filled with sodium vapors have demonstrated the occurrence of both time oscillations and spatial pattern formation in the output beam [173, 124, 139, 140, 141, 66] (Fig 1.5). Only few

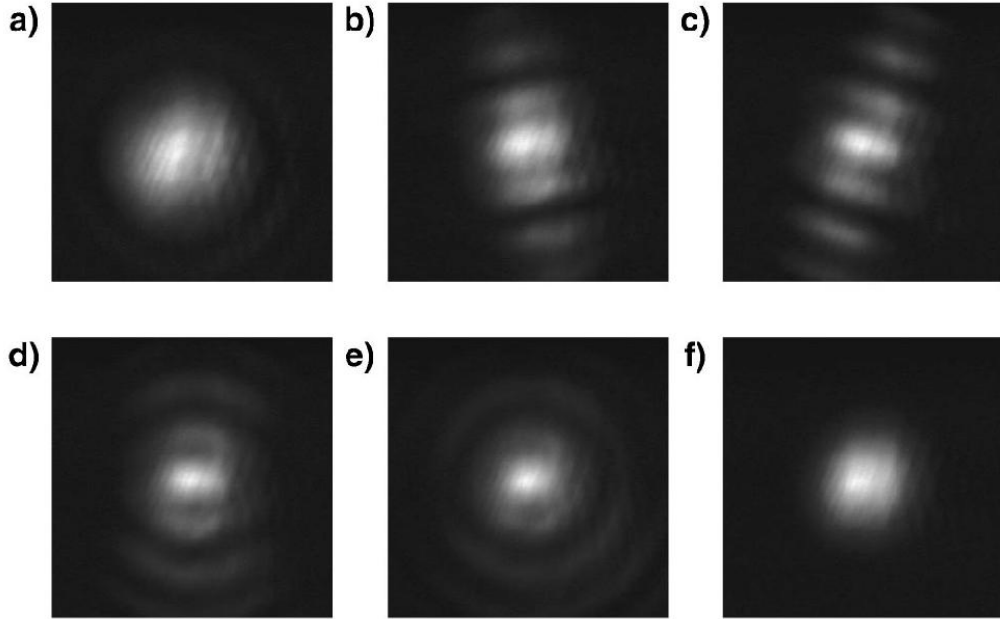


Figure 1.5: From Ref. [66]. Patterns in a nonlinear Fabry-Perot resonator with curved mirrors. Sodium vapor is used as a nonlinear medium. The figure shows a sequence of patterns on the focusing side of the atomic resonance as a function of the resonator phase.

years ago, spatial structures have also been reported in a OPO [241] (Fig. 1.6) and in SHG [143]. However, for different reasons (spherical mirrors, thick nonlinear media, thermal effects in the crystal, ...), a direct comparison between the experimental results and the theoretical predictions is difficult.

The study of systems with a single feedback mirror produce the best compromise between simplicity of theoretical treatment and accessibility to experimental realization. The first model, proposed by Firth et al. [55, 41, 42], consists of a thin slice of a Kerr medium irradiated by a plane wave with a feedback mirror placed behind to generate a counterpropagation beam. The evolution of the phase ϕ in the transverse plane of the field is ruled by

$$\partial_t \phi(\vec{x}) = -\frac{\phi(\vec{x})}{\tau} + D \nabla^2 \phi(\vec{x}) + \alpha I_0 \left| e^{\frac{id}{k_0} \nabla^2} e^{i\phi(\vec{x})} \right|, \quad (1.5)$$

where τ and D are, respectively, the local relaxation time and diffusion constant of the medium, α gives the sign and strength of the Kerr nonlinearity, I_0 is the intensity of the uniform input field, d the distance between the feedback-mirror and the nonlinear medium, and k_0 the optical wavenumber. The scheme is an idealization of an experimental set-up [79]. The basic idea is the spatial separation of the region in which nonlinearities act and the region in which diffraction takes place. As a consequence of this spatial separation, an identification of the specific role played by nonlinearity and propagation in pattern formation is possible. Unfortunately, the assumption of a perfect Kerr nonlinearity is not a realistic approximation. Sodium vapor, for instance, is often used as a nonlinear medium, and it is not properly

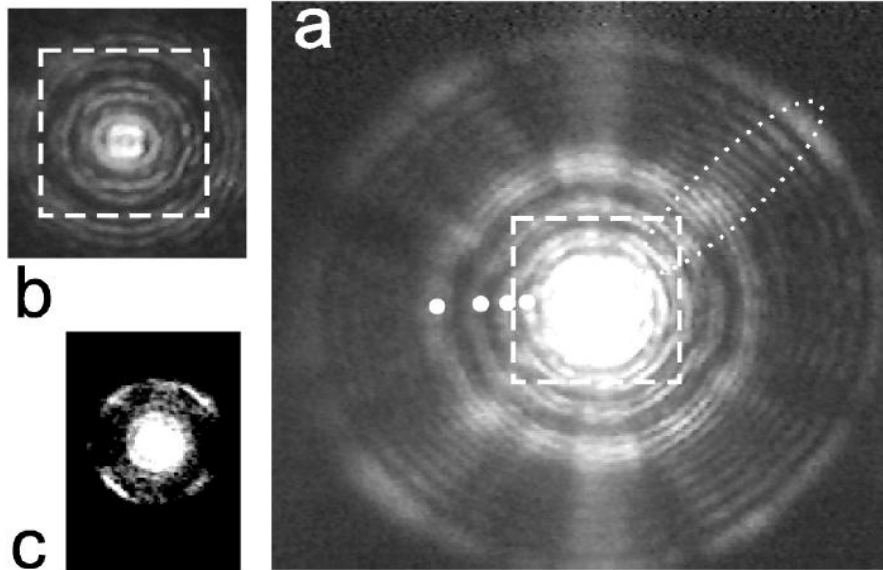


Figure 1.6: From Ref. [241]. Transverse structures observed in the signal field of a near-confocal, type II, triply resonant OPO. (a) near field with a saturated center, wide rings, and thin fringes (see, for example, inside the dotted ellipse), (b) detail of the central part of the near field, and (c) far field with a saturated center and bright ring.

described by a simple Kerr nonlinearity. In particular, the polarization state of the light plays an important role in the light-matter interaction due to the spin of the sodium atoms. Proper models taking into account the features of alkali metal vapors have been derived [126, 127]. The basic arrangement, as well as a modified version including a quarter-wave plate that mixes different light polarizations, have shown to display a very rich variety of spatial structures [4], as e.g. positive and negative hexagons or squares [128, 129, 14] (Fig. 1.7). Interesting secondary bifurcations from negative hexagonal patterns to positive hexagons, irregular time-dependent states and “flower-like” patterns [128, 129], as well as to superlattices [6, 94] and quasipatterns [106] have been also experimentally observed. In chapter 4 we study in detail the secondary bifurcations of hexagonal patterns in a microscopic model for a sodium vapor cell in a single-mirror arrangement including a quarter-wave plate in the feedback loop.

A description common to all the systems described above, and in general to any optical pattern forming system, is given by the nonlinear analysis of bifurcations. This analysis also provides a link between optics and other fields of physics where pattern formation takes place, as e.g. hydrodynamics or chemical reaction. As a result of such analysis, amplitude equations describing the dynamics of unstable modes close to bifurcation points are obtained. This behavior is universal and depends only on the type of bifurcation, and not on the microscopic details of the model. Thus, for instance, in the region of nascent bistability for the homogeneous solution of a Kerr cavity, the amplitude equation for the optical field is a modified real Swift-Hohenberg equation [162, 226], originally derived as an order parameter

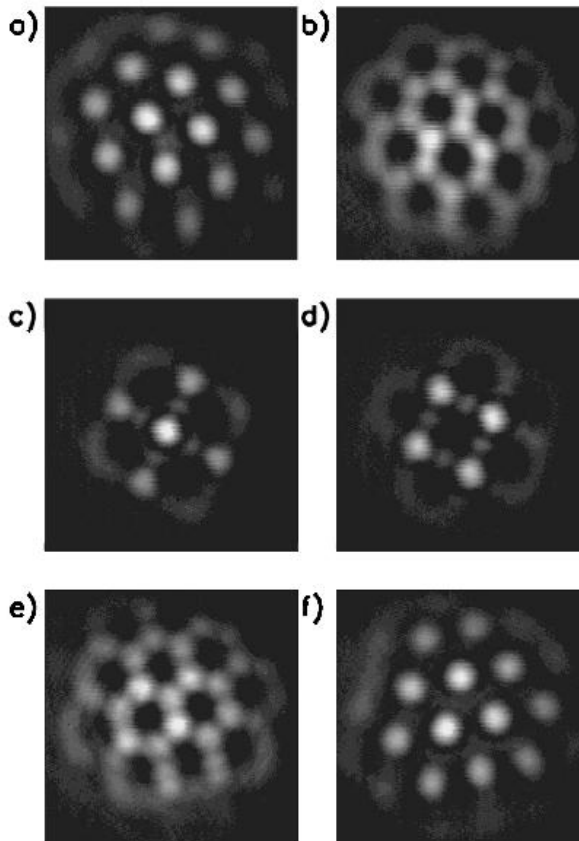


Figure 1.7: From Ref. [14]. Transition from positive to negative hexagons via squares in the circular polarization components of the beam (left-hand column, left circular polarization; right-hand column, right circular polarization) induced by a change of sign of the input polarization ellipticity. The transverse size of the images is 2.6 mm.

equation for Rayleigh-Benard convection [223]. In the same way, models for vectorial Kerr cavities and optical parametric oscillators can be reduced to the parametrically driven Ginzburg-Landau equation [207, 216], the generic amplitude equation for an oscillatory system parametrically forced at twice its natural frequency [34, 35, 189].

Another universal description comes from the analysis of the dynamics of the phases of patterns. The preferred spatial structures associated to the breaking of the translational symmetry are periodic patterns. As a result of this spontaneous breaking of a continuous symmetry, continuous families of such patterns exist, and these families are characterized by their phases. The dynamics of these phases is universal and describe the long-wavelength modulations of periodic structures. Eckhaus and zig-zag instabilities are secondary bifurcations of stripe patterns associated to phase dynamics [39, 245].

Secondary bifurcations of modulated solutions link, once more, the field of nonlinear optics to hydrodynamics and nonlinear chemical reactions. The different ways in which a pattern can destabilize are common to all systems, and, as in any bifurcation, the dynamics close to the bifurcation point is universal. Secondary bifurcations from stripe pattern and hexagon-roll transitions were studied long ago in hydrodynamics [39, 23, 31]. More complex secondary bifurcations, as e.g. to superlattices or quasipatterns, has been recently experimentally observed in Faraday waves [121, 243, 244, 190, 198] and optics [185, 6, 94]. From a theoretical point

of view, generic secondary bifurcations of spatial periodic structures, both in one and two dimension, have been analyzed and classified by means of symmetry-based approaches [33, 78, 46, 47, 236, 191]. These are mathematical techniques that classifies the different ways in which the spatial symmetry can be broken, however, they do not predict which instability will occur in a given particular model. Secondary bifurcations of hexagonal patterns in two different optical systems are analyzed in detail in chapters 2 and 4.

The different scenarios for the transition to chaos are also a universal description of nonlinear systems. In low dimensional dynamical systems different routes have been established [183, 165, 18], however in spatially extended systems the transition from regular patterns to spatio-temporal chaos is only partially understood. The understanding of tertiary and further bifurcations of regular patterns is an important open issue for the identification of the general scenarios to spatio-temporal chaos. In chapter 2 we address this problem in a self-focusing Kerr cavity.

Finally, the properties of the fluctuations and correlations in patterns in different spatially extended systems share also many features. Effects of noise on patterns out of thermodynamical equilibrium were studied long ago in the context of hydrodynamic systems [64, 242, 105, 203]. More recently there has been a new surge of interest in the field of nonlinear and quantum optics since Lugiato and Castelli pointed out the existence of purely quantum phenomena in a spatial stationary pattern in a 1D self-focusing Kerr cavity [152]. Quantum features are found both below and above the instability threshold for pattern formation in optical systems. In particular it has been shown that below, but close to, threshold, the quantum noise can excite the weakly damped spatial modes that will become unstable at threshold [71, 156, 72, 73]. In an isotropic system with two spatial dimensions, the spectrum of fluctuations below threshold has a radially symmetric distribution with maxima on a ring of radius equal to the wavenumber of the pattern formed just above threshold. Therefore, the spectrum of fluctuations below the instability threshold is considered to be a noisy precursor [247] that anticipates the above-threshold pattern wavenumber. Furthermore, in optical systems where a stripe pattern is formed, strong correlations exist, even at quantum level, between the fluctuations in the number of photons emitted at the critical wavenumber and opposite wavevectors. This is an effect of the parametric coupling associated with transverse momentum conservation. It has been interpreted as a below-threshold signal of the form of the pattern that will arise above threshold, namely a stripe pattern. The fact that the correlations are associated with quantum entanglement among spatial modes has originated the term “quantum images” [71].

Here we concentrate in the case above threshold, namely in the effect of noise in a stationary pattern. The properties of the fluctuations in the near field are well described by universal phase equations. In this framework the role of the neutrally stable modes (Goldstone modes) due to the breaking of the translational invariance by the pattern and the so called soft modes associated to them is well understood [64, 158, 250]. Due to noise, the Goldstone modes are excited inducing a rigid displacement of the pattern, while the soft modes are responsible of long wavelength

distortions of the regular structure. The correlation between the different far-field modes is particularly interesting in optics and has been widely studied in the case of stripe patterns [155, 27, 108, 110, 250]. The intensity of these modes can be interpreted as the number of photons emitted in each transverse direction, and therefore, transverse momentum conservation plays a very important role in the structure of their correlations. This is a very general statement independent of the details of the system. The case of hexagonal patterns is particularly interesting because transverse momentum conservation does not completely determine the correlations between the different modes [155]. Moreover, since hexagonal patterns are generally sub-critical, they appear, even at threshold, with a finite amplitude, and the higher harmonics are not negligible making a few modes approximation not fully justified. In chapter 3 we study of the fluctuations and correlations of a hexagonal pattern in a Kerr cavity using a continuous model.

1.2 Localized structures in nonlinear optics

So far we have discussed the formation of extended patterns, i.e. structures that fill the whole area of the system. But spatial structures localized in a small area can also to be sustained under certain conditions. In propagation systems, localized structures have been mainly studied in the nonlinear Schrödinger equation [100, 107, 118, 132, 200]. In this system, a balance between the tendency to spread due to diffraction and the focusing properties of the nonlinear medium may lead to the propagation of light beams that conserve a limited transverse size. This mechanism is very related to the problem of filamentation discussed in the previous section. In the case of one transverse spatial dimension, the NSE is integrable [248] and soliton solutions can be found by means of the inverse scattering method [176, 208]. For a focusing (defocusing) medium, the fundamental bright (dark) soliton solution is a spatial hyperbolic secant (tangent) which propagates without changing its shape [174, 119, 248, 249, 1, 116, 123]

$$A(x, z) = \frac{A_0 e^{iA_0^2 z}}{\cosh(A_0 x)} \quad \left(A(x, z) = A_0 \tanh(A_0 x) e^{iA_0^2 z} \right), \quad (1.6)$$

where A_0 is the soliton amplitude. In one transverse spatial dimension these solitons are stable. 1D bright solitons has been reported in nonlinear liquids [17, 163, 164, 196] and planar waveguides [8], while dark solitons have been observed in photorefractive crystals [111].

In two spatial transverse dimensions the NSE present very different features. To start with, the NSE with two transverse spatial dimensions is not known to be an integrable equation, and bright solitons are unstable. Depending on the energy of the localized structure, it either spreads around due to diffraction, or collapses its amplitude reaching an infinite value in a finite time [194, 82, 49, 221]. In fact, it has been shown in general that a soliton propagating in D transverse dimensions through a focusing medium described by a nonlinearity of the type $\Delta n \propto I^\sigma$ is

stable only for $\sigma < 2/D$ [201]. From a physical point of view, the dependence of the soliton stability upon the transverse dimensionality is due to the fact that focusing in a Kerr medium depends on D while spreading by diffraction is independent.

Other nonlinearities, as e.g. quadratic, do not display collapse. Parametric interaction in quadratic materials can also counterbalance spreading caused by diffraction leading to the formation of localized structures, commonly referred as quadratic solitons [232, 233] (Fig. 1.8). Formation of localized structures in quadratic materials was experimentally demonstrated few years ago [234, 65].

In fact, the catastrophic collapse in the 2D NSE is unphysical. Several approximations (paraxial, slowly varying envelope, cubic nonlinearity) used to obtain the NSE from fundamental principles are not valid close to the collapse event. Different mechanisms, such as linear damping [82], saturation of the nonlinearity [194] or non paraxial beams [215, 30], have been proposed to avoid collapse. Linear damping is, for instance, a mechanism present in a Kerr cavity. This system is described by Eq. (1.3) which is, in fact, the driven and damped NSE. The existence of stable localized structure in a 2D Kerr cavity model was documented in [58, 59]. These are localized intensity peaks that form in a stable homogeneous background of radiation. Despite these systems are dissipative, the term *soliton*, borrowed from the exact solutions of integrable nonlinear partial differential equations, is used because the mechanism behind the formation of localized structures in these systems also implies, somehow, a balance between nonlinearity and diffraction.

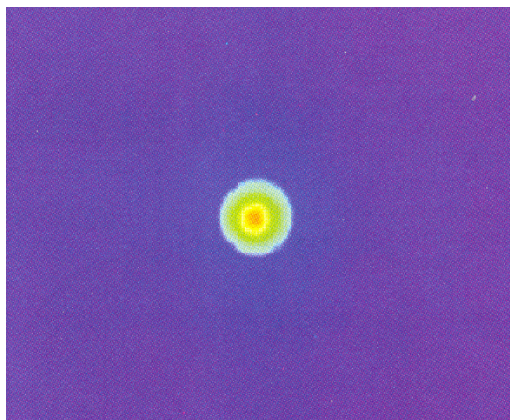


Figure 1.8: From Ref. [232]. Quadratic soliton at the output of a bulk piece of periodically poled potassium titanyl phosphate (PPKTP).

There are, however, other mechanisms leading to the formation of localized structures in optical cavities, both with cubic and quadratic media, as well as in single feedback-mirror system. Localized structures in these systems are, in general, known as *cavity* and *feedback solitons* [63]. Cavity and feedback solitons have attracted a great deal of attention due to potential future applications as “bits” in all-optical logical components [166, 201, 22, 60, 61, 199, 16].

There are, however, other mechanisms leading to the formation of localized structures in optical cavities, both with cubic and quadratic media, as well as in single feedback-mirror system. Localized structures in these systems are, in general, known as *cavity* and *feedback solitons* [63]. Cavity and feedback solitons have attracted a great deal of attention due to potential future applications as “bits” in all-optical logical components [166, 201, 22, 60, 61, 199, 16].

Different mechanisms may lead to the formation of stable localized structures [37]. Localized structures can be, very generally, classified in two large groups, namely the ones that appear in regimes where a homogeneous and a spatially modulated solution coexist, and those associated with the existence of two homogeneous solutions.

1.2.1 Localized structures in presence of modulation instabilities

In subcritical pattern forming bifurcations, the homogeneous steady state coexists with the pattern solution arising from the instability (usually referred as modulation instability). This is the most common situation when the arising patterns are hexagons. In some cases, a portion of these patterns, even an isolated peak, embedded in the homogeneous solution may be stable leading to a localized structure. This is, in fact, the case of the self-focusing Kerr cavity [211], where this localized structures have been called Kerr cavity solitons. The existence of this kind of localized structures in nonlinear optics was first reported in a Swift-Hohenberg equation describing, in the weak dispersion limit, nascent optical bistability with transverse effects [227], and have also been found in degenerate [230, 147, 217] and non degenerate [148] OPO models, as well as in single feedback-mirror experimental systems [209] (Fig. 1.9).

These kind of structures have also been experimentally observed in fluids [89], granular media [237] and chemical reactions [237], and described by means of generic Ginzburg-Landau [53] and Swift-Hohenberg [80, 184] models.

A sufficient condition for the existence of such structures in 1D systems was demonstrated by Coulet and coworkers [36]. This condition is based on the robust existence of stable stationary fronts between a stable homogeneous solution and a stable periodic pattern. Localized structures containing from one to infinite pattern cells exist around the boundaries of the region of existence of the stationary fronts in parameter space. Despite the demonstration is, strictly speaking, only valid for 1D systems the same phenomena is observed in 2D systems with cellular patterns. In this context, localized structures are understood as spatial heteroclinic orbits of the stationary system equations connecting the homogeneous and pattern solutions.

A well-known but not yet completely understood situation typically enhancing the existence of localized structures is nascent bistability [227], i.e. when, in addition to the pattern forming instability to a subcritical cellular pattern, the homogeneous solution of the system is close to be, or is bistable. In fact, most of the experimental observations of localized structures in optical systems have been done in this

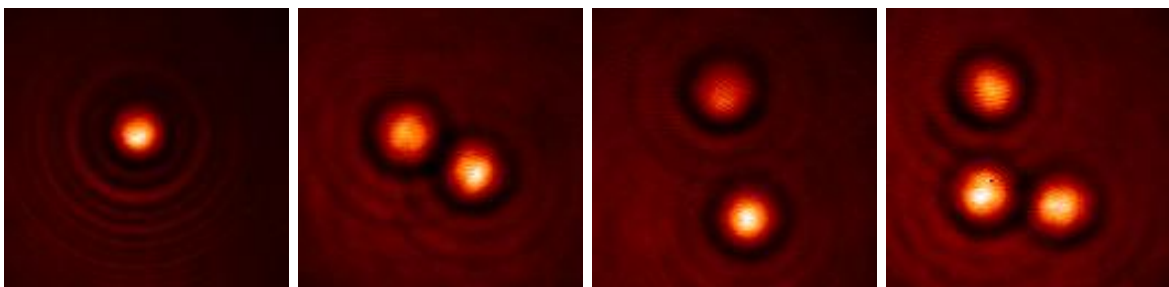


Figure 1.9: From Ref. [209]. Localized structures in sodium vapor with single feedback mirror. The light distribution of a localized structures is characterized by a central bright spot surrounded by diffraction fringes. The interaction between localized structures may lead to the formation of stable clusters. The transverse size of the images is 2.58 mm.

situation [209, 16].

In Chapter 5 we study the dynamical properties of Kerr cavity solitons. We find an interesting azimuthal instability leading to the formation of an expanding five fold symmetry pattern with a topological defect at the place where the localized structure was located. An oscillatory instability is also found, and a careful study proves the existence of a novel regime of excitability in localized structures. This regime is associated to a subsequent instability, namely a saddle-loop bifurcation, of the oscillating Kerr cavity soliton.

1.2.2 Localized structures in presence of bistability

The localized structures discussed in this section are not associated to a pattern forming instability but simply to the existence of two equivalent homogeneous solutions (usually called phases) in an extended system. In nonlinear optical systems, these two solutions may differ from each other by a π phase shift in the slowly varying amplitude of the electric field or by their polarization state. Systems which satisfy these conditions are commonplace in optics due to either the quadratic nature of the nonlinearity or the polarization symmetry. The different regions occupied by different phases are called domains and they are delimited by fronts or interfaces, also called domain walls. The formation and stability properties of this kind of localized structures is then intimately related to the general problem of domain growth and domain wall motion.

In systems momentarily driven out of equilibrium, spatial structures may appear as a transient until the system reaches thermodynamic equilibrium. Growth processes in this case are generally well-known [99]. Only recently, however, transient dynamics when the final state is not of thermodynamic equilibrium have been studied [40, 113, 67, 229, 68, 179, 180, 181, 187, 136, 69]. Two cases can be distinguished: systems for which a Lyapunov potential exist (potential systems) and systems for which do not (nonpotential systems).

In potential systems, the Lyapunov potential [25] plays the role of a free energy, so that the relative stability between asymptotic states can be measured. Thus, the general behavior of a potential system is qualitatively identical to that of systems approaching thermodynamic equilibrium. In one dimension, the direction of motion of an isolated front is determined through the relative stability of the two asymptotic solutions. Specifically the front velocity is proportional to the Lyapunov potential difference and the detailed shape of the interface does not play an important role. Therefore, when the two asymptotic states are equivalent, an isolated wall between the two states does not move. In large systems with several walls between homogeneous asymptotic states, short-range interactions due to the tails of the fronts may come into play [117, 32]. In general, these interactions are negligible in the case of nonequivalent states as compared with the force associated to the Lyapunov potential difference, but they may manifest in the case of equivalent states or states with very similar values of the potential. When the profile of the front approaches monotonically the asymptotic states, the interaction between two walls is attractive and,

for equivalent states, a domain delimited by two of these fronts tends to contract until the domain walls annihilate each other. When the front profiles show damped spatial oscillations, the interaction of two distant domain walls can be described by a potential with several wells which become progressively deeper the shorter the distances between the domain walls [32]. The wells of the interaction potential are located at the distances where the extrema of the oscillations of the tails overlap with each other. Thus, oscillating domain walls may not annihilate each other, but they may locate at a certain equilibrium distances. This leads to a frozen steady state configurations due to the random pinning of interfaces [32]. Nonlinear optical systems often are not potential, but equilibrium distances in $d = 1$ and $d = 2$ are also found whenever the extrema of the local oscillations of the domain walls overlap with each other [179, 181].

In two dimensions the curvature of the wall of the domain plays an important role [99, 168]. In the case of equivalent homogeneous asymptotic states, the system tends to reduce the excess of energy located at the interfaces by decreasing their length. The normal front velocity v turns out to be proportional to the local curvature κ , $v = -\gamma\kappa$, which is the well known Allen-Cahn law [10, 99]. As a consequence, if $\gamma > 0$, a circular domain of radius R of one phase surrounded by the other ($\kappa = 1/R$ and $v = dR/dt$) tends to reduce its radius with the growth law $R(t) \sim \sqrt{R(t=0)^2 - 2\gamma t}$. Equivalently, arbitrarily shaped closed domains shrink and the system coarsens in a self-similar way. This means that the domain structure is, in a statistical sense, independent of time up to a global scale factor: the system exhibits dynamical scaling (Fig. 1.10). The characteristic domain size L evolve in time following the power law $L \sim t^{1/2}$ [69, 214, 239, 138, 10]. This simple description is modified when the dynamics is restricted by a conservation law. In this case the growth of a domain of one phase embedded in the other follows a power law of the form $L \sim t^{1/3}$ [137]. If $\gamma < 0$ (negative surface tension), the presence of walls is energetically favored and the system prefers to have as long walls as possible. Thus, any perturbation of a front grows and flat walls becomes modulationally unstable. The system develops labyrinthine patterns [83, 184, 219] (Figs. 1.4 and 1.11).

The short-range interactions due to the tails of the front are, in general, negligible as compared with the curvature driving force. However, when the interfaces are very close to each other and the system is in a parameter region where the curvature driving force is not so large, the oscillatory tails may cause the interfaces to be mutually repelling, thus stopping their movement due to the curvature. The repulsive forces induced by spatial oscillations may lead to the stabilization of a closed domain of a stable phase at a certain radius. The result is a localized structure [184, 179]. Interaction of oscillatory tails can also explain the existence of localized structures in nonpotential optical systems [68, 179, 135, 193]. The intensity profile of these localized structures in nonlinear optical cavities is characterized by a peak surrounded by a darker ring and then by a homogeneous phase. This kind of localized structures, usually referred as dark ring cavity solitons have been described in the mathematical context of the Swift-Hohenberg equation [184, 219], in the degenerate OPO model [218, 179, 181], and in the vectorial Kerr cavity model when polarization effects are

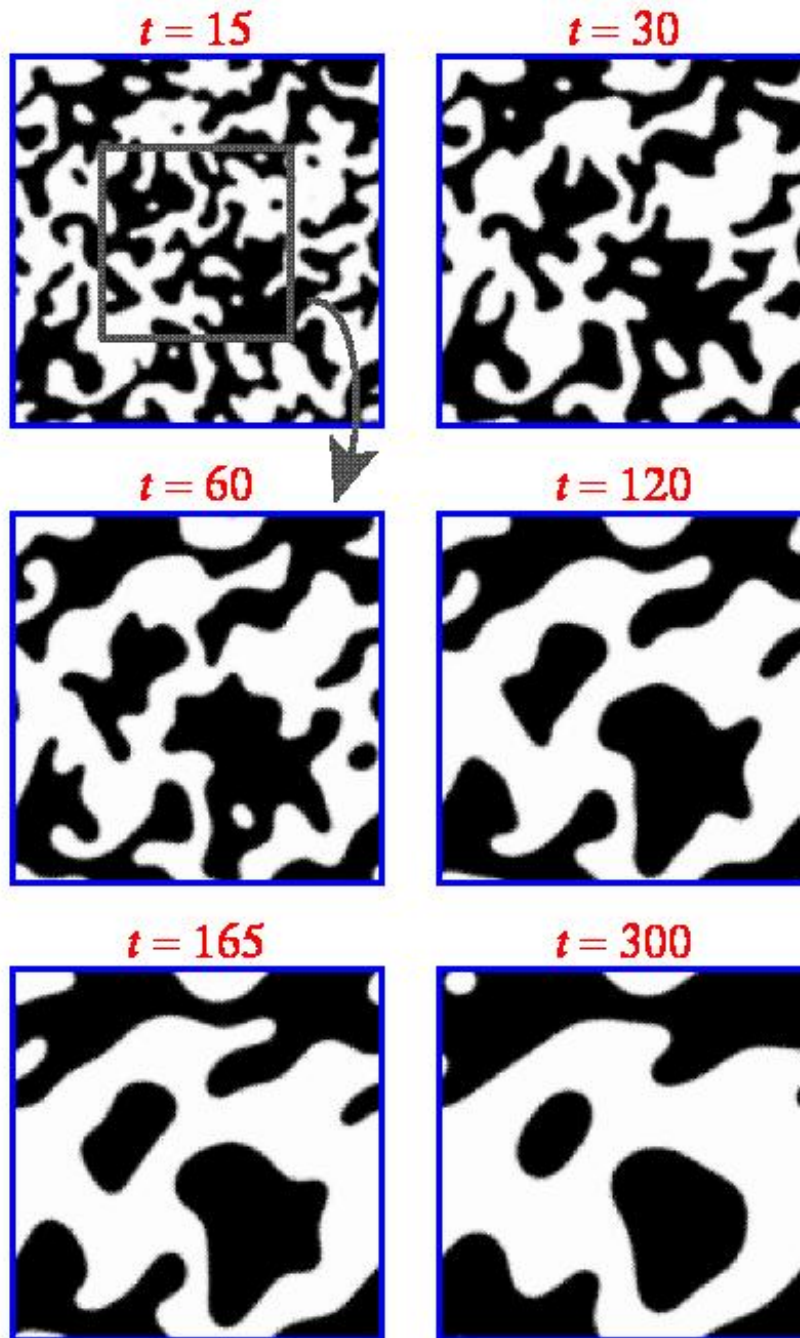


Figure 1.10: From Ref. [69]. Several snapshots corresponding to a numerical simulation of a potential system described by a non-conserved order parameter, namely the Ginzburg-Landau equation ($\partial_t \psi = \nabla^2 \psi - V'(\psi)$, where $V(\psi) = (1 - \psi^2)^2$). The structure of domains evolve self-similarly. Since the growth law for this system is $L(t) \sim t^{1/2}$, the structure of domains in a region of size A at time t is statistically equivalent to that of a region of size $2A$ at time $4t$ as illustrated in the figure.

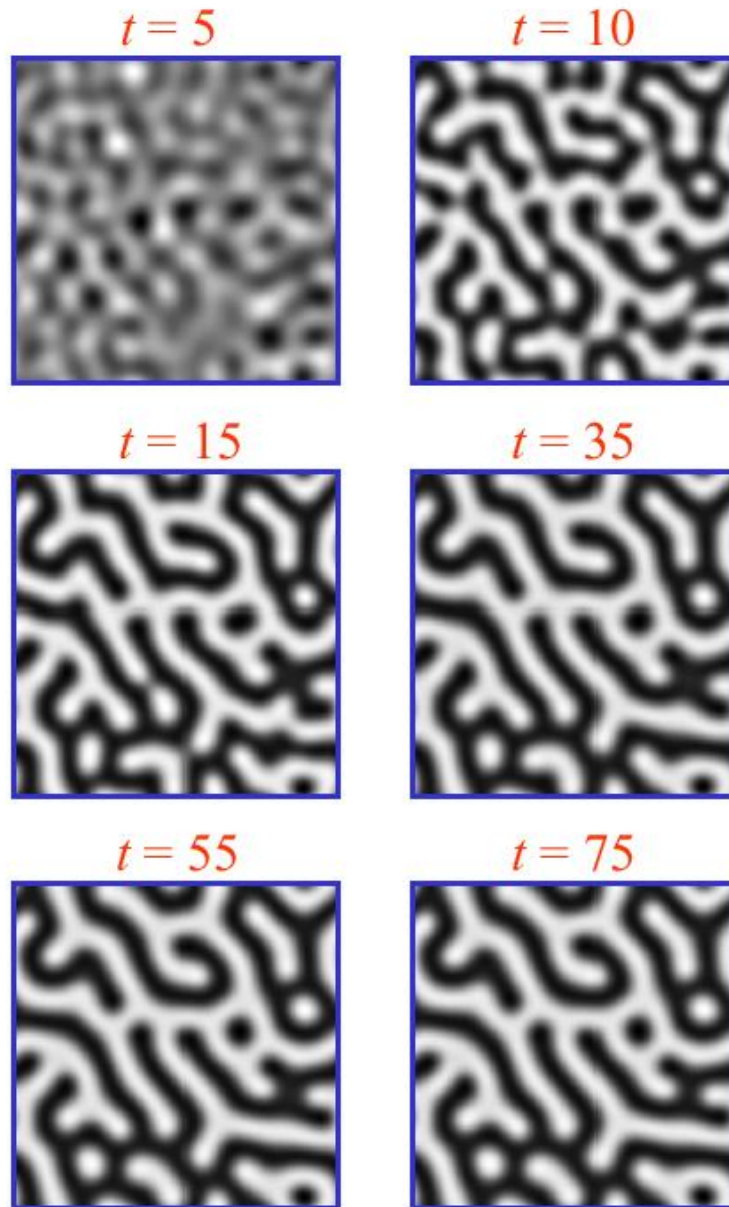


Figure 1.11: Several snapshots corresponding to a numerical simulation of a potential system described by a non-conserved order parameter, namely the Swift-Hohenberg equation ($\partial_t \psi = \psi - (\nabla^2 + k_0^2)\psi - \psi^3$). Here $k_0^2 = 0.5$. The system develops a labyrinthine structure until reaches a nearly frozen state.

taken into account [68]. They have also been experimentally observed in degenerate four wave mixing using a photorefractive nonlinear media [224] (Fig. 1.12). The oscillatory tails plays also an important role in the formation of labyrinthine patterns, stopping the proliferation of domain walls due to interaction forces.

In the case of nonequivalent phases the main source of movement of the walls in two dimensions is the 1d mechanism explained previously. In diffusive systems, in general, the curvature acts to smooth out short-wavelength perturbations during propagation [168]. In some cases, however, the shrinking effect of the curvature may counterbalance the expansion of a more stable phase into a less stable one. In this case an stationary radius for a circular domain exist. However, in the absence of any other mechanism, it is always unstable (nucleation theory) [99]. More complex mechanisms have been used to explain the existence of stable radius in a analogous situation in reaction-diffusion systems, as well as describe modulational instabilities of propagating fronts [83].

For systems without a Lyapunov potential the study of domain growth and domain wall motion is by far more complicate. The study of front propagation can no longer be done in terms of a free energy. It is known that a domain wall between two equivalent states may move in one dimension in either directions due to non-potential dynamics [34, 170]. In two dimensions more complicated effects may appear. Despite the fact that many physical systems of interest out of equilibrium are governed by nonpotential dynamics, there is no universal characterization of domain growth dynamics in two dimensions. There is presently only a partial understanding of a variety of possible situations [40, 69, 168]. In particular, in the case of two equivalent phases, a number of results have been recently reported for domain growth and domain wall motion in the transverse plane of nonlinear optical systems [229, 68, 179, 187, 136]. Existence of dynamical scaling has been numerically shown only in [68, 179], where a $t^{1/2}$ power law has been found, but no derivation of such a law has been given for these systems.

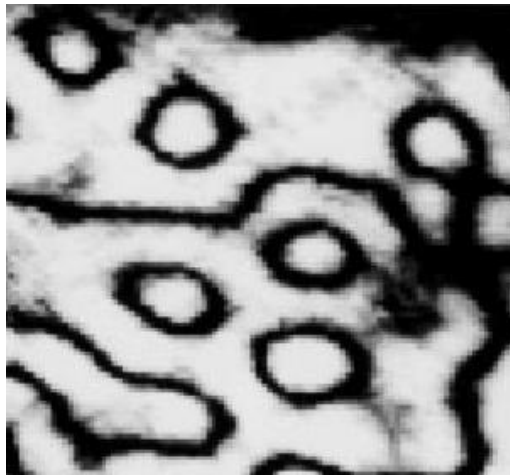


Figure 1.12: From Ref. [224]. Localized structures and domain walls of complicated shape as obtained experimentally from degenerate optical parametric mixing. Stable localized structures are formed after a transient shrinking of the domains. The transverse size of the image is around 2 mm.

In chapter 6 we provide a universal description for the motion of domain walls in a very general class of systems including those of nonlinear optical cavities. We demonstrate in which parameter regions the growth rate of a domain follows a power law, and therefore exhibits dynamical scaling, and for which parameter region this is not the case. As a consequence of our general theory a novel kind of localized

structures is found, the stable droplets. These structures are large stable circular domain walls separating the two homogeneous phases. At difference, with previously reported localized structures, stable droplets do not exist in one dimension because their stability is due to curvature effects. In the regime of existence of stable droplets, a small (very large) circular domain grows (shrinks) until the equilibrium radius is reached. Arbitrary shaped domains evolve first to circular domains and then to stable droplets, making the stable droplet an attractor and the most relevant localized structure in appropriated parameter regions.

Part I

Dynamics of extended structures

Chapter 2

Dynamics of hexagonal patterns in a self-focusing Kerr cavity

2.1 Introduction

As discussed in chapter 1, the mean field equation describing a Kerr medium in a cavity with flat mirrors and driven by a coherent plane wave is one of the simplest models showing spatial structures in nonlinear optics. This prototype model have been used to study a wide variety of phenomena such as pattern formation in optical bistability or formation of localized structures [150, 56, 211, 61] (the last, called Kerr Cavity Solitons, are studied in Chapter 5). In the self-focusing case, a weakly nonlinear analysis shows that, for pump intensities above a certain threshold, the system spontaneously develops hexagonal patterns while stripes are unstable [211, 228]. In the self-defocusing case, however, patterns are not formed [211]. An extension of the model including the polarization degree of freedom of the light shows that in the self-defocusing case the system can undergo polarization instabilities leading to stripe patterns [75, 109]. Localized structures have also been observed in this extended model (the dynamics of polarization domains and the formation of localized structures in this system is studied in chapter 6) [68].

Once a hexagonal pattern is formed, increasing further the intensity of the pump, it may undergo secondary instabilities. Secondary bifurcations of hexagonal patterns have been already experimentally observed, not only in optics [185, 106, 6, 94, 95] but also in hydrodynamical systems [121, 243, 244, 190, 198]. From a theoretical point of view, they have been studied mainly by means of amplitude equations or symmetry-based approaches [46, 47, 213, 236, 114, 33, 78, 191]. In the first case, amplitude equations are only valid close to the primary instability leading to the formation of the pattern, therefore, only secondary bifurcations occurring close to this point can be analyzed. The second technique classifies the different ways in which the spatial symmetry can be broken, however does not predict which instability will occur in a particular model. Is then interesting to study in more detail secondary bifurcations of hexagonal patterns in specific systems. In this chapter we perform a linear stability analysis of hexagonal pattern solutions in the mean field model for a

Kerr cavity. This simple model not only allow us to develop numerical techniques, but also study generic instabilities associated to the self-focusing effect.

For its additional complexity, instabilities of oscillatory modulated solutions have been much less studied. Instabilities of traveling waves have been experimentally observed, for example, in a liquid crystal light valve with a ring mask simulating a 1d system with periodic boundary conditions [195]. A simultaneous period and wavelength doubling route to spatio-temporal chaos has been also reported in a one dimensional coupled map lattice [11]. We have developed a method to perform numerically a Floquet analysis of oscillating modulated solutions. Using this technique, we analyze the tertiary bifurcation of oscillating hexagons. Furthermore, we study subsequent instabilities fully characterizing the transition from regular patterns to spatio-temporal chaos in the Kerr cavity.

This chapter is organized as follows: In Sec. 2.2 we describe the model and perform a linear stability analysis of the homogeneous solution. In Sec. 2.3 we find the stationary hexagonal pattern solutions of the model. Then, in Sec. 2.4, we perform a linear stability analysis of the hexagonal patterns and discuss their different instabilities. In Sec. 2.5, we study the series of bifurcations from a stationary hexagonal pattern to a spatio-temporal chaotic regime called optical turbulence: we perform a Floquet stability analysis of a oscillatory hexagonal pattern and characterize numerically further bifurcations until the turbulent regime is reached. Finally in Sec. 2.6 we give some concluding remarks.

2.2 Model

In the mean field approximation, the dynamics of the electric field inside an optical cavity filled with a Kerr medium can be described by a equation for the scaled slowly varying amplitude of the field $E(\vec{x}, t)$ [150, 56]:

$$\partial_t E = -(1 + i\eta\theta)E + i\nabla^2 E + E_0 + i\alpha\eta|E|^2 E \quad (2.1)$$

where E_0 is the input field, θ the cavity detuning, α the strength of the nonlinearity, $\eta = \pm 1$ determines whether the nonlinearity is of focusing (+) or defocusing (-) type, and ∇^2 is the transverse Laplacian. Eq. (2.1) has been normalized by the cavity decay rate. The homogeneous solution E_s of Eq. (2.1) is given by the following implicit equation:

$$E_0 = E_s[1 - i(\alpha I_s - \theta)] \quad (2.2)$$

where $I_s \equiv |E_s|^2$. The relation between the input and output optical intensities is then given by

$$I_0 = I_s[1 + (\alpha I_s - \theta)^2], \quad (2.3)$$

where $I_0 \equiv |E_0|^2$. It follows from Eq. (2.3) that the cavity is bistable for $\theta > \sqrt{3}$ independently of the sign of the nonlinearity (Fig. 2.1).

Let us consider now the self-focusing case ($\eta = +1$) in more detail. A linear stability analysis of the homogeneous solution with respect to spatially periodic

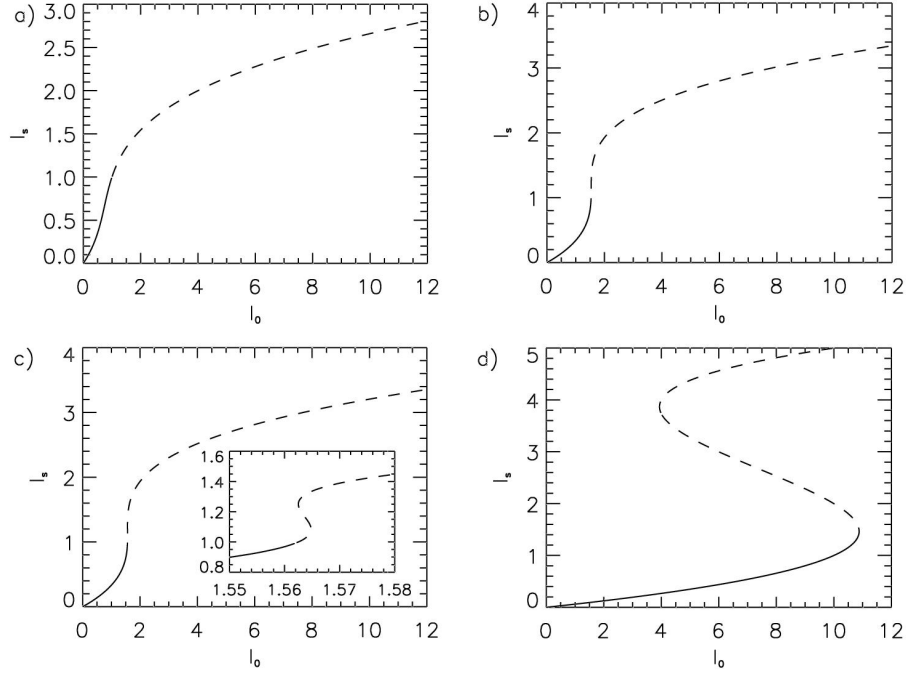


Figure 2.1: Intensity of the homogeneous solution I_s as a function of the input intensity I_0 for a self-focusing Kerr cavity. a) $\theta = 1.0$, b) $\theta = \sqrt{3}$, c) $\theta = 1.75$ (the inset shows a close up of the bistable region) and d) $\theta = 4.0$. $\alpha = 1$. Solid (dashed) lines indicate stable (unstable) solutions.

perturbations yields to the dispersion relation

$$\lambda(\vec{k}) = -1 \pm \sqrt{-(\theta + k^2 - 3\alpha I_s)(\theta + k^2 - \alpha I_s)}, \quad (2.4)$$

where $\lambda(\vec{k})$ is the linear growth rate of a perturbation with wavevector \vec{k} and $k = |\vec{k}|$. Fig. 2.2 shows the marginal stability curve $\lambda(k) = 0$ of the homogeneous solution for different values of the detuning.

For $\theta < \sqrt{3}$ (Figs. 2.1a and 2.2a), the homogeneous solution is monostable, and I_s , directly related to I_0 via Eq. (2.3), can be considered as a proper control parameter. In this case, a pattern forming instability takes place at $I_s = I_{th} = 1/\alpha$ with a critical wavenumber $k_c = \sqrt{2 - \theta}$. For pump intensities above threshold the maximum linear growth rate is for wavevectors with modulus

$$k_u = \sqrt{2\alpha I_s - \theta}. \quad (2.5)$$

At threshold $k_u = k_c$. The selection of the wavenumber k_u (which as follows from Eq. (2.5) and (2.2) depends on the pump intensity I_s) arises from a balance between the diffractive phase modulation k_u^2 , the nonlinear phase modulation $2\alpha I_s$, and the cavity detuning θ . Exact compensation among these three effects, expressed by Eq. (2.5), results in a perfect phase-matching of the four-wave mixing interaction (annihilation of two photons of the steady uniform solution and creation of one pair of photons with opposite transverse wavenumber k_u) that enhances the perturbation, and hence in an optimum gain. Notice that physical values of k_u are real, so that Eq. (2.5) is meaningful only for $\theta < 2$.

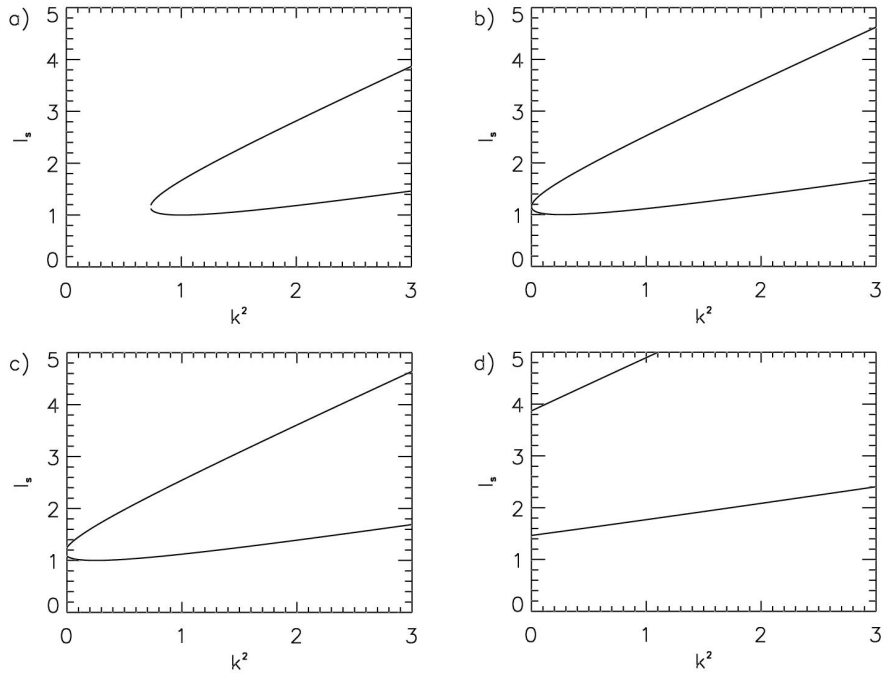


Figure 2.2: Marginal stability curve $\lambda(k) = 0$ for a self-focusing Kerr cavity. a) $\theta = 1.0$, b) $\theta = \sqrt{3}$, c) $\theta = 1.75$ and d) $\theta = 4.0$. $\alpha = 1$.

At $\theta = \sqrt{3}$ the marginal stability curve reaches the vertical axis indicating the threshold for bistability of the homogeneous solution (Figs. 2.1b and 2.2b). For $\sqrt{3} < \theta < 2$ (Figs. 2.1c and 2.2c), as in the previous case, the lower branch is unstable with respect to finite wavenumber perturbations for pump intensities above the threshold I_{th} , while the upper branch is always unstable.

Finally, for $\theta > 2$ the lower branch homogeneous solution is stable, but the upper branch is always unstable with respect to finite transverse wavenumbers perturbations (Figs. 2.1d and 2.2d).

In the self-defocusing case ($\eta = -1$), the pattern forming instability exist only for $\theta > 2$, hence only in conditions of bistability, but, since the upper branch is always stable, the pattern forming instability is frustrated by the bistable switching [211]. Hence, no pattern formation takes place in the defocusing case.

In the following, we will restrict ourselves to the self-focusing case and the non bistable regime $\theta < \sqrt{3}$ ($\theta = 1.0$ and $\alpha = 2$).

2.3 Stationary hexagonal patterns

The linear stability analysis gives information about where the homogeneous solution becomes unstable to small perturbations, but not about the non-trivial solution that may emerge from the bifurcation. In two transverse dimensions, a nonlinear analysis predicts the formation of hexagonal patterns [56, 211]. This is a general feature related to the existence of quadratic nonlinearities in the equation for

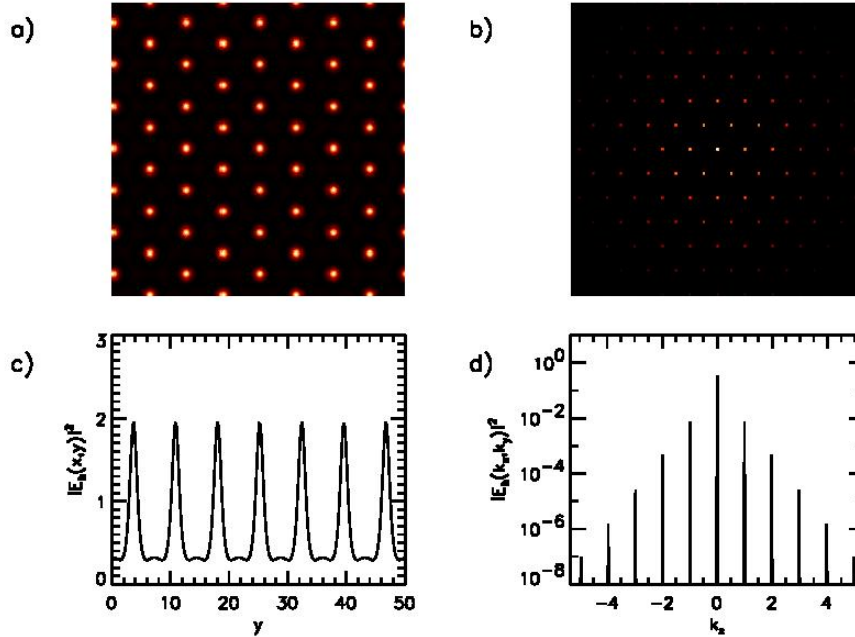


Figure 2.3: $|E(x, y)|^2$ (a) and power spectrum (far-field) $|E(\vec{k})|^2$ (b) of a stationary hexagonal solution. Note the presence in the far-field of the higher harmonics. Panel c shows a cross section along a y axis of the pattern and panel d a cross section along the k_x axis of the power spectrum.

the dynamics of the perturbations of the homogeneous solution. Writing $E(\vec{x}, t) = E_s(1 + A(\vec{x}, t))$ one has from Eq. (2.1)

$$\partial_t A = -[1 + i(\theta - |E_s|^2)]A + i\nabla^2 A + i|E_s|^2(A + A^* + A^2 + 2|A|^2 + |A|^2 A). \quad (2.6)$$

Depending on the value of I_s , the hexagons may appear oscillating. The transition is subcritical and the hexagonal pattern, once it is formed, is stable for a range of values of the pump intensity including values below threshold. In the case of oscillating hexagons, the amplitude of the oscillations decreases when the pump intensity is decreased adiabatically until they become, in all cases, stationary. Due to the subcriticality of the hexagonal patterns, they have always, even at threshold, a finite amplitude. Then, the harmonics of the six fundamental wavevectors have a significant intensity and they have to be considered. This is particularly important in the self-focusing case considered here because the sharp peaks of the pattern have a strongly anharmonic far-field (Figs. 2.3 and 2.4).

The stationary hexagonal patterns can be written in the form

$$E_h(\vec{x}) = \sum_{n=0}^{N-1} a_n e^{i\vec{k}_n^0 \cdot \vec{x}}, \quad (2.7)$$

where \vec{k}_n^0 are the wavevectors of the pattern, a_n are complex coefficients and $N = 91$ is the number of Fourier modes considered in the analysis. \vec{k}_0^0 is the homogeneous mode and \vec{k}_n^0 for $n = 1, N - 1$ are the off-axis wavevectors of the hexagonal pattern

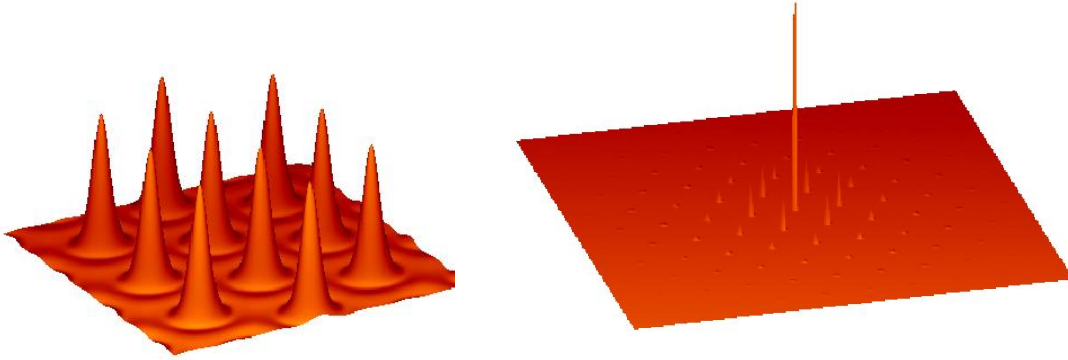


Figure 2.4: 3D view of the stationary hexagonal solution of Fig. 2.3. At the left the near field $|E(\vec{x})|^2$, and at the right the power spectrum (far-field) $|E(\vec{k})|^2$.

containing the six fundamental wavevector with modulus k ($n = 1, 6$) and harmonics up to $5k$. The coefficients a_n can be obtained either by numerical simulations or by solving the stationary form of Eq. (2.1)

$$-(1 + i\theta)E + i\nabla^2 E + E_0 + i2|E|^2 E = 0. \quad (2.8)$$

The second method allows us to find the stationary hexagonal solution with very high accuracy much faster than from numerical simulations. Substituting (2.7) in (2.8) a set of coupled nonlinear equations for the amplitudes of the Fourier components a_n is obtained

$$[-(1 + i\theta) - i|\vec{k}_n^0|^2]a_n + i2 \sum_{l=0}^{N-1} \sum_{m=0}^{N-1} a_l a_m^* a_{n-l+m} = 0, \quad (2.9)$$

where $a_{n-l+m} = a_j$ with $\vec{k}_j^0 = \vec{k}_n^0 - \vec{k}_l^0 + \vec{k}_m^0$. From a suitably chosen initial condition a Newton-Raphson method is used to find solutions of the set of nonlinear equations. The first guess is obtained from a numerical simulation of Eq. (2.1). Once a single stationary solution has been found, any parameter region can be reached by means of continuation techniques [122]. Roughly speaking, these techniques consist in varying by a small amount the control parameters and use the previous stationary solution as initial condition of the Newton method for the new parameter values. With this method the wavenumber k of the hexagonal pattern is treated as a parameter and, therefore, we can look for stationary hexagonal solutions with different fundamental wavenumbers. We can also find unstable stationary hexagonal patterns.

Fig. 2.5 shows the region of existence of stationary hexagons (above the grey solid line). For each value of I_s above threshold there is a whole band of possible stationary hexagonal patterns with very different wavenumbers k . The hexagons are subcritical and therefore exist below the marginal stability curve of the homogeneous solution (black solid line). The lower limit for the existence of a subcritical hexagonal pattern is given by the saddle-node bifurcation where the stable hexagonal pattern

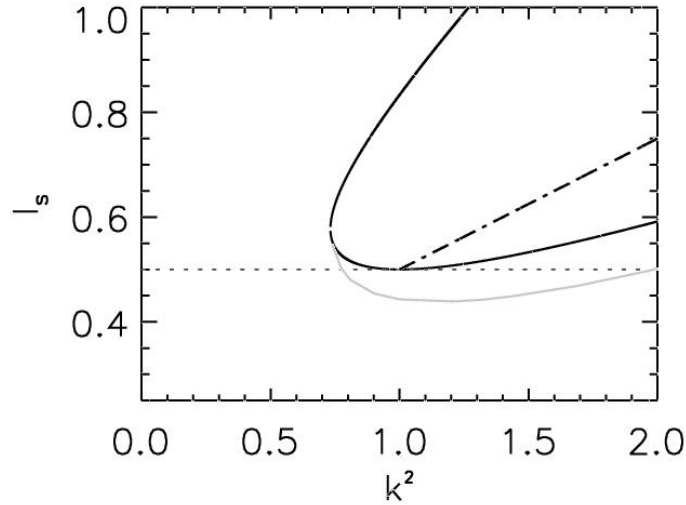


Figure 2.5: Marginal stability curve of the homogeneous solution (solid black line), most unstable wavenumber (dashed line) and the lower limit (saddle-node bifurcation) for the existence of stationary hexagonal patterns (grey line).

branch collides with the unstable branch of hexagonal patterns that starts from the homogeneous solution at the point where $\lambda(k) = 0$ (marginal stability curve).

2.4 Secondary bifurcations of stationary hexagonal patterns

In this section we perform a numerical linear stability analysis of the stationary hexagonal solutions with different fundamental wavenumbers in order to determine their stability as a function of the input power. Our method is a generalization of the technique described in [103]. Linearizing Eq. (2.1) around the stationary solution (2.7) the following equation for the perturbations $\delta E(\vec{x}, t) = E(\vec{x}, t) - E_h(\vec{x})$ is obtained

$$\partial_t \delta E = -(1 + i\theta)\delta E + i\nabla^2 \delta E + i2[2|E_h|^2 \delta E + E_h E_h \delta E^*]. \quad (2.10)$$

The solution of this equation can be written as a superposition of Bloch waves (see Appendix A and [102] for details), and a set of linear equations for the complex amplitudes $\delta a_n(\vec{q}, t)$ of the Fourier modes $e^{i(\vec{k}_n^0 + \vec{q})\vec{x}}$ of the fluctuations $\delta E(\vec{x}, t)$ can be obtained from Eq. (2.10)

$$\begin{aligned} \partial_t \delta a_n(\pm\vec{q}) &= \left[-(1 + i\theta) - i|\vec{k}_n^0 \pm \vec{q}|^2 \right] \delta a_n(\pm\vec{q}) \\ &+ i2 \left[2 \sum_{l=0}^{N-1} \sum_{m=0}^{N-1} a_l a_m^* \delta a_{n-l+m}(\pm\vec{q}) + \sum_{l=0}^{N-1} \sum_{m=0}^{N-1} a_l a_m \delta a_{-n+l+m}(\mp\vec{q}) \right] \end{aligned} \quad (2.11)$$

where $\delta a_{n-l+m}(\vec{q}, t) = \delta a_j(\vec{q}, t)$ with $\vec{k}_j^0 = \vec{k}_n^0 - \vec{k}_l^0 + \vec{k}_m^0$. By considering $\vec{\Sigma}(\vec{q}, t) = (\delta a_1(\vec{q}, t), \delta a_2(\vec{q}, t), \dots, \delta a_N(\vec{q}, t), \delta a_1^*(-\vec{q}, t), \dots, \delta a_N^*(-\vec{q}, t))^T$, Eq. (2.11) can be

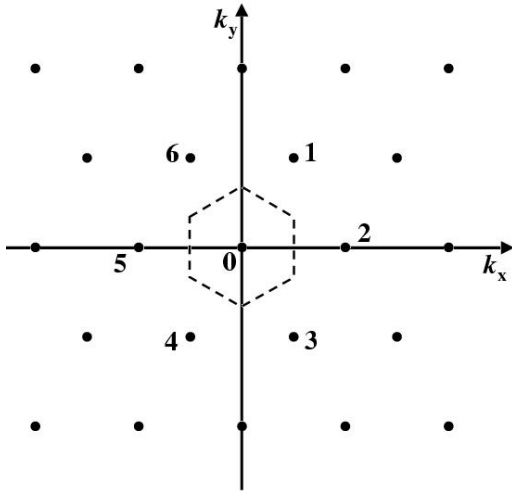


Figure 2.6: First Brillouin zone (dashed hexagon) of the hexagonal lattice defined by the wavevectors of a hexagonal pattern in the Fourier space.

written as

$$\partial_t \vec{\Sigma}(\vec{q}, t) = M(a_n, \vec{q}) \vec{\Sigma}(\vec{q}, t). \quad (2.12)$$

Then, we find the $2N$ eigenvalues $\lambda_n(\vec{q})$ ($n=0, \dots, 2N-1$) of the matrix $M(a_n, \vec{q})$, and its corresponding eigenvectors, for each vector \vec{q} . These eigenvalues may be either real or complex conjugates and determine the stability of the solution against periodic perturbations containing any set of wavevectors $\vec{k}_n^0 \pm \vec{q}$. As explained in Appendix A it is sufficient to explore $1/6$ of the first Brillouin zone¹ plotted in Fig. 2.6. We order the eigenvalues $\lambda_i(\vec{q})$ according to the values of their real part $Re[\lambda_i(\vec{q})] \geq Re[\lambda_{i+1}(\vec{q})]$.

We find that the stationary hexagonal patterns are stable only in the shadowed region of Fig. 2.7. Lines LW (long-wavelength), HS (homogeneous stationary), HO (homogeneous oscillatory) and FW (finite wavelength) indicate different types of instabilities. The places where two instability lines cross correspond to a codimension two bifurcation point. Increasing or decreasing the pump intensity the stable hexagonal patterns may become unstable in different ways depending on their wavenumber. In the following subsections we analyze the different instabilities.

2.4.1 Long-wavelength instability

Hexagons with wavenumbers in region 1 become unstable against long-wavelength perturbations ($\vec{q} \sim 0$) when the pump is changed such that I_s goes across the dashed border (LW). As the hexagonal patterns are the result of a spontaneous breaking of the translational invariance there are continuous families of such patterns characterized by their phases. The present instability is associated to the dynamics of these phases [245] and, for this reason, it is also called *phase instability* (see e.g. [131, 19, 222, 50] for previous work on phase instabilities of hexagons). The branches of eigenvalues $\lambda_{0,1}(\vec{q})$, for small $|\vec{q}|$, have a parabolic shape $Re[\lambda_{0,1}(\vec{q})] \propto |\vec{q}|^2$, and

¹Numerically we change \vec{q} with $\Delta q_x = k/20$ and $\Delta q_y = k \sin(60^\circ)/20$

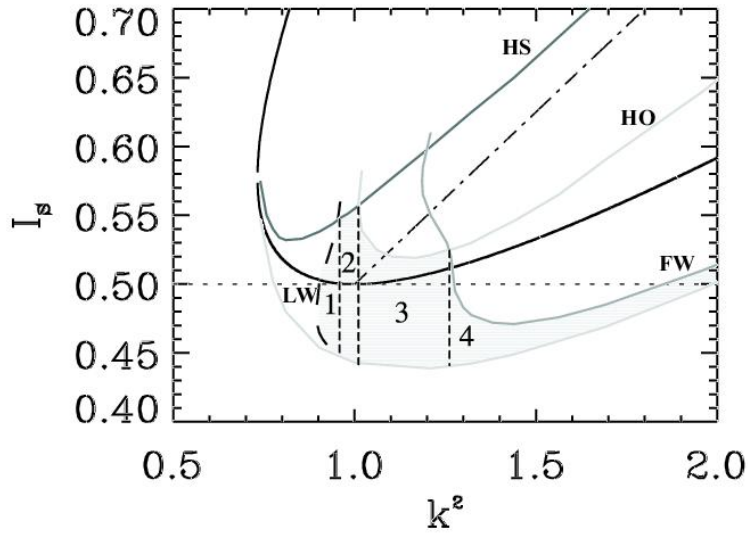


Figure 2.7: Marginal stability diagram of the hexagonal pattern solutions. The shadowed region corresponds to the parameter values where the stationary hexagonal patterns are stable. Each numerated sub-region correspond to hexagonal patterns that undergo different instabilities when the pump is set out of the stable region.

this instability is characterized by a change of their convexity. These branches corresponds to the so called *soft modes* associated to the *Goldstone modes*, the neutrally stable eigenmodes due to the breaking of the translational invariance [64]. More details of the Goldstone modes are given in chapter 3 in connection with its role in determining the fluctuations of a pattern in presence of noise. Fig. 2.8 shows in detail the result of the stability analysis for a hexagonal pattern with $k = 0.95$ for different values of the pump from below to above the instability border of region 1 (LW). A numerical simulation for $I_s = 0.52$, taking as initial condition a stationary unstable hexagonal pattern with $k = 0.95$, shows the development of the instability (Fig. 2.9)². In the first stages of the simulation the unstable wavevectors close to the wavevectors of the hexagonal pattern can be seen growing linearly (second row in Fig. 2.9). Finally the original hexagonal structure is replaced by another hexagonal structure with the same orientation but a larger wavenumber ($k = 1.11$). In finite systems, the minimum change in the wavenumber is imposed by the discrete Fourier space. However this structure is not stationary. As we will see later, for these values of the pump a stationary hexagonal structure with such a wavenumber is unstable and a regime of temporal chaos, we labelled it “chaotic hexagons”, is observed. The long-wavelength instability may take place also by decreasing the pump across the left border of region 1 (LW). As shown in Fig. 2.10, again an hexagonal pattern with the same orientation and larger wavenumber is formed. In this case the stationary pattern is stable.

²Numerical simulations have been performed on a 512×512 rectangular grid with periodic boundary conditions and $\Delta k_x = k/6$ and $\Delta k_y = k \sin(60^\circ)/7$, to fit exactly the hexagonal pattern.

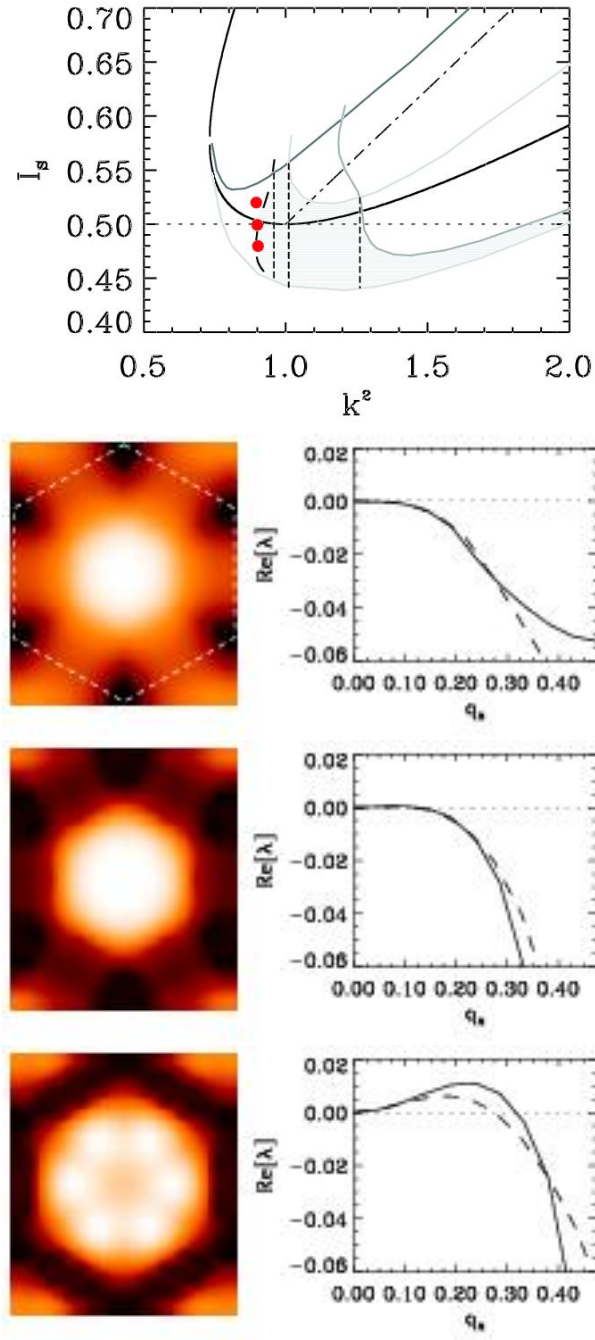


Figure 2.8: Left: $Re[\lambda_0(q_x, q_y)]$ as a function of the vector \vec{q} for a hexagonal pattern with a wavenumber inside the region 1 ($k = 0.95$). The center corresponds to a Goldstone mode $\lambda_0(\vec{q} = 0) = 0$. The dashed line shows the limits of the first Brillouin zone. Dark (bright) color indicates low (large) values of $Re[\lambda_0(q_x, q_y)]$. From top to bottom $I_s = 0.48$ (stable), $I_s = 0.50$ (critical point) and $I_s = 0.52$ (unstable). Right: transverse cut of $Re[\lambda_0(q_x, q_y)]$ along the q_x (solid line) and q_y (dashed line) axis. The spots in the top figure indicate the values of I_s and k in the marginal stability diagram (Fig. 2.7).

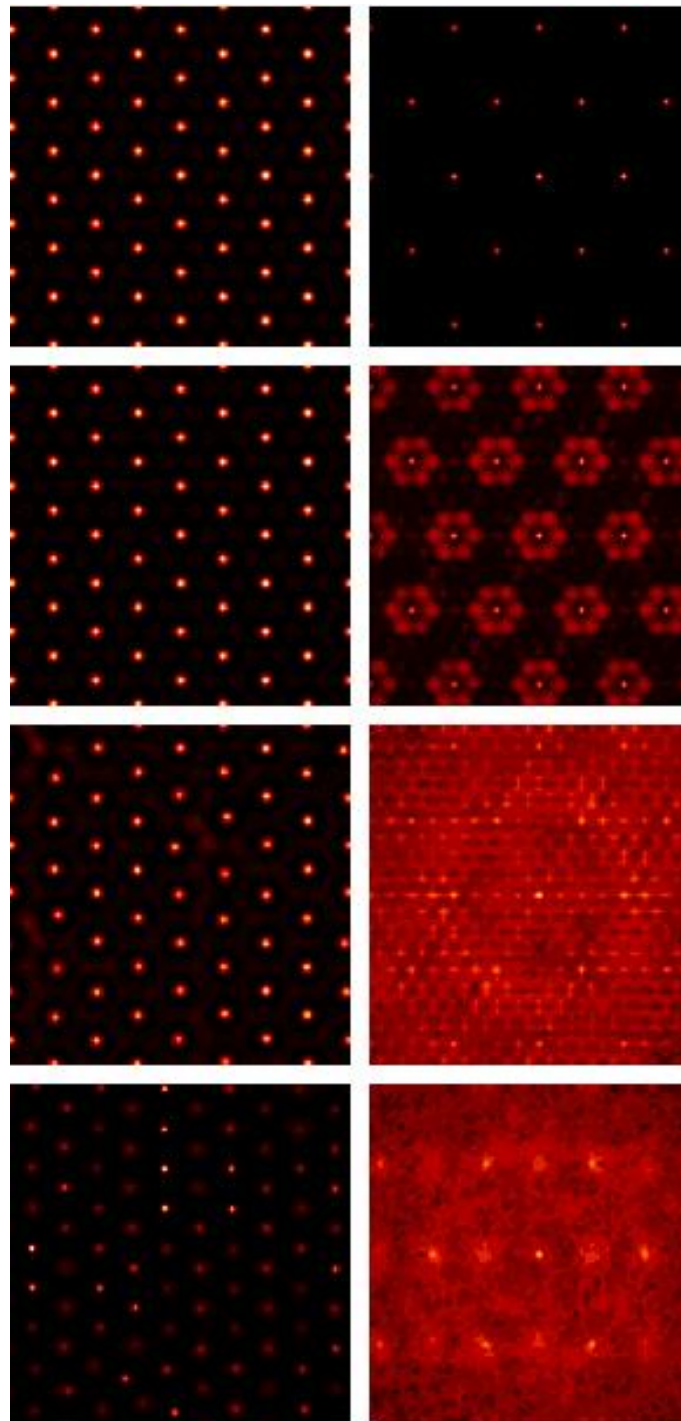


Figure 2.9: Time evolution of the near (left) and far-field (right) of an unstable hexagonal pattern. The wavenumber of the initially unstable hexagons is $k = 0.95$ and $I_s = 0.52$. The time increases from top to bottom. Note in the second row the linear growth of the Fourier components of the Eckhaus unstable modes.

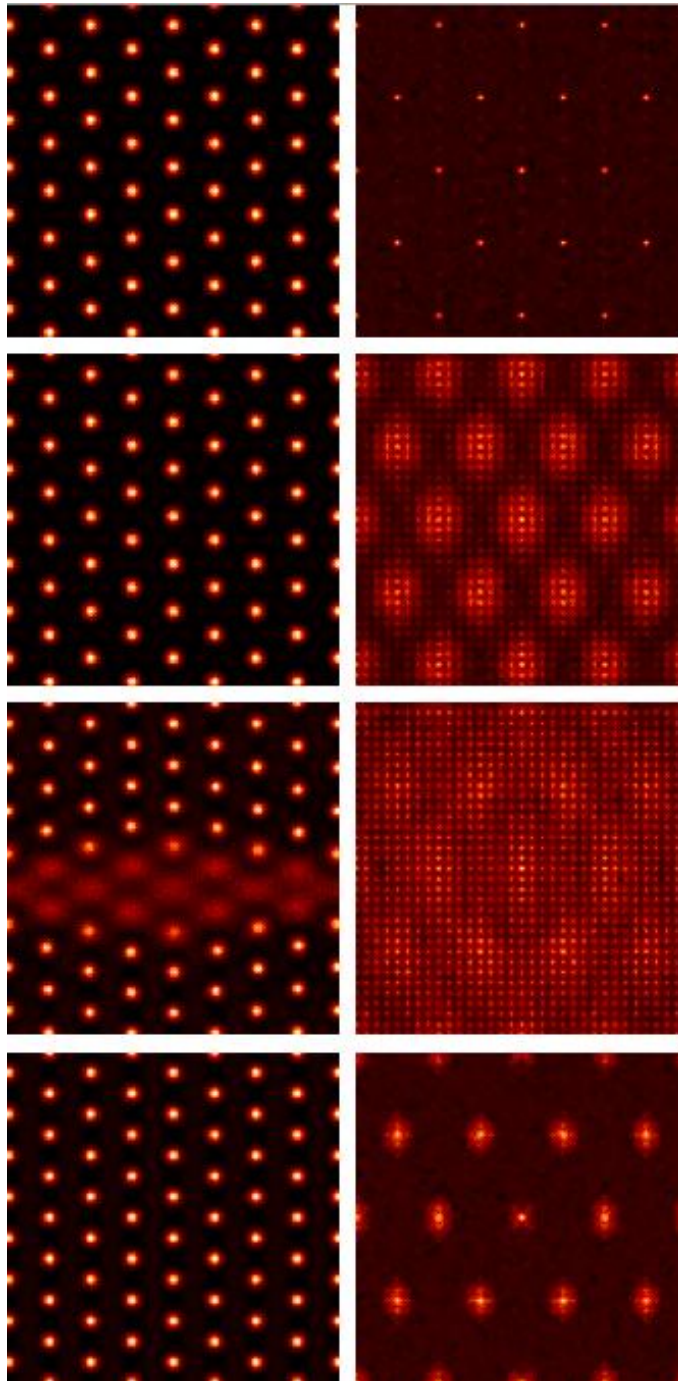


Figure 2.10: The same as in Fig. 2.9 for $I_s = 0.46$. In this case the final state is a stationary hexagonal pattern with one more spot in the y direction.

2.4.2 Amplitude instabilities

Hexagonal patterns within regions 2 and 3 become unstable for perturbations with $\vec{q} = \vec{0}$ when the pump intensity is increased in such a way that I_s goes above the instability lines HS and HO. In region 2 the instability is stationary (HS), while in region 3 it is oscillatory (HO). These instabilities are associated to the growth of complex amplitude perturbations of the Fourier modes of the hexagonal pattern and, therefore, they are called *amplitude instabilities*. These instabilities are characterized by a parabolic branch $\lambda_3(\vec{q})$ centered at $\vec{q} = \vec{0}$ and whose maximum $\lambda_3(\vec{0})$ goes from negative to zero, and then becomes positive. In fact, if we follow strictly the ordering of the eigenvalues, when it becomes positive, the branch $\lambda_3(\vec{q})$ should be called $\lambda_0(\vec{q})$, because it has crossed the two branches associated to the Goldstone modes.

2.4.2.a Stationary instability

In this case $\lambda_3(\vec{q})$ is a branch of real eigenmodes, so, when I_s is increased above the instability line HS the hexagonal patterns undergo a stationary bifurcation (Fig. 2.11). The unstable mode is shown in Fig. 2.12. It has the same spatial wavelength that the pattern but the hexagonal structure in the near field is shifted a distance $l/\sqrt{3}$, where $l = 2\pi/k$ is the wavelength of the original pattern, in the direction forming a 30° angle with the primary pattern. Fig. 2.13 shows a numerical simulation above the region 2 ($I_s = 0.555$) starting with an unstable stationary hexagonal pattern with $k = 1.0$ as initial condition. The unstable mode (Fig. 2.12) predicted by the linear stability analysis can be seen in the second and third rows of Fig. 2.13. As a result, a new shifted hexagonal lattice appears in the near-field. The interaction between the new peaks and those of the primary hexagonal pattern makes them oscillate, in a similar way as will be described in section 2.4.3 for patterns with larger wavenumbers. As a consequence spatial sub-harmonics are also generated. Finally the system ends up into a spatio-temporal chaotic attractor. This last regime will be described in more detail in section 2.5.

2.4.2.b Oscillatory instabilities

In region 3, when the pump is increased above the instability line HO, the stationary hexagonal patterns undergo a homogeneous ($\vec{q} = \vec{0}$) Hopf bifurcation. In this case $\lambda_3(\vec{q})$ and $\lambda_4(\vec{q})$ are branches of complex conjugate eigenvalues. The real part of $\lambda_3(0)$ and $\lambda_4(0)$ become positive at the critical point with a imaginary part ω different from zero (Fig. 2.14). As a result, the hexagonal pattern starts to oscillate uniformly with a period $T = 2\pi/\omega$. Fig. 2.15 shows the result of a simulation for $I_s = 0.52$ starting from a Hopf unstable hexagonal pattern with $k = 1.05$. Since the form of the unstable mode is similar to the stationary pattern, the hexagons simply start to oscillate. The period T of the oscillation (Fig. 2.16) is in very good agreement with the value $T \simeq 4.5$ obtained from the imaginary part of the unstable eigenvalue of the stability analysis.

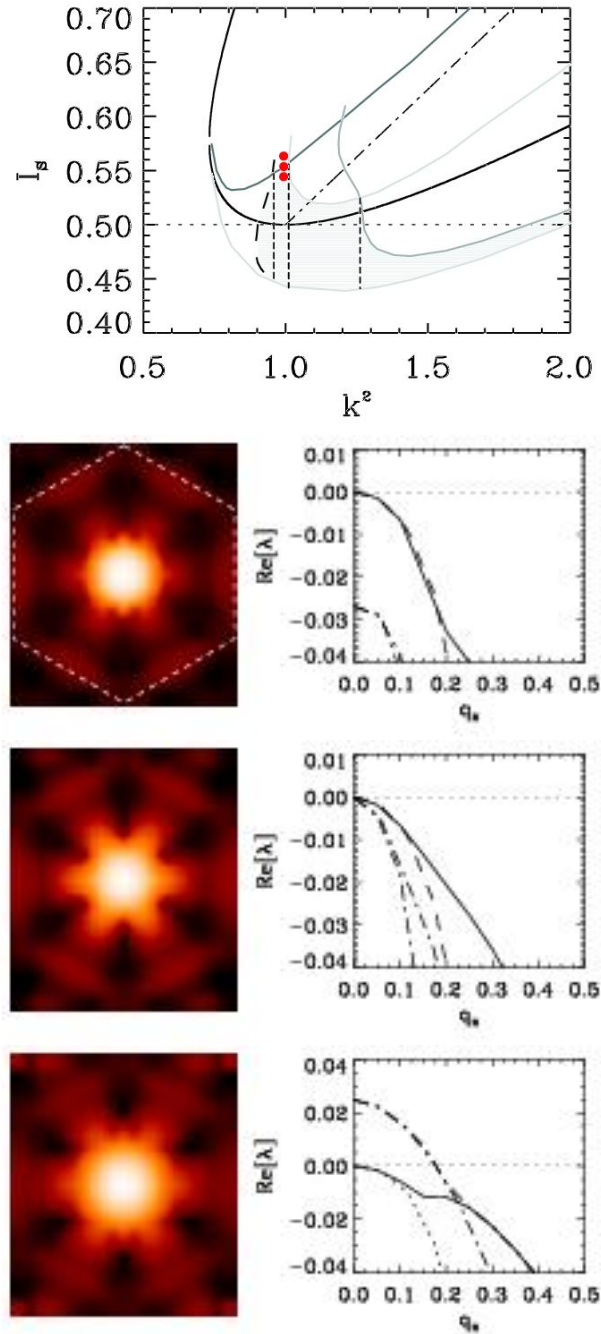


Figure 2.11: The same as in Fig. 2.8 for hexagons with a wavenumber $k = 1.0$ crossing the upper border of region 2. From top to bottom $I_s = 0.55$ (stable), $I_s = 0.555$ (critical point) and $I_s = 0.56$ (unstable). Note that the branch that become unstable (dotted-dashed lines) is not the branch of the Goldstone and soft modes (solid and dashed lines).

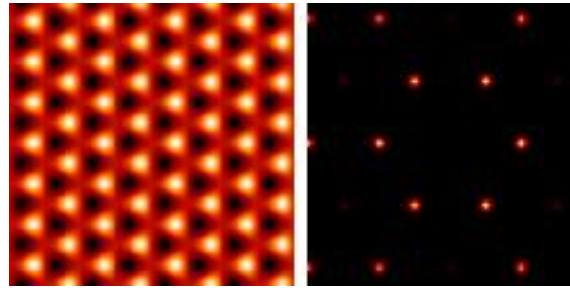


Figure 2.12: Real part of the near field and far-field intensity of the mode than become unstable when the upper border of region 2 is crossed.

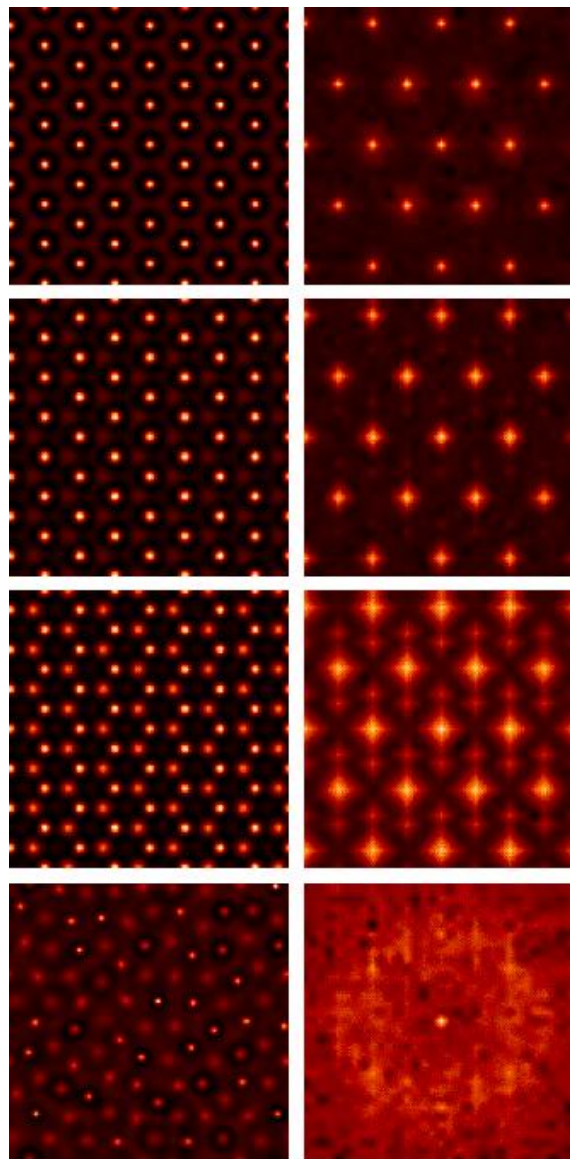


Figure 2.13: The same as in Fig. 2.9 for unstable hexagons from region 2 ($k = 1.0$ and $E_0 = 0.56$). Note in the second row that the spots in the far-field become wider due to the linear growth of the unstable branch around $\vec{q} = 0$ (Fig. 2.11).

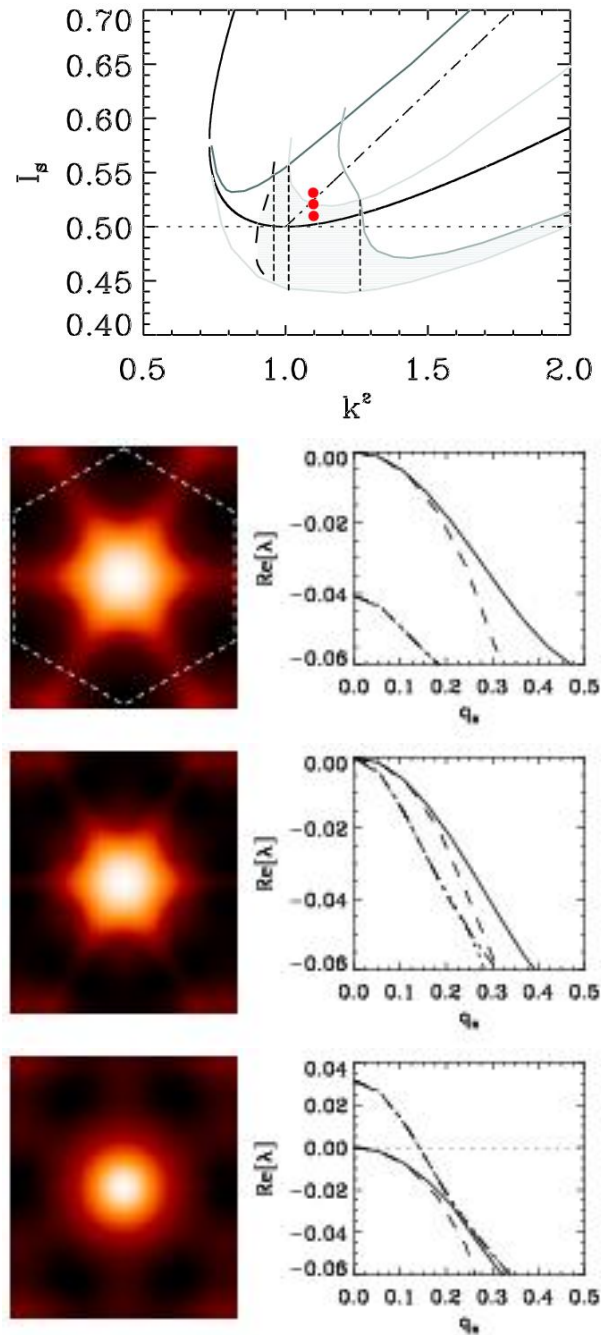


Figure 2.14: The same as in Fig. 2.8 for hexagons with a wavenumber $k = 1.05$, crossing the upper border (HO) of region 3. From top to bottom $I_s = 0.51$ (stable), $I_s = 0.52$ (critical point) and $I_s = 0.53$ (Hopf unstable). In this case, the eigenvalues have a non zero imaginary part.

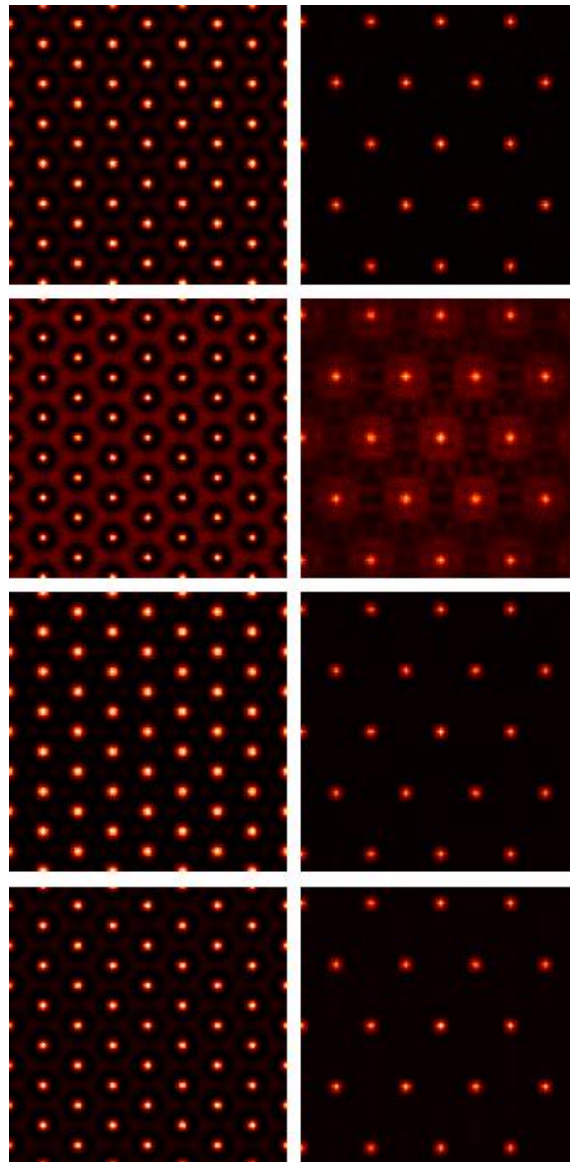


Figure 2.15: The same as in Fig. 2.9 for Hopf unstable hexagons from region 3 ($k = 1.05$ and $E_0 = 0.52$). The final hexagonal pattern oscillates homogeneously.

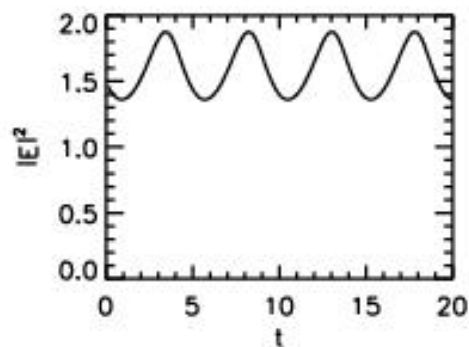


Figure 2.16: Time evolution of the maximum of a hexagonal pattern peak in Fig. 2.15.

2.4.3 Finite wavelength Hopf instability

In the region 4 hexagonal patterns undergo a finite wavelength instability when the pump is increased above the instability line FW (Fig. 2.17). The unstable mode has a vector $\vec{q}_1 = (\vec{k}_1^0 + \vec{k}_2^0)/3$, located on the vertex of the first Brillouin zone ($|\vec{q}_1| = k/\sqrt{3}$) (Fig. 2.18). As a consequence hexagons do not oscillate uniformly, instead they are divided into three superlattices of wavelength $l_1 = \sqrt{3}l$, corresponding to the spatial structure of the unstable eigenmodes (Fig. 2.18). Fig. 2.19 shows the result of a numerical simulation for $I_s = 0.48$ starting from an unstable hexagonal pattern with $k = 1.15$. The peaks in each superlattice oscillate synchronously. Two of the superlattices oscillate in antiphase with a relatively large amplitude while the third oscillate at twice that frequency and has a smaller amplitude. Fig. 2.20 shows the time evolution of one of the peaks of each superlattice as well as the power spectrum corresponding to the time trace plotted with a solid line. As shown in the power spectrum, the frequency of the oscillations is in very good agreement with the value $\omega_1 = \text{Im}[\lambda_0(\vec{q}_1)] \simeq 1.0$ obtained from the imaginary part of the unstable eigenvalues of the stability analysis (plotted with a dashed line).

Physically this reflects an interchange of energy between two of the superlattices, mediated by the third while the total energy remains practically constant. Both in the homogeneous and finite wavelength Hopf instabilities, the high Fourier harmonics play an important role in the oscillations. Neglecting or filtering out successive rings of high harmonics shift the bifurcations to larger pump values and may eventually suppress the bifurcations altogether [160, 102, 133]. Therefore the oscillations are associated to a transfer of energy from large scales to small scales. The bifurcation is supercritical, close to I_1 amplitude of the oscillations grows as $\sqrt{I_s - I_1}$ as shown in Fig. 2.21. Mathematically, this bifurcation is a spatial-period multiplying [236]. Stationary instabilities with the same wavevector \vec{q}_1 has been observed in surface waves [121] leading to superlattices.

This instability can be also understood as a collective behavior of a hexagonal lattice of coupled oscillators. We will see in chapter 5 that this system can support localized structures (Kerr Cavity Solitons), which can be basically considered as isolated peaks of a hexagonal pattern. We will show how these peaks have also an oscillatory instability. The dynamics of this coherent structures is essentially two dimensional, and therefore the hexagonal pattern can be interpreted as a hexagonal lattice of coupled oscillators. The coupling between to nearby peaks comes through diffraction. When the wavevector of the pattern is small (as it is the case for the patterns in region 3) the peaks are quite far away from each other, and the coupling is small. Then the system prefers to oscillate synchronously. Patterns in region 4 have a larger wavenumber and therefore a larger coupling between the peaks. In this circumstance a splitting in three superlattices is selected.

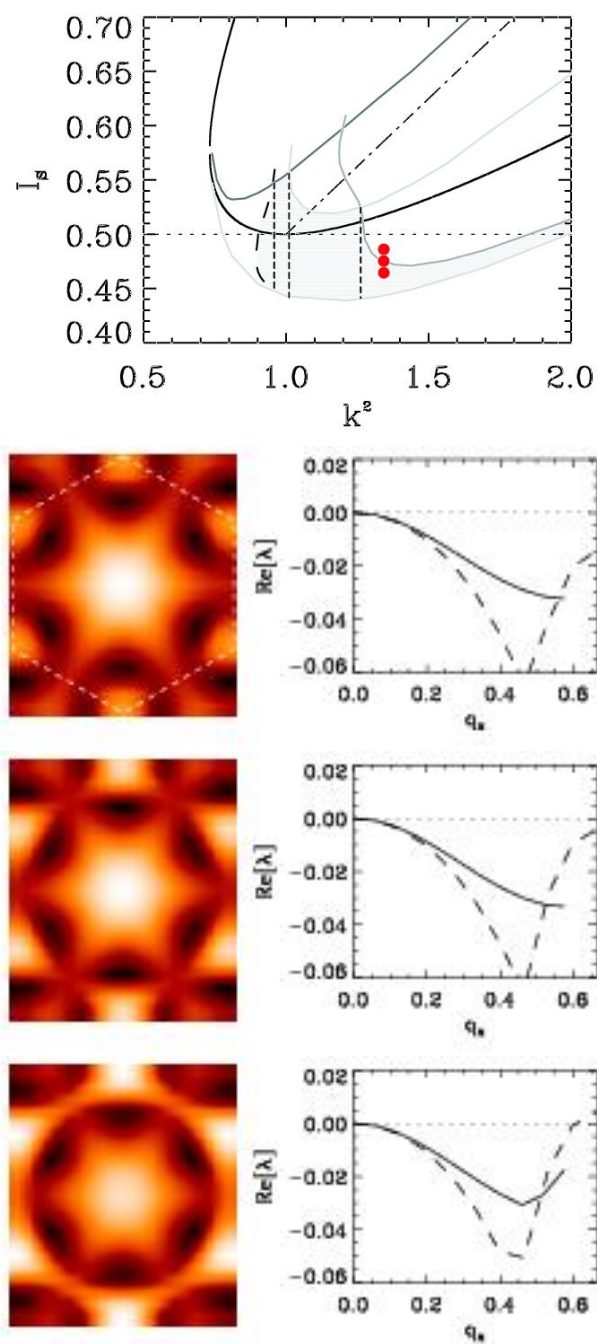


Figure 2.17: The same as in Fig. 2.8 for hexagons with a wavenumber $k = 1.15$, crossing the upper border (FW) of region 4. From top to bottom $I_s = 0.47$ (stable), $I_s = 0.475$ (critical point) and $I_s = 0.48$ (Hopf unstable).

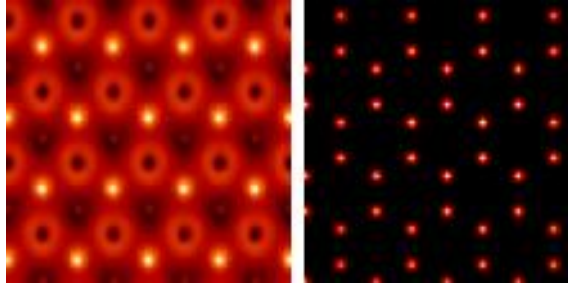


Figure 2.18: Near and far-field of the mode than become unstable when the upper line of region 4 (FW) is crossed.

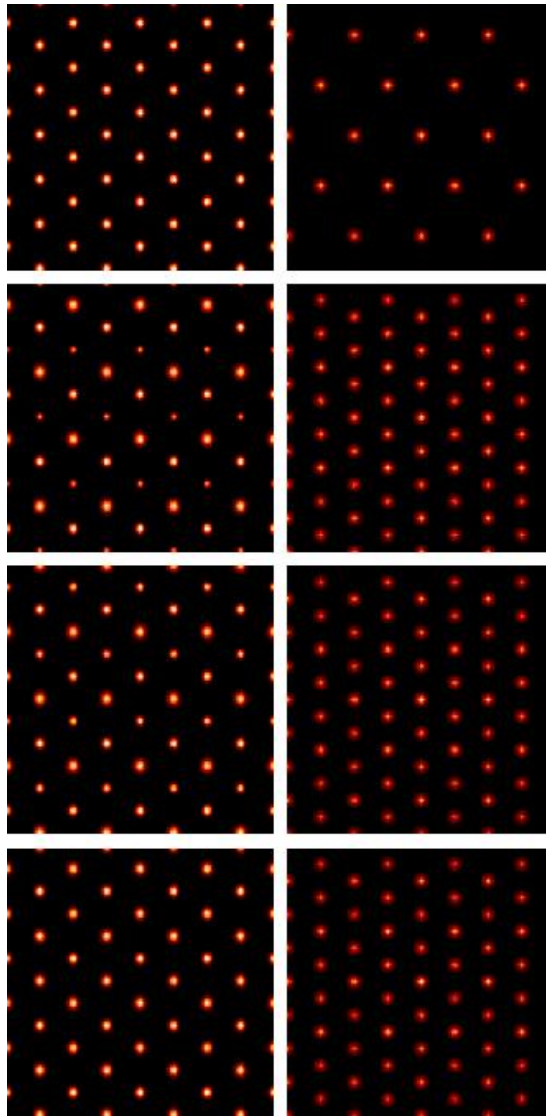


Figure 2.19: Time evolutions of $|E(\vec{x}, t)|^2$ (left) and $|E(\vec{k}, t)|^2$ (right) for Hopf unstable hexagons from region 4 ($k = 1.15$ and $I_s = 0.48$). The hexagons do not oscillate homogeneously but nearby peaks are dephased. A super-structure corresponding to the unstable mode of Fig. 2.18 with a wavenumber $k/\sqrt{3}$ can be seen in the simulation.

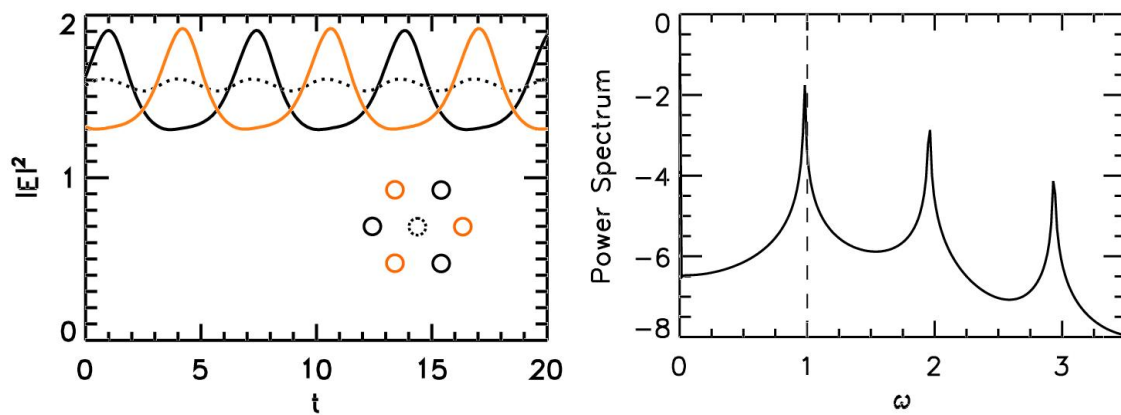


Figure 2.20: Left: Time evolution of the maximum of three dephased peaks of the hexagonal pattern in Fig. 2.19. Right: Power spectrum of the time trace plotted with a solid line on the left. The value of the frequency of the oscillations predicted by the stability analysis is indicated with a vertical dashed line.

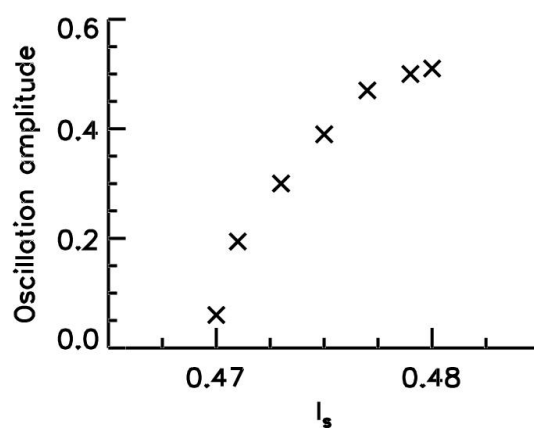


Figure 2.21: Amplitude of the oscillations as a function of the control parameter I_s .

2.5 Transition to spatio-temporal chaos

In this section we study the transition to spatio-temporal chaos of a stationary pattern in region 4 with wavenumber $k = 1.15k_c$ ($k^2 = 1.3225$). Such a pattern can be spontaneously formed by decreasing adiabatically the pump from a initial non stationary pattern formed at $I_s = 1.1I_s^c$ (for which $k_u = 1.15k_c$). Hexagons with smaller wavenumbers usually undergo instabilities that change their wavenumbers to larger values, ending in spatio-temporal regimes characteristic of the transition to spatio-temporal chaos of patterns in region 4, thus making the case we consider the most relevant one. As shown in sub-section 2.4.3 this stationary hexagonal pattern undergoes a finite wavelength Hopf instability. Here we analyze in detail the tertiary bifurcation of the oscillating superlattices and further instabilities until optical turbulence is reached. The sequence of instabilities is illustrated in Fig. 2.22

2.5.1 Floquet analysis of oscillating hexagons

We next analyze the stability of the periodically oscillating hexagons resulting from the finite wavelength Hopf instability explained in sub-section 2.4.3. The oscillating hexagons are a limit cycle solution of Eq. (2.1), which can be written in the form

$$E_{oh}(\vec{x}, t) = \sum_{n=0}^{N-1} a_n(t) e^{i\vec{k}_n^0 \vec{x}}, \quad (2.13)$$

where $a_n(t)$ are time periodic coefficients with period $T_1 = 2\pi/\omega_1$ ($a_n(t + T_1) = a_n(t)$). As in section 2.4, we include all the modes up to $5k$, therefore we have now a large number of sub-harmonics that have been excited in the finite wavelength Hopf bifurcation, so, now we have $N = 369$. Linearizing Eq. (2.1) around the limit cycle solution (2.13) the following equation for the fluctuations $\delta E(\vec{x}, t) = E(\vec{x}, t) - E_{oh}(\vec{x}, t)$ is obtained

$$\partial_t \delta E = -(1 + i\theta) \delta E + i\nabla^2 \delta E + i2[2|E_{oh}|^2 \delta E + E_{oh} E_{oh} \delta E^*]. \quad (2.14)$$

In a similar way as in section 2.4, the solution of this equation can be written as a superposition of Bloch waves (see Appendix A), and a set of linear equations for the complex amplitudes $\delta a_n(\vec{q}, t)$ of the Fourier modes $e^{i(\vec{k}_n^0 + \vec{q})\vec{x}}$ of the fluctuations $\delta E(\vec{x}, t)$ can be obtained from Eq. (2.14)

$$\begin{aligned} \partial_t \delta a_n(\pm\vec{q}, t) = & [-(1 + i\theta) - i|\vec{k}_n^0 \pm \vec{q}|^2] \delta a_n(\pm\vec{q}, t) \\ & + i2\{2 \sum_{l=0}^{N-1} \sum_{m=0}^{N-1} a_l(t) a_m^*(t) \delta a_{n-l+m}(\pm\vec{q}, t) \\ & + \sum_{l=0}^{N-1} \sum_{m=0}^{N-1} a_l(t) a_m(t) [\delta a_{-n+l+m}(\mp\vec{q}, t)]^*\}, \end{aligned} \quad (2.15)$$

where $\delta a_{n-l+m}(\vec{q}, t) = \delta a_j(\vec{q}, t)$ with $\vec{k}_j^0 = \vec{k}_n^0 - \vec{k}_l^0 + \vec{k}_m^0$. By considering $\vec{\Sigma}(\vec{q}, t) = (\delta a_1(\vec{q}, t), \delta a_2(\vec{q}, t), \dots, \delta a_N(\vec{q}, t), \delta a_1^*(-\vec{q}, t), \dots, \delta a_N^*(-\vec{q}, t))^T$, Eq. (2.15) reads

$$\partial_t \vec{\Sigma}(\vec{q}, t) = M(a_n(t), \vec{q}) \vec{\Sigma}(\vec{q}, t). \quad (2.16)$$

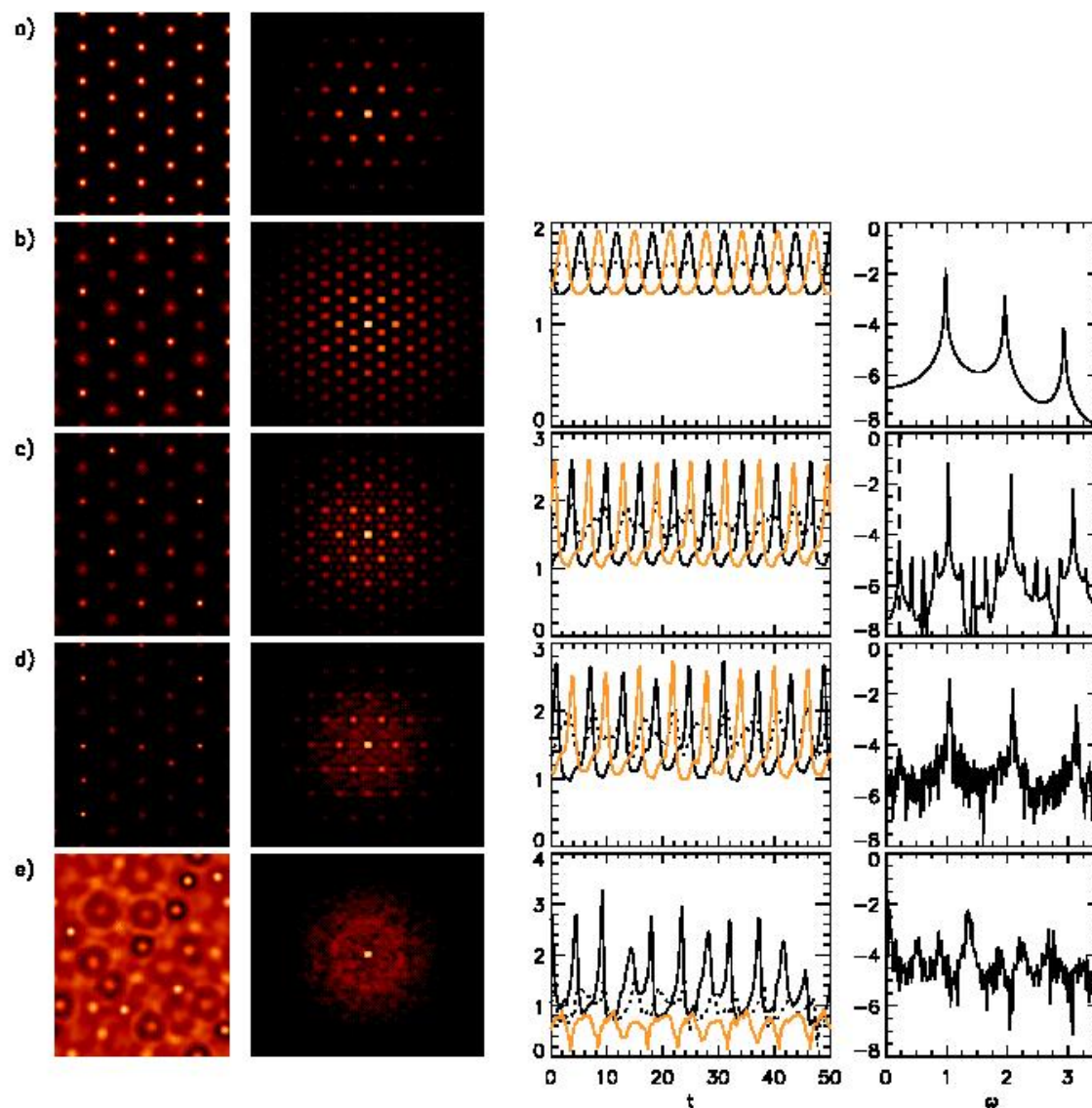


Figure 2.22: Spatio-temporal regimes of a hexagonal pattern: From top to bottom, stationary ($I_s = 0.46$), periodic ($I_s = 0.48$), quasiperiodic ($I_s = 0.525$), chaotic ($I_s = 0.54$) and spatio-temporal chaos ($I_s = 0.62$). From left to right: $|E(\vec{x})|^2$, $|E(\vec{k})|^2$, time evolution of three hexagonal peaks (see text) and power spectra corresponding to the time trace plotted with a solid line.

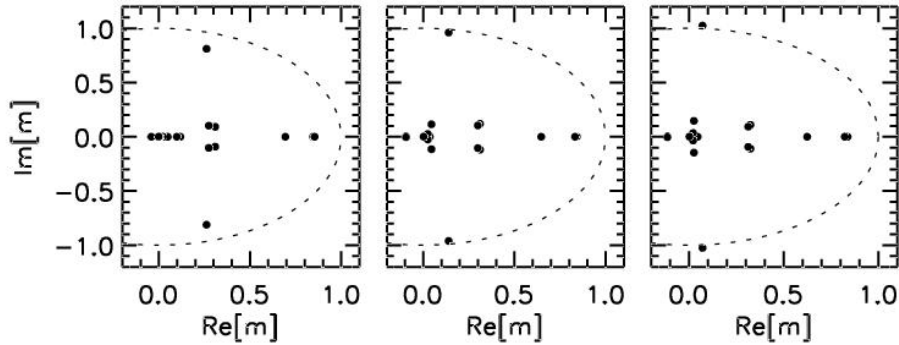


Figure 2.23: Floquet multipliers for perturbations with $\vec{q} = \vec{q}_2$ for (from left to right) $I_s = 0.51, 0.52, 0.525$.

Eq. (2.16) is a set of linear differential equations with time-periodic coefficients, so, by the Floquet theorem the general solution has the form

$$\vec{\Sigma}(\vec{q}, t) = \vec{\Sigma}(\vec{q}, 0)P(t)e^{\Lambda(\vec{q})t} \quad (2.17)$$

where $P(t)$ is a period- T_1 matrix and $\Lambda(\vec{q})$ is a time-independent matrix. The limit cycle is numerically determined integrating Eq. (2.1) over a period T_1 . Simultaneously, the matrix $e^{\Lambda(\vec{q})T_1}$ is computed integrating Eq. (2.16) [26]. The $2N$ eigenvalues of the matrix $e^{\Lambda(\vec{q})T_1}$ (Floquet multipliers) $m_j(\vec{q})$, determine the stability of the oscillating hexagons under any possible perturbation with wavevectors $\vec{k}_n^0 \pm \vec{q}$. It is sufficient to explore $1/6$ of the first Brillouin zone of the new hexagonal lattice in Fourier space whose fundamental wavevectors have a modulus $k/\sqrt{3}$.

The oscillating hexagons have one Floquet multiplier with value 1 corresponding to the neutral mode associated to the translation along the limit cycle. For pump intensities $0.470 < I_s < 0.523$ all the Floquet multipliers (except the neutral mode) have modulus smaller than one and therefore the oscillating hexagons are stable. For $I_s = 0.523$ there is a couple of complex conjugate Floquet multipliers with non-vanishing imaginary part that cross the unit circle (Fig. 2.23). This signals a Neimark-Sacker bifurcation [122] which introduces a new temporal frequency $\omega_2 = \text{Im}[\log(m_0(\vec{q}_2))]/T_1 = 0.220$ and, therefore, the temporal behavior will be quasiperiodic. The frequency predicted from the Floquet analysis, vertical dashed line in Fig. 2.22c, is in very good agreement with the second frequency present in the quasiperiodic time series obtained from numerical simulations of Eq. (2.1). The Floquet multipliers with modulus greater than one are those for perturbations with $\vec{q}_2 = (\vec{k}_1^0 + \vec{k}_2^0)/3$ located at the vertex of the new Brillouin zone, being $\vec{k}_{1,2}^0$ fundamental wavevectors of the new lattice. Since the fundamental wavevectors have now a modulus $k/\sqrt{3}$, $|\vec{q}_2| = k/3$. Thus, this second bifurcation introduces also a new characteristic wavelength $l_2 = \sqrt{3}l_1 = 3l$ (Fig. 2.22c). At this point the solution the system displays has three characteristic spatial wavelength and two temporal frequencies. The spatial structure of this series of bifurcations is the equivalent in hexagonal patterns to the wavelength doubling bifurcations found in 1d systems. The temporal behavior, however, does not correspond to period doubling but to a quasiperiodic route.

2.5.2 From quasiperiodicity to chaos

The quasiperiodic oscillating hexagons are stable for pump intensities $0.523 < I_s \lesssim 0.528$. Note that the parameter range between successive bifurcations decreases. Numerical simulations done for different system sizes, including very large systems, indicate that the quasiperiodic hexagons become unstable for $I_s \sim 0.528$. A close inspection to the far-field shows that the system becomes unstable against long-wavelength perturbations. A continuum of small wavevectors ($q \sim 0$) grow and the whole background of Fourier modes become excited (Fig. 2.22d). Peaks are still located on a hexagonal lattice but the spatial structure of the oscillations is lost, so this is somehow a regime of spatio-temporal chaos on top of a hexagonal lattice. The continuum of excited Fourier modes have a continuum of associated temporal frequencies that make the oscillations of the peaks temporally chaotic, showing a broad-band power spectrum (Fig. 2.22d). The temporal behavior of the system would fit within the Ruelle-Takens scenario in that a chaotic regime is observed after the instability of a torus. However this scenario do not say anything about the spatial structure of the system which play also an important role in the transition to spatio-temporal chaos. We have seen that each bifurcation introduce a new spatial wavelength making the system spatially more complicated. Chaotic hexagons are observed in a quite broad parameter range ($0.528 \lesssim I_s \lesssim 0.62$)

2.5.3 Transition to optical turbulence

For pump intensities above $I_s \sim 0.62$ a sudden change occurs. The spatial order is completely lost and all the Fourier modes with wavenumber close to k_u become equally excited (Fig. 2.22e). This is a regime of spatio-temporal chaos where peaks at random positions suddenly grow and decay. There is a persistence time so once a peak grows in a given position, it oscillates several times around the same position. Later on, the peaks grow in other positions. As the pump is increased the amplitude of the oscillations becomes larger and the persistence time shorter. The peaks burst producing circular waves that propagate in the transverse plane and dissipate away [175], a behavior similar to Langmuir turbulence in plasmas [197, 221]. As discussed in chapter 1 Eq. (2.1) is, in fact, a modified nonlinear Schrödinger equation, and the phenomenon of wave collapse [202] is behind the oscillation of the peaks in our system [175]. Peaks grow following the self-similar collapse law and, before collapse takes place, they are damped by losses [82]. This regime of optical turbulence is the attractor of the dynamics starting from the homogeneous solution. In fact, it was already an attractor of the dynamics for lower values of the pump, coexisting with the chaotic hexagons. The sudden change from oscillating hexagons to this regime is characteristic of a system undergoing a crisis [183, 18, 165]. In particular, our case is very similar to the pattern resonance described for a 1d system [104] where a temporally chaotic state leads to a spatio-temporal chaos regime due to a resonance with a pre-existent unstable solution, which here could be any of the solutions that lost their stability at the previous bifurcations (stationary, periodic or quasiperiodic hexagons).

2.6 Conclusions

In this chapter we have first analyzed in detail the secondary bifurcations of stationary hexagonal patterns in a prototype model of nonlinear optics. The stability analysis of the stationary hexagonal patterns predicts different instabilities depending on their fundamental wavenumber. Hexagons with wavenumbers smaller than the critical one undergo phase instabilities, patterns with wavenumbers close to the critical one undergo stationary and oscillatory amplitude instabilities, and hexagons with larger wavenumbers undergo finite wavelength Hopf instabilities leading to three superlattices oscillating periodically in antiphase.

We have also studied in detail the complete transition to optical turbulence for a stationary hexagonal pattern after it has undergone the finite wavelength Hopf bifurcation. The periodic oscillating hexagons undergo a Neimark-Sacker bifurcation, which introduces a new incommensurate frequency, leading to a subsequent division in three of each superlattice. For larger pumps a long-wavelength instability, which is present only in extended systems, leads to chaotically oscillating peaks which, nevertheless, are still located on a hexagonal lattice. Finally the system loses completely the spatial order, probably through a crisis, entering in a regime of spatio-temporal chaos called optical turbulence. We expect the scenario presented here to be relevant for other systems displaying hexagonal patterns whose peaks undergo an oscillatory instability. Also the sequence of transitions up to chaotic hexagons can be relevant for hexagonal lattices of coupled oscillators.

At difference with low dimensional dynamical systems, where different scenarios for the transition to chaos have been established, in spatially extended systems this transition is only partially understood. In our case, while the temporal behavior would fit in the Ruelle-Takens scenario, the breaking of the spatial synchrony would rather be a generalization of the one dimensional spatial period doubling [11]. The role of the spatial degrees of freedom in the transition from regular patterns to spatio-temporal chaos is, then, still an open question.

These results does not change significantly for small changes of the detuning parameter. Qualitative changes are observed for somehow much larger detunings, close to the bistability of homogeneous solution ($\theta = \sqrt{3}$). The nascent bistability is known to favor the formation of localized structures [227], and the existence of localized structures may strongly modify the region of existence and stability of the hexagonal patterns.

Chapter 3

Fluctuations and correlations in hexagonal patterns

3.1 Introduction

In this chapter we study the fluctuations and correlations of a subcritical hexagonal pattern in a Kerr cavity. The properties of the fluctuations and correlations have been widely studied in supercritical stripe patterns that appear in different optical models [152, 155, 27, 108, 110, 250]. In supercritical bifurcations, close to the threshold for pattern formation, the harmonics of the fundamental wavevectors can be neglected. Therefore stripe patterns are usually described in terms of the homogeneous mode and the two modes of the stripes which simplifies the problem allowing for an analytic treatment. The analysis of fluctuations in optical stripe patterns considering the whole infinite set of transverse modes has been addressed numerically in [250]. At difference with the few modes approximation, the continuous problem makes evident the role of the so called soft modes in the fluctuations of the near field. However a very good agreement between the few modes approximation and the continuous treatment is still found for the correlations of the fluctuations of the far-field mode intensities close to threshold.

Due to the additional complexity, fluctuations and correlations in hexagonal optical patterns have been much less studied [97, 74]. Furthermore, these two papers use an approximation in few modes to describe the pattern, which in the case of subcritical patterns is not fully justified.

Here we treat the case of a subcritical hexagonal pattern using a continuous model, i.e., avoiding any restriction to a reduced number of spatial modes. In particular, we consider the same system as in the previous chapter: an optical cavity filled with a nonlinear isotropic Kerr medium. We find that the fluctuations of the near-field are dominated by the two Goldstone modes associated to the translational invariance in the x and y directions, and by the soft modes close to them in large systems. We also show that the modes that dominate the near-field fluctuations do not contribute at first order in noise intensity to the far-field intensity fluctuations.

We identify the modes responsible for the far-field intensity correlations and we find: (a) strong correlations between arbitrary pairs of wavevectors of the pattern, but stronger between those forming a 120° angle; (b) anti-correlation between the zero wavevector of the spectrum of fluctuations and any wavevector of the pattern. While the anti-correlation of the homogeneous mode with the off-axis wavevectors can be understood in terms of energy conservations, the common microscopic interpretation of the far-field intensity correlations in terms of emission of twin photons would naively suggest that the strongest correlation is between the wavevectors forming a 180° angle. In fact, the total transverse momentum conservation involve always at least four modes simultaneously and give some hints about how the correlations should be, but does not identify the pairs with stronger correlations. Our results here are obtained within a semi-classical approach in which specific features of quantum statistics are neglected.

This chapter is organized as follows: In Sec. 3.2 we describe the model we are considering. In Sec. 3.3 we linearize around the hexagonal pattern and describe the linear response of the system to noise perturbations. In Sec. 3.4 we discuss in detail the field fluctuations, and in Sec. 3.5 we describe the correlations of the field Fourier components. Finally, in Sec. 3.6 we give some concluding remarks.

3.2 Description of the model

As in chapter 2, an optical cavity filled with an isotropic Kerr medium can be described in terms of the Lugiato-Lefever model, however, in order to study the fluctuations and correlations of the hexagonal pattern, we need to introduce a source of noise in the model. We follow an approach previously used in a one-dimensional version of this model [7], and in a vectorial model including the polarization degree of freedom of the light [108]. In a semiclassical description of the problem we can represent different sources of fluctuations by adding noise to the right-hand side of Eq. (2.1)

$$\partial_t E = -(1 + i\theta)E + i\nabla^2 E + E_0 + i2|E|^2 E + \xi(\vec{x}, t), \quad (3.1)$$

where E is the scaled slowly varying amplitude of the field, E_0 is the input field, θ is the cavity detuning, ∇^2 is the transverse Laplacian and $\xi(\vec{x}, t)$ is a complex Gaussian white noise with zero mean and correlations

$$\begin{aligned} \langle \xi(\vec{x}, t) \xi^*(\vec{x}', t') \rangle &= \epsilon \delta(\vec{x} - \vec{x}') \delta(t - t') \\ \langle \xi(\vec{x}, t) \xi(\vec{x}', t') \rangle &= 0. \end{aligned} \quad (3.2)$$

3.3 Linearization around a hexagonal pattern

The stationary hexagonal pattern can be written in the form

$$E_h(\vec{x}) = \sum_{n=0}^N a_n e^{i\vec{k}_n^0(\vec{x} - \vec{x}_0)}. \quad (3.3)$$

where \vec{x}_0 is the origin of the hexagons in the near field, \vec{k}_0^0 correspond to the homogeneous mode and \vec{k}_n^0 for $n = 1, \dots, N$ are the off-axis wavevectors of the hexagonal pattern. As in the previous chapter, we take $N = 90$ which corresponds to considering up to the fifth order harmonics in the far-field. The six fundamental harmonics have modulus k . Linearizing Eq. (3.1) around the stationary solution (3.3) the following equation for the fluctuations $\delta E(\vec{x}, t) = E(\vec{x}, t) - E_h(\vec{x})$ is obtained

$$\partial_t \delta E = -(1 + i\theta)\delta E + i\nabla^2 \delta E + i2[2|E_h|^2 \delta E + E_h E_h \delta E^*] + \xi(\vec{x}, t). \quad (3.4)$$

As in Sec. 2.4 we decompose the fluctuations and the noise term in Bloch waves (see Appendix A) and, from Eq. (3.4), we obtain a set of linear equations for the complex amplitudes $\delta a_n(\vec{q})$ of the Fourier modes $e^{i(\vec{k}_n^0 + \vec{q})\vec{x}}$ of the fluctuations $\delta E(\vec{x}, t)$

$$\begin{aligned} \partial_t \delta a_n(\pm \vec{q}, t) = & [-(1 + i\theta) - i|\vec{k}_n^0 \pm \vec{q}|^2] \delta a_n(\pm \vec{q}, t) + i\{4 \sum_l^N \sum_m^N a_l a_m^* \delta a_{n-l+m}(\pm \vec{q}, t) \\ & + 2 \sum_l^N \sum_m^N a_l a_m [\delta a_{-n+l+m}(\mp \vec{q}, t)]^*\} + \xi_n(\vec{q}, t), \end{aligned} \quad (3.5)$$

where $\delta a_{n-l+m}(\vec{q}, t) = \delta a_j(\vec{q}, t)$ with $\vec{k}_j^0 = \vec{k}_n^0 - \vec{k}_l^0 + \vec{k}_m^0$ and $\xi_n(\vec{q}, t)$ is the complex amplitude of the $e^{i(\vec{k}_n^0 + \vec{q})\vec{x}}$ Fourier component of the noise $\xi(\vec{x}, t)$. By considering $\vec{\Sigma}(\vec{q}, t) = (Re[\delta a_0(\vec{q}, t)], Im[\delta a_0(\vec{q}, t)], \dots, Im[\delta a_N(\vec{q}, t)], Re[\delta a_0(-\vec{q}, t)], \dots, Im[\delta a_N(-\vec{q}, t)])^T$ and $\vec{\Xi}(\vec{q}, t) = (Re[\xi_0(\vec{q}, t)], Im[\xi_0(\vec{q}, t)], \dots, Im[\xi_N(\vec{q}, t)], Re[\xi_0(-\vec{q}, t)], \dots, Im[\xi_N(-\vec{q}, t)])^T$ Eq. (3.5) reads

$$\partial_t \vec{\Sigma}(\vec{q}, t) = M(a_n, \vec{q}) \vec{\Sigma}(\vec{q}, t) + \vec{\Xi}(\vec{q}, t). \quad (3.6)$$

At this point we can study the linear response to noise perturbations. We can write an Ornstein-Uhlenbeck process [70] for the amplitude $\Theta_i(\vec{q}, t)$ of each eigenvector of $M(a_n, \vec{q})$

$$\partial_t \Theta_i(\vec{q}, t) = \lambda_i(\vec{q}) \Theta_i(\vec{q}, t) + \eta_i(\vec{q}, t), \quad (3.7)$$

where $\lambda_i(\vec{q})$ is the i -th eigenvalue of $M(a_n, \vec{q})$ (ordered according to the value of its real part, $Re[\lambda_i(\vec{q})] \geq Re[\lambda_{i+1}(\vec{q})]$). $\eta_i(\vec{q}, t) = \sum_{n=0}^{4N+3} C_{ij}^{-1}(\vec{q}) \Xi_j(\vec{q}, t)$ is the noise expressed in the eigenvectors basis and $C(\vec{q})$ is the matrix for the change of basis as obtained diagonalizing $M(a_n, \vec{q})$. The coefficients $\delta a_n(\vec{q}, t)$ are related to the amplitudes of the eigenmodes $\Theta_i(\vec{q}, t)$ by

$$\begin{aligned} Re[\delta a_n(\vec{q}, t)] &= \Sigma_i \Theta_i(\vec{q}, t) C_{2n-1i}(\vec{q}) \\ Im[\delta a_n(\vec{q}, t)] &= \Sigma_i \Theta_i(\vec{q}, t) C_{2ni}(\vec{q}) \\ Re[\delta a_n(-\vec{q}, t)] &= \Sigma_i \Theta_i(\vec{q}, t) C_{2n-1+2Ni}(\vec{q}) \\ Im[\delta a_n(-\vec{q}, t)] &= \Sigma_i \Theta_i(\vec{q}, t) C_{2n+2Ni}(\vec{q}). \end{aligned} \quad (3.8)$$

The noises $\eta_i(\vec{q}, t)$ are Gaussian and white in time and have cross-correlations

$$\langle \eta_i(\vec{q}, t) \eta_j^*(\vec{q}', t') \rangle = \frac{\epsilon}{2} D_{i,j}(\vec{q}) \delta(t - t') \delta(\vec{q} - \vec{q}') \quad (3.9)$$

$$\langle \eta_i(\vec{q}, t) \eta_j(\vec{q}', t') \rangle = \frac{\epsilon}{2} \tilde{D}_{i,j}(\vec{q}) \delta(t - t') \delta(\vec{q} - \vec{q}'). \quad (3.10)$$

where

$$\begin{aligned} D_{i,j}(\vec{q}) &= \sum_{k=0}^{4N+3} C_{ik}^{-1}(\vec{q}) C_{jk}^{-1*}(\vec{q}) \\ \tilde{D}_{i,j}(\vec{q}) &= \sum_{k=0}^{4N+3} C_{ik}^{-1}(\vec{q}) C_{jk}^{-1}(\vec{q}). \end{aligned} \quad (3.11)$$

The solution of the stochastic process is then

$$\Theta_i(\vec{q}, t) = e^{\lambda_i(\vec{q})t} \int_0^t e^{-\lambda_i(\vec{q})s} \eta_i(\vec{q}, s) ds. \quad (3.12)$$

The average value of the eigenmodes amplitude is $\langle \Theta_i(\vec{q}, t) \rangle = 0$. The correlations between the amplitudes of the eigenvectors are given by:

$$\langle \Theta_i(\vec{q}, t) \Theta_j^*(\vec{q}', t') \rangle = \frac{\epsilon D_{ij}(\vec{q})}{-4(\lambda_i(\vec{q}) + \lambda_j^*(\vec{q}'))} (1 - e^{(\lambda_i(\vec{q}) + \lambda_j^*(\vec{q}'))t}) \delta(\vec{q} - \vec{q}') \quad (3.13)$$

$$\langle \Theta_i(\vec{q}, t) \Theta_j(\vec{q}', t') \rangle = \frac{\epsilon \tilde{D}_{ij}(\vec{q})}{-4(\lambda_i(\vec{q}) + \lambda_j(\vec{q}'))} (1 - e^{(\lambda_i(\vec{q}) + \lambda_j(\vec{q}'))t}) \delta(\vec{q} - \vec{q}') \quad (3.14)$$

In particular, the time evolution of the mean value of the squared amplitude of the eigenvectors with non zero eigenvalue is

$$\langle |\Theta_i(\vec{q}, t)|^2 \rangle = \frac{\epsilon D_{ii}(\vec{q})}{-8\text{Re}[\lambda_i(\vec{q})]} (1 - e^{2\text{Re}[\lambda_i(\vec{q})]t}). \quad (3.15)$$

For times much longer than a characteristic time $\tau_i(\vec{q}) \sim -1/\text{Re}[\lambda_i(\vec{q})]$ this mean squared amplitude reaches a stationary value

$$\langle |\Theta_i(\vec{q})|^2 \rangle = \frac{\epsilon D_{ii}(\vec{q})}{-8\text{Re}[\lambda_i(\vec{q})]}. \quad (3.16)$$

As Eq. (2.1) is translationally invariant, $E_h(\vec{x} + \vec{x}')$ is also a stationary solution for any fixed \vec{x}' , the two modes $\partial_x E_h$ and $\partial_y E_h$ are eigenvectors of $M(a_n, \vec{q} = 0)$ with zero eigenvalue. These neutrally stable modes of the linearized dynamics are the so-called Goldstone modes [64, 250] and correspond to homogeneous perturbations that displace rigidly the pattern along the x or y directions

$$\partial_x E_h(\vec{x}) = i \sum_n a_n k_{nx}^0 e^{i\vec{k}_n^0 \vec{x}} \quad (3.17)$$

$$\begin{aligned} E_h(x, y) + x' \partial_x E_h &= \sum_n a_n (1 + i k_{nx}^0 x') e^{i\vec{k}_n^0 \vec{x}} \\ \simeq \sum_n a_n e^{i\vec{k}_n^0 (x+x', y)} &= E_h(x + x', y). \end{aligned} \quad (3.18)$$

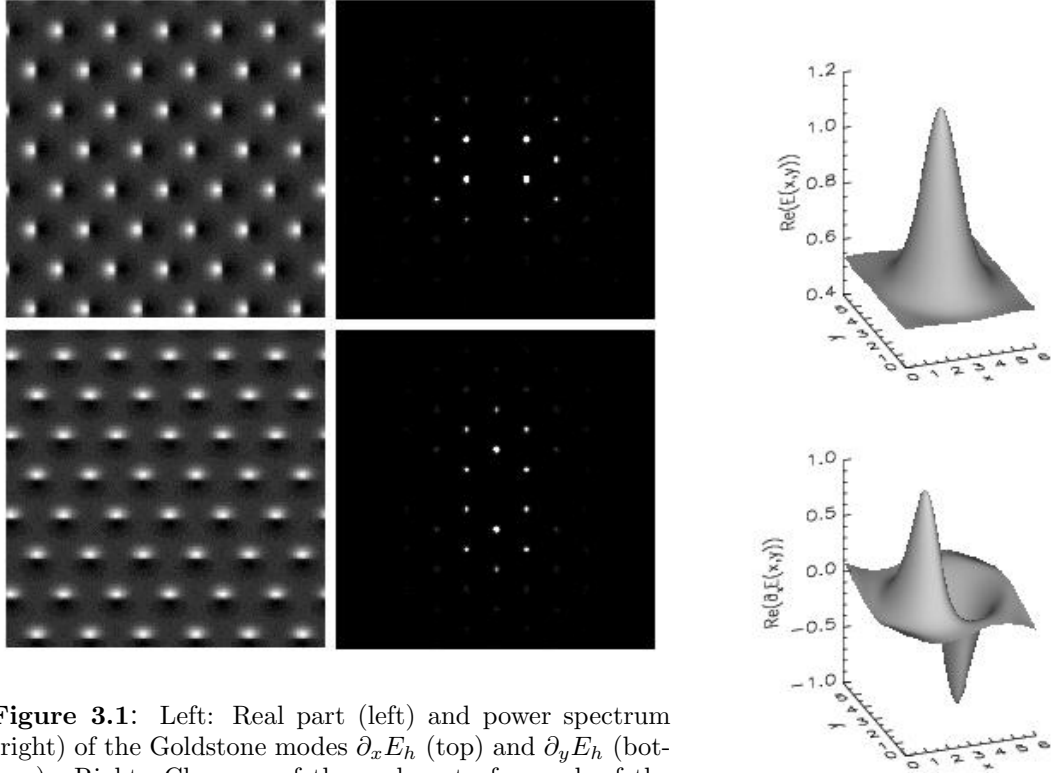


Figure 3.1: Left: Real part (left) and power spectrum (right) of the Goldstone modes $\partial_x E_h$ (top) and $\partial_y E_h$ (bottom). Right: Close up of the real part of a peak of the hexagonal pattern (top) and the real part of the Goldstone mode $\partial_x E_h$ (bottom).

For the hexagonal pattern considered here the Goldstone modes have the profile shown in Fig. 3.1. In the near-field they have a larger amplitude at the borders of the hexagonal peaks, where the gradient is larger and show a sharp transition from negative to positive values just at the center of the peak (Fig. 3.1 left). Then, Eq. (3.16) does not apply to the Goldstone modes as they have zero eigenvalue ($\lambda_0(\vec{q} = \vec{0}) = 0$). Its time evolution is given by (from Eq. (3.12))

$$\Theta_i(\vec{q}, t) = \int_0^t \eta_i(\vec{q}, s) ds. \quad (3.19)$$

This is a purely diffusive motion which never reaches a stationary state. Its mean squared amplitude grows linearly in time

$$\langle |\Theta_0(\vec{q} = \vec{0}, t)|^2 \rangle = \frac{\epsilon}{8} D_{00}(\vec{q} = 0) t. \quad (3.20)$$

Therefore, the linearization fails for times $t \sim 1/\epsilon$, when the amplitude of the Goldstone modes $|\Theta_0(\vec{q} = \vec{0})|^2$ reaches values comparable to one. In a situation where the hexagonal pattern is stable the Goldstone modes are the only neutral modes while all the other eigenvectors have eigenvalues with strictly negative real part.

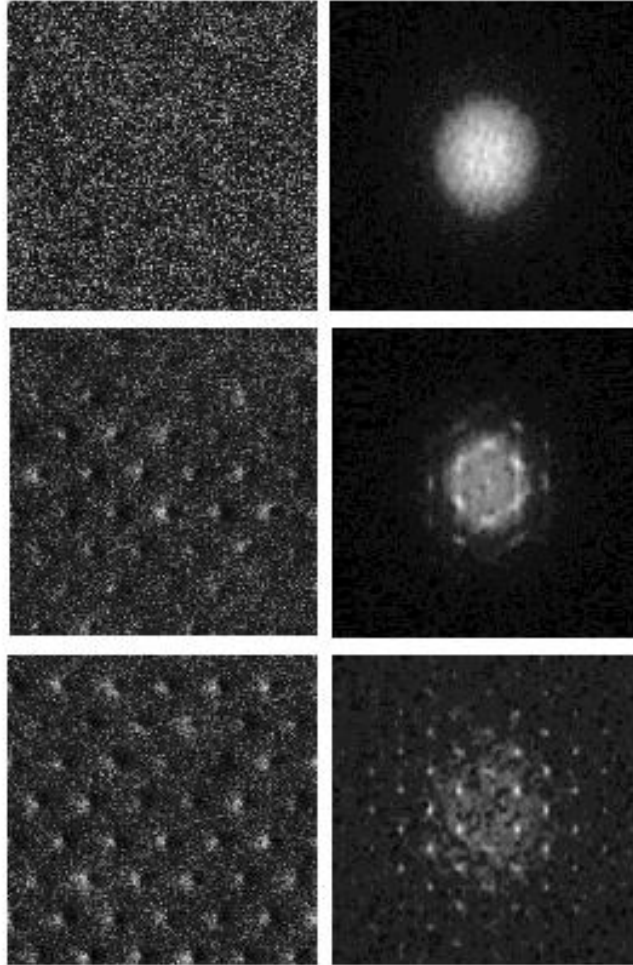


Figure 3.2: Near-field (left: $Re[\delta E(\vec{x})]$, $\delta E(\vec{x}) = E(\vec{x}) - \langle E(\vec{x}) \rangle$) and far-field (right: $|\delta E(\vec{k})|$, $\delta E(\vec{k}) = E(\vec{k}) - \langle E(\vec{k}) \rangle$) pattern fluctuations after switching on the noise. From top to bottom: $t = 2, t = 200$, and $t = 2000$. We have considered $\epsilon = 10^{-6}$.

3.4 Fluctuations in the near-field

Starting from a stationary hexagonal solution of the system equations without noise, a typical evolution of the pattern fluctuations when the noise is switched on, obtained from numerical integration¹ of the nonlinear equations (3.1), is shown in Fig. 3.2.

From Eq. (3.15) we get that for short time all the modes $\Theta_i(\vec{q}, t)$ have a similar

¹We integrate Eq. (3.1) using a pseudo-spectral method where the linear terms in Fourier space are integrated exactly while the nonlinear ones are integrated using a first-order in time approximation following the scheme described in Ref. [205]. The random number generator used is described in Ref. [231]. A rectangular lattice of size 256×256 points was used. In Fourier space we took $\Delta k_y = 1/8$ and $\Delta k_x = \sin(60^\circ)/6$, which corresponds in real space to a system of size $L_y \approx 50.3$ and $L_x \approx 43.5$. The time step for integration was $dt = 0.001$.

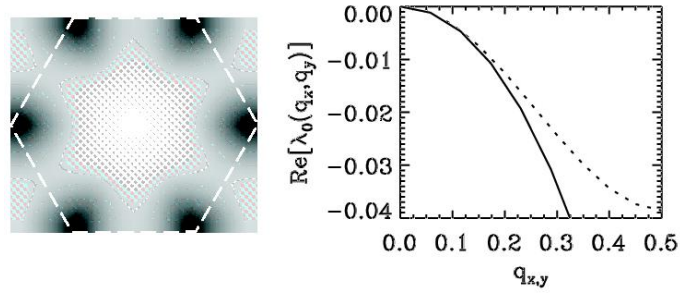


Figure 3.3: Left: $Re[\lambda_0(\vec{q})]$, darker color indicates smaller values. The white line shows the first Brillouin zone. The center of the figure corresponds to the Goldstone modes ($Re[\lambda_0(\vec{q}=0)] = 0$). Right: transverse cut of $Re[\lambda_0(\vec{q})]$ along q_x (solid line) and q_y (dotted line) axis.

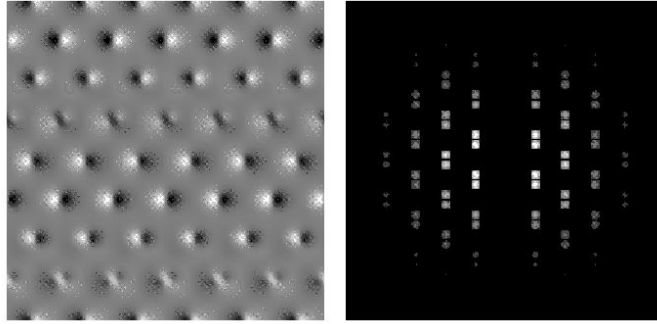


Figure 3.4: Soft mode $\vec{q} = (0, 2\pi/L_y)$ whose decay rate is $Re[\lambda(\vec{q} = (0, 2\pi/L_y))] = -0.0052$.

mean squared amplitude which is proportional to the noise intensity and grows linearly with time

$$\langle |\Theta_i(\vec{q}, t)|^2 \rangle = \frac{\epsilon}{4} D_{ii}(\vec{q}) t. \quad (3.21)$$

All the modes will contribute with a similar weight to the field fluctuations and therefore there is a complete lack of structure in the field fluctuations at short times as shown in Fig. 3.2 (top).

As time goes on, following (3.15), the mean squared amplitude of the modes does not grow linearly any more. It reaches a steady state value given by (3.16) which is larger for the modes which have a smaller decaying rate $Re[\lambda_i(\vec{q})]$. According to the way the eigenvalues has been ordered, for a given \vec{q} , the smaller decaying rate is $Re[\lambda_0(\vec{q})]$. The eigenmodes with eigenvalue $\lambda_0(\vec{q})$ are the so-called soft modes [64, 250, 158] which are connected with the Goldstone modes and for which $\lambda_0(\vec{q} \gtrsim 0) \sim -|\vec{q}|^2$ (see Fig. 3.3). While the Goldstone modes correspond to neutrally stable homogeneous perturbations, the soft modes correspond to weakly damped long-wavelength perturbations. For systems with a finite size L the less damped of the soft modes are the ones with the smallest \vec{q} vector allowed by the size of the system, $|\vec{q}| = 2\pi/L$. These modes have a decay rate proportional to $1/L^2$ and therefore a stationary mean squared amplitude proportional to ϵL^2 . The shape of one soft mode is illustrated in Fig. 3.4. Its profile is similar to a Goldstone mode but with a long-wavelength modulation on top of it. The wavevector of the modulation is

precisely the wavevector \vec{q} that identifies the soft mode. While the Goldstone modes describe an overall rigid motion of the pattern, the soft modes add some distortion so the pattern moves in slightly different form at different locations.

For the numerical simulations shown in Fig. 3.2, at $t = 200$ the mean squared amplitude of most of the modes has already saturated at small values, while the amplitude of the soft modes is, on average, just reaching the stationary value. Therefore, as shown in the figure (center) the field fluctuations are dominated by the soft and Goldstone modes and short range spatial structures start to appear. The typical correlation length of the fluctuations is determined by the wavelength of the soft modes.

According to (3.20) the mean square amplitude of the Goldstone mode keeps growing linearly in time and does not saturate. At times of the order $t \sim 1/\epsilon$ the linear theory for fluctuations described in the previous section fails (this time is around 10^6 for the simulation shown in Fig. 3.2) Assuming linearization is valid, at times $t \gg L^2$, the mean squared amplitudes of the Goldstone modes ($\sim \epsilon t$, (3.20)) become much larger than the amplitude of any of the soft modes ($\sim \epsilon L^2$) and dominate the fluctuations. In our system at time $t \sim 2000$ the profile of the field fluctuations is already determined only by the Goldstone modes as shown in Fig. 3.2 (bottom). In the far field the largest fluctuations are those of the wavevectors of the pattern, while the near-field fluctuations show a long range structure with strong correlation over all the system size. Integrating for larger times, the profile of the fluctuations will be dominated by macroscopic rigid displacements of the pattern. On top of that there will be the deformations generated by the soft modes.

For systems with a larger system size, the soft modes will take a longer time to reach the stationary amplitude (and in fact its amplitude will be larger). However, provided that $L^2 < 1/\epsilon$, the evolution will be basically the same, showing the three stages discussed before. If the system size is larger than $1/\sqrt{\epsilon}$ then the stationary amplitude of the soft modes will be determined by the system nonlinearities and if L is large enough, their amplitude may have a very large size, in which case Goldstone and soft modes will contribute to the near-field fluctuations even at very large times ($t \sim 1/\epsilon$).

3.5 Fluctuations and correlations in the far-field

In the following subsections, we address the fluctuations in Fourier space of the field, intensity and momentum.

3.5.1 Field fluctuations

In the Fourier space the field fluctuations are also dominated by the Goldstone and soft modes. From Eqs. (3.17) and (3.18), we can see how the Goldstone modes, which have the same wavevectors than the hexagonal pattern, induce opposite and very large phase fluctuations in opposite Fourier components, which correspond to the rigid translation of the hexagons in the near-field. The homogeneous component of the field is not affected by the Goldstone modes. The soft modes do not have exactly the same Fourier components than the hexagonal pattern but they are still very close to it and therefore their main contribution is to broaden the spots of the far-field fluctuations (see the far-field for the intermediate time in Fig. 3.2).

3.5.2 Intensity fluctuations and correlations

The intensity fluctuations of the far-field peaks are

$$\delta I(\vec{k}) = I(\vec{k}) - I_h(\vec{k}), \quad (3.22)$$

where $I(\vec{k}) = |E(\vec{k})|^2$ and $I_h(\vec{k}) = |E_h(\vec{k})|^2$. The correlation function of the far-field intensity fluctuations of a fundamental wavevector of the pattern, for instance \vec{k}_3^0 , with the far-field intensity fluctuations of any other wavevector \vec{k} is given by

$$C_1(\vec{k}_3^0, \vec{k}) = \frac{\langle \delta I(\vec{k}_3^0) \delta I(\vec{k}) \rangle}{\sqrt{\langle |\delta I(\vec{k}_3^0)|^2 \rangle \langle |\delta I(\vec{k})|^2 \rangle}}. \quad (3.23)$$

From the numerical integration of Eq. (3.1), and averaging over two hundred realizations of the noise, we find strong correlations between the intensity fluctuations of all the modes of the pattern, not only among the fundamental harmonics but also with the higher order ones (Fig. 3.5). For the fundamental harmonics, the correlation $C_1(\vec{k}_3^0, \vec{k}_i^0) = \langle \delta I(\vec{k}_3^0) \delta I(\vec{k}_i^0) \rangle$, with $i = 1, 6$, is larger for the modes forming an angle $\theta = \frac{2\pi}{3}$ and smaller for $\theta = \frac{\pi}{3}$ (Fig. 3.7). Using a 6 modes approximation [97, 74] one finds that $N_i + N_{i+1} - N_{i+3} - N_{i+4}$ (N_i being the number of photons of the mode i) is a conserved quantity for the interaction Hamiltonian related to momentum conservation. This means that one should expect strong correlations among these sets of four Fourier modes. However this reasoning can not reveal which modes within these sets are more correlated in pairs. So, the stronger correlation between those modes forming a $\theta = \frac{2\pi}{3}$ angle, despite fulfilling momentum conservation, can

Figure 3.5: Correlation function of the intensity fluctuations $C_1(\vec{k}_3^0, \vec{k})$. The brightest spot takes the value 1 corresponding to the autocorrelation of \vec{k}_3^0 . Note the strong correlation with the other six fundamental wavevectors of the pattern and with the first rings of harmonics. The correlation decay as one consider higher and higher harmonics. Note also the anti-correlation with the homogeneous stated as a black spot at the center. The grey background is around 0

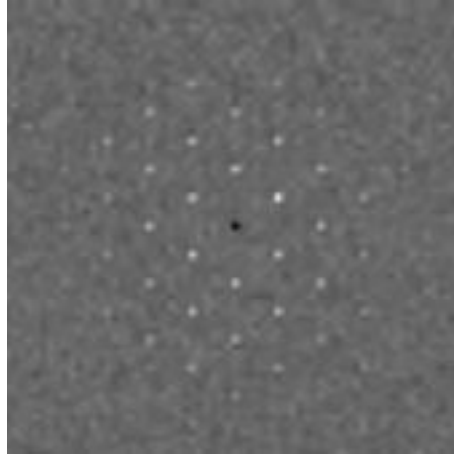
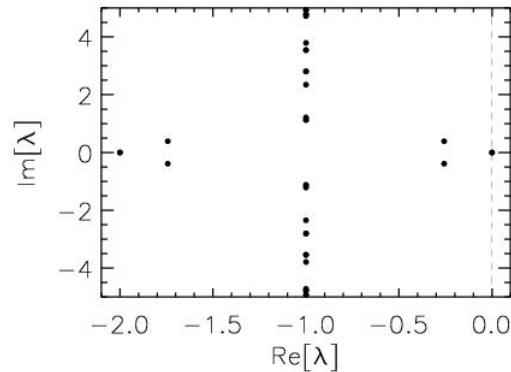


Figure 3.6: Eigenvalues of the eigenvectors with $\vec{q} = \vec{0}$. There are two zero eigenvalues corresponding to the Goldstone modes. Note also the symmetry of the spectrum with respect to the axis $Re[\lambda] = -1$.



not be completely understood in these terms. We also find strong anti-correlations between the intensity fluctuations of the modes of the pattern and the homogeneous mode which are related to energy conservation (Fig. 3.5).

Neglecting terms of order ϵ^2 , the far-field intensity fluctuations can be approximated as

$$\delta I(\vec{k}) \approx 2Re[E_h^*(\vec{k})\delta E(\vec{k})], \quad (3.24)$$

where $\delta E(\vec{k}) = E(\vec{k}) - E_h(\vec{k})$. As $E_h(\vec{k}) = \sum_n a_n (2\pi)^2 \delta(\vec{k}_n^0 - \vec{k})$ we have to consider only perturbations that have the same wavevectors of the pattern ($\vec{q} = \vec{0}$). Therefore, the soft modes ($\vec{q} \gtrsim \vec{0}$) do not contribute, in the linear approximation, to the fluctuations of the far-field intensity peaks. The Goldstone modes are indeed $\vec{q} = 0$ perturbations, but the intensity fluctuations associated to the Goldstone modes are $\delta I(\vec{k}) = 2Re[E_s(\vec{k})^* \partial_x E_s(\vec{k})]$ which from (3.3) and (3.17) is exactly zero. So, neither the Goldstone modes contribute, in the linear approximation, to the fluctuations of the far-field intensity peaks. They only contribute to phase fluctuations. Therefore, fluctuations of the far-field intensity peaks have to be described by the other eigenvectors of $M(E_h, \vec{q} = \vec{0})$. These eigenvectors have the same Fourier components than the hexagonal pattern and their eigenvalues $\lambda_i(\vec{q} = \vec{0})$, ($i = 1, \dots, N$) are shown in Fig. 3.6.

Using Eqs. (3.8), (3.13) and (3.14) we can compute the correlation function

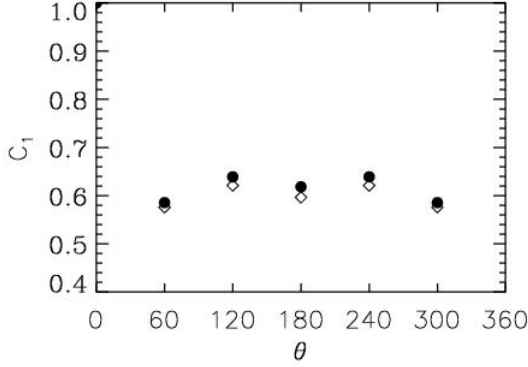


Figure 3.7: Correlations between the intensity fluctuations of the fundamental wavevectors obtained from the numerical integration of equation (3.1) (rhombi), and analytically from Eq. (3.25) (dots).

$C_1(\vec{k}_n^0, \vec{k}_m^0)$ analytically

$$C_1(\vec{k}_n^0, \vec{k}_m^0) = 2\text{Re} \left[E_h^*(\vec{k}_n^0) E_h^*(\vec{k}_m^0) \langle \delta E(\vec{k}_n^0) \delta E(\vec{k}_m^0) \rangle + E_h(\vec{k}_n^0) E_h(\vec{k}_m^0) \langle \delta E(\vec{k}_n^0) \delta E^*(\vec{k}_m^0) \rangle \right], \quad (3.25)$$

where

$$\langle \delta E(\vec{k}_n^0) \delta E(\vec{k}_m^0) \rangle = \sum_i \sum_j \frac{\epsilon}{-4(\lambda_i + \lambda_j)} (1 - e^{(\lambda_i + \lambda_j)t}) \tilde{D}_{ij}(\vec{q} = 0) (C_{2n-1i} C_{2m-1j} - C_{2ni} C_{2mj} + i(C_{2m-1i} C_{2nj} + C_{2n-1i} C_{2mk})) \quad (3.26)$$

$$\langle \delta E(\vec{k}_n^0) \delta E^*(\vec{k}_m^0) \rangle = \sum_i \sum_j \frac{\epsilon}{-4(\lambda_i + \lambda_j^*)} (1 - e^{(\lambda_i + \lambda_j^*)t}) D_{ij}(\vec{q} = 0) (C_{2n-1i} C_{2m-1j} + C_{2ni} C_{2mj} + i(C_{2m-1i} C_{2nj} - C_{2n-1i} C_{2mk})) \quad (3.27)$$

Fig. 3.7 shows the stationary value ($t \rightarrow \infty$) of (3.25) for the fundamental wavevectors of the pattern as a function of the angle θ between them. The results obtained from the linearized theory are in very good agreement with the correlations obtained from the numerical simulations of the nonlinear equation (3.1).

From Fig. 3.6 we can see that the most important eigenvectors are those associated to the complex conjugate eigenvalues with $\text{Re}[\lambda_2(\vec{q} = 0)] = \text{Re}[\lambda_3(\vec{q} = 0)] = -0.25$. This pair of eigenvectors give the strong correlation between all the Fourier components and a strong anti-correlation with the homogeneous field. The excitation of this eigenvectors implies also anti-correlations between the homogeneous mode and the off-axis Fourier components of the pattern (Fig. 3.8 left). Some eigenvectors with $\text{Re}[\lambda_n(\vec{q} = 0)] = -1$ are finally the responsible for the differences between the correlations in the fluctuations of the six first harmonics. The typical profile of one of these eigenmodes is shown on the right of Fig. 3.8. The symmetry of the three peaks located at 120° yields to larger correlations between the fluctuations of the corresponding far-field intensity peaks.

We note that the modes that determine the correlations of the far-field intensity peaks reach stationary values in a much shorter time ($t \sim -1/\text{Re}[\lambda_2(\vec{q} = 0)] = 4$) than the Goldstone and soft modes contributing to the near-field fluctuations ($t \sim$

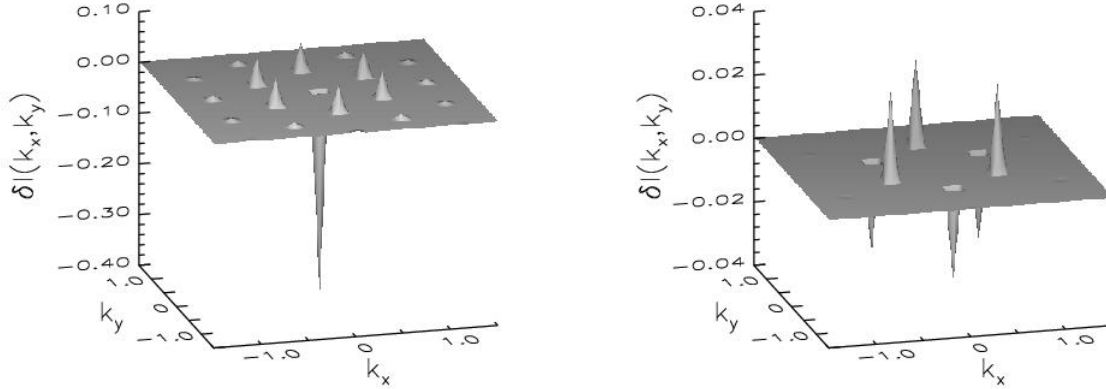


Figure 3.8: Intensity fluctuations due to the eigenmodes with $Re[\lambda] = -0.25$ (left) and $Re[\lambda] = -1$ (right).

$1/\epsilon \sim 10^6$ as discussed in the previous section). As these correlations are determined by $\vec{q} = 0$ perturbations, these calculations can be performed in systems with relatively small size. Increasing the system size, may change the near-field profile of the fluctuations, as discussed before, but nevertheless the dynamical evolution of the modes contributing to the far-field intensity fluctuations and their mean squared stationary amplitude will be basically the same.

3.5.3 Transverse momentum fluctuations

We finally address the fluctuations of the transverse momentum. Without noise the total transverse momentum of the pattern is $\vec{P} = \sum_n |a_n|^2 \vec{k}_n^0 = 0$. The noise induce fluctuations given by $\delta\vec{P} = \sum_n 2Re[a_n^* \delta a_n] \vec{k}_n^0$. One finds that all the eigenvectors that contribute to the far-field intensity fluctuations strictly fulfill momentum conservation except for two modes with $\lambda_{2N}(q=0) = \lambda_{2N-1}(q=0) = -2$, which are exactly those symmetric to the Goldstone modes respect to the line $Re[\lambda] = -1$ (Fig. 3.6). Therefore momentum fluctuations are determined by the two modes with maximum damping which are shown in Fig. 3.9, the one on the top figure breaks the conservation of the P_y momentum component while the one in the bottom breaks the conservation of P_x . Alternatively it is possible to see from the classical field theory that the momentum fluctuations are damped with a coefficient -2. A Lagrange density can be defined for Eq. (3.1) [58]

$$L = e^{2t} [a|\nabla E|^2 + \frac{i}{2}(E\dot{E}^* - \dot{E}E^*) + i(E_0 E^* - E_0^* E) + \theta|E|^2 - |E|^4] \quad (3.28)$$

Substituting (3.3) in (3.28) and integrating over all the space we get a Lagrangian for the amplitude of the modes a_n and for the position of the rolls in the near-field

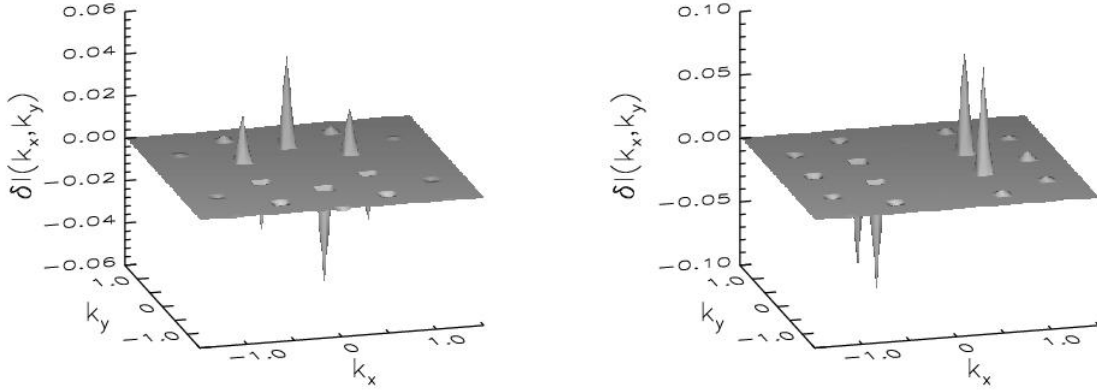


Figure 3.9: Intensity fluctuations due to the two modes $Re[\lambda_{2N}(\vec{q} = 0)] = Re[\lambda_{2N-1}(\vec{q} = 0)] = -2$.

\vec{x}_0

$$L = e^{2t} [\sum_n |a_n|^2 |\vec{k}_n|^2 + \frac{i}{2} \sum_n (\dot{a}_n^* a_n - \dot{a}_n a_n^* - i2|a_n|^2 \vec{k}_n \cdot \dot{\vec{x}}_0) + i(E_0 a_0^* - E_0^* a_0) + \sum_n |a_n|^2 - \sum_n \sum_{n'} \sum_m a_n a_{n'} a_m^* a_{n+n'+m}^*]. \quad (3.29)$$

\vec{x}_0 is a cyclic coordinate, so its conjugate momentum

$$\frac{\partial L}{\partial \dot{\vec{x}}_0} = -i2e^{2t} \sum_n |a_n|^2 \vec{k}_n = -2e^{2t} \vec{P} \quad (3.30)$$

is constant. Therefore $\dot{\vec{P}} = -2\vec{P}$. \vec{P} is identically zero without noise. When noise is present momentum fluctuations should satisfy

$$\dot{\delta \vec{P}} = -2\delta \vec{P} + \chi(t), \quad (3.31)$$

where $\chi(t)$ is a Gaussian white noise. Therefore, momentum fluctuations have the maximum damping. The same damping coefficient for the momentum fluctuations has been found by Gatti and Mancini from a few modes quantum formulation [74].

3.6 Conclusions

We have analyzed the fluctuations and correlations in a hexagonal pattern of a prototypical model in nonlinear optics. In the near-field fluctuations are dominated by the neutrally stable Goldstone modes associated to the translational invariance as well as by the soft modes connected with them. The soft modes destroy the long range correlation in the fluctuations. However in small systems these modes reach a stationary amplitude much earlier (and at a smaller value) than the Goldstone mode so that they are important only at intermediate times. At long times the fluctuations are dominated by the Goldstone modes which correspond to rigid displacements of the overall pattern. For very large systems, both the Goldstone and soft modes may have similar amplitudes and contribute to the fluctuations.

In the far-field, the most relevant effect of noise are the intensity fluctuations of the Fourier modes of the hexagonal pattern. At first order in the noise intensity, these fluctuations are not affected neither by the Goldstone modes nor by the soft modes. They are dominated by damped modes, so they reach stationary values in relatively short times. Their main characteristics are: i) strong correlations between the intensity fluctuations of any arbitrary pair of the six fundamental wave vectors of the pattern, and also with their higher harmonics, ii) larger correlation between intensity fluctuations of the Fourier modes forming 120° angles than between modes forming 180° , and iii) strong anti-correlations between the zero wavevector and the pattern Fourier modes. Finally only the eigenmodes with maximum damping contribute to the fluctuations of the total transverse momentum, therefore the total transverse momentum has the least possible fluctuations.

Our results are obtained from both semianalytical calculations based on linearization around the hexagonal pattern and from numerical simulations of the nonlinear system. Some of our results and predictions are very general, and depend only on basic symmetry properties of the system such as translational invariance. Thus we expect that similar structure and properties of the fluctuations and correlations can be found in other nonlinear systems displaying hexagonal patterns.

From a computational point of view, correlations in the far-field intensity peaks are practically independent of the system size and therefore can be calculated accurately in relatively small systems, provided all the relevant harmonics of the pattern are considered. Good statistics can be obtained integrating the nonlinear partial differential equations over relatively short times (even though the near-field fluctuations are quite far away from reaching a stationary value). Of course, alternatively a linear semianalytical approach as the one described in Sec. 3.3 can also be used to calculate far-field correlations.

Chapter 4

Secondary bifurcations of hexagonal patterns in sodium vapor in a single-mirror arrangement

4.1 Introduction

In this chapter we study the secondary bifurcations of hexagonal patterns in a single feedback-mirror system. This arrangement is an archetype system for optical pattern formation [41, 42]. A thin nonlinear optical medium is irradiated by a laser beam which is homogeneous in amplitude and phase. The transmitted beam is reflected back into the medium by a plane high-reflectivity mirror placed behind the medium. During the propagation of the light field to the mirror and back, different points in the transverse plane are coupled by diffraction.

A spatial instability might arise because a fluctuation of the refractive index inside the medium causes a phase modulation of the transmitted wave. Due to diffraction, this phase modulation is – at least partially – converted to amplitude modulation. Under suitable conditions this amplitude modulation can reinforce the original fluctuation of the refractive index, which is assumed to be intensity dependent. Thus a macroscopic modulation – a pattern – can develop in the transverse cross section of the laser beam as well as in the transverse distribution of the refractive index within the medium [41, 42, 4].

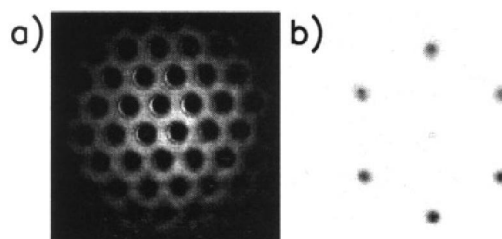


Figure 4.1: From Ref. [15]. Hexagonal pattern with a relatively large aspect ratio: (a) near field, (b) far field.

The particular system studied here is a microscopic model for an experimental

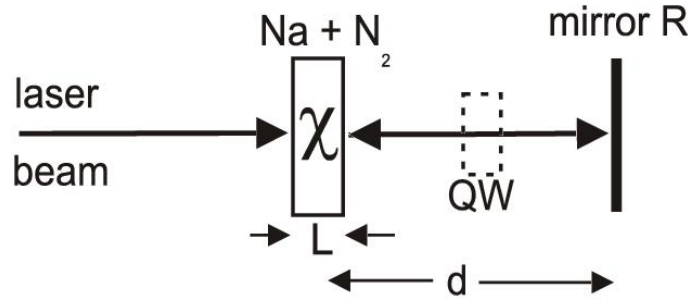


Figure 4.2: Scheme of the investigated nonlinear optical system. See text

realization where sodium is used as a nonlinear medium and a quarter wave plate is introduced between the nonlinear medium and the feedback-mirror. This configuration has shown to display hexagonal patterns (Fig. 4.1) that undergo very interesting secondary bifurcations to patterns with twelve wavevectors. These are the instabilities studied in this chapter from a theoretical point of view.

This chapter is organized as follows: In Sec. 4.2 we describe the experimental setup and the microscopic model. In Sec. 4.3 we perform the linear stability analysis of the homogeneous solution. In Sec. 4.4 we find the stationary hexagonal pattern solutions of the model. Then, in Sec. 4.5, we perform a linear stability analysis of the hexagonal patterns and discuss their different instabilities. In Sec. 4.6 the theoretical results are compared with the experiment. Finally, in Sec. 4.7 we give some concluding remarks.

4.2 Experimental setup and model

In the system we are going to discuss (see Fig. 4.2), sodium vapor in a nitrogen buffer gas atmosphere is used as the nonlinear medium. The input light field is circularly polarized and its frequency is tuned to the vicinity of the D₁-line. The nonlinearity stems from optical pumping between Zeeman sublevels of the ground state [115, 171, 4]. If the system is suitably prepared, it is possible to describe the light-matter interaction in the framework of a simple four-level model ($J=1/2 \rightarrow J'=1/2$ -transition) [171, 4, 5]. Then the decisive dynamical variable is the orientation w which is the normalized population difference between the two Zeeman sublevels of the ground state [171, 4, 5]. The z -axis is chosen to be parallel to the direction of the wavevector of the input light field. x, y denote the coordinates transverse to the direction of propagation. Then a longitudinally averaged orientation ϕ is introduced by defining

$$\phi(x, y, t) = \frac{1}{L} \int_0^L w(x, y, z, t) dz. \quad (4.1)$$

Here L denotes the length of the medium in z -direction. In the following, we will discuss a situation in which there is an additional polarization changing element – a quarter-wave plate (QW) – in the feedback loop. This system has a rather

low threshold [5, 15] and displays interesting secondary bifurcations of hexagons [106, 6, 94].

The dynamics of ϕ is governed by the partial differential equation [171, 4, 5]

$$\begin{aligned} \partial_t \phi = & -(\gamma - D\nabla^2)\phi + \frac{1}{2L\alpha_0} \left[(1 - e^{-2L\alpha_0(1-\phi)})P^0 \right. \\ & \left. - (1 - e^{-2L\alpha_0(1+\phi)})P^0 R \left| e^{-i\frac{d}{k_0}\nabla^2} e^{-L\alpha_0(1-i\bar{\Delta})(1-\phi)} \right|^2 \right]. \end{aligned} \quad (4.2)$$

γ models relaxation by collisions, $D\nabla^2$ the thermal motion of the atoms (∇^2 Laplacian in transverse space, D diffusion constant). The parameter α_0 parameterizes the optical depth of the medium, and is half the small-signal absorption coefficient. $\bar{\Delta}$ denotes the detuning of the incident laser beam to the D_1 -resonance. It is normalized to the linewidth (half width at half maximum) and is positive if the laser frequency is higher than the resonance frequency. $k_0 = 2\pi/569.6$ nm is the wavenumber of the pump light field in vacuum, R the reflectivity of the mirror. The pump rate P^0 is proportional to the intensity of the input light field. It is also the main bifurcation parameter. The two exponentials in the last term of Eq. (4.2) describe diffraction (the one including the Laplacian) and the action of the medium on phase and amplitude of the light field. Details on the system and on the derivation of Eq. (4.2) can be found in [171, 4, 5, 15].

In this chapter, only the case of a plane wave input field is discussed. We remark that for a description of a spatially varying input field Eq. (4.2) needs to be modified slightly.

4.3 Linear stability analysis of the homogeneous solution

The steady state plane wave solution ϕ_0 of equation (4.2) is implicitly given by

$$2\gamma L\alpha_0\phi_0 = P^0 \left[(1 - e^{-2L\alpha_0(1-\phi_0)}) - R(1 - e^{-2L\alpha_0(1+\phi_0)})e^{-2L\alpha_0(1-\phi_0)} \right]. \quad (4.3)$$

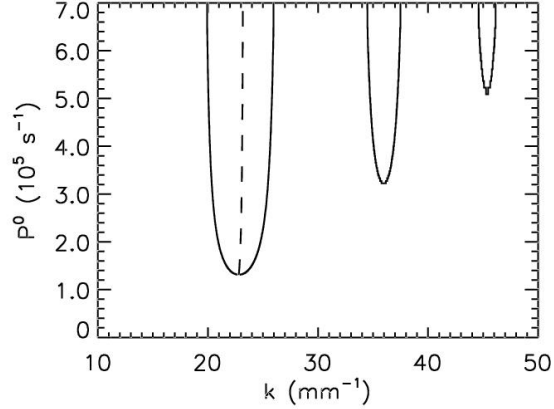
A linear stability analysis of the homogeneous solution with respect to spatially periodic perturbations yields the dispersion relation

$$\begin{aligned} \lambda(k) = & -\gamma - Dk^2 - e^{-2L\alpha_0(1-\phi_0)}P^0 \\ & - P^0 R \left[(1 - e^{-2L\alpha_0(1+\phi_0)})e^{-2L\alpha_0(1-\phi_0)} \left(\cos\left(\frac{d}{k_0}k^2\right) + \bar{\Delta}\sin\left(\frac{d}{k_0}k^2\right) \right) - e^{-4L\alpha_0} \right] \end{aligned} \quad (4.4)$$

where $\lambda(k)$ is the growth rate of a periodic perturbation of wavenumber k . In Fig. 4.3 we display the marginal stability curve ($\lambda(k) = 0$). The homogeneous solution never becomes unstable against homogeneous perturbations ($k = 0$). In fact, for large values of the pump the eigenvalue $\lambda(k = 0) \propto -P^0$. An important point to notice is that the marginal stability curve has a vertical asymptote¹ for

¹The value of the asymptote has been numerically evaluated for the parameter values given in the caption of Fig. 4.3.

Figure 4.3: The solid lines indicate the values of the pump P^0 for which a periodic perturbation of wavenumber k becomes unstable. The dashed line indicates the wavenumber with maximum growth rate. Here $\gamma = 1.5 \text{ s}^{-1}$, $D = 0.0003563 \text{ m}^2\text{s}^{-1}$, $L\alpha_0 = 2.595$, $R = 0.915$, $d/k_0 = 8.258 \times 10^9 \text{ m}^2$ and $\bar{\Delta} = 4.0$. For these values of the parameters the instability threshold is at $P^0 \simeq 1.31 \times 10^5 \text{ s}^{-1}$ and the critical wavenumber is $k_c \simeq 22.8 \text{ mm}^{-1}$.



$k_a \simeq 1.9 \times 10^4 \text{ m}^{-1}$, and therefore perturbations of the homogeneous solution with a wavenumber smaller than k_a are never unstable. For pump intensities above but close to threshold the system develops stationary hexagonal patterns [15].

4.4 Stationary hexagonal patterns

Stationary hexagonal solutions of the form

$$\phi_h(\vec{x}) = \sum_{n=0}^{N-1} \phi_n e^{i\vec{k}_n^0 \vec{x}}, \quad (4.5)$$

where \vec{k}_n^0 are the wavevectors of the pattern, ϕ_n are complex coefficients and N is the number of Fourier modes, can be found by solving the stationary form ($\partial_t \phi_h = 0$) of equation (4.2) in a similar way as it is done in chapter 2 for a Kerr cavity. A set of coupled nonlinear equations for the amplitudes of the Fourier components ϕ_n is obtained

$$-(\gamma + D|\vec{k}_n^0|^2)\phi_n + \frac{P^0}{2L\alpha_0}[b_n - Rc_n] = 0, \quad (4.6)$$

where b_n and c_n are the Fourier coefficients of the nonlinear terms of Eq. (4.2)

$$(1 - e^{-2L\alpha_0[1-\phi_h(\vec{x})]}) = \sum_{n=0}^{N-1} b_n e^{i\vec{k}_n^0 \vec{x}} \quad (4.7)$$

$$(1 - e^{-2L\alpha_0[1+\phi_h(\vec{x})]}) \left| e^{-i\frac{d}{k_0}\nabla^2} e^{-L\alpha_0(1-i\bar{\Delta})[1-\phi_h(\vec{x})]} \right|^2 = \sum_{n=0}^{N-1} c_n e^{i\vec{k}_n^0 \vec{x}}. \quad (4.8)$$

Since ϕ_h is real, $\phi_n = \phi_m^*$ if $\vec{k}_n^0 = -\vec{k}_m^0$. As in the case of the Kerr cavity (Chapter 2) we have to consider not only the homogeneous and the six fundamental wave-vectors, but a total of $N = 91$ modes in Fourier space, since the bifurcation to hexagons is generally subcritical and, hence, higher harmonics have finite amplitudes even at threshold (Fig. 4.4). From a suitably chosen initial condition, a Newton-Raphson method is used to find solutions of the set of nonlinear equations (4.6). As explained

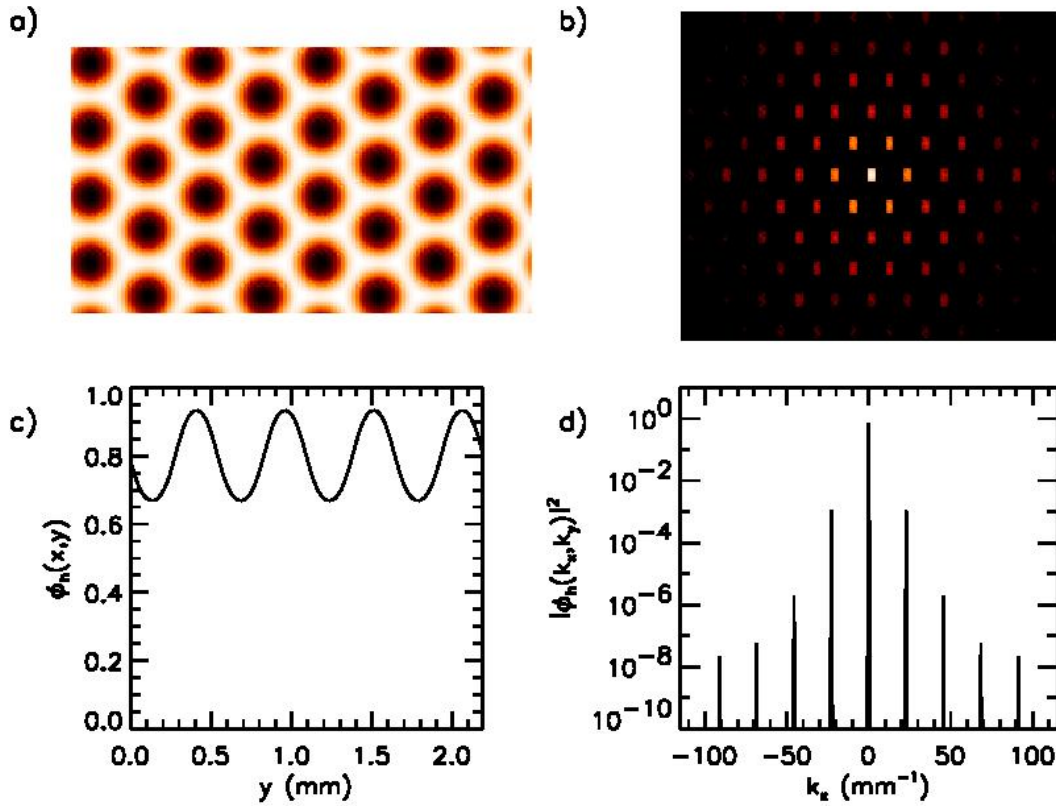


Figure 4.4: $\phi(x, y)$ (a) and power spectrum $|\phi(\vec{k})|^2$ (b) of a stationary hexagonal solution. Note the presence of the higher harmonics in the power spectrum. Panel (c) shows a cross section along a y axis of the pattern and panel (d) a cross section along the k_x axis of the power spectrum.

is section 2.3, the first guess is obtained from numerical simulation of Eq. (4.2), while continuation techniques are used to explore the whole parameter range where stationary solutions exist. With this method the wavenumber is treated as a parameter, and we can look for stationary hexagonal solutions with different fundamental wave numbers. Fig. 4.5 shows the region of existence of stationary hexagons around the first instability balloon as a function of the fundamental wavenumber k . The solid line is the first instability balloon shown in Fig. 4.3. The critical wavenumber is $k_c \simeq 22.8 \text{ mm}^{-1}$. The dashed line in Fig. 4.5 indicates the minimum value of the pump for which a stationary hexagonal pattern solution with a wavenumber k exist. Hexagons with a wavenumber around the critical one are subcritical. For subcritical hexagons, the dashed line in Fig. 4.5 correspond to a saddle-node bifurcation where a eigenvalue of the hexagonal pattern branch becomes zero as a result of the collision with the unstable branch coming from the homogeneous solution. Hexagons with a wavenumber much smaller than the critical one have a very large subcritical region, while hexagons with a wavenumber somehow much larger than k_c are in fact supercritical. In the supercritical case the dashed line in Fig. 4.5 coincides with the marginal stability curve of the homogeneous solution (solid line). Typically, a

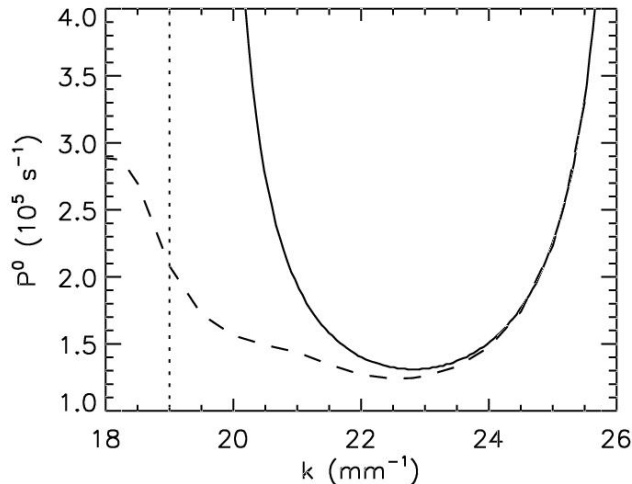


Figure 4.5: Region of existence of stationary hexagonal solutions. Stationary hexagons with a wavenumber k exist above the dashed line. The solid line is the marginal stability curve of the homogeneous solution. The values of k for which the two lines coincide correspond to a supercritical transition to hexagons from the homogeneous solution, while for the values of k where the dashed line is below the marginal stability curve the transition is subcritical. The dotted line indicates the vertical asymptote k_a of the marginal stability curve.

hexagonal branch with a given k starts subcritically from the homogeneous solution at the pump value where $\lambda(k) = 0$ (solid line). This is not always the case here where depending on the wavenumber of the hexagons, both subcritical and supercritical transitions can be observed. The region of existence of stationary hexagons extends also far beyond the vertical asymptote k_a of the marginal stability curve (vertical dotted line). This implies the existence of stationary hexagons with wavenumbers that never become linearly unstable from the homogeneous solution. However, as we will see in the next section, both the supercritical hexagons and the hexagons with wavenumbers beyond the vertical asymptote ($k < k_a$) are always unstable.

4.5 Linear stability analysis of stationary hexagonal patterns

In this section we perform a linear stability analysis of the stationary hexagonal solutions found in the previous section in order to determine their stability as a function of the input power and the fundamental wavenumber k of the pattern. Here we briefly remind how to perform such a stability analysis. We proceed as in chapter 2. Details can be found in Appendix A (see also [103]). Linearizing Eq. (4.2) around the stationary solution (4.5) the following equation for the fluctuations $\delta\phi(\vec{x}, t) = \phi(\vec{x}, t) - \phi_h(\vec{x})$ is obtained

$$\begin{aligned} \partial_t \delta\phi &= -(\gamma - D\nabla^2)\delta\phi - P^0 f_1(\vec{x})\delta\phi \\ &- \frac{P^0 R}{2} \left[(1 + i\bar{\Delta})f_2(\vec{x})e^{i\frac{d}{k_0}\nabla^2} f_3(\vec{x})\delta\phi + c.c. \right], \end{aligned} \quad (4.9)$$

where

$$\begin{aligned} f_1(\vec{x}) &= e^{-2L\alpha_0(1-\phi_h)} + Re^{-2L\alpha_0(1+\phi_h)} \left| e^{-i\frac{d}{\kappa_0}\nabla^2} e^{-L\alpha_0(1-i\bar{\Delta})(1-\phi_h)} \right|^2 \\ &\equiv \sum_{n=0}^{N-1} b_n e^{i\vec{k}_n^0 \vec{x}} \end{aligned} \quad (4.10)$$

$$\begin{aligned} f_2(\vec{x}) &= (1 - e^{-2L\alpha_0(1+\phi_h)}) \left(e^{-i\frac{d}{\kappa_0}\nabla^2} e^{-L\alpha_0(1-i\bar{\Delta})(1-\phi_h)} \right) \\ &\equiv \sum_{n=0}^{N-1} c_n e^{i\vec{k}_n^0 \vec{x}} \end{aligned} \quad (4.11)$$

$$f_3(\vec{x}) = e^{-L\alpha_0(1+i\bar{\Delta})(1-\phi_h)} \equiv \sum_{n=0}^{N-1} d_n e^{i\vec{k}_n^0 \vec{x}}. \quad (4.12)$$

Eq. (4.9) can be written as $\partial_t \delta\phi = L(\phi_h) \delta\phi$, where $L(\phi_h)$ is the Jacobian matrix. The stability of the hexagonal patterns reduces to study the eigenvalue problem

$$L\psi = \lambda\psi. \quad (4.13)$$

Since L is linear operator with periodic coefficients a general bounded solution can be found under a Bloch form [33]:

$$\psi(\vec{x}, \vec{q}) = e^{i\vec{q}\vec{x}} \tilde{\phi}(\vec{x}, \vec{q}), \quad (4.14)$$

where $\tilde{\phi}(\vec{x}, \vec{q})$ is a function with the same spatial periodicity than the stationary pattern ϕ_h , so that it can be written as

$$\tilde{\phi}(\vec{x}, \vec{q}) = \sum_{n=0}^{N-1} \delta\phi_n(\vec{q}) e^{i\vec{k}_n^0 \vec{x}}. \quad (4.15)$$

Since $\delta\phi$ is real, $\delta\tilde{\phi}(\vec{x}, \vec{q}) = \delta\tilde{\phi}^*(\vec{x}, -\vec{q})$. The eigenvalue problem (4.13) can be then written for the coefficients $\delta\phi_n(\vec{q})$

$$\begin{aligned} & -(\gamma + D|\vec{k}_n^0 + \vec{q}|^2) \delta\phi_n(\vec{q}) - P^0 \sum_{m=0}^{N-1} b_m \delta\phi_{n-m}(\vec{q}) \\ & \frac{P^0 R}{2} \left[(1 + i\bar{\Delta}) \sum_{l=0}^{N-1} \sum_{m=0}^{N-1} c_l d_m \delta\phi_{n-l-m}(\vec{q}) e^{-i\frac{d}{\kappa_0} |\vec{k}_n^0 + \vec{q} - \vec{k}_l^0|^2} \right. \\ & \left. (1 - i\bar{\Delta}) \sum_{l=0}^{N-1} \sum_{m=0}^{N-1} c_l^* d_m^* \delta\phi_{l+m+n}(\vec{q}) e^{i\frac{d}{\kappa_0} |\vec{k}_n^0 + \vec{q} + \vec{k}_l^0|^2} \right] = \lambda(\vec{q}) \delta\phi_n(\vec{q}), \end{aligned} \quad (4.16)$$

where b_n , c_n and d_n are the Fourier coefficients of f_1 , f_2 and f_3 as defined in Eqs. (4.10), (4.11) and (4.12). By considering $\vec{\Sigma}(\vec{q}) = [\delta\phi_0(\vec{q}), \delta\phi_1(\vec{q}), \dots, \delta\phi_{N-1}(\vec{q})]^T$, Eq. (4.16) reads

$$M(\phi_n, \vec{q}) \vec{\Sigma}(\vec{q}) = \lambda(\vec{q}) \vec{\Sigma}(\vec{q}). \quad (4.17)$$

Then, we find the N eigenvalues $\lambda_n(\vec{q})$ ($n=0, \dots, N-1$) of the matrix $M(\phi_n, \vec{q})$, and its corresponding eigenvectors, for each vector \vec{q} inside 1/6 of the first Brillouin

zone. These eigenvalues may be either real or complex conjugates and determine the stability of the solution against periodic perturbations containing any set of wavevectors $\vec{k}_n^0 \pm \vec{q}$. For each \vec{q} we order the eigenvalues $\lambda_i(\vec{q})$ according to the value of their real part $Re[\lambda_i(\vec{q})] > Re[\lambda_{i+1}(\vec{q})]$. When a hexagonal pattern becomes unstable against perturbations with a vector \vec{q} , wavevectors at that precise distance from the wave vectors of the pattern, corresponding to the Fourier components of the unstable eigenmode, are expected to grow linearly.

The result of the linear stability analysis of hexagonal patterns with different modulus k of the fundamental wavevectors is shown in Fig. 4.6. The dark shadowed area indicates the region of stability of the hexagonal solutions (Busse balloon). The different unstable regions are labeled with the modulus q of the perturbation vector \vec{q} that is unstable. The place where two instability lines cross correspond to a codimension two bifurcation point. The three most important instabilities are those corresponding to the three balloons labelled as $q = k/2$, $q = k/4$ and $q \sim k/2$. These are the instabilities that hexagons with wavenumbers close to the critical one will encounter by increasing the pump. In the following subsections we analyze all the different instabilities.

4.5.1 Long-wavelength instability

In the regions of Fig. 4.6 labelled as $q \sim 0$ the hexagonal patterns are unstable against long-wavelength perturbations as illustrated in Fig. 4.7 (see e.g. [131, 19, 222, 50] for previous work on phase instabilities of hexagons). This is the same instability found in the Kerr cavity for hexagons with wavenumber smaller than the critical one as discussed in chapter 2 (Sec. 2.4.1). Thus, wavevectors very close to those of the hexagonal pattern are expected to grow linearly. In an infinite system and close to threshold, an unstable hexagonal pattern changes its wavenumber and orientation continuously until it reaches the stable region. In finite size systems, the discrete Fourier space imposes a lower limit to the change of modulus and orientation of the wavevectors of a hexagonal pattern. The growth of the Fourier modes of the grid closest to those of the unstable hexagonal pattern leads to a discrete change in the wavenumber and orientation of the pattern towards the stable region. Fig. 4.8 shows the time evolution of an unstable stationary hexagonal pattern with $k = 23.5 \text{ mm}^{-1}$ and $P^0 = 1.35 \times 10^5 \text{ s}^{-1}$ in a rather large system. In the first stages of the simulation wave vectors very close to those of the pattern grow linearly in time. As soon as these wavevectors get a large amplitude they deform the pattern in the real space with a long wavelength modulation (second and third snapshots) and, finally, the original pattern is replaced by another one with a slightly smaller wavenumber (fourth snapshot) inside the stable region ($k = 22.2 \text{ mm}^{-1}$).

Far from the threshold of the long-wavelength instability the dispersion relation $\lambda_0(\vec{q})$ has a maximum at a finite wave number (Fig. 4.7, bottom). Therefore, the wave vectors with this maximum growth rate are more likely to dominate the system and a finite change in the wavenumber and orientation of an unstable hexagonal pattern may occur even in an infinite system.

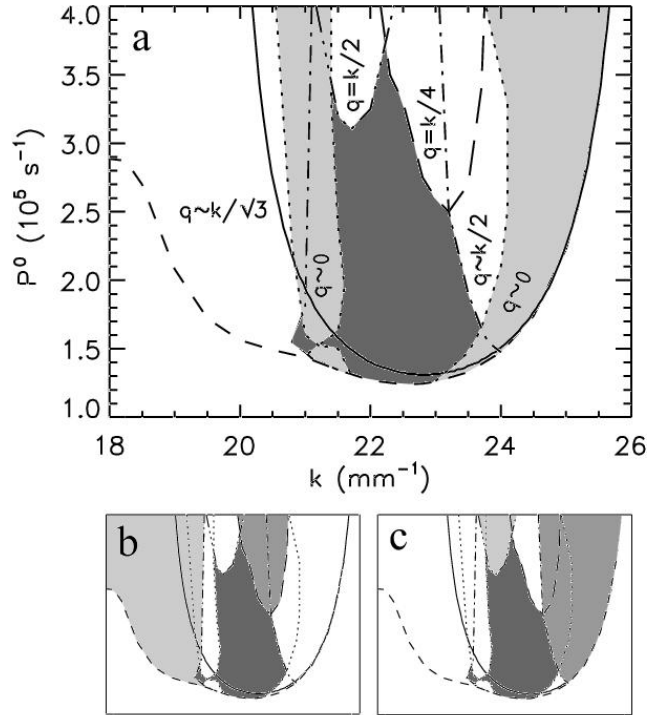


Figure 4.6: Marginal stability diagram of the hexagonal patterns. The dark grey area indicates the region in the P^0 - k -diagram where the stationary hexagonal patterns are stable (Busse balloon). The solid and lowest dashed lines are the marginal stability curve of the homogeneous solution and the limit of existence of the hexagonal patterns as in Fig. 4.5. The other discontinuous lines indicate the threshold for different instabilities of the hexagonal solutions. The light grey areas in the main figure **a** indicate the regions where the hexagonal patterns are unstable against long-wavelength perturbations (Subsec. 4.5.1). In the sub-panel **b**, the dark grey is the stable region as in panel **a** while the grey and light grey correspond to the $q = k/4$ (Subsec. 4.5.4) and $q \sim k/\sqrt{3}$ (Subsec. 4.5.2) instability regions. In **c**, the dark grey is also the stable region and the instability regions $q \sim k/2$ (Subsec. 4.5.5) and $q = k/2$ (Subsec. 4.5.3) are indicated in grey and light grey.

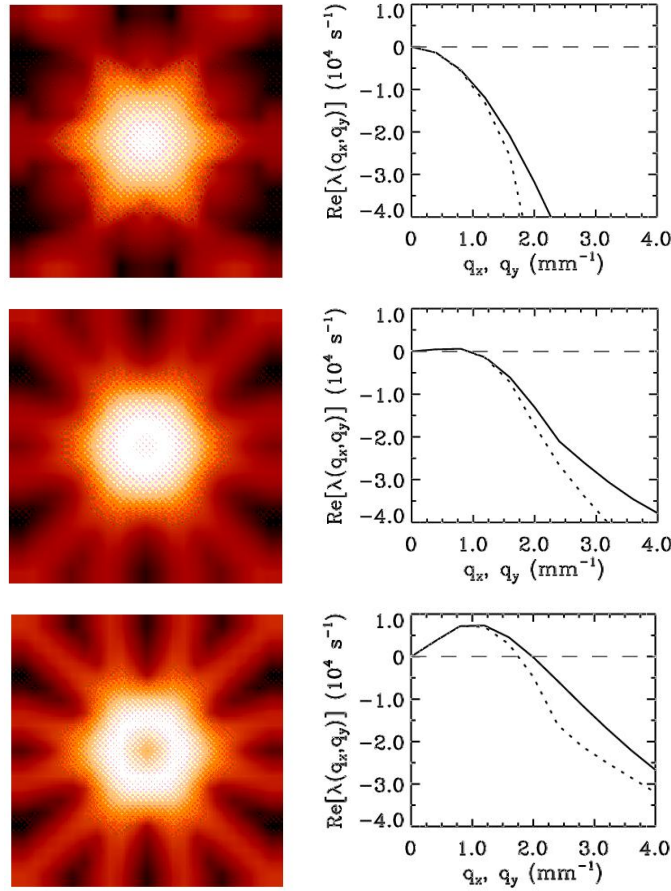


Figure 4.7: Left: Largest real part of the eigenvalues $Re[\lambda_0(q_x, q_y)]$ of a stationary hexagonal pattern of fundamental wavenumber $k = 23.5 \text{ mm}^{-1}$. As shown in Fig. 4.6a, for this value of k the hexagonal pattern becomes unstable as the pump is decreased at $P_{eck}^0 = 1.47 \times 10^5 \text{ s}^{-1}$ (from top to bottom $P^0 = 1.95 \times 10^5 \text{ s}^{-1}$, $1.45 \times 10^5 \text{ s}^{-1}$ and $1.35 \times 10^5 \text{ s}^{-1}$). In each figure the grey scale is taken between the minimum (black) and maximum (white) values of $Re[\lambda_0(q_x, q_y)]$. The center of the figures corresponds to $\vec{q} = 0$, where $\lambda_0(0, 0) = 0$. In the first two figures the center is the maximum value. In the last figure the center takes a reddish color because it is surrounded by the positive eigenvalues corresponding to the long-wavelength unstable modes. Right: transverse cut of $Re[\lambda_0(q_x, q_y)]$ in the q_x (solid line) and q_y direction (dotted line).

The narrow long-wavelength instability region on the left of Fig. 4.6 can only be observed by considering large systems since, in that region, only perturbations with a considerably long wavelength have a positive growth rate. For systems small enough ($L < 6 \text{ mm}$) this long-wavelength instability region is not present and hexagons with small wavenumbers are stable until k enters the region labeled as $q \sim k/\sqrt{3}$.

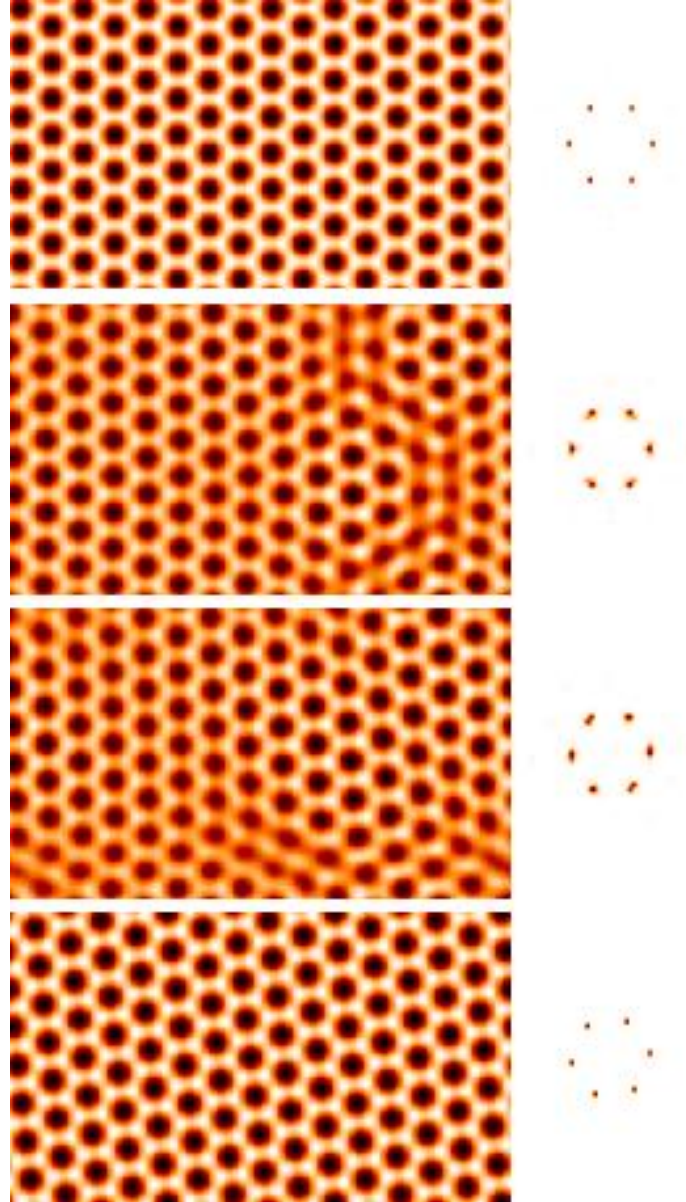


Figure 4.8: Time evolution of the orientation $\phi(\vec{x}, t)$ (left) and its Fourier spectra (right) for unstable hexagons. In the left panels dark (white) color indicates low (large) values of the orientation. In the right panels the white background is zero and darker colors indicate larger values of the amplitude of the Fourier modes. The wavenumber of the initial unstable hexagons is $k = 23.5 \text{ mm}^{-1}$ and $P^0 = 1.35 \times 10^5 \text{ s}^{-1}$. The time increases from top to bottom. Note the linear growth of the Fourier modes close to the fundamental ones and the final state with a smaller wavenumber $k' = 22.2 \text{ mm}^{-1}$. The numerical simulations have been performed on a 256×256 rectangular grid with $\Delta k_x = k/16$ and $\Delta k_y = \sqrt{3}\Delta k_x$.

4.5.2 $q \sim k/\sqrt{3}$ instability

In this region (light grey area in Fig. 4.6b) perturbations with \vec{q} close to the vertexes of the 1st Brillouin zone (see Fig. 2.6) have positive linear growth rate as shown in Fig. 4.9. These vertexes are located at a distance $k/\sqrt{3}$ in the direction forming a 30° angle with the fundamental wave-vectors. Strictly speaking the perturbations with positive linear growth are not those with \vec{q} exactly at the vertexes of the first Brillouin zone but those located in their surroundings as shown in Fig. 4.9. Thus, when starting as initial condition with an unstable stationary hexagonal pattern inside this region, we observe wavevectors at a distance $\sim k/\sqrt{3}$ from the wavevectors of the pattern forming a $\sim 30^\circ$ angle that grow linearly (as shown in Fig. 4.10, second snapshot). As soon as these modes get a large amplitude, nonlinear dynamics come into play. For low values of the pump, as it is the case in Fig. 4.10, a hexagonal pattern with the wavenumber of the linearly unstable modes replace the original pattern (third and fourth snapshots). The wavenumber of the new hexagonal pattern lie inside the stable region. At difference with the long-wavelength instability, in this case the wave-vectors of the hexagons do not change continuously, but there is a discrete change even in the case of an infinite system. In particular, in addition to the finite change in the modulus, the hexagons rotate almost 30° . For larger values of the pump, the nonlinear dynamics does not lead to the selection of a hexagonal pattern but a more complex non-stationary state with many excited wavevectors. These structures are similar to those observed starting from random initial conditions for the same values of the pump.

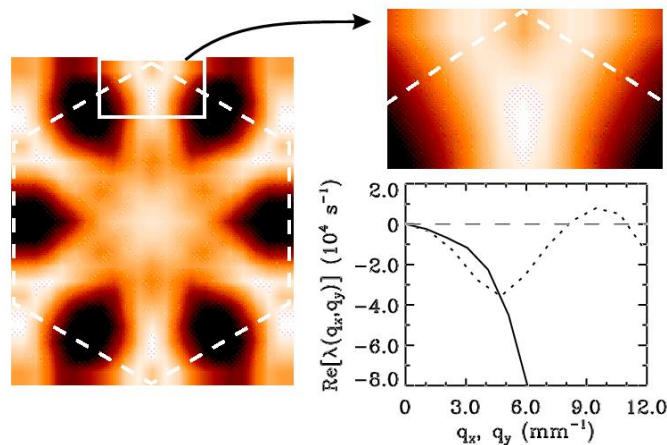


Figure 4.9: The same as in Fig. 4.7 for a hexagonal pattern with $k = 20.5 \text{ mm}^{-1}$ in the region $q \sim k/\sqrt{3}$. For this value of k , as shown in Fig. 4.6, the hexagonal pattern is unstable for any value of the pump P^0 . Here we take $P^0 = 1.5 \times 10^5 \text{ s}^{-1}$. The white dashed hexagon indicate the limits of the first Brillouin zone. Note that the largest eigenvalues are located at the neighborhood of the vertex of the first Brillouin zone.

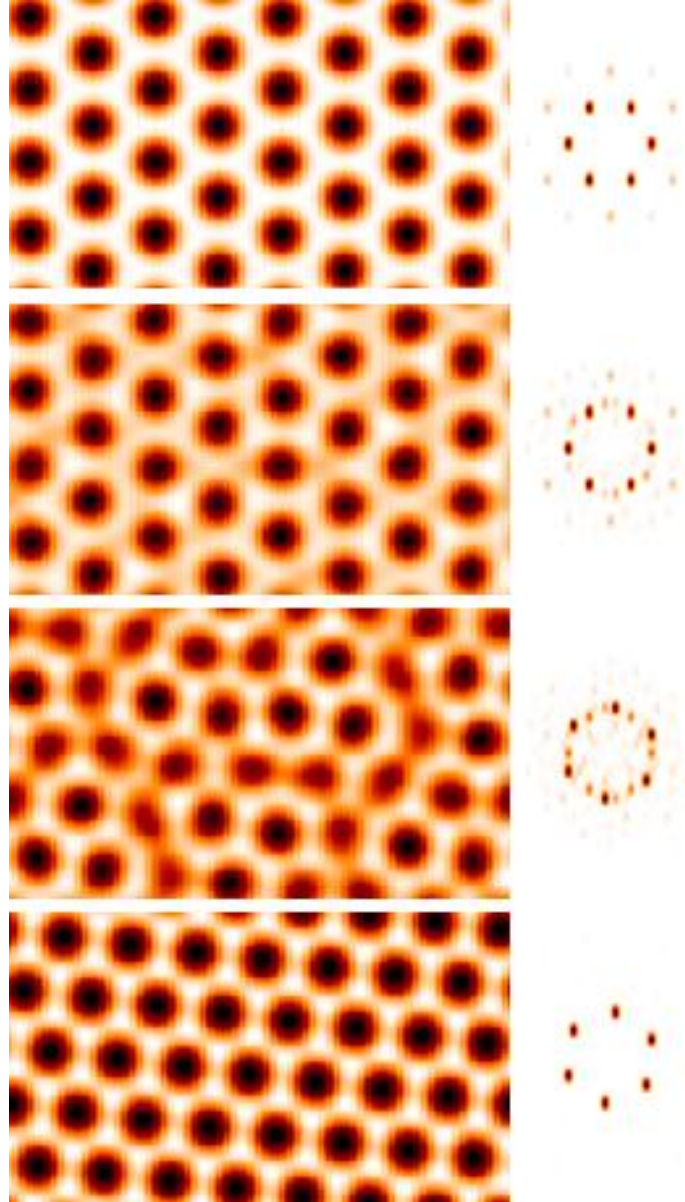


Figure 4.10: The same as in Fig. 4.8 for a hexagonal pattern inside the $q \sim k/\sqrt{3}$ region ($k = 20.5 \text{ mm}^{-1}$, $P^0 = 1.5 \times 10^5 \text{ s}^{-1}$). Note the linear growth of the Fourier modes at a distance $\sim k/\sqrt{3}$ in the $\sim 30^\circ$ direction with respect to the fundamental wave-vectors of the solution in the second snapshot. The final hexagonal pattern has a wavenumber $k' = 22.3 \text{ mm}^{-1}$ which is within the stable region. In the following the numerical simulations are performed on a 128×128 rectangular grid with $\Delta k_x = k/8$ and $\Delta k_y = \sqrt{3}\Delta k_x$

4.5.3 $q = k/2$ instability

In the region $q = k/2$ (light grey area in Fig. 4.6c) the perturbations with vectors \vec{q} of modulus $k/2$ located at the border of the 1st Brillouin zone in the direction of the wave-vectors of the pattern have a positive growth rate (Fig. 4.11). Fig. 4.12 shows a simulation where the pump has been increased above the instability threshold. In the first stages of the simulations (second and third snapshots) subharmonic wavevectors at the half of the fundamental wavenumbers can be seen growing linearly as predicted by the stability analysis. In this case the bifurcation is supercritical since close to the critical point the amplitude of the linearly unstable modes remain small due to nonlinear saturation. As a result of this bifurcation a stationary superlattice is observed. Its periodicity length is two times the one of the underlying primary hexagons (fourth snapshot in Fig. 4.12).

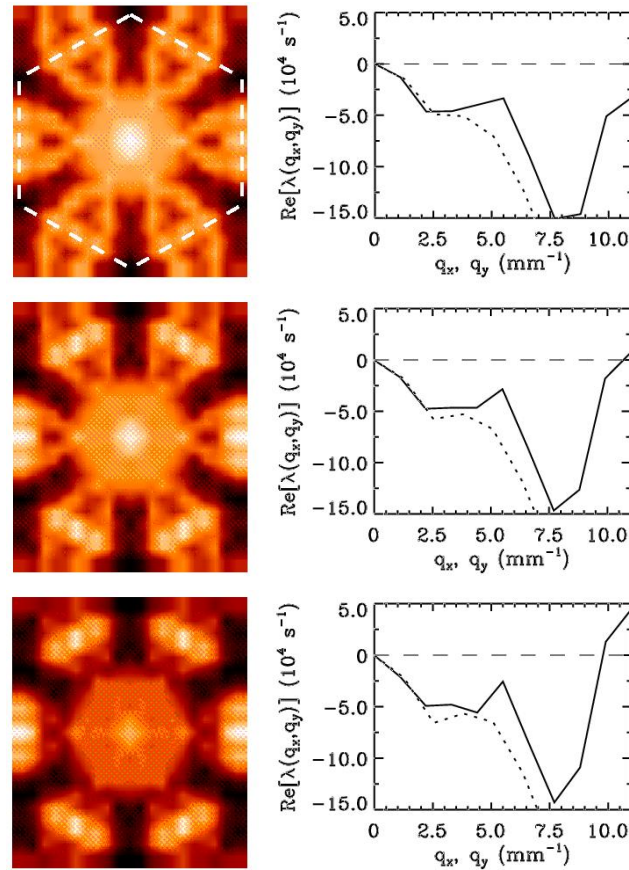


Figure 4.11: The same as in Fig. 4.7 for a stationary hexagonal pattern with wavenumber $k = 22.0 \text{ mm}^{-1}$ crossing the instability line of the region $q = k/2$ located at $P_{k/2}^0 = 3.25 \times 10^5 \text{ s}^{-1}$ (from top to bottom $P^0 = 3.0 \times 10^5 \text{ s}^{-1}$, $3.3 \times 10^5 \text{ s}^{-1}$ and $3.6 \times 10^5 \text{ s}^{-1}$). In the first picture the white dashed line indicates the limits of the first Brillouin zone. Note that the largest eigenvalues are located on the border of the first Brillouin zone in the direction of the fundamental wave-vectors of the hexagonal pattern.

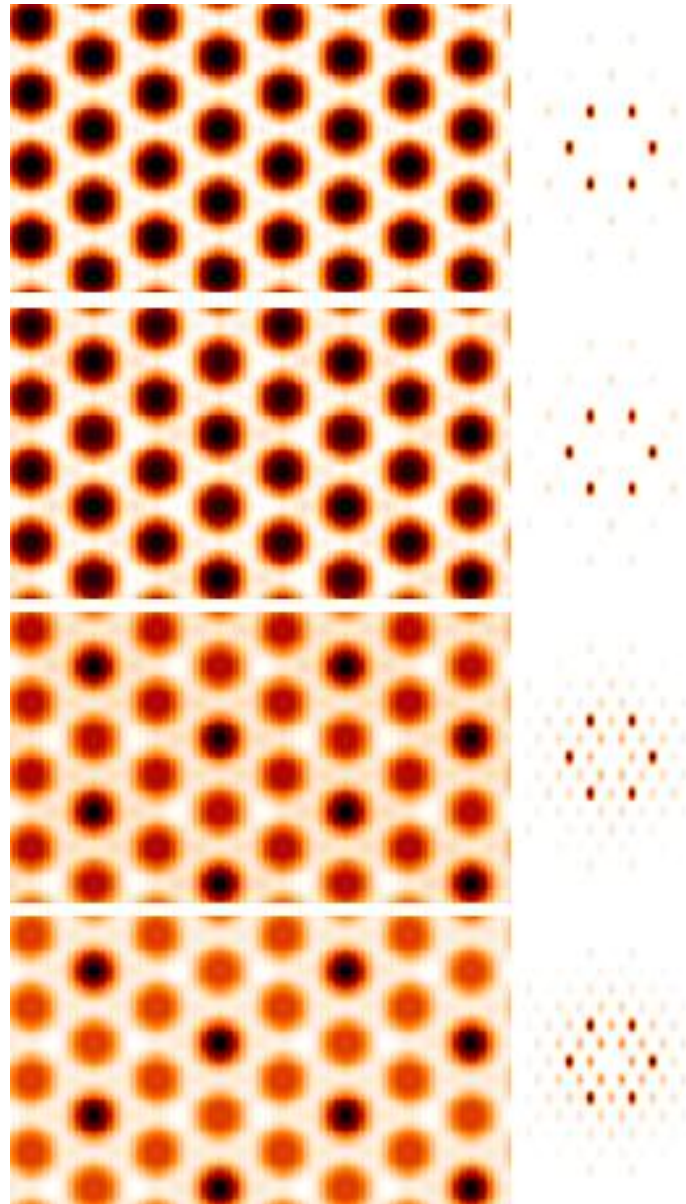


Figure 4.12: The same as in Fig. 4.8 for a hexagonal pattern inside the $q = k/2$ region ($k = 22.0 \text{ mm}^{-1}$, $P^0 = 3.5 \times 10^5 \text{ s}^{-1}$). Note the linear growth and nonlinear saturation of sub-harmonics exactly at the half of the wavevectors of the original hexagonal pattern and the final super-lattice.

4.5.4 $q = k/4$ instability

In the region $q = k/4$ (grey area in Fig. 4.6b) perturbations with $q = k/4$ in the direction of the fundamental wave-vectors of the pattern have positive growth rate (Fig. 4.13). This wavevectors can be seen growing linearly in the first stages of a numerical simulation where the pump has been increased above the instability line (Fig. 4.14). This simulation shows, however, that the transition is subcritical, and the nonlinear dynamics leads to a spatial structure with twelve fundamental wave-vectors. The second hexagonal set has modulus $k = \sqrt{3}k/2$ and it forms a 30° angle with the wave-vectors of the original pattern (Fig. 4.14). The resulting structure is also a superlattice with a periodicity length twice the one of the initial hexagonal pattern.

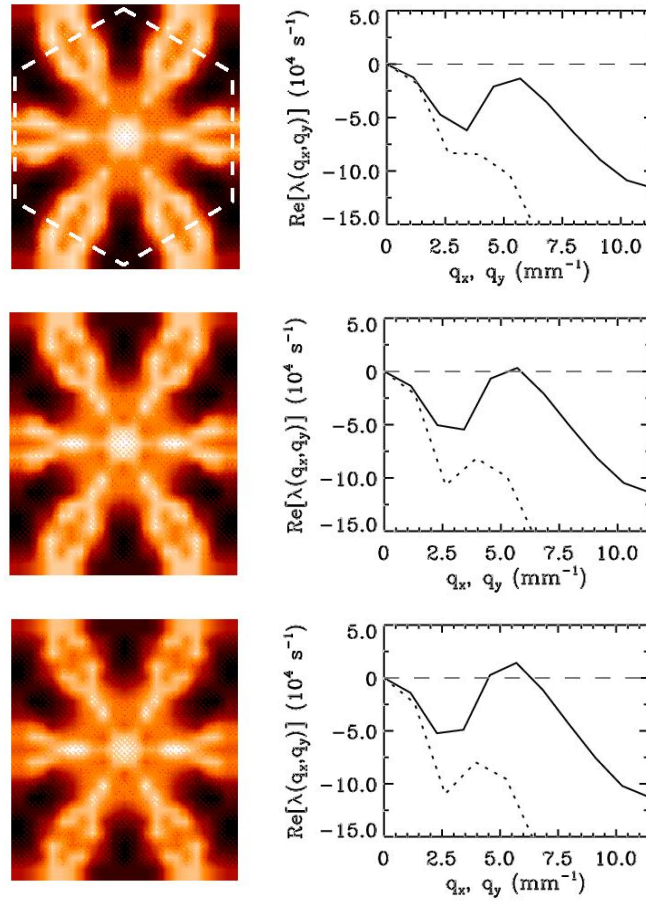


Figure 4.13: The same as in figure 4.7 for a stationary hexagonal pattern with wavenumber $k = 22.8 \text{ mm}^{-1}$ crossing the $q = k/4$ instability threshold located at $P_{k/4}^0 = 2.75 \times 10^5 \text{ s}^{-1}$ (from top to bottom $P^0 = 2.5 \times 10^5 \text{ s}^{-1}$, $2.8 \times 10^5 \text{ s}^{-1}$ and $3.0 \times 10^5 \text{ s}^{-1}$).

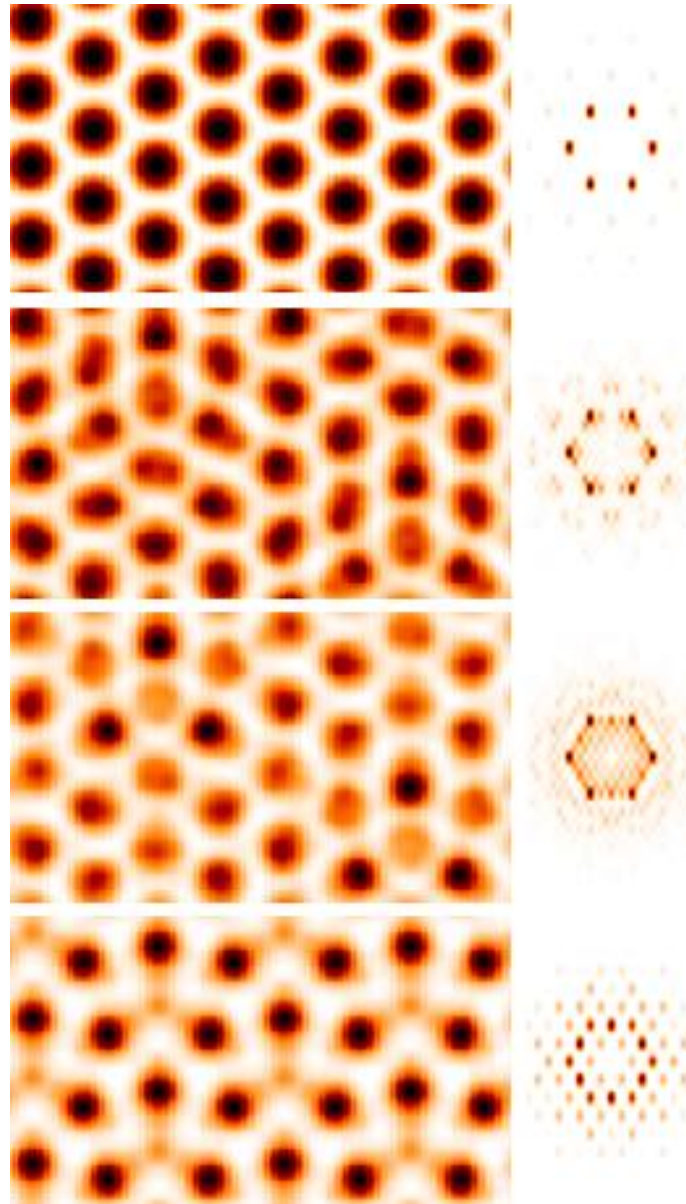


Figure 4.14: The same as in Fig. 4.8 for a hexagonal pattern inside the $q = k/4$ region ($k = 22.8 \text{ mm}^{-1}$, $P^0 = 3.0 \times 10^5 \text{ s}^{-1}$). Note the final nonlinear selection of Fourier modes different from those that growth linearly. The final state is a pattern formed by twelve wavevectors.

4.5.5 $q \sim k/2$ instability

Finally, in the $q \sim k/2$ region (grey area in Fig. 4.6c), the stationary hexagonal patterns are unstable against perturbations with \vec{q} close to the limits of the first Brillouin zone in the direction of the fundamental wave-vectors. However, at difference with the case discussed in Subsection 4.5.3, the perturbations that first become unstable are not those with $q = k/2$ but those in their vicinity (Fig. 4.15). In the second row of Fig. 4.15 the growth rate of perturbations with \vec{q} close to $\vec{k}_n^0/2$ ($n = 1, 6$) is already positive while the perturbation with $\vec{q} = \vec{k}_n^0/2$ ($n = 1, 6$), exactly half of a fundamental wave-vector, have negative growth rate as can be seen in the transverse cut. A numerical simulation increasing the pump above the instability line yields the linear growth of these Fourier modes at a distance $q \sim k/2$ in the direction of the fundamental wavevectors (Fig. 4.16). At difference also with the case $q = k/2$, the transition is subcritical and drive the system away from the hexagonal pattern solution. In small systems, as it is the case in Fig. 4.16, the system ends up, after a long excursion in the phase space, in a stationary pattern with twelve modes and rectangular symmetry (last snapshot in Fig. 4.16). Notice that two of the Fourier modes (the ones over the vertical axis) have the largest amplitude while the two perpendicular modes have a small intensity. All the other eight modes have the same intensity which is in between the previous ones. This pattern, due to its four fold symmetry, is not directly connected with the unstable manifold of the original hexagonal branch and it probably belongs to a separated branch starting from the homogeneous solution. However, for some parameter range it seems to be an important attractor of the dynamics. As discussed below, this pattern is also often observed in the experiment. In larger system, the nonlinear dynamics leads, in general, to a complex non stationary pattern with many excited Fourier components.

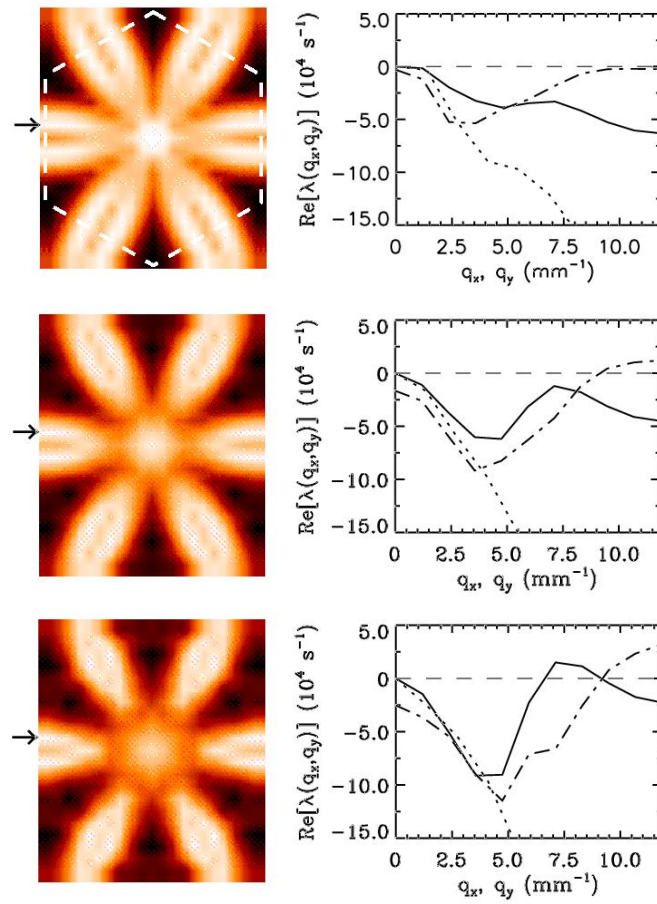


Figure 4.15: The same as in Fig. 4.7 for a hexagonal pattern with wavenumber $k = 23.7 \text{ mm}^{-1}$ crossing the instability line ($P_{\sim k/2}^0 = 1.65 \times 10^5 \text{ s}^{-1}$) of region $q \sim k/2$. From top to bottom $P^0 = 1.6 \times 10^5 \text{ s}^{-1}$, $2.0 \times 10^5 \text{ s}^{-1}$ and $2.5 \times 10^5 \text{ s}^{-1}$. The dot-dashed line correspond to the transverse cut of $Re[\lambda_0(q_x, q_y = 1.37)]$ as indicated by the arrow on the left.

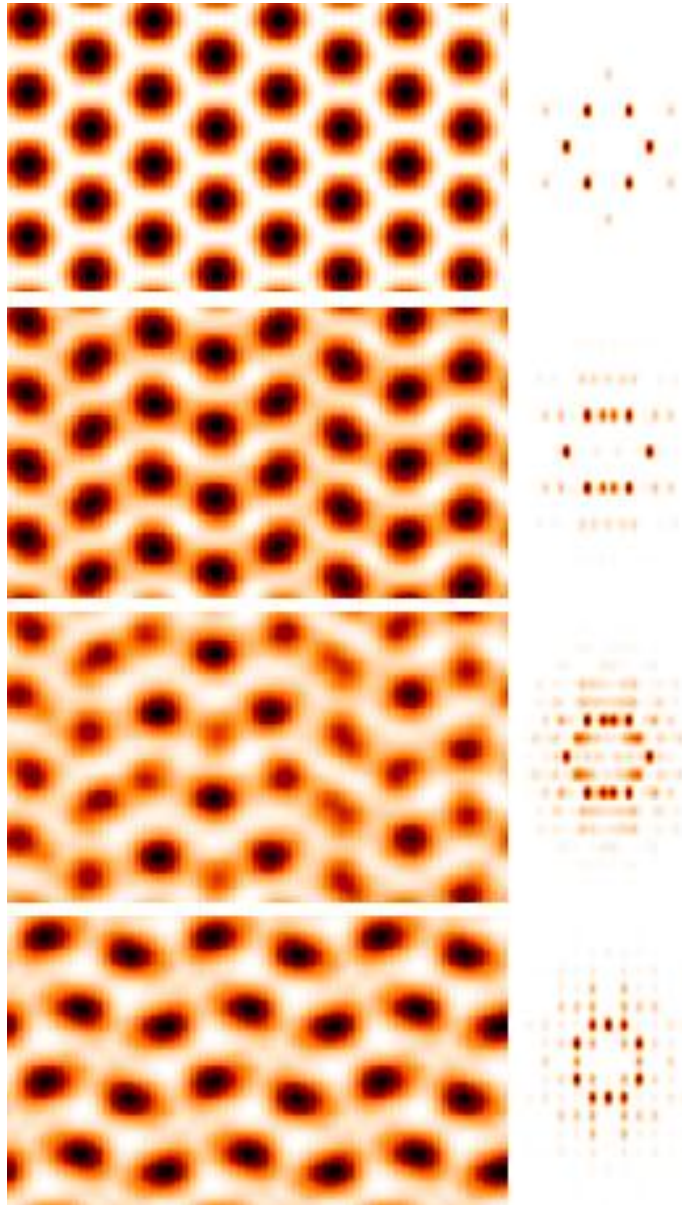


Figure 4.16: The same as in Fig. 4.8 for a hexagonal pattern inside the $q \sim k/2$ region ($k = 23.7 \text{ mm}^{-1}$, $P^0 = 2.5 \times 10^5 \text{ s}^{-1}$). Note the linear growth of the wavevectors predicted by the stability analysis. The final stationary state with twelve modes and four fold symmetry is reached after a long excursion in phase space.

4.5.6 Discussion of the theoretical results

The analysis described above establishes that hexagonal patterns are stable only in a closed subspace of the P^0 - k -diagram. This region is the ‘hexagonal’ analog of the ‘Busse-balloon’ for stripes [23, 39]. At the sides, it is limited by long-wavelength instabilities and the finite wavelength $q \sim k/\sqrt{3}$ - and $q \sim k/2$ -instability, respectively. The long-wavelength instability results in the formation of a hexagonal pattern with a different stable wavenumber. The same is true for the $q \sim k/\sqrt{3}$ -instability for low pump values.

The upper boundary of the stability balloon is given by finite wavelength instabilities which result in the formation of more complex patterns consisting of twelve wavevectors (regions $q = k/4$, $q = k/2$ and $q \sim k/2$). Only the $q = k/2$ -instability is supercritical. Hence the coexistence of hexagons and more complex patterns can be expected.

We have performed also numerical simulations including noise on a square grid over long time integration to explore the asymptotic states. The noise should help in shortening the transients. The simulations confirm that the hexagonal pattern formed spontaneously at threshold does not destabilizes for a pump rate lower than $P^0 = 3.4 \times 10^5 \text{ s}^{-1}$, if the pump rate is increased. If the pump rate is decreased again, patterns with twelve Fourier component persist down to a level of about $P^0 \approx 1.7 \times 10^5 \text{ s}^{-1}$, i.e. 30% above the primary threshold. Starting from noisy initial conditions hexagons form up to a pump rate of typically $P^0 = 1.8 \times 10^5 \text{ s}^{-1}$ and patterns with twelve Fourier components form above this value. This transition level amounts to a pumping level of 38% above threshold. If the size of the system is large enough, the resulting structures are somehow irregular and/or consists of several domains of patterns with twelve wavevectors of different kind and/or orientation in most cases. The competition has long transient and for times up to 500000 iterations, or 50 ms for testing purposes, the structure does not reach a stationary state. However, the form of the patterns do not change qualitatively. Typically, perfect stationary patterns are found, if a suitable seed is used. These results demonstrate that hexagons and more complex pattern coexist over a rather large range of pump values.

4.6 Comparison with experiment

As discussed in [15], negative hexagons (honeycombs) develop spontaneously from the unstructured state, if some threshold of input power is crossed. This is in agreement with the analysis of Sec. 4.4 and previous numerical [15, 95] and analytical studies [95]. If the power is increased to a value of about 30-40% above threshold, the hexagons become unstable and patterns consisting of twelve fundamental Fourier modes arise [106, 6, 94]. This power level is considerably lower than the limit at which the hexagons should become linearly unstable (about 2.6 times threshold, Fig. 4.6), i.e., the secondary instabilities in the experiment take place at lower values of the pump power than in the theoretical analysis. This might be due to different reasons. First, the power level for the secondary instabilities in the experiment

approximately matches the power level at which multistability between hexagons and secondary patterns appears in the simulations (see the previous section). This observation gives some support to the hypothesis that noise – inevitably present in the experiment – might induce transitions to a coexistent state before the point of linear instability is reached. Second, due to the Gaussian profile of the input profile the boundary conditions differ in the experiment and in theory. Especially the fact that the bifurcation parameter has a spatial dependence might play a role in advancing (or delaying) secondary instabilities. These questions need further consideration in future work.

Patterns consisting of twelve Fourier modes are also obtained in the simulations as discussed above. In the following, we will compare the patterns observed in the experiment with the ones obtained in the simulations. However, one should keep in mind that the main aim of the theoretical investigations was to describe the onset of the instability of the hexagons and not a survey and classification of all possible asymptotic states. The preliminary simulations indicate a high level of multistability between different patterns, which make a determination of the complete solution space a formidable task which has to be postponed to forthcoming work.

In the experiment, the orientation is not directly accessible. The observed quantities are the intensity distribution of the transmitted field at the exit facet of the medium (‘near-field pattern’) and the Fourier power spectrum of the transmitted field (‘far-field pattern’). The near-field pattern can be calculated by

$$I(\vec{x}) \sim e^{-2\alpha_0 L(1-\phi(\vec{x}))}, \quad (4.18)$$

which has a monotonous but highly nonlinear dependence on $\phi(x, y)$. The far-field pattern is obtained from

$$I(\vec{k}) \sim \left| \int e^{-\alpha_0 L(1-i\bar{\Delta})(1-\phi(\vec{x}))} e^{i\vec{k}\vec{x}} d\vec{x} \right|^2. \quad (4.19)$$

In the parameter range considered in the theoretical results presented in Section 4.5, there is a region with multi-stability between different patterns consisting of twelve wavevectors far enough above the secondary threshold (see Fig. 4.17). Apart from quasipatterns with a twelve-fold rotational symmetry (Fig. 4.17a, b, [106, 4, 6]) and patterns in which neither in Fourier space nor in real space a particular order is apparent (Fig. 4.17c, d), there are two dominant types of patterns which have a Fourier power spectrum with a sixfold (Fig. 4.17e, f) or a fourfold rotational symmetry (Fig. 4.17g, h).

The latter pattern strongly resembles the result of the numerical simulation depicted in Fig. 4.16. It also consists of four rows with three wave vectors that are mutually at an angle of 90° . The patterns differ in the ratio of the wave numbers in the orthogonal directions. While the ratio is 1 within an accuracy of less than 2% in Fig. 4.17g, h, the wave numbers differ by more than 10% in the numerical simulation (Fig. 4.16), i.e. the pattern is squeezed in comparison to the form observed experimentally. However, in the experiment patterns similar to the squeezed ones of the simulations occur for higher input power as depicted in Fig. 4.18a,b. In this

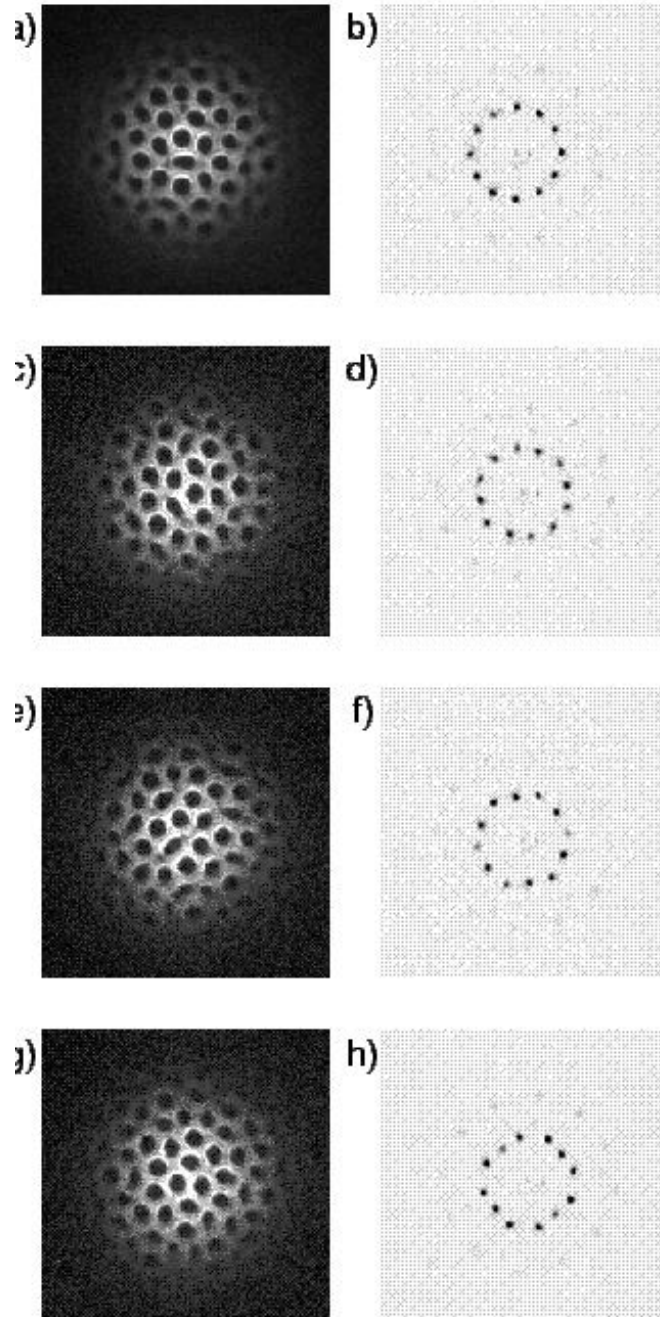


Figure 4.17: Experimentally observed near (a,c,e,g) and far-field (b,d,f,h) intensity distributions of the transmitted beam for nominal constant parameters. Parameters: nitrogen buffer gas pressure $p_{\text{N}_2} = 200$ hPa, sodium cell temperature $T = 318$ °C, distance between the sodium cell and the feedback mirror $d = 88$ mm, input power $\mathcal{P}_{in} = 113$ mW, detuning from the sodium-D₁-line is $\Delta = 3.6$ GHz.

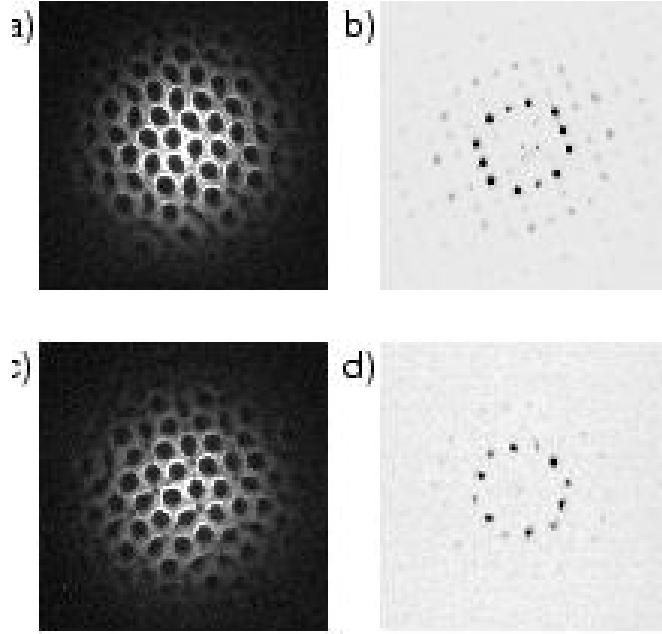


Figure 4.18: Experimentally observed near (a,c,e,g) and far-field (b,d,f,h) intensity distributions of the transmitted beam. The detuning from the sodium-D₁-line Δ and input power \mathcal{P}_{in} are in a,b) $\Delta = 3.6$ GHz, $\mathcal{P}_{in} = 113$ mW c,d) $\Delta = 3.6$ GHz, $\mathcal{P}_{in} = 188$ mW, and e-h) $\Delta = 2.5$ GHz, $\mathcal{P}_{in} = 200$ mW. The other parameters are as in Fig. 4.17.

pattern the four-fold symmetry is clearly broken and the discussed ratio is 1.063. Therefore it resembles quite closely the pattern obtained numerically in Fig. 4.16. It is also apparent in the simulations as well as in the experiments that the wave vectors at the ends of the rows have approximately the same amplitude, whereas the pairs of wave vectors in the center of the rows have a lower or a higher amplitude than the former ones.

The numerically obtained pattern in Fig. 4.14 has the same wave vector configuration as the experimentally observed pattern in Fig. 4.17e, f, i.e. it consists of two hexagonal triads of slightly different wavenumber which are rotated by 30° . The triad with the larger wavenumber has a lower amplitude than the one with the smaller wavenumber. Nevertheless, differences in the near field patterns hint to the fact that the phases of the Fourier peaks are not the same. In order to clarify the deviation, three generated patterns with the same Fourier spectrum but different phase distributions are shown in Fig. 4.19.

If all phases are π as in Fig. 4.19a the near field obeys a sixfold rotational symmetry. The depicted structure resembles neither the experimental nor the numerical result. In the case of Fig. 4.19b, in which the phases are $\pi/3$ for all Fourier modes, the pattern has a threefold rotational symmetry. It is built by minima that constitute triangles. This structure is also obtained as the asymptotic pattern in Fig. 4.14. The same symmetry properties hold for the numerically calculated near field pattern, which is displayed in Fig. 4.20.

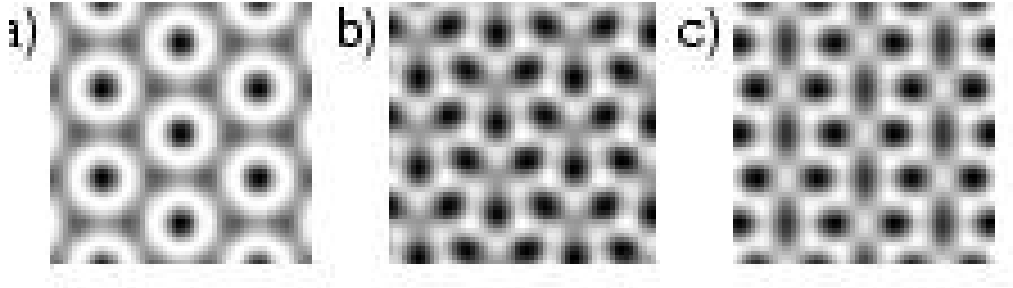


Figure 4.19: Hexagonal superlattices generated by the addition of twelve Fourier modes with the same wave vectors and different phases: a) all phases are π , b) all phases are $\pi/3$ and c) one phase in each triad is π , all others are zero. The wave vectors are given by two hexagonal triads with different wave numbers that are mutually at an angle of 30° (see e.g. Fig. 4.14). The amplitude of the triad with the smaller wavenumber is twice the amplitude of the triad with the larger wavenumber.

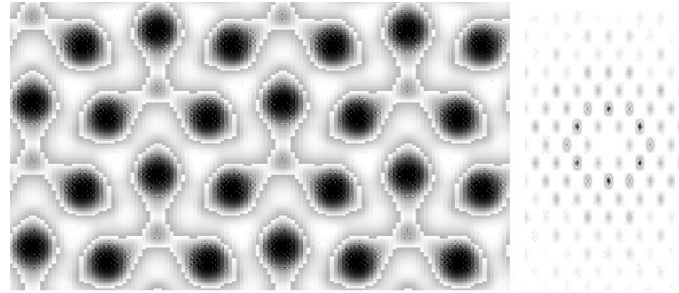


Figure 4.20: Near field (left) and far-field (right) pattern calculated using Eqs. (4.18) and (4.19) from the distribution of the orientation displayed in the lowest panel of Fig. 4.14.

The pattern observed in the experiment (Fig. 4.17e, f) resembles the structure depicted in Fig. 4.19c. For this structure one phase in each triad is π , all others are zero. The resulting pattern has a twofold rotational symmetry in real space. The basic structure is a squeezed hexagon of which the center is built by an elongated minimum. This basic structure is typical for experimentally observed near field intensity distributions (cf. e.g. Fig. 4.17e, f). However, for lower values of the detuning the phase distribution of the observed patterns is less clear. In this parameter region, some of the experimentally observed patterns (Fig. 4.18c, d) contains groups of triangular arrangements of three minima around a smaller central minima (Fig. 4.18c, d). These patterns bear a quite close resemblance to the numerically obtained ones depicted in Figs. 4.14, 4.20. We conclude that the phase selection within the hexagonal superstructure is weak.

4.7 Conclusions

We have analyzed in detail the secondary bifurcations of hexagonal patterns in a microscopic model for an alkali metal vapor in a single-mirror arrangement. The stability analysis of the stationary hexagonal patterns predicts different instabilities depending on their fundamental wavenumber. Hexagons with wave numbers much lower or much larger than the critical one undergo phase instabilities or instabilities at $q \sim k/\sqrt{3}$ or $q \sim k/2$, while hexagonal patterns with wavenumber close to the critical one are stable for moderated pumps and undergo finite wavelength instabilities (regions $q = k/4$, $q = k/2$ and $q \sim k/2$) for large values of the pump. After the instability has produced a growing disturbance, the system moves towards a new state because of intrinsically nonlinear mechanisms. In some cases, the perturbation is found to saturate to finite amplitude and the new state resembles the unstable deformation of the original pattern. This is the case only for the $q = k/2$ instability which result in the formation of a pattern with twelve wave vectors. In the other cases, the system undergoes a long excursion in the phase space until it reaches a new attractor. In some cases it is a hexagonal pattern with a different – stable – wavenumber or a periodic pattern (superlattices) with twelve wave vectors.

Since most of the important instabilities are subcritical, hexagons and superlattice patterns might coexist and there is also coexistence between different superlattice patterns. Due to the high level of multistability present it is very difficult to get an overview on all possible behaviors and transition scenarios. This is especially true in a large system in which competition between several coexistent attractors might lead to long-lasting transients and non-stationary states.

Experimentally, secondary instabilities of the hexagons versus more complex patterns consisting of twelve wavevectors were observed. There is a correspondences between some of the experimentally observed superlattice patterns to some of the patterns obtained numerically. In the experimental system noise induce transitions between the different coexisting multistable patterns. Also the Gaussian profile of the pump beam may affect the stability of some of the patterns. A thorough analysis of the asymptotic states is beyond the scope of the present thesis and needs considerable further efforts.

The present analysis established the limits of the stability of hexagons and identified the modes relevant for the destabilization. Future work will be directed to a detailed investigation of the nonlinear evolution of the secondary instabilities and the asymptotic states, and needs to address the possible influence of further branches emerging from the homogeneous solutions.

Part II

Dynamics of localized structures

Chapter 5

Dynamical properties of two-dimensional Kerr cavity solitons

5.1 Introduction

In this chapter we study the dynamics of Kerr cavity solitons, localized structures in Kerr cavities that arise as a consequence of a modulational instability of the homogeneous solution, the kind of localized structures described in subsection 1.2.1. They exist in the parameter range where the homogeneous solution coexists with stable subcritical hexagonal patterns. Kerr cavity solitons share some properties with propagating spatial solitons in a Kerr medium, but there are interesting differences. While in one transverse dimension (1D) Kerr spatial solitons are stable, it is well known that their 2D counterparts are unstable against self-focusing collapse [9, 174]. The stability and dynamics of 2D Kerr cavity solitons (KCS) are thus of particular interest. Their existence and structure was documented some years ago [58], but only unstable KCS were found, though with indications that they might stabilize for smaller cavity detunings. This was subsequently confirmed in a brief report [59], but few details were presented, and only stability against cylindrically-symmetric perturbations was established, so that the question of the azimuthal stability of 2D KCS was left open.

In this chapter we study the dynamical properties of KCS and their instabilities. In part of the domain in which they are radially stable, 2D KCS are in fact azimuthally unstable. The existence of a broad domain of absolute stability for moderately small cavity detunings is, however, fully confirmed [62].

The character of the cylindrically symmetric instability is a Hopf bifurcation, resulting in a breathing oscillation of the KCS. The amplitude of this oscillation increases with the background intensity. The oscillating soliton is rather robust, and neither collapses nor decays [62]. Increasing further the background intensity a *saddle-loop* bifurcation occurs. The oscillating KCS collides with its unstable branch and the limit cycle is destroyed. At this point the period of the oscillations

diverges to infinity, and beyond it, KCS's decay to the homogeneous solution. Above this instability the system presents excitability mediated by the unstable lower-branch KCS. To our knowledge this is the first example of excitability in a localized structure.

Where azimuthal instability to a mode $e^{\pm im\phi}$ dominates, it may be preferentially of index $m = 5$, or $m = 6$. In this case the resulting dynamics leads to formation of an expanding pattern, which for the $m = 5$ instability maintains five-fold symmetry as it grows. In both cases the emerging pattern is dynamical, each spot oscillating with a location-dependent phase as discussed in chapter 2.

We establish these results by an essentially exact, if numerically-based, method [61, 167], which enables us to provide a much more complete dynamical picture of 2D KCS than previously available. This method gives information on the nature and spatial structure of the internal modes of the KCS which become undamped at the stability boundaries. We confirm our findings using dynamical simulations with starting conditions governed by our calculated mode structures.

5.2 Kerr cavity solitons

As in chapter 2, we describe KCS using the standard mean-field cavity model of Lugiato and Lefever [150]. However, let us now write Eq. (2.1) in a slightly different way to make clear the connection of this model with the NSE

$$i\frac{\partial E}{\partial t} + \nabla^2 E + |E|^2 E = i\varepsilon(-E - i\theta E + E_0). \quad (5.1)$$

The three terms on the right side of this equation are in fact perturbations of the NSE, all small if ε is small. The first term is a linear loss ($\varepsilon > 0$), the last the driving field E_0 needed to sustain E against that loss, while the middle term, in θ , describes the cavity detuning with regard to the driving field. This equation is also known as the Driven and Damped NSE (DDNSE).

With the following re-scaling

$$\begin{aligned} E &= E/\sqrt{\varepsilon} \\ E_0 &= E_0/\sqrt{\varepsilon} \\ \vec{x} &= \varepsilon\vec{x} \\ t &= \varepsilon t, \end{aligned} \quad (5.2)$$

which is equivalent to set $\varepsilon = 1$, Eq. (5.1) becomes identical to Eq. (2.1) used in chapter 2¹. In the following we set, then, $\varepsilon = 1$ and restrict ourselves to the non-bistable regime $\theta < \sqrt{3}$. We can thus use the intra-cavity background intensity I_s together with θ as convenient control parameters. In this case, as discussed in

¹At difference with chapter 2, where $\alpha = 2$, throughout this chapter $\alpha = 1$. Both cases are equivalent and can be converted one into the other by rescaling the field E with a factor $\sqrt{2}$. As a result in this chapter the threshold values of I_s have a factor 2 with respect to chapter 2.

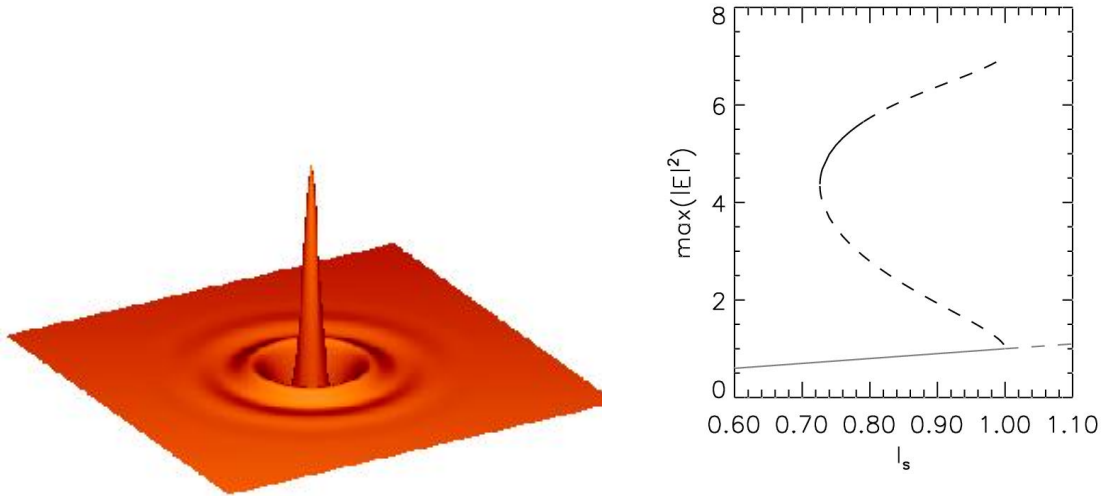


Figure 5.1: Left: A typical cavity soliton shows a bright peak on a darker homogeneous background, with a few weak diffraction rings. Plotted is the modulus of the intracavity field as a function of the transverse coordinates x and y ; parameters are $\theta = 1.3$, $I = 0.9$. Right: The maximum amplitude of the stationary Kerr cavity solitons versus I_s for $\theta = 1.3$. Solid (dashed) lines indicate that the solutions are stable (unstable). The upper branch undergoes a Hopf instability at $I_s \approx 0.79$. The grey line corresponds to the homogeneous solution.

section 2.2 the plane wave solution is always unstable to some transverse wave-vector whenever $I_s \geq 1$. Stable KCS can thus only exist for $I < 1$, since they must asymptote to a stable E_s .

Fig. 5.1 (left) shows a typical 2D KCS for $\theta = 1.3$, $I = 0.9$. It consists of a bright peak on a flat background, with a few weak diffraction rings. The period and spatial damping rate of these rings follows from the fact that the KCS is asymptotically given by a pair of generalized Bessel functions [58, 59]. The rings become much more pronounced as $I_s \rightarrow 1$.

For convenience, we set $E = E_s(1 + A)$, so that $A(\vec{x})$ describes the solution without the background

$$\frac{\partial A}{\partial t} = -[1 + i(\theta - |E_s|^2)]A + i\nabla^2 A + i|E_s|^2(A + A^* + A^2 + 2|A|^2 + |A|^2 A). \quad (5.3)$$

Notice that no linear approximation has been used in passing from Eq. (5.1) to (5.3). The stationary KCS solutions A_s are calculated using a Newton method. The procedure is similar to the one explained in sec. 2.3 to find stationary hexagonal patterns but in real space instead of Fourier space. We discretize the radial version of Eq. (5.3) ($\nabla^2 \rightarrow d_r^2 + \frac{1}{r}d_r$, where r is the radial coordinate) and obtain a set of coupled nonlinear complex equations. The number of equations is the number of discretization points in the radial coordinate. A Fast Fourier Transform is used to compute the spatial derivatives in Fourier space. Zero derivatives at the boundaries ($d_r A(r = 0) = d_r A(r = L) = 0$, where L is the system size that we take much

larger than the size of the soliton) are imposed. Then, from a suitable chosen initial condition, a Newton-Raphson method is used to find solutions of the set [61, 181]. The first guess is usually obtained from a radial cut of a 2D simulation of Eq. (5.1). Similarly to what was done to find stationary extended patterns in chapter 2 continuation techniques [122] are used to explore the region of existence of KCS in the parameter space. This approach is extremely accurate and, furthermore, automatically generates the Jacobian operator whose eigenvalues determine the stability of the solution obtained. With this method we can also find unstable solutions.

To study the stability of cylindrically symmetric solutions with respect to all possible perturbations in the 2D plane, an extended stability analysis including azimuthal perturbations has to be performed. Linearizing Eq. 5.3 around the stationary KCS solution $A_s(r)$ in radial coordinates (r, ϕ) , the following equation for the perturbations $\delta A(r, \phi, t) = A_s(r) - A(r, \phi, t)$ is obtained

$$i \frac{\partial \delta A}{\partial t} = -[1 + i(\theta - |E_s|^2)]\delta A + i \left(\frac{\partial^2 \delta A}{\partial^2 r} + \frac{1}{r} \frac{\partial \delta A}{\partial r} + \frac{1}{r^2} \frac{\partial \delta A}{\partial \phi} \right) + i|E_s|^2(\delta A + \delta A^* + 2A_s \delta A + 2A_s^* \delta A + 2A_s \delta A^* + 2|A_s|^2 \delta A + A_s^2 \delta A^*). \quad (5.4)$$

We analyze the stability with respect to azimuthally periodic perturbations of the form

$$\delta A(r, \phi, t) = (R_+(r)e^{im\phi} + R_-(r)e^{-im\phi})e^{\lambda t}, \quad (5.5)$$

for arbitrary integer m . Notice that for $m \neq 0$ closure of the linearized perturbation equations (5.4) requires terms in both m and $-m$ due to the coupling between δA and δA^* . From (5.4) and (5.5) the following eigenvalue problem for the radial functions $R_{\pm}(r)$ is obtained

$$- [1 + i(\theta - |E_s|^2)]R_{\pm} + i \left(\frac{\partial^2 R_{\pm}}{\partial^2 r} + \frac{1}{r} \frac{\partial R_{\pm}}{\partial r} - \frac{m^2}{r^2} R_{\pm} \right) + i|E_s|^2(R_{\pm} + 2A_s R_{\pm} + 2A_s^* R_{\pm} + 2|A_s|^2 R_{\pm} + R_{\mp}^* + 2A_s R_{\mp}^* + A_s^2 R_{\mp}^*) = \lambda R_{\pm} \quad (5.6)$$

The eigenvalues of the Jacobian associated to this linear problem give the stability of the KCS with respect to azimuthal perturbations of periodicity $2\pi/m$. The shape of the radial functions $R_{\pm m}(r)$ is given by the corresponding eigenvectors of the Jacobian.

Fig. 5.1 (left) shows the maximum intensity of the KCS ($|E(r=0)|^2$). Two branches are found. The branch in the middle, with negative slope, corresponds in fact to unstable KCS. The upper branch has a positive slope and it is usually stable at lower values of I , but becomes unstable as I increases. In the next section we discuss the role of the lower branch as a barrier in the writing mechanism for solitons. In the following sections we discuss the different instabilities of the upper branch.

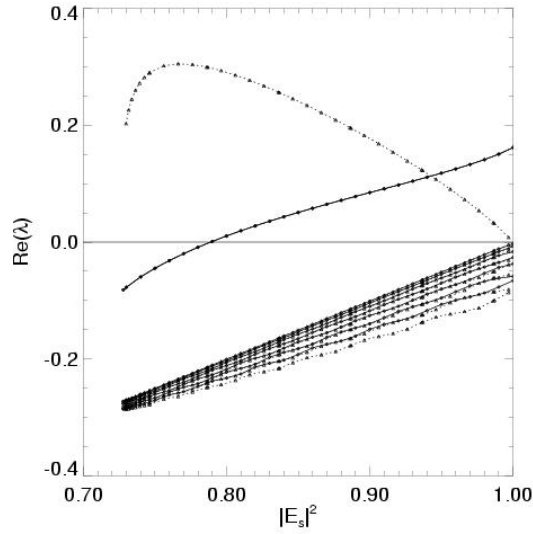


Figure 5.2: Stability of the upper (solid lines) and lower branch (dashed lines) cavity solitons: it shows how the eigenvalues with largest real parts change with $I \equiv |E_s|^2$. The detuning is $\theta = 1.3$.

5.3 Lower Kerr cavity soliton branch

The lower branch KCS has only one unstable mode (Fig. 5.2) and, therefore, in the eigenmodes function space, the unstable manifold is one dimensional and the stable manifold is infinite dimensional. Close to this saddle point, the dynamics collapse, at least as fast as the least-damped stable mode, to the unstable manifold and thus, it rapidly becomes one dimensional. In one direction, the unstable manifold of the lower branch connects with the stable manifold of the upper branch KCS. In the opposite direction it connects with the stable manifold of the homogeneous solution. The lower branch KCS acts then as a barrier: if a initial condition is somehow above the lower branch in phase space it will evolve to the upper branch while if it is below it will decay to the homogeneous solution.

The mechanism by which the unstable manifold of the lower branch cavity soliton acts as a phase space barrier seems quite general, so this phenomenon should not be limited to pure Kerr, or even Kerr-like, media. Recent studies on a liquid crystal light valve [210] and semiconductor model [159] identified the role of the lower branch soliton as a separatrix, in that below a certain amplitude an address pulse failed to write a soliton, while above that critical amplitude the pulse successfully initiated one (which in the case in question was stable). In terms of the above picture, a weak pulse creates a bump below the lower branch, leading to decay, while the critical address pulse corresponds to separatrix given by the stable manifold. Any stronger pulse generates a bump above the lower branch, which evolves into an upper-branch soliton. Such a separatrix behavior in the writing of solitons has been experimentally observed for feedback solitons [209, 210] and in a semiconductor cavity [225]. In the first cases the critical switching dynamics was used to map out the unstable lower branch.

5.4 Hopf bifurcation

As illustrated in Fig. 5.1 KCS in the upper branch are stable only for low values of the intensity I_S . For $\theta = 1.3$, a complex conjugate pair of eigenvalues crosses the imaginary axis at $I \approx 0.79$, rendering the KCS unstable. The underlying mechanism for this instability is a Hopf bifurcation [59, 212]. A perturbed cavity soliton exhibits damped oscillations in the stable domain, which become undamped as the stability boundary is crossed. Notice that as discussed in chapter 2 hexagonal patterns can also be unstable to a Hopf mode. Hopf instability and oscillation of a dark cavity soliton was previously reported and analyzed in a cavity with saturating defocusing nonlinearity [169].

The stability of the 2D KCS for general (θ, I_s) is displayed in Fig. 5.3. The lowest curve corresponds to the saddle-node bifurcation where the upper and middle KCS branches collide. There are no KCS solutions below this line. The area above the saddle-node curve shows where 2D KCS exist and the colored shaded regions show where they are unstable. For a given detuning, they exist only for a finite range of background intracavity intensities $I_{min} < I_s < 1$. This range is broader for large θ . They are stable against $m = 0$ perturbations only over a range $I_{min} < I_s < I_{hopf}$ due to the presence of a Hopf bifurcation in the red shaded area. The Hopf-stable strip is very narrow for $\theta > 1.5$, which is the reason why no stable stationary 2D KCS were found in an earlier study [58].

Figure 5.4 shows the results of a numerical integration of Eq. (5.1) inside the Hopf unstable region ($\theta = 1.3, I = 0.9$). The initial condition was the unstable solution

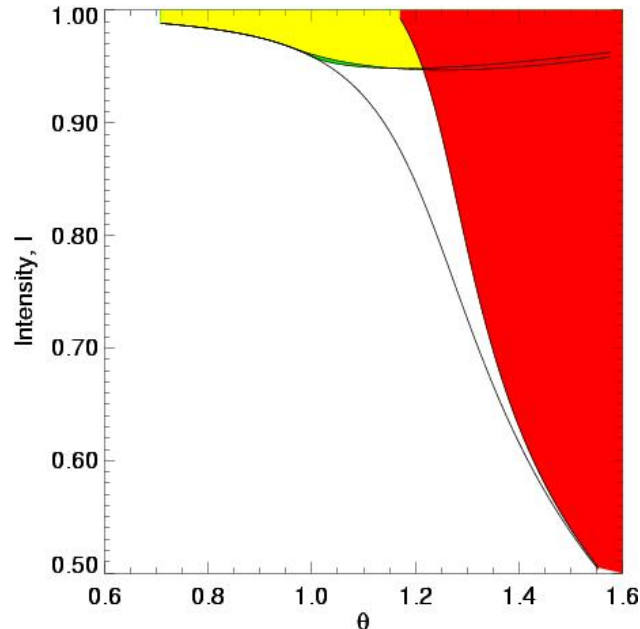


Figure 5.3: Stability of 2D KCS in the θ, I plane. Solitons exist above the lowest of the curves and are stable in the unshaded region. In the red area they are unstable to a Hopf mode with $m = 0$, while in the green and yellow regions they are unstable to $m = 5$ and $m = 6$ modes (see Sec. 5.6).

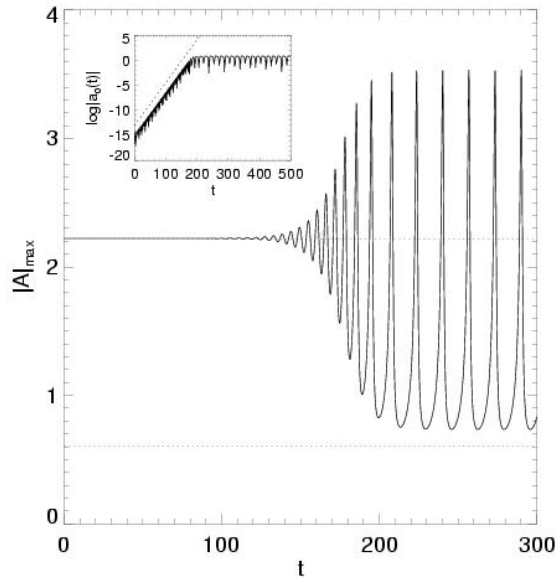


Figure 5.4: Dynamics of oscillating 2D KCS beyond the Hopf bifurcation: $|A(0)|$ as a function of time ($\theta = 1.3$, $I = 0.9$). Dashed lines show $|A(0)|$ for the upper and lower branch solitons. The inset shows the amplitude $|a_0|$ of the Hopf unstable eigenmode $v_0(\vec{x})$ where $A(\vec{x}, t) \approx A_u(\vec{x}) + a_0(t)v_0(\vec{x})$; A_u is the Hopf-unstable KCS and the dashed line is the gradient predicted by the corresponding eigenvalue from the linear stability analysis.

found using the Newton method. The exponential, oscillatory divergence is clear. In fact, the projection of the dynamics onto the Hopf eigenmode of the initial soliton shows an exponential growth in excellent agreement with the computed positive eigenvalue. In Fig. 5.5 the cross-section of the oscillatory solution is shown as a function of time.

The upper branch KCS has an important manifold corresponding to the Hopf eigenmode. Below the Hopf instability trajectories spiral in. Above threshold, trajectories spiral out toward the newly bifurcated limit cycle. The oscillation of the Hopf unstable KCS is such that it approaches the stable manifold of the lower branch soliton. The soliton is attracted towards the lower branch and then escapes along the unstable manifold. Figure 5.6 shows phase plots of the upper and lower branch solitons together with the trace of the Hopf oscillation of its central peak. The full phase profiles over all r are also plotted for the extrema. Clearly, at the lower extremum of its oscillation, the soliton “dwells” close to the lower branch KCS. Even at $I = 0.8$, only just beyond the Hopf threshold, the oscillating soliton’s profile comes close, in both amplitude and phase, to that of the lower branch KCS. The surprising robustness of the oscillating 2D KCS is potentially significant in relation to applications, since an oscillating soliton is almost as clearly distinguishable from no soliton as a stable one (because its amplitude is bounded below by that of the lower branch soliton).

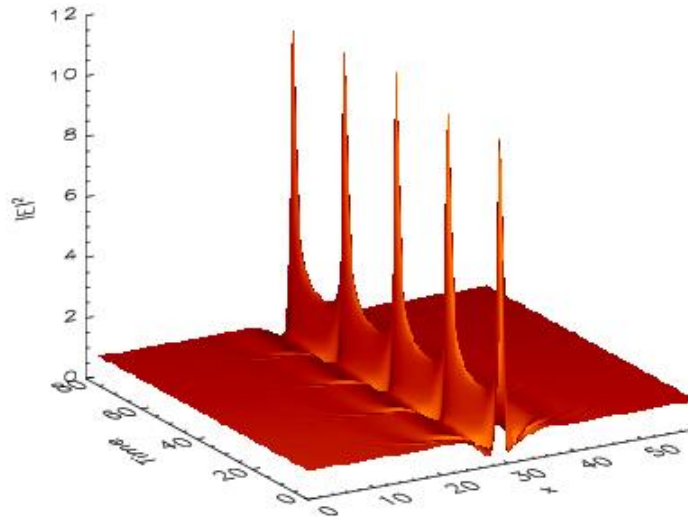


Figure 5.5: The dynamics of an oscillating 2D KCS beyond the Hopf bifurcation ($\theta = 1.3$, $I = 0.9$): cross-section $|E(x, y = 0, t)|$ vs x and t . (The oscillation preserves cylindrical symmetry).

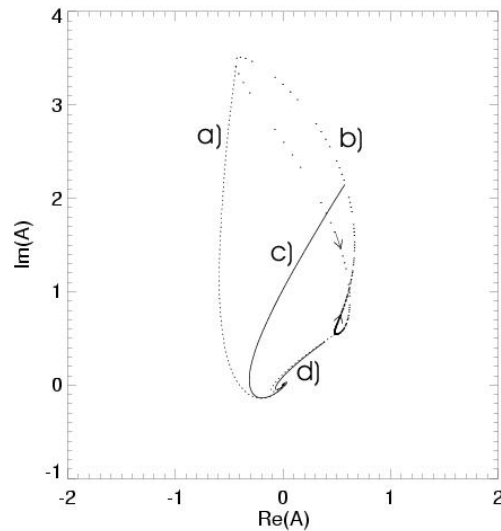


Figure 5.6: Phase-plane representation of the dynamics of an oscillating 2D KCS ($\theta = 1.3$, $I = 0.9$). The dashed lines (a) show the phase portrait of $A(r)$ at the time in which the KCS reaches the extrema of the oscillation, while the dots (b) correspond to the time evolution of the maximum $A(0)$ of the KCS. Arrows show the direction of rotation. The upper (c) and lower (d) solid lines represent the (Hopf unstable) upper and (amplitude unstable) lower KCS respectively.

5.5 Saddle-loop bifurcation

As the control parameter is increased part of the limit cycle moves closer and closer to the lower KCS saddle point. At a certain critical value a global bifurcation takes place: the cycle touches the saddle point and becomes a homoclinic orbit. This is an infinite-period bifurcation called *saddle-loop* or *homoclinic bifurcation* [220, 122]. If we keep the intensity of the background fixed to $I = 0.9$, and change the cavity detuning θ , the bifurcation is found to occur at $\theta_c = 1.30478592$. Fig. 5.7 shows the minimum distance d between the limit cycle and the lower-branch KCS as a function of the control parameter θ . We take d as the minimum value of

$$\sqrt{\int |A(\vec{x}, t) - A_l(\vec{x})|^2 d\vec{x}} \quad (5.7)$$

over a period T . $A_l(\vec{x})$ is the unstable lower-branch KCS obtained by means of the Newton method. $A(\vec{x}, t)$ has been obtained integrating numerically Eq. (5.1). As shown in Fig. 5.7, for θ close to θ_c we obtain $d \sim (\theta_c - \theta)^{1/2}$, which is the behavior expected close to a saddle-loop bifurcation [81].

The dynamics of the KCS as the bifurcation is crossed is illustrated in Fig. 5.8. On the left column we plot the time evolution of the KCS maximum obtained from numerical integrations of Eq. 5.1, the dashed line shows for comparison the maximum of the lower branch unstable KCS. On the right column we sketch the evolution on phase space projected into two variables. For $\theta < \theta_c$ the stable limit cycle corresponding to the periodic orbit of the KCS passes close to the unstable KCS, which is a saddle point in the phase space (Fig. 5.8a). As θ approaches θ_c , the limit cycle swells (Fig. 5.8b) and collides with the saddle point, creating a homoclinic orbit (Fig. 5.8c). Once $\theta > \theta_c$, the saddle connection breaks and the loop is destroyed (Fig. 5.8d). After following a trajectory in phase space close to the previous loop

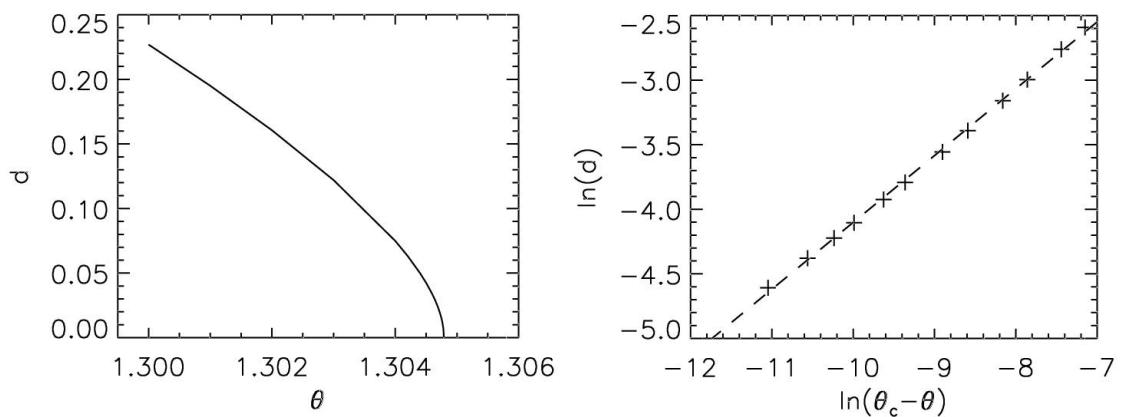


Figure 5.7: Minimum distance d between the limit cycle and the lower-branch KCS as a function of the control parameter θ , in a linear (left) and logarithmic (right) scales. On the right, crosses correspond to the numerical simulations while the dashed line is a linear fitting with a slope $\alpha = 0.509$

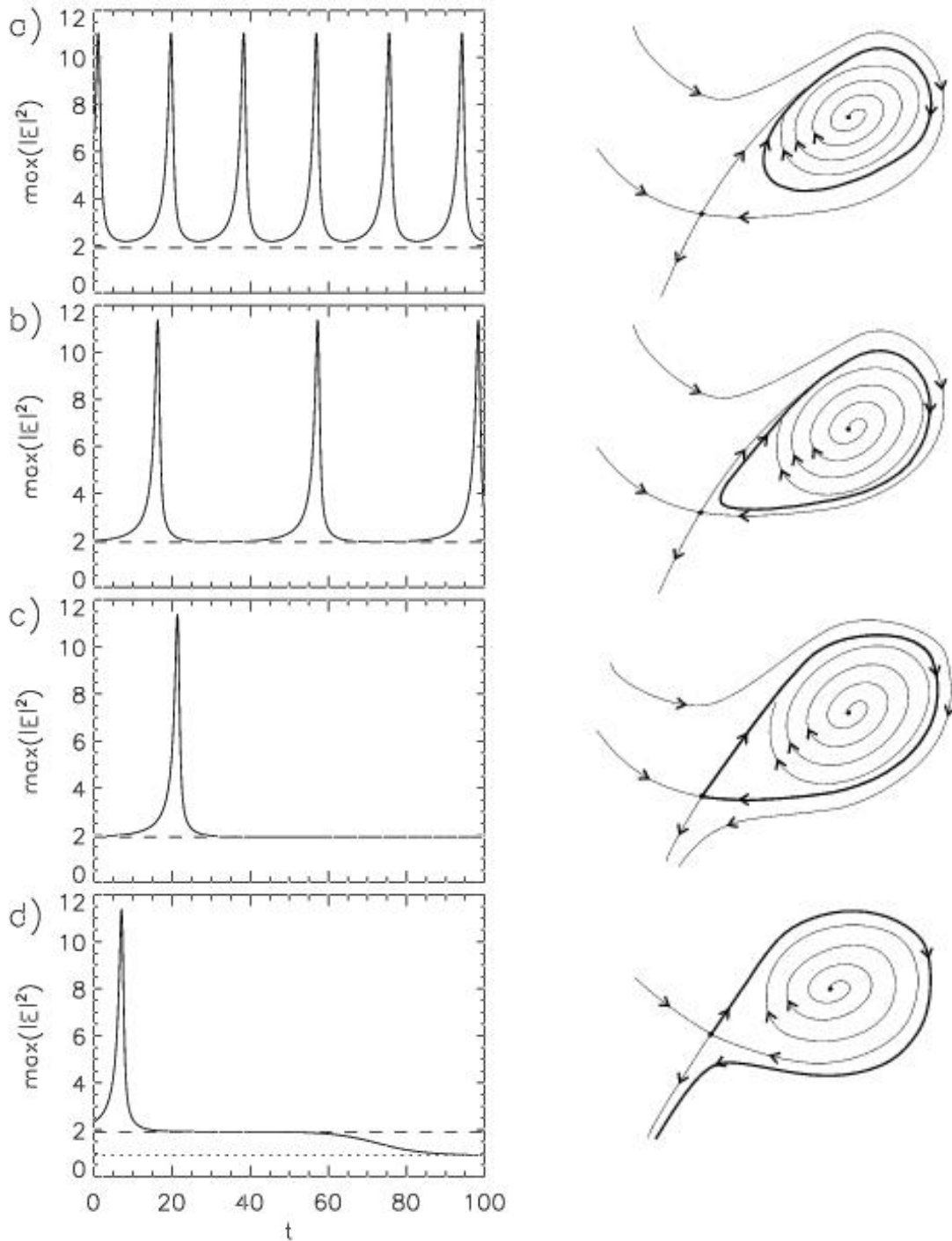


Figure 5.8: Left: KCS maximum intensity as a function of time for increasing values of the detuning parameter θ . From top to bottom $\theta = 1.3, 1.3047, 1.30478592, 1.304788$. We have considered $I_s = 0.9$. The dashed line shows the maximum of the unstable KCS. The dotted line in the last panel corresponds the homogeneous solution. Right: Sketch of the phase space for each parameter values. The thick line would correspond to the trajectory of the KCS in phase space. The saddle point correspond to the lower-branch KCS. The unstable focus correspond to the Hopf unstable upper-branch KCS.

the KCS approaches the saddle point (dashed line) where the evolution is very slow, as shown by the long plateau between $t = 15$ and $t = 60$ in Fig. 5.8d. Finally the KCS decays to the homogeneous solution (dotted line). For larger values of θ the trajectory moves away from the saddle and, therefore, the decay to the homogeneous solutions takes place in shorter times.

The saddle-loop bifurcation has a characteristic *scaling law* that govern the period of the limit cycle as the bifurcation is approached. Close to the critical point the system spends most of the time close to the saddle (lower-branch KCS). The period of the oscillation T can be then estimated by the linearized dynamics close to the saddle [81, 220, 122]

$$T \sim -\frac{1}{\lambda_1} \ln(\theta_c - \theta), \quad (5.8)$$

where λ_1 is the unstable eigenvalue of the saddle point. We are now going to show that this scaling law is verified in our system. Fig. 5.9 shows the period of the KCS limit cycle as a function of the control parameter θ_c . As expected, the period of the limit cycle diverges logarithmically as the bifurcation is approached. We can then evaluate λ_1 from the stability analysis of the unstable KCS. The results of the stability analysis are shown in Fig. 5.10. The lower-branch KCS has one single positive eigenvalue $\lambda_1 = 0.177$. In Fig. 5.9 (right) we plot using crosses the period of the oscillation KCS as a function of $\ln(\theta_c - \theta)$ obtained from numerical simulations of Eq. (5.1). Performing a linear fitting we obtain a slope $A = -5.56$. This value should be compared with the theoretical prediction $1/\lambda_1 = 5.65$. The excellent agreement proves the existence of a saddle-loop bifurcation for the oscillating KCS. We should note however that the theory as explained in Refs. [81, 220, 122] is, strictly speaking, only valid for planar bifurcations, for which the phase space is a plane and therefore the saddle has one unstable direction and one attracting direction.

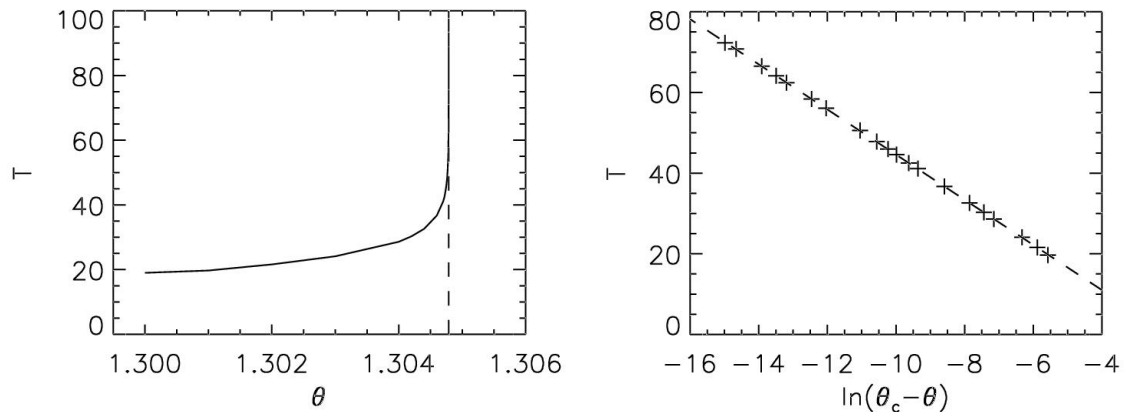


Figure 5.9: Left: Period of the limit cycle T as a function of the detuning θ for $I = 0.9$. The vertical dashed line indicates the threshold of the saddle-loop bifurcation $\theta_c = 1.30478592$. Right: Period T as a function of $\ln(\theta_c - \theta)$. Crosses correspond to numerical simulations while the dashed line is a linear fitting to $T = A \ln(\theta_c - \theta) + B$, with $A = -5.56$ and $B = -11.4$ in very good agreement with the theoretical prediction (5.8)

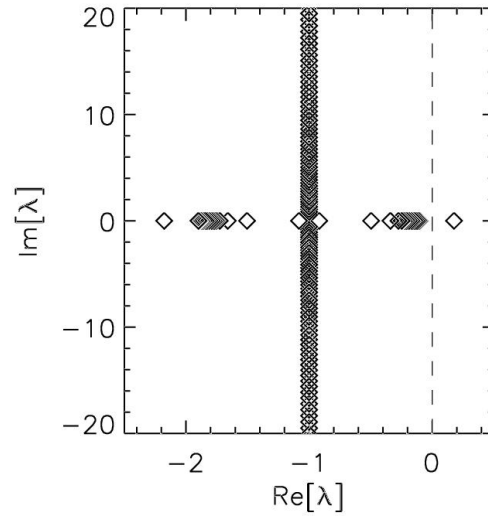


Figure 5.10: Spectra of the saddle KCS at θ_c ($I = 0.9$). The positive eigenvalue is $\lambda_1 = 0.177$.

The stable manifold of the unstable KCS is infinite dimensional, as indicated by the presence of a whole band of stable eigenvalues with real part close to zero in Fig. 5.10. The success of the planar theory to describe our infinite dimensional system can be attributed to the fact that, somehow, the dynamics of the KCS is still basically two-dimensional with a strong damping in the other directions.

Beyond the saddle-loop bifurcation the phase space shows a typical configuration displaying excitability (Fig. 5.11): it has a globally attracting fixed point (homogeneous solution), but localized disturbances (above the lower-branch KCS) can send the system on a long excursion through phase space before returning to the fixed point. Fig. 5.12 shows the resulting trajectories of applying a Gaussian beam with three different maximum intensities, one below (left) and two above (center and right) the critical value to excite the system. In the first case the system relax exponentially to the homogeneous solution, while in the latter case it performs a long excursion before returning to the stable fixed point. In the excitable regime a long excursion takes place independent of the size of the perturbation provided that it is above the excitable threshold. The spatial profile of the localized structure is shown in Fig. 5.13. The peak grows to a large value, in a similar way as the collapse in the NSE, until the losses stop it. Then it decays exponentially until it disappears. A remnant wave is emitted out of the center dissipating the remaining energy.

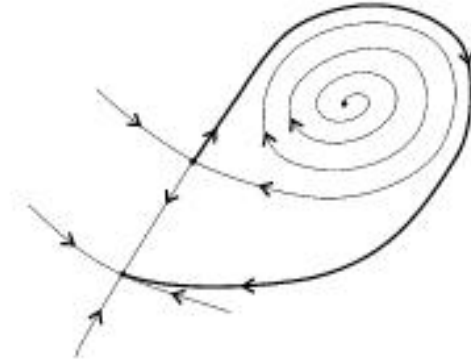


Figure 5.11: Sketch of the phase space beyond the saddle-loop bifurcation. The stable fixed point correspond to the homogeneous solution, while the saddle is the lower-branch KCS and the unstable focus the Hopf unstable upper-branch KCS. Any perturbation of the homogeneous solution beyond the stable manifold of the saddle point induces a long excursion in phase space before returning to the stable fixed point: the system exhibits excitability.

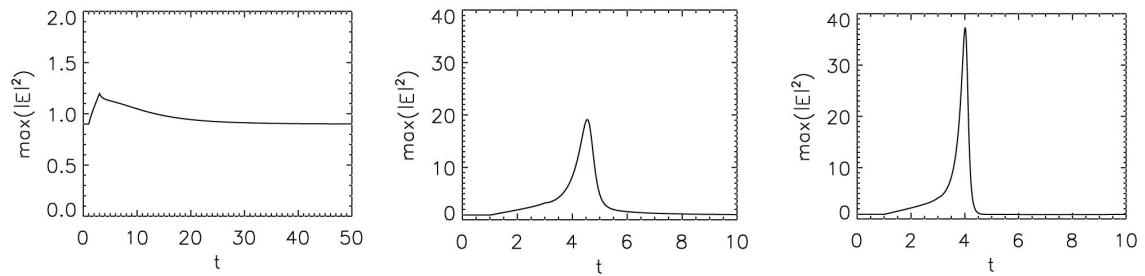


Figure 5.12: Maximum intensity of a perturbation as a function of time. Starting from the homogeneous solution (stable fixed point) with a background intensity $I = 0.9$, Gaussian beams of width $\sigma = 3.75$ and maximum intensities $I^{max} = 1.3$ (left), $I^{max} = 1.9$ (center), and $I^{max} = 2.0$ (right) are applied at $t = 1.0$ during 2 time units ($\theta = 1.31$).

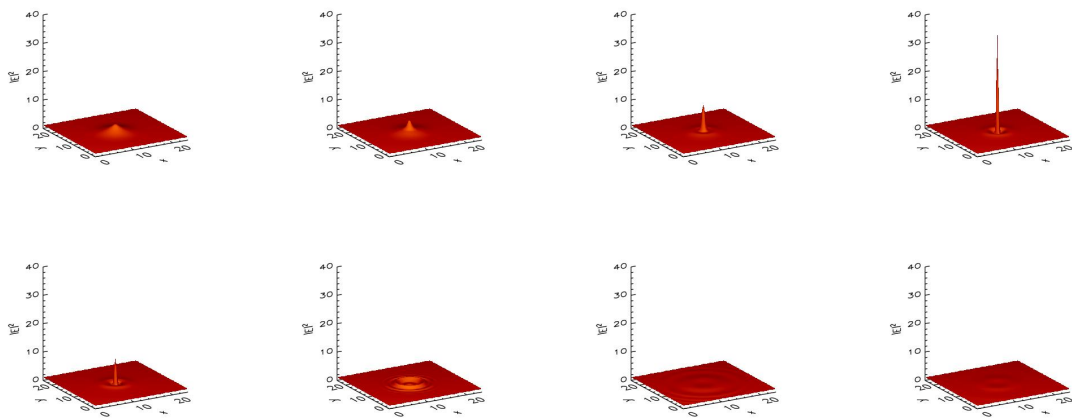


Figure 5.13: Spatial distribution of the intensity $I = |E|^2$ corresponding to the right trajectory in Fig. 5.12. From left to right, top and bottom $t = 2.8, 3.2, 3.6, 4.0, 4.2, 4.8, 6.4,$ and 8.0 .

5.6 Azimuthal instabilities

For the approximate range $\theta < 1.22$, shown in Fig. 5.3, the leading instability observed is not the Hopf mode (which is cylindrically symmetric), but instead to modes with $m = 5$ or $m = 6$. This azimuthal instability leads to its surrounding ring breaking up into five or six spots respectively. Numerical integration of Eq. 5.1 shows that the resulting structure then grows to invade the homogeneous background. For $\theta < 1.1$ the system is unstable to perturbation with azimuthal number $m = 6$, leading to an hexagonal pattern (Fig. 5.14). Due to the values of I_s and θ this pattern is not stationary but oscillate in a similar way as explained in sec. 2.4.3 for $\theta = 1.0$. For a narrow domain around $\theta = 1.2$ (Fig. 5.3), $m = 5$ dominates and the growing pattern, though locally hexagonal, retains its global five-fold symmetry (Figs. 5.15 and 5.16). Due to periodic boundary conditions, as soon as the pattern fill the whole system, penta-hepta defects are created.

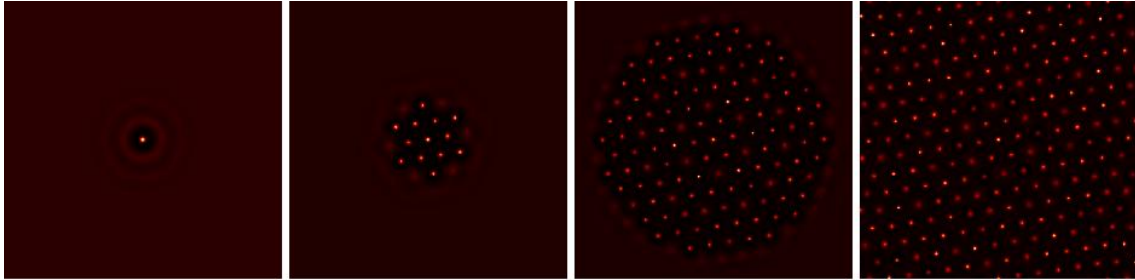


Figure 5.14: Development of a $m = 6$ azimuthal instability. From left to right: $t = 0, 100, 200, 300$. $\theta = 1.1$, $I = 0.97$.

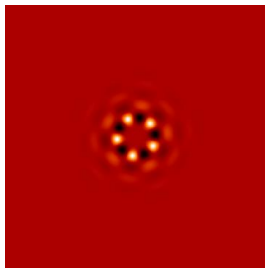


Figure 5.15: Eigenmode corresponding to an azimuthal $m = 5$ instability. $\theta = 1.2$, $I = 0.95$.

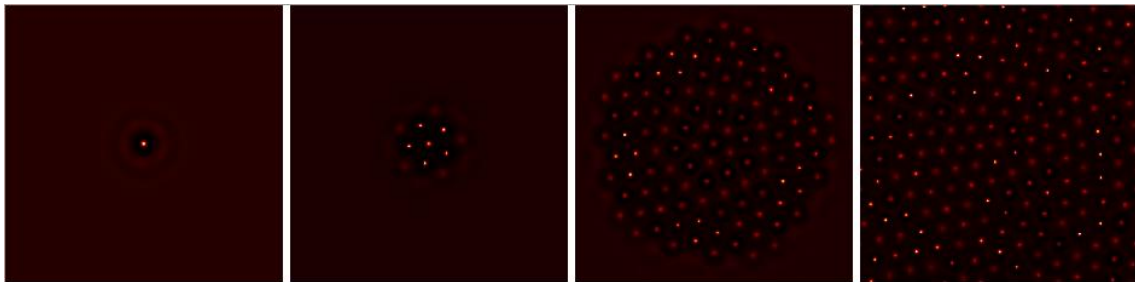


Figure 5.16: Development of a $m = 5$ azimuthal instability. From left to right: $t = 0, 200, 400, 600$. $\theta = 1.2$, $I = 0.95$.

5.7 Conclusions

We have demonstrated existence of stable 2D Kerr cavity solitons in the archetype mean-field model of a Kerr medium in an optical cavity. This is a behavior qualitatively different from its bulk-medium equivalent, and so clearly demonstrates that cavity solitons are qualitatively different from propagating spatial solitons. We have also presented detailed and accurate investigations of the nature of the processes by which this 2D Kerr cavity soliton may become unstable. We found a novel and interesting azimuthal instability leading to formation of an unstable quasi-hexagonal pattern. This instabilities impose in a region of the parameter space the upper limit for the existence of stable stationary Kerr cavity solitons. There is also a very interesting instability of Hopf type. We showed that the resulting dynamics preserves the soliton even when the oscillation reaches quite high amplitude, and demonstrated the key role of the lower-branch soliton in this phenomenon. The lower-branch soliton takes also part in a saddle-loop bifurcation that impose an upper limit in the parameter space to the existence of stable oscillating Kerr cavity solitons. Above this limit, the system exhibits excitability. At difference with other excitable systems, here the overall dynamics of the model is not excitable, but this is a characteristic of the soliton solutions. Strictly speaking our system is not globally excitable since other stable fixed points exist, for instance hexagonal patterns. Only the dynamics projected on the soliton solutions is strictly excitable. Then, the system presents excitability to spatially localized perturbations, as for example a Gaussian beams, but not to spatially extended perturbation that may excite a hexagonal solution.

Chapter 6

Dynamics of domain walls: dark ring cavity solitons and stable droplets

6.1 Introduction

In the previous chapter we considered localized structures that arise as a consequence of bistability between a pattern and a homogeneous solution, the case described in subsection 1.2.1. Here we consider the other possible situation for localized structures, namely when there is bistability between two homogeneous solutions, as described in subsection 1.2.2. As discussed there, the dynamics of such localized structures is strongly related to the growth of a spatial domain of one homogeneous solution embedded in the other. In this chapter we develop a general theory for the movement of a domain wall connecting two equivalent stable homogeneous solutions (labeled as phases).

In particular we analyze the transition from a coarsening regime characterized by a $t^{1/2}$ growth law to one of labyrinthine pattern formation due to a modulational instability of a flat domain wall connecting two equivalent homogeneous solutions. Such transition has been observed experimentally in reaction diffusion [189] (Fig. 6.1) and optical [224] (Fig. 6.2) systems, and numerically in Ref. [68], as well as in Swift-Hohenberg models [184, 219].

In the case of optical systems several contradictory growth laws have been reported in the literature, including $t^{1/2}$ [68, 179] and $t^{1/3}$ [229, 136]. These results were obtained from numerical simulations but only in [68, 179] evidence of scaling was given. Here, on the basis of our general theory, we demonstrate for which parameter regions there is dynamical scaling, so that, the growth follows a power law, and for which parameters there is no dynamical scaling. Furthermore we find a novel kind of localized structures, the stable droplets, large circular domains of one phase embedded in the other.

This chapter is organized as follows: in section 6.2 we develop a perturbation theory for the movement of domain wall between two equivalent states. In section 6.3 we apply this theory to two models in nonlinear optics, a Kerr cavity with polarization degree of freedom and an optical parametric oscillator.

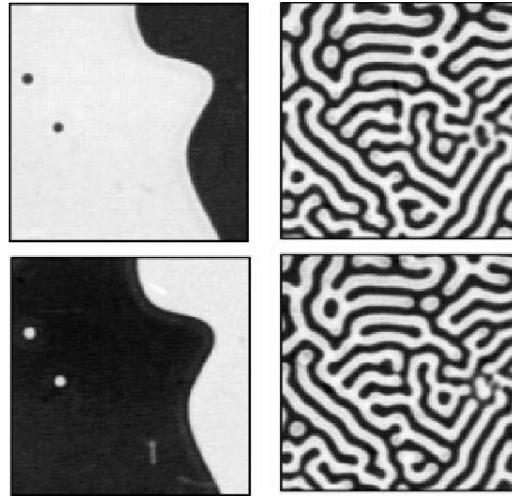


Figure 6.1: From Ref. [189]. Frequency-locked regimes observed experimentally in a Belousov-Zhabotinsky chemical reaction, forced at a frequency around two times the natural one, as a function of the forcing frequency. Patterns are shown in pairs, one above the other, at times separated by $\Delta t = 1/f_p$. The pictures on the left displaying localized structures correspond to a frequency rate slightly smaller than two, while the labyrinthine patterns are formed for frequency rates a little bit above.

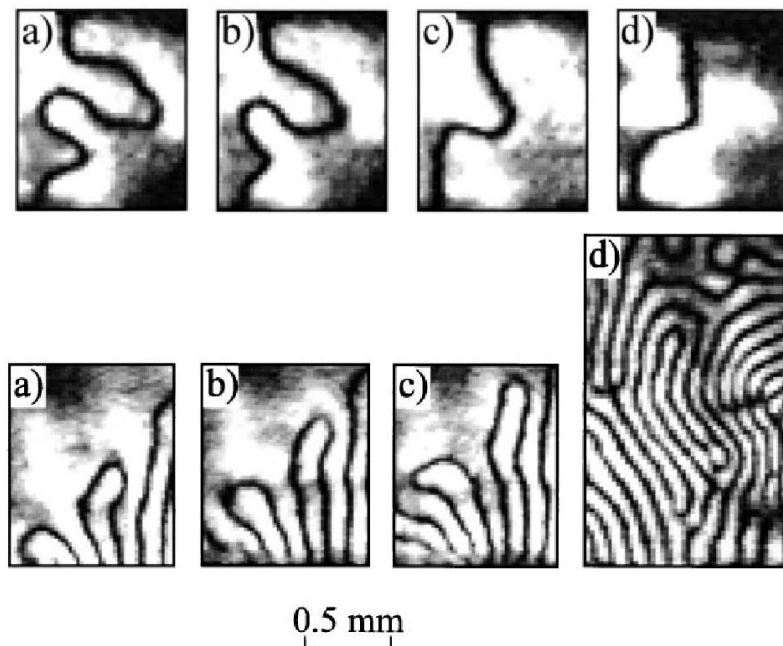


Figure 6.2: From Ref. [224]. Transition from a coarsening regime to a regime of labyrinthine pattern formation obtained experimentally in degenerate four wave mixing. Top: A shrinking domain boundary; experimental detuning near zero. Time between successive snapshots is 2 s. Bottom: Expanding domain boundaries ending in a labyrinth structure. Detuning is around 0.7 (normalized to the width of the resonator mode). Time between snapshots a), b) and c) is 2 s. Time between snapshots c) and d) is 10 s.

6.2 General theory of domain wall dynamics

In this section we develop a perturbation theory for the movement of domain walls connecting two equivalent homogeneous solutions in two spatial dimensions. First we describe the systems to which our theory applies and derive a first order eikonal equation for the velocity of gently curved fronts. Then, close to the bifurcation point where the velocity vanishes, we extend our analysis to include nonlinear terms. For the sake of clarity we will illustrate our general results in a prototypical model: the Parametrically driven Complex Ginzburg-Landau Equation (PCGLE). The PCGLE [34, 35] is the generic amplitude equation for an oscillatory system parametrically forced at twice its natural frequency [189]:

$$\partial_t A = (1 + i\alpha)\nabla^2 A + (\mu + i\nu)A - (1 + i\beta)|A|^2 A + pA^*, \quad (6.1)$$

where μ measures the distance from the oscillatory instability threshold, ν is the detuning and $p > 0$ is the forcing amplitude. This model has been used to describe a light sensitive form of the Belousov-Zhabotinsky reaction [189]. In the next section two nonlinear optical systems, the Vectorial Kerr Resonator and the Degenerate Optical Parametric Oscillator, are also discussed in detail.

6.2.1 System description

We consider any system described by real N components vector field $\vec{\Psi}(\vec{x})$ whose dynamical evolution in two spatial dimensions can be written as

$$\partial_t \vec{\Psi} = D\nabla^2 \vec{\Psi} + \vec{W}(\vec{\Psi}, p), \quad (6.2)$$

where the matrix D describes the spatial coupling, \vec{W} is a local nonlinear function of the fields and p a control parameter. Eq. (6.2) is invariant under translations and under the change $\mathcal{P} : \vec{x} \rightarrow -\vec{x}$ (parity). We also assume that it has a discrete symmetry \mathcal{Z} that allows for the existence of two, and only two, equivalent stable homogeneous solutions, and that, in a 1d system, they are connected by stable Ising fronts $\vec{\Psi}_0(x, p)$. As explained in Appendix B, a Ising front is invariant with respect to $\mathcal{S} = \mathcal{Z}\mathcal{P}_0$, where the subscript $_0$ means that the reference frame for the spatial inversion is chosen at the center of the wall x_0 . Thus, the 1d front (and equivalently a flat front in 2d) is stationary, $D\nabla^2 \vec{\Psi}_0 + \vec{W}(\vec{\Psi}_0, p) = 0$.

The PCGLE is an example fulfilling the hypothesis required above. For $p \sim \nu \sim \alpha$ large compared to other parameters a pattern forming instability takes place for $p < p_h$, while for $p > p_h$ there are two equivalent stable homogeneous solutions (frequency locked solutions) (Fig. 6.3). In the PCGLE both Ising and Bloch walls can be observed. We restrict ourselves to parameter regions where the fronts connecting the two homogeneous solutions are of Ising type. The real vector field describing the state of the system is $\vec{\Psi}(\vec{x}) = (\text{Re}[A(\vec{x})], \text{Im}[A(\vec{x})])$, the spatial coupling is described by the matrix $D = ((1, \alpha)^T, (-\alpha, 1)^T)$, $\mathcal{Z} = -I$ and $\vec{\Psi}_0(x)$ describes a Ising front connecting the two homogeneous solutions (we consider $p > p_h$). Performing a spatial stability analysis as described in Appendix B we obtain that the front profile has oscillatory tails as shown in Fig. 6.4.

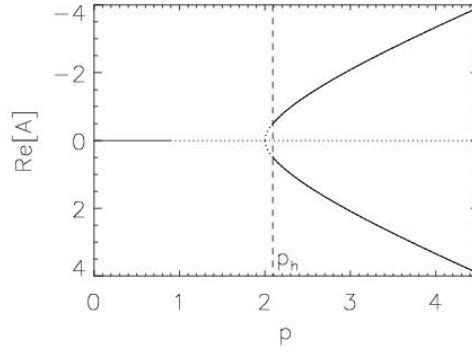


Figure 6.3: Bifurcation diagram of the homogeneous solutions of the PCGLE for $\alpha = 2$, $\beta = 0$, $\nu = 2$ and $\mu = 0$. Solid lines indicate linearly stable solutions while dotted lines indicate solutions that are unstable under finite wavelength perturbations. For the parameter values considered, $p_h = 2.09$ (dashed line).

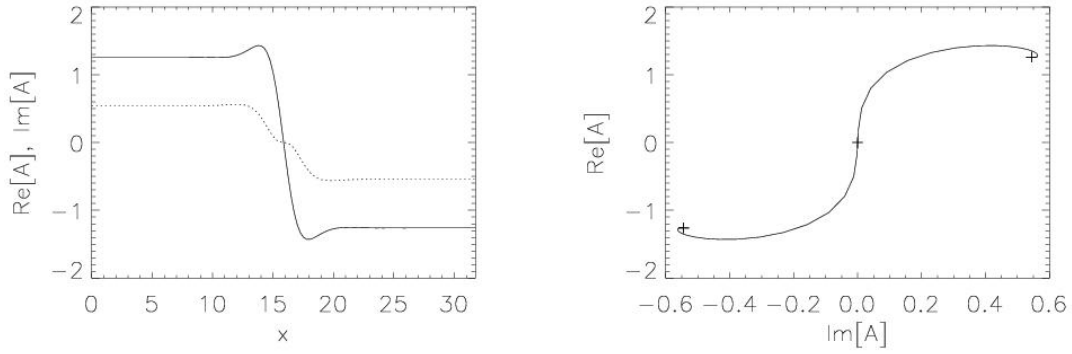


Figure 6.4: A heteroclinic solution consisting of a Ising wall for $p = 2.75$. Other parameters as in Fig. 6.3. Left: Real part (solid line) and imaginary part (dotted line) of the complex field A as a function of x in the PCGLE. The center of the wall $x_0 = 16$ is the point where the two lines cross each other, which in this case corresponds to point where the field vanishes. Note the invariance with respect to $\mathcal{S} = \mathcal{ZP}_0$. Right: The domain wall plotted in the A -complex plane. The crosses indicate the two equivalent homogeneous stable solutions and the zero unstable solution.

6.2.2 Eikonal equation

In the reference frame moving with a front Eq. (6.2) becomes (see Appendix C for details):

$$\begin{aligned}
 D\partial_u^2 \vec{\Psi} + \left(v_n I + \frac{\kappa}{1 + u\kappa} D \right) \partial_u \vec{\Psi} + \frac{u\kappa^2 \partial_\theta \kappa}{(1 + u\kappa)^3} D\partial_\theta \vec{\Psi} \\
 + \frac{\kappa^2}{(1 + u\kappa)^2} D\partial_\theta^2 \vec{\Psi} + \vec{W}(\vec{\Psi}, p) = \partial_t \vec{\Psi}, \quad (6.3)
 \end{aligned}$$

where u is the coordinate normal to the front, s is the arclength of the line front, v_n is the normal front velocity, κ is the local curvature of the front line, $\theta = \kappa s$ is

the azimuthal angle and I the identity matrix. We analyze the dynamics of slightly curved fronts $\vec{\Psi}(u, s, t)$ as a perturbation of the flat front $\vec{\Psi}_0(u)$

$$\vec{\Psi}(u, s, t) = \vec{\Psi}_0(u) + \vec{\Psi}_1(u, s, t). \quad (6.4)$$

We assume that i) $\kappa w \ll 1$, with w the front width, ii) in the moving frame the front profile depends at most weakly on t ($|\partial_t \vec{\Psi}| \ll |\kappa D \partial_u \vec{\Psi}|$) and iii) κ is a function which depends at most weakly on s , thus $|\kappa \partial_\theta^2 \vec{\Psi}| \sim |\kappa \partial_\theta \vec{\Psi}| \ll |\partial_u \vec{\Psi}|$. Linearizing Eq. (6.3) around $\vec{\Psi}_0$ keeping only first order terms in κ and $\vec{\Psi}_1$ we have

$$M \vec{\Psi}_1 = -(v_n I + \kappa D) \partial_u \vec{\Psi}_0, \quad (6.5)$$

where $M_j^i = D_j^i \partial_u^2 + \delta_{\Psi^j} W^i|_{\vec{\Psi}_0, p}$. The last term is the functional derivative of the i th component of the nonlinear vector function $\vec{W}(\vec{\Psi}, p)$ with respect to the j th component of the real vector field $\vec{\Psi}$. Due to the translational invariance of (6.2), which is broken by the presence of the front, each front has a neutrally stable Goldstone mode \vec{e}_0 ($M \vec{e}_0 = 0$), which has the form of the gradient of the front $\vec{e}_0 \equiv \partial_u \vec{\Psi}_0$. Since the front is symmetric with respect to \mathcal{S} , its gradient \vec{e}_0 is antisymmetric. Due to the existence of the neutrally stable mode, M is singular and there exist a condition for Eq. (6.5) to have a solution, the so called solvability condition (see Appendix A in Ref. [39]). The condition is obtained multiplying on the left both sides of (6.5) by the null vector of M^\dagger , \vec{a}_0 :

$$\int_{-\infty}^{\infty} \vec{a}_0 \cdot (v_n I + \kappa D) \vec{e}_0 = 0. \quad (6.6)$$

Equation (6.6) leads to the eikonal equation

$$v_n = -\gamma(p) \kappa, \quad (6.7)$$

where

$$\gamma(p) \equiv \frac{1}{\Gamma} \int_{-\infty}^{\infty} \vec{a}_0 \cdot D \vec{e}_0 du, \quad (6.8)$$

and $\Gamma \equiv \int_{-\infty}^{\infty} \vec{a}_0 \cdot \vec{e}_0 du$. Γ vanishes at a Ising-Bloch transition [170]. Here we only consider parameter regions far away from any Ising-Bloch transition for which Γ is never zero. For a circular domain $\kappa = 1/R$ and

$$v_n = \dot{R} = -\gamma(p)/R. \quad (6.9)$$

From Eq. (6.5) one obtains that the front perturbation $\vec{\Psi}_1(u, t) = \kappa(t) \vec{\varphi}_1(u)$ is independent of s while the dependence on t comes only through κ . $\vec{\varphi}_1$ satisfies

$$M \vec{\varphi}_1 = -(-\gamma I + D) \vec{e}_0. \quad (6.10)$$

For systems such that the diffusion matrix is proportional to the identity, $D = dI$,

$$\gamma = \frac{1}{\Gamma} d \int_{-\infty}^{\infty} \vec{a}_0 \cdot I \vec{e}_0 du = \frac{1}{\Gamma} d \Gamma = d. \quad (6.11)$$

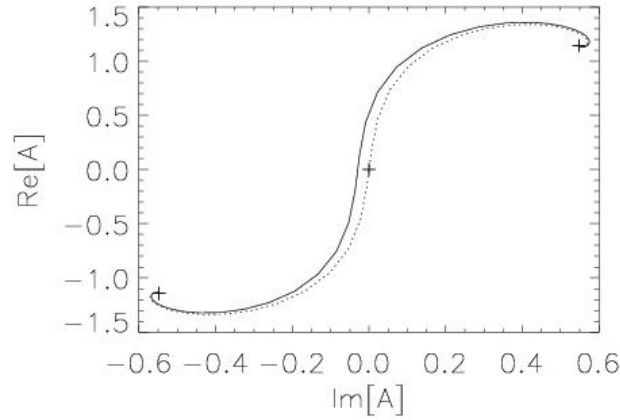


Figure 6.5: Wall profile plotted in the A -complex plane. The dotted line correspond to the 1d wall and the solid line to a slightly curved front in 2d. The symbols correspond to the zero solution and the two non-trivial homogeneous equivalent solution. The difference between the curved front and the flat wall is the effect of the deformation due to the first order correction $\vec{\Psi}_1$.

Thus, γ takes the constant value d independently of the profile of the front and any system parameter. In this case, the rhs of (6.10) vanishes and $\vec{\varphi}_1$ must be either zero or proportional to the Goldstone mode \vec{e}_0 . Physically this means that the fronts translate without changing their radial profile. The front velocity is proportional to the curvature with opposite sign $v_n = -d\kappa$, which is the well known Allen-Cahn law [99, 10]. This law implies a coarsening regime with a $t^{1/2}$ growth law and shrinking of circular domains following $R(t) = \sqrt{R(0)^2 - \gamma t}$, as obtained from (6.9) (Fig. 6.6).

In general, $D = dI + C$ with a non zero matrix C , so that

$$\gamma = d + \frac{1}{\Gamma} \int_{-\infty}^{\infty} \vec{a}_0 \cdot C \vec{e}_0 du. \quad (6.12)$$

C leads to a contribution to γ that depends on the profile of the front $\vec{\Psi}_0$ and therefore, on the system parameters. From Eq.(6.10) we have that $\vec{\varphi}_1$ is no longer proportional to the Goldstone mode. This means that the transverse profile of the front is now deformed. Since $\vec{\Psi}_1(u, t) = \kappa(t)\vec{\varphi}_1(u)$, the amount of deformation is proportional to the curvature and C (Fig. 6.5). The d contribution is generally positive and, for wide parameter regions, γ is also positive. Here flat walls are stable and the Allen-Cahn law still applies [68, 181] (Fig. 6.6). Circular domains shrink but in the parameter regions where the γ coefficient takes moderated values the 1d interaction due to presence of oscillatory tails in the front may prevent the droplet to disappear forming a localized structure (LS) (Fig. 6.7).

The crucial point is that for some parameter values the contribution to γ due to C may be negative and larger than d . γ changes sign and a bifurcation occurs. Figure 6.8 shows the value of γ versus p for the PCGLE. The value of p for which $\gamma = 0$ identifies the bifurcation point p_c . This is particularly relevant in nonlinear optics where the spatial coupling is diffractive and therefore $d = 0$. For $\gamma < 0$ the

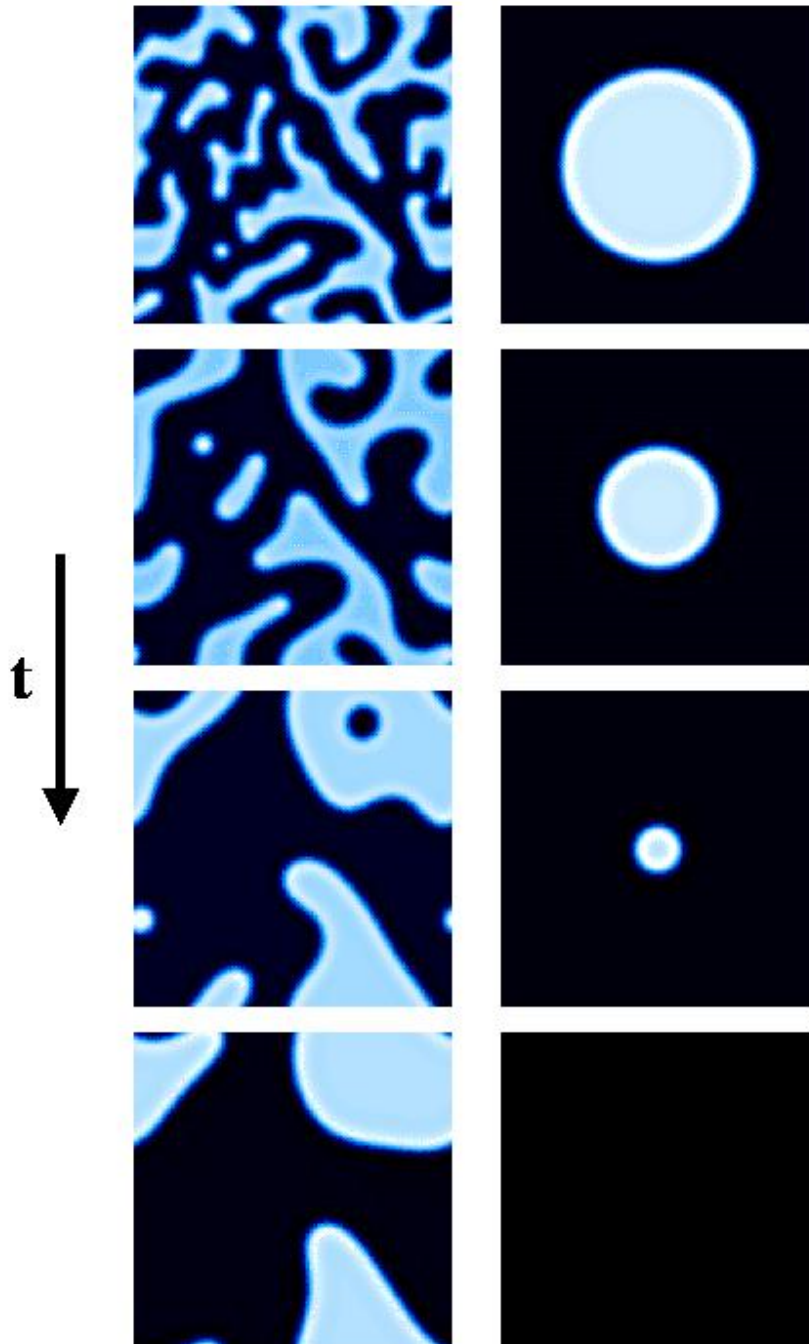


Figure 6.6: Snapshots corresponding to the time evolution of the real part of the complex field A for the parametrically driven complex Ginzburg-Landau equation in the domain coarsening regime ($\gamma > 0$). Left: evolution starting from random initial conditions. Right: evolution of an isolated circular drop.

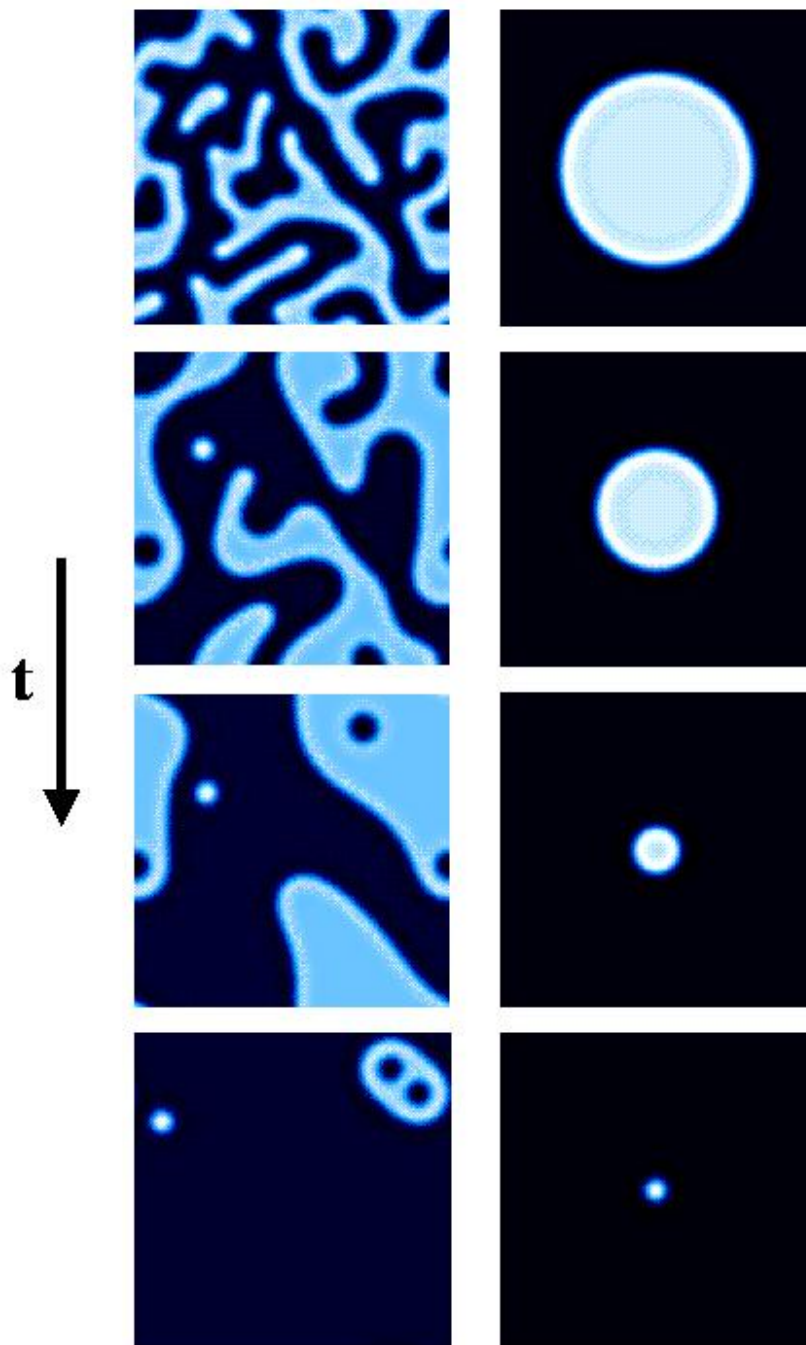


Figure 6.7: The same as Fig. 6.6 in the regime of formation of LS ($\gamma \gtrsim 0$).

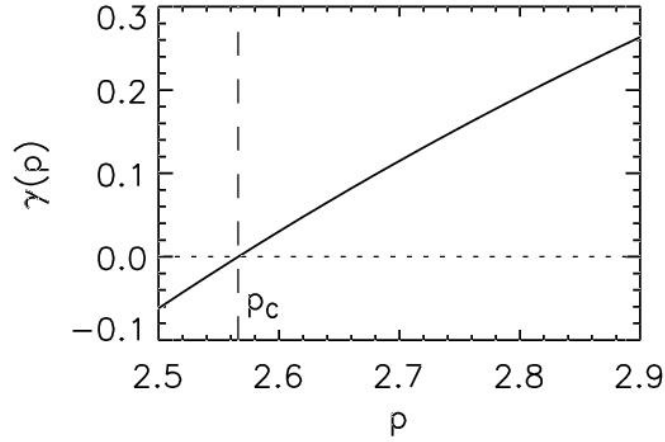


Figure 6.8: γ as function of p calculated from Eq. (6.8) for the PCGLE. Parameters taken as in Fig. 6.3. γ becomes zero at $p_c = 2.56629$ (dashed line).

velocity has the same sign of the curvature leading to the growth of any perturbation of the flat wall. The condition for vanishing γ , $\int_{-\infty}^{\infty} \vec{a}_0 \cdot D\vec{e}_0 du = 0$, is in fact the criterion for the modulational instability of a flat front. Modulational instabilities in fronts connecting two equivalent homogeneous states have been observed in numerical models [68, 187] (Fig. 6.9). Starting from a random initial condition, the system develops labyrinthine patterns [68, 189, 224]. Also, a circular domain grows like (6.9) until its boundary breaks up because of the modulational instability leading to the formation of a labyrinthine pattern (Fig. 6.10).

The values of γ shown in Fig. 6.8 have been calculated from its definition Eq. (6.8). The 1d front profile $\vec{\Psi}_0$ is obtained by solving the 1d stationary equation of (6.1), namely

$$(1 + i\alpha)\frac{d^2 A}{dx^2} + (\mu + i\nu)A - (1 + i\beta)|A|^2 A + pA^* = 0. \quad (6.13)$$

As in the previous chapter, equation (6.13) is solved using a Newton method in which the transverse derivatives are computed in Fourier space [61, 181]. From the discretized profile $\vec{\Psi}_0$ we evaluate the operator M , which now takes the form of a $N \times N$ matrix where N is the number of grid points. The null mode of M^\dagger is easily

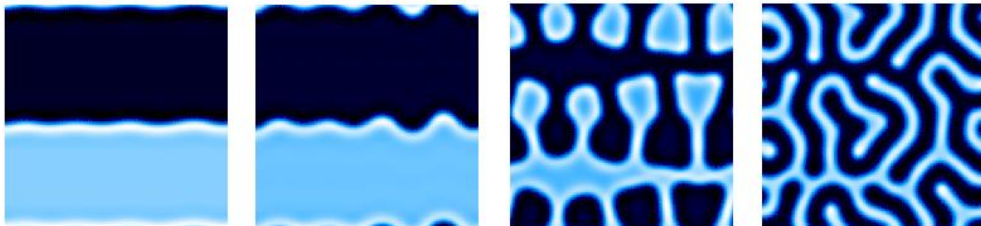


Figure 6.9: Images showing the development of a modulational instability of a flat wall for the PCGLE. The time increases from left to right.

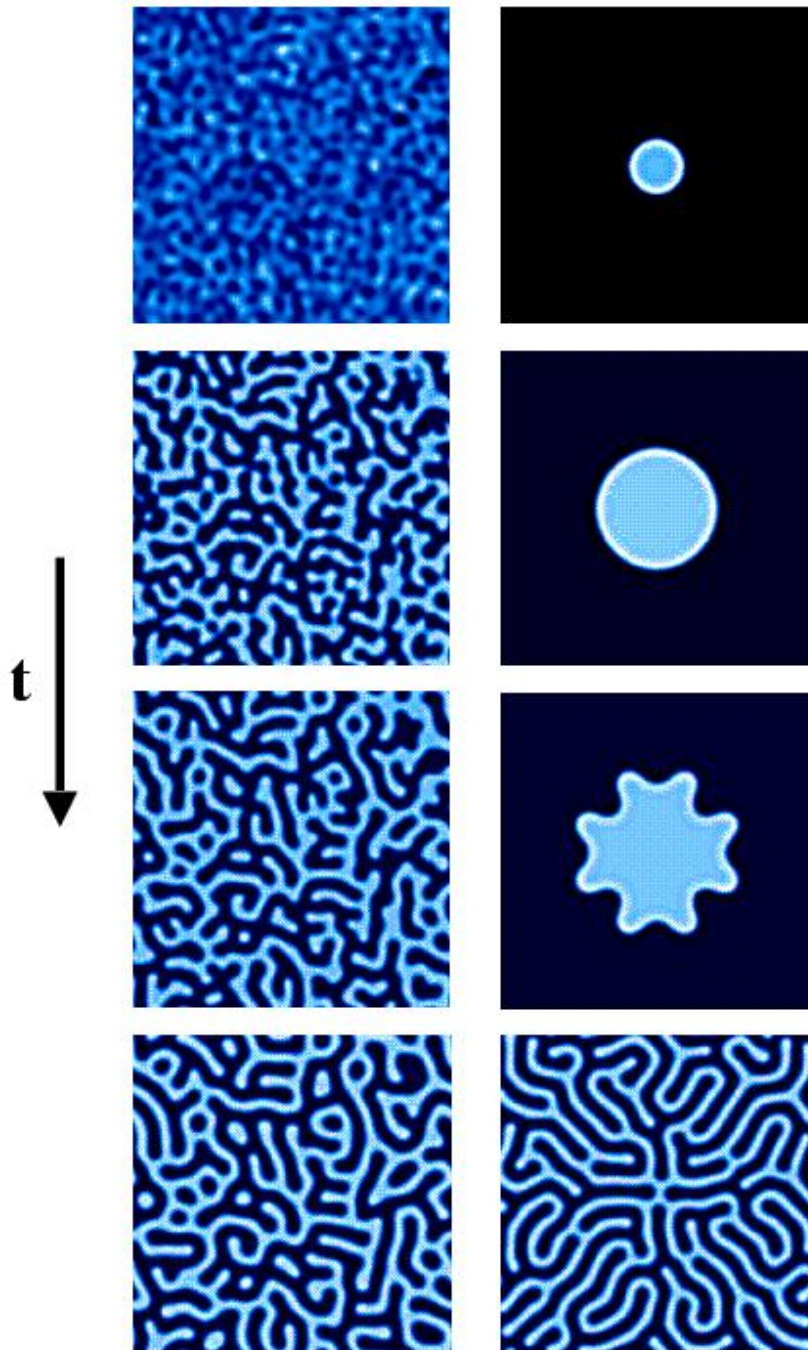


Figure 6.10: The same as Fig. 6.6 in the regime of formation of labyrinthine structures ($\gamma < 0$).

obtained by finding the eigenmodes of the transposed of the matrix M . This process allows us to calculate γ with very high accuracy much faster than following the time evolution of a 2d circular droplet from a numerical integration of equation (6.1).

6.2.3 Amplitude equation for the curvature: Stable Droplets

In the previous sub-section we have developed a perturbation theory at first order in the curvature κ . However, for values of the control parameter p close to p_c , where the proportionality coefficient γ between the velocity and the curvature vanishes (modulational instability of a domain wall), higher order contributions in κ , that have been neglected in the previous sub-section, may become relevant. In order to study these nonlinear contributions we perform a multiple scale analysis in ϵ of Eq. (6.3). We start considering the case of a circular domain wall (for which $v_n = -\dot{\kappa}/\kappa^2$). Assuming the following scaling:

$$\begin{aligned} p &= p_c + \epsilon p_1, \\ \vec{\Psi} &= \vec{\Psi}_0 + \epsilon^{1/2} \vec{\Psi}_1 + \epsilon \vec{\Psi}_2 + \epsilon^{3/2} \vec{\Psi}_3, \\ \kappa &= \epsilon^{1/2} \kappa_1 \quad \text{and} \\ \partial_t &= \epsilon^2 \partial_T, \end{aligned} \quad (6.14)$$

at order $\epsilon^{1/2}$ we obtain

$$M \vec{\Psi}_1 = -\kappa_1 D \vec{e}_0. \quad (6.15)$$

Now the solvability condition is $\int_{-\infty}^{\infty} \vec{a}_0 \cdot D \vec{e}_0 dr = 0$, which is precisely the criterion for the modulational instability of a domain wall, and therefore is automatically satisfied at p_c . Then a solution of (6.15) can be found:

$$\vec{\Psi}_1 = \kappa_1 \vec{\varphi}_1 \quad (6.16)$$

with $M \vec{\varphi}_1 = -D \vec{e}_0$. At order ϵ we obtain

$$M_j^i \Psi_2^j = -p_1 \partial_p W^i|_0 - \kappa_1^2 D_j^i (\partial_u \varphi_1^j - u e_0^j) - \frac{\kappa_1^2}{2} \delta_{\Psi^j \Psi^k} W^i|_0 \varphi_1^j \varphi_1^k \quad (6.17)$$

where $|_0$ means evaluated at $\vec{\Psi}_0$ and p_c , and the solvability condition is

$$\int_{-\infty}^{\infty} a_{0i} \left[p_1 \partial_p W^i|_0 + \kappa_1^2 D_j^i (\partial_u \varphi_1^j - u e_0^j) + \frac{\kappa_1^2}{2} \delta_{\Psi^j \Psi^k} W^i|_0 \varphi_1^j \varphi_1^k \right] = 0. \quad (6.18)$$

\vec{a}_0 has the same symmetry with respect to \mathcal{S} as the Goldstone mode \vec{e}_0 , namely it is antisymmetric, while the expression in brackets is symmetric. Therefore the integral (6.18) vanishes, and the solvability condition at this order is always fulfilled. Then, a solution of the form

$$\vec{\Psi}_2 = p_1 \vec{\varphi}_2 + \kappa_1^2 \vec{\varphi}_3 \quad (6.19)$$

with $M\vec{\varphi}_2 = -\partial_p \vec{W}|_0$ and $M_j^i \varphi_3^j = -D_j^i (\partial_r \varphi_1^j - r e_0^j) - \frac{1}{2} \delta_{\Psi^j \Psi^k} W^i|_0 \varphi_1^j \varphi_1^k$ can be found. To obtain an amplitude equation for the curvature κ_1 we have to go to order $\epsilon^{3/2}$. We have

$$M_j^i \Psi_3^j = \frac{\partial_T \kappa_1}{\kappa_1^2} e_0^j - p_1 \kappa_1 (D_j^i \partial_r \varphi_2^j + \delta_{\Psi^j} \partial_p W^i|_0 \varphi_1^j + \delta_{\Psi^j \Psi^k} W^i|_0 \varphi_1^j \varphi_2^k) - \kappa_1^3 [D_j^i (\partial_r \varphi_3^j - r \partial_r \varphi_1^j + r^2 e_0^j) + \delta_{\Psi^j \Psi^k} W^i|_0 \varphi_1^j \varphi_3^k + \delta_{\Psi^j \Psi^k \Psi^l} W^i|_0 \varphi_1^j \varphi_1^k \varphi_1^l / 6]. \quad (6.20)$$

The solvability condition is:

$$\frac{\partial_T \kappa_1}{\kappa_1^2} = c_1 p_1 \kappa_1 + c_3 \kappa_1^3 \quad (6.21)$$

with

$$c_1 = \frac{1}{\Gamma} \int_{-\infty}^{\infty} a_{0i} (D_j^i \partial_r \varphi_2^j + \delta_{\Psi^j} \partial_p W^i|_0 \varphi_1^j + \delta_{\Psi^j \Psi^k} W^i|_0 \varphi_1^j \varphi_2^k) dr \quad (6.22)$$

$$c_3 = \frac{1}{\Gamma} \int_{-\infty}^{\infty} a_{0i} [D_j^i (\partial_r \varphi_3^j - r \partial_r \varphi_1^j + r^2 e_0^j) + \delta_{\Psi^j \Psi^k} W^i|_0 \varphi_1^j \varphi_3^k + \delta_{\Psi^j \Psi^k \Psi^l} W^i|_0 \varphi_1^j \varphi_1^k \varphi_1^l / 6] dr. \quad (6.23)$$

Equation (6.21) is written in the scaled curvature (6.14). Undoing the scaling we get

$$\frac{\partial_t \kappa}{\kappa^2} = c_1 (p - p_c) \kappa + c_3 \kappa^3. \quad (6.24)$$

For the radius of a circular domain ($R = 1/\kappa$) Eq. (6.24) becomes

$$\partial_t R = -c_1 (p - p_c) / R - c_3 / R^3. \quad (6.25)$$

$c_1 > 0$ since $\gamma = c_1 (p - p_c)$, and we are considering $\gamma > 0$ for $p > p_c$. If c_3 is negative (supercritical bifurcation) our analysis predicts just above p_c the existence of stable stationary circular domains (SD) with a very large radius R_0 :

$$R_0 = \frac{1}{\sqrt{p - p_c}} \sqrt{\frac{-c_3}{c_1}}. \quad (6.26)$$

In Fig. 6.11 we show the form of the SD for the PCGLE. At the SD center the field closely approaches the value of one of the homogeneous solutions so the wall of this structure is very close to a heteroclinic orbit between the two homogeneous states (Fig. 6.11 (right)). The radius of the SD diverges to infinity at p_c . Figure 6.12 displays the radius of the SD and that of the LS calculated by solving numerically $(1 + i\alpha)(\partial_r^2 + \frac{1}{r}\partial_r)A + (\mu + i\nu)A - (1 + i\beta)|A|^2 A + pA^* = 0$.

Fig. 6.12 (right) shows the linear dependence of $1/R_0^2$ with p as predicted by (6.26). In spite of the fact that there is a smooth transition from LS to SD (Fig. 6.12 (left)), these two localized states are intrinsically different. As the radius of the stable droplets is so large, the oscillatory tails interaction, responsible for the existence of

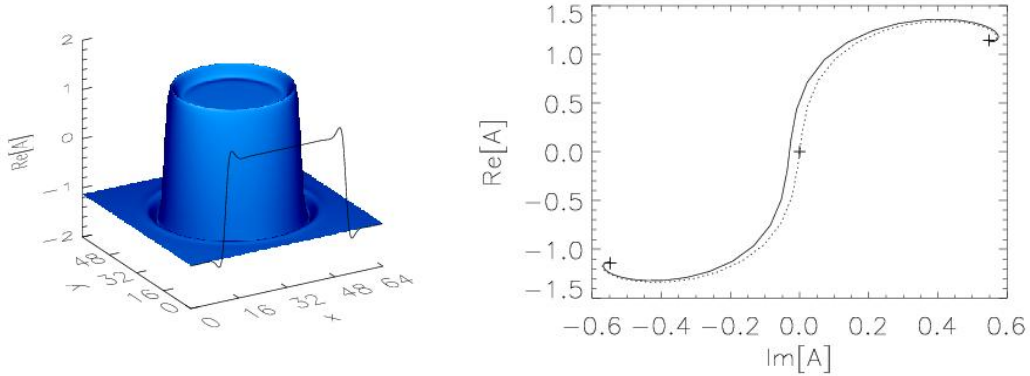


Figure 6.11: Left: spatial dependence and transverse section of a stable droplet. Right: the wall of the structure plotted in the A -complex plane (solid line). The 1d wall (dotted line) is also plotted for comparison with the wall of the stable droplet. The crosses indicate the two equivalent homogeneous solutions and the zero solution. Note that the profile of the wall of the stable droplet is slightly deformed with respect to the 1d wall due to the first order correction $\tilde{\Psi}_1$.

LS (Fig. 6.13), does not play any role in the SD. The stabilization mechanism comes from the counterbalance between the R^{-3} contribution to the front velocity and the shrinking due to the R^{-1} contribution¹. If $c_3 > 0$ (subcritical bifurcation) there would exist an unstable circular domains with radius R_0 just below p_c . However, we have never encountered this situation.

Another interesting feature of the nonlinear contributions of the curvature to the front velocity is the growth law of the circular domains at p_c . At p_c , Eq. (6.25) becomes

$$\partial_t R = -c_3/R^3, \quad (6.27)$$

¹Crossover between different growth laws has been found in systems with conserved order parameter [125]. In that case, however, the coefficients have the same sign and there is no stationary radius for the domains.

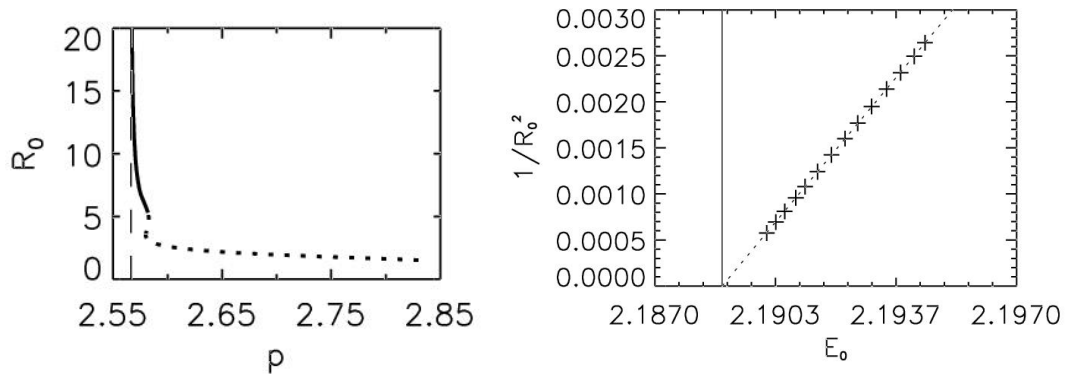


Figure 6.12: Left: Radius of SD (solid line) and LS (dotted line) as a function of the forcing p . Right: Linear dependence of $1/R_0^2$ with p close to the bifurcation point p_c (dashed line) as predicted by (6.26).

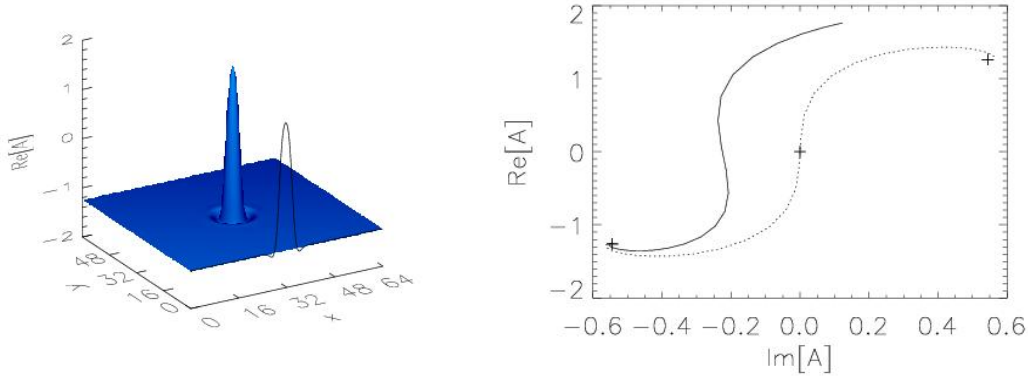


Figure 6.13: Left: spatial dependence and transverse section of a LS. Right: a cross-section of the LS plotted in the A -complex plane (solid line). The 1d wall (dotted line) is also plotted for comparison with the wall of the LS. The crosses indicate the two equivalent homogeneous solutions and the zero solution. Note that a LS can not be considered as a heteroclinic connection between the two homogeneous solutions.

and any circular domain of one solution embedded in the other grows as $R(t) \sim t^{1/4}$. In Fig. 6.14 we show the time evolution of the radius of a circular domain at p_c for the PCGLE. The numerical integration of Eq. (6.1) (circles) fits nicely the theoretical dependence we predict (solid line). Note that, since we calculate the value of c_3 from the solvability condition, we are able to predict not only the asymptotic power law but also the growth at earlier stages.

Close to p_c , in the regime of existence of the SD, there is no asymptotic power law of domain growth since at very long times the SD is formed stopping the growth process. During the transient, an initially small (very large) circular domain will grow (shrink) following (6.25) (Fig. 6.15).

So far we have considered the dynamics of domains with radial symmetry. When the system evolves from random initial conditions other dynamical mechanisms come into play. The main non-radially symmetric contribution to the velocity comes from the variation of the curvature along the front. Taking this effect into account, we

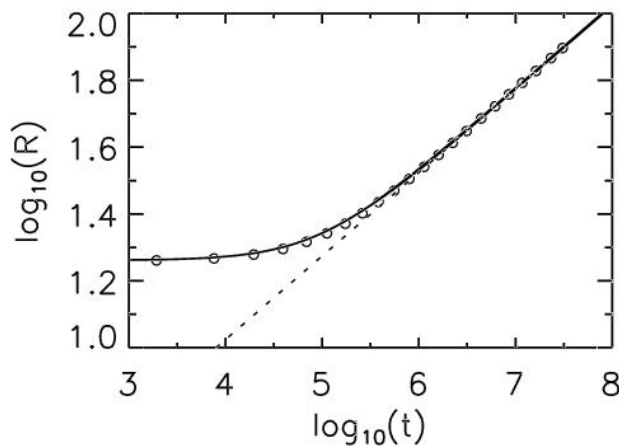


Figure 6.14: Growth of a circular domain as function of the time at $p = p_c$. Symbols correspond to the numerical integration of Eq. (6.1), the solid line is the theoretical prediction (6.25) with $c_3 = 0.3129$ calculated from (6.23) and the dotted line has a slope $1/4$ showing the asymptotic behavior.

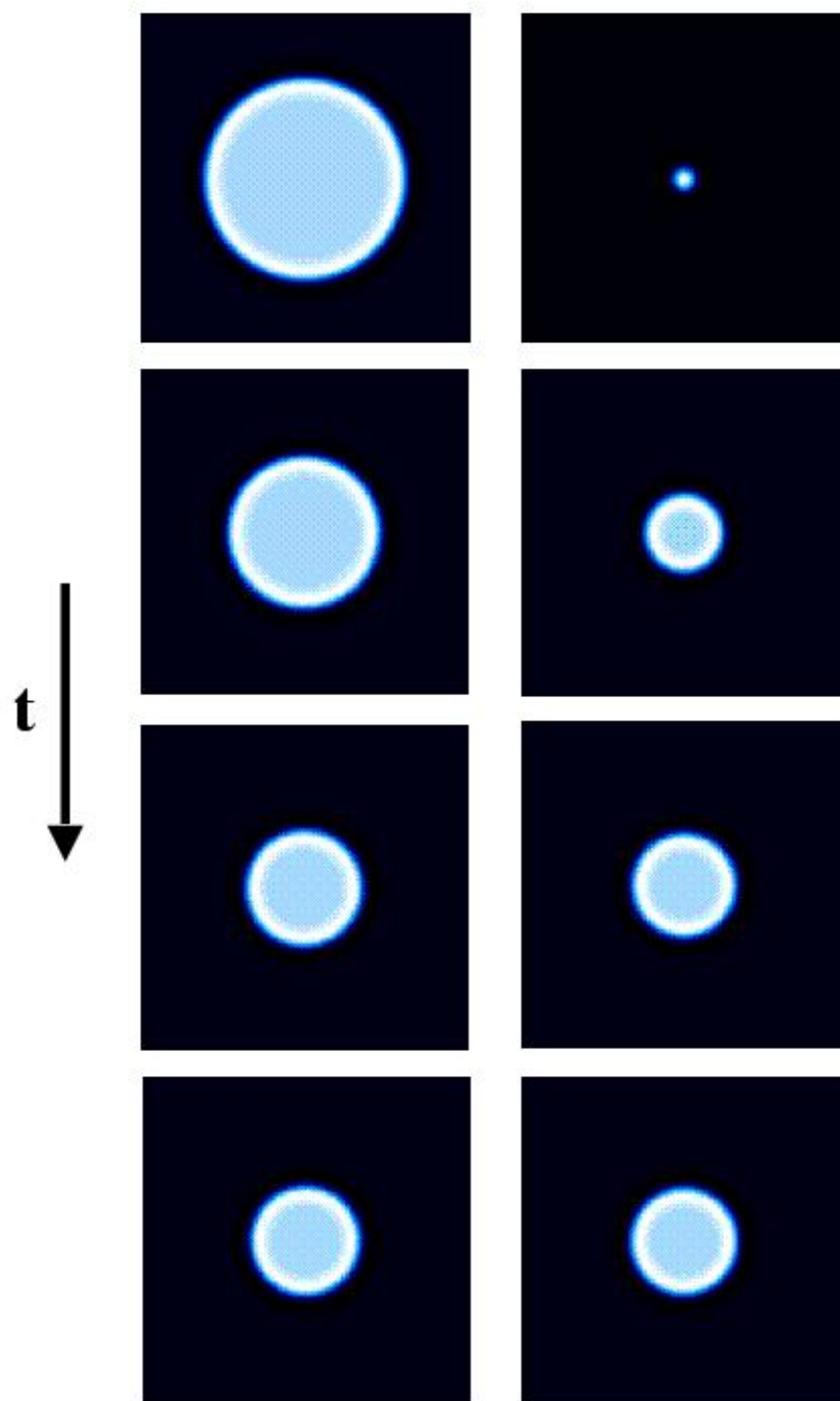


Figure 6.15: Snapshots corresponding to the time evolution of a very large and a small circular domains for the parametrically driven complex Ginzburg-Landau equation in the regime of existence of stable droplets.

can derive an amplitude equation for the normal velocity v_n . Using the fact that for circular domains $v_n = \partial_t \kappa / \kappa^2$, which is of order $\epsilon^{1/2}$, we now assume the scaling $v_n = \epsilon^{1/2} v_{n1}$. We obtain at order $\epsilon^{3/2}$ an additional term with respect to the case of radial symmetry (6.21):

$$c_2 \kappa_1^2 \partial_\theta^2 \kappa_1, \quad (6.28)$$

where $c_2 = \frac{1}{\Gamma} \int_{-\infty}^{\infty} \vec{a}_0 \cdot D\vec{\varphi}_1 dr$. Thus,

$$v_{n1} = c_1 p_1 \kappa_1 + c_2 \kappa_1^2 \partial_\theta^2 \kappa_1 + c_3 \kappa_1^3. \quad (6.29)$$

Undoing the scaling, the front velocity becomes

$$v_n = -c_1(p - p_c)\kappa - c_2 \kappa^2 \partial_\theta^2 \kappa - c_3 \kappa^3. \quad (6.30)$$

Consistently with our approximations, $\partial_\theta^2 \kappa$ will change at most at order κ^0 , so the non-radial contribution is at least of order κ^2 . At p_c , $c_1(p - p_c)\kappa$ vanishes, and the term given by $-c_2 \kappa^2 \partial_\theta^2 \kappa$ may be dominant compared with $c_3 \kappa^3$. The front velocity is then proportional to κ^2 . However, for any closed boundary

$$\int_0^{2\pi} \partial_\theta^2 \kappa = \partial_\theta \kappa \Big|_0^{2\pi} = 0, \quad (6.31)$$

so $\partial_\theta^2 \kappa$ has to be positive in some parts of the wall and negative in others, therefore, this term does not lead to an asymptotic growth law. If $c_2 < 0$, which is the case for the PCGLE, this term tends to reduce the curvature differences, so at p_c an arbitrarily shaped domain first becomes circular until the contribution of $\partial_\theta^2 \kappa$ vanishes and then the circular domain grows as $R(t) \sim t^{1/4}$ due to the c_3 term. Fig. (6.16) shows the time evolution of an arbitrarily shaped domain at $p = p_c$ for the PCGLE. At early stages we can observe the reduction of curvature differences along the front due to the nonradially symmetric contribution, until the domain become circular. Then, the contribution from the $\partial_\theta^2 \kappa$ term vanishes and the cubic radial symmetric term makes the circular domain to grow with a $t^{1/4}$ power law (a much slower time scale).

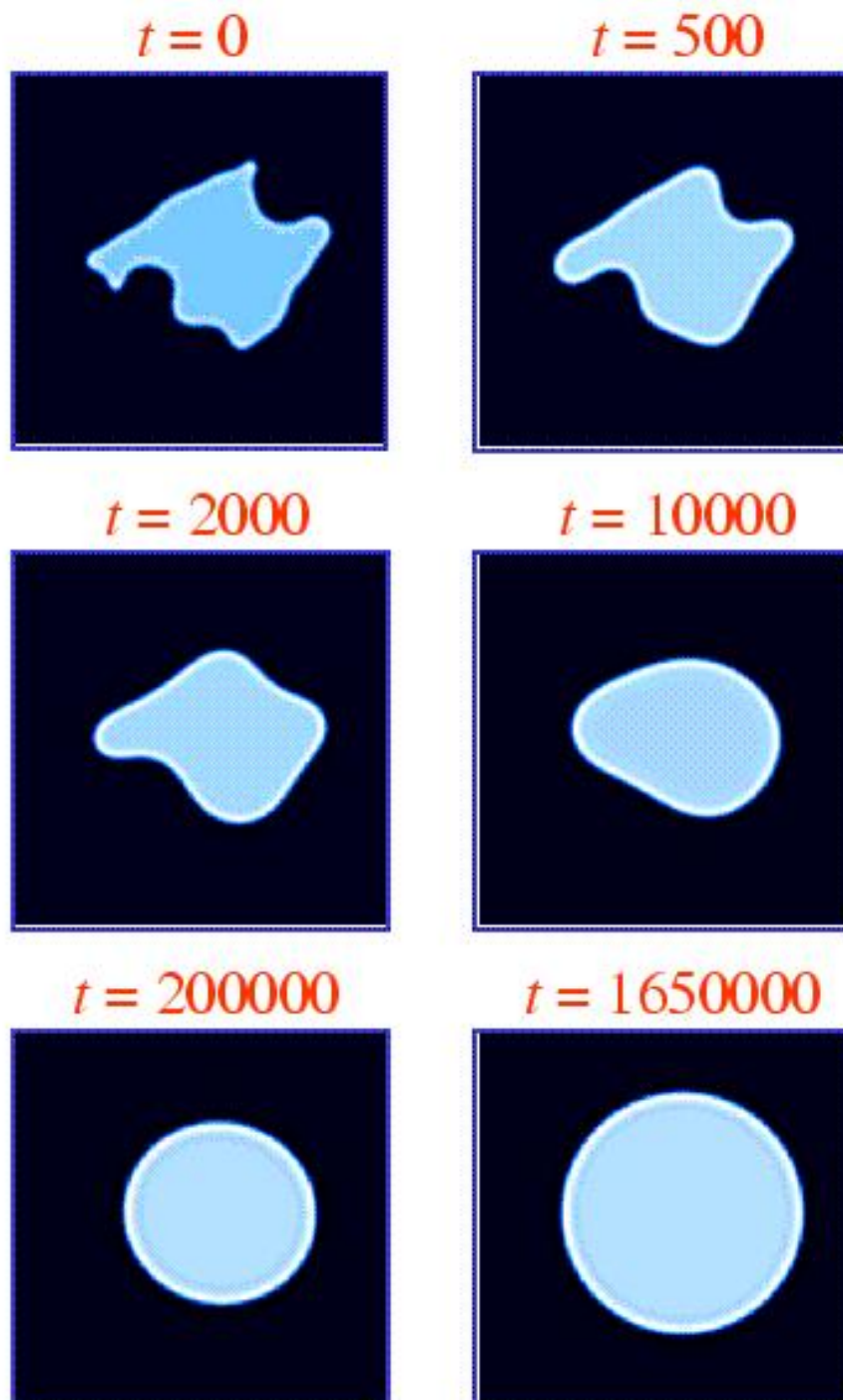


Figure 6.16: Evolution of an arbitrarily shaped domain at $p = p_c$.

6.3 Stable Droplets and Dark Ring Cavity Solitons in nonlinear optical cavities

In this section we apply the theory developed in the previous section to two nonlinear optical systems, the vectorial Kerr resonator and the degenerate optical parametric oscillator.

6.3.1 Vectorial Kerr Resonator

The mean field equations for a self-defocusing vectorial Kerr resonator are [75, 109]:

$$\partial_t E_{\pm} = -(1 - i\theta)E_{\pm} + i\nabla^2 E_{\pm} + E_0 - \frac{1}{4}i[|E_{\pm}|^2 + \beta|E_{\mp}|^2]E_{\pm} \quad (6.32)$$

where E_{\pm} are the circularly polarized field components, E_0 is the pump (x -polarized), θ is the cavity detuning, ∇^2 is the transverse Laplacian and β is related to the susceptibility tensor. In this paper we consider $\theta = 1$ and $\beta = 7$. For $E_0 < E_{th} \approx 0.95$ the homogeneous symmetric solution $I_+ = I_-$ (where $I_{\pm} = |E_{\pm}|^2$) is stable [109]. At this threshold value a y -polarized stripe pattern is formed. For pump values above a second threshold, $E_0 \approx 1.5$, there is bistability between two homogeneous solutions, namely E_{\pm}^a and E_{\pm}^b , which are asymmetric ($I_+^a \neq I_-^a$, $I_+^b \neq I_-^b$) and therefore elliptically polarized. These two solutions are equivalent in the sense that $E_{\pm}^a = E_{\mp}^b$, so that they have the same total intensity, polarization ellipticity and stability properties for all values of the control parameter. They differ in the orientation and in the direction of rotation of the polarization ellipse. A domain of one of these homogeneous solutions embedded in the other can therefore be identified as a polarization domain. The profile of a $d = 1$ front connecting these two solutions for $E_0 = 1.6$ is shown in Fig. 6.17. The shape of these fronts has been obtained by solving numerically the $d = 1$ stationary form of Eq. (6.32), namely

$$0 = -(1 - i\theta)E_{\pm}(x) + id_x^2 E_{\pm}(x) + E_0 - \frac{1}{4}i[|E_{\pm}(x)|^2 + \beta|E_{\mp}(x)|^2]E_{\pm}(x), \quad (6.33)$$

and imposing zero derivative as left and right boundary conditions, $d_x E_{\pm}(x = 0) = 0$ and $d_x E_{\pm}(x = L) = 0$, where L is the system size. From the $d = 1$ front profile and using Eq. (6.8) we determine the value of the growth coefficient for a circular domain γ . It follows from Eq. (6.33) that the $d = 1$ front profile depends on the pump strength E_0 and therefore, the value of γ will also be dependent on E_0 as shown in Fig. 6.18.

In the bistability region, depending on the value of γ , three dynamical regimes can be identified when increasing the control parameter E_0 (see Fig. 6.18) [68]. They are, respectively, a regime of labyrinthine pattern formation for $E_0 < E_{0,1}$, a regime of formation of localized structures for $E_{0,1} < E_0 < E_{0,2}$ and a regime of domain coarsening for $E_0 > E_{0,2}$ (see Fig. 6.18). These three regimes have been experimentally observed in a four wave mixing resonator [224] (see Fig. 6.2). As

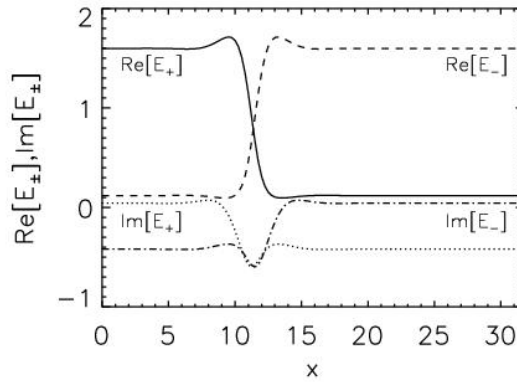


Figure 6.17: Profile of the $d = 1$ front connecting the two equivalent homogeneous solutions of the vectorial Kerr resonator for $E_0 = 1.6$.

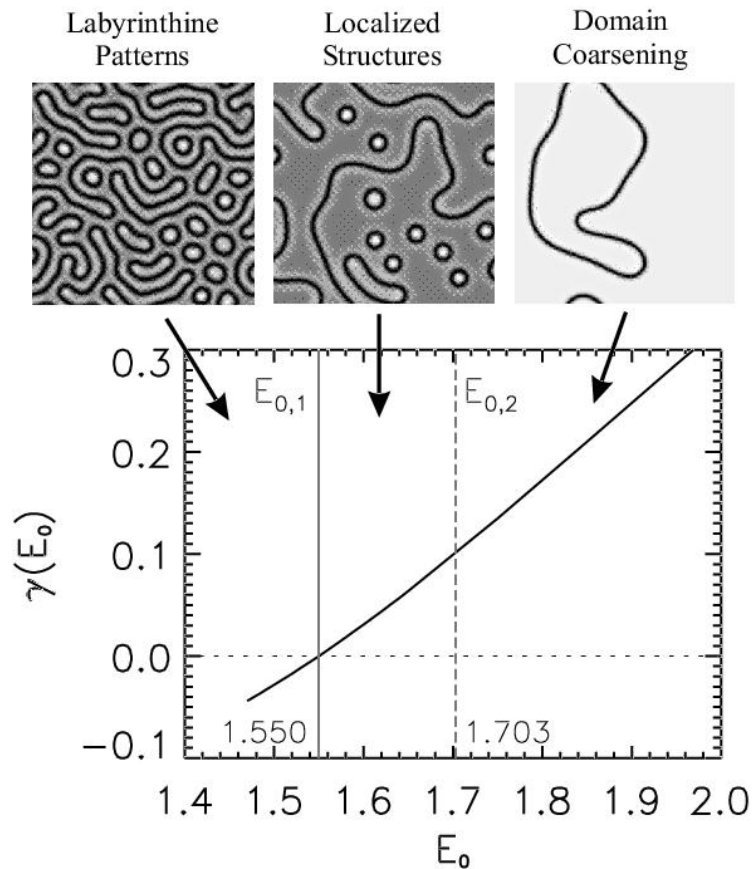


Figure 6.18: Growth rate γ versus the pump E_0 for the vectorial Kerr resonator. The vertical solid line indicates the modulation instability threshold for the flat front $E_{0,1} = 1.550$ and the vertical dashed line indicates the upper limit of existence of localized structures $E_{0,2} = 1.703$. The upper figures show, from left to right, snapshots of typical configurations of the total intensity $I_+ + I_-$ in the labyrinthine, localized structures and coarsening regimes.

indicated previously, $E_{0,1}$ is the modulational instability threshold of a flat domain wall connecting the two asymmetric homogeneous states. $E_{0,2}$ is the limit of existence of localized structures as will be explained below. In the regime of labyrinthine pattern formation ($E_0 < E_{0,1}$) $\gamma < 0$, a flat domain wall is modulationally unstable and a circular domain grows until its boundary breaks up because of the modulational instability. This behavior indicates that the system prefers to have the longest possible domain walls, or equivalently the largest possible curvature.

For $E_0 > E_{0,1}$, $\gamma > 0$ and very large circular domains progressively shrink. Away from the flat wall modulational instability threshold ($E_0 > 1.57$), however, but before $E_{0,2}$ the shrinking is halted by the formation of a LS. These structures owe their stability to the interaction of the oscillatory tails of the domain walls, the interaction being stronger the larger the amplitude of the local oscillation. For the vectorial Kerr resonator we found that only the locking at the first maxima of the oscillations is effective to counterbalance the shrinking while for the DOPO, as will be shown in the next section, there are several equilibrium distances. Figure 6.19 shows a typical cross section of the LS for $E_0 = 1.6$ and obtained by numerically solving the stationary radial equation [181]

$$0 = -(1 - i\theta)E_{\pm}(r) + i \left(d_r^2 + \frac{1}{r}d_r \right) E_{\pm}(r) + E_0 - \frac{1}{4}i[|E_{\pm}(r)|^2 + \beta|E_{\mp}(r)|^2]E_{\pm}(r) \quad (6.34)$$

with zero derivative at the boundaries: $d_r E_{\pm}(r = 0) = 0$ and $d_r E_{\pm}(r = L) = 0$, where L is the system size (which we take much larger than the size of the soliton). The vertical variable in Figure 6.17 is the real part of the circularly polarized E_+ field. The profile of the total intensity $I_+ + I_-$ of this LS is characterized by a peak surrounded by a dark ring as shown, for example, in the upper panels of Figure 6.18. Therefore they are called dark-ring cavity solitons (DRCS) [179]. There is an important difference between the $d = 1$ and $d = 2$ cases. While in 1d the localized structured originated from the tails interaction always exist, in $d = 2$, increasing the pump there is a threshold ($E_0 = E_{0,2}$, see Figs. 6.18, 6.20) for the interaction of the local oscillations to counterbalance the shrinking of the circular domains due to the local curvature of the walls. Fig. 6.20 shows the size of the cavity solitons in $d = 2$. It has been calculated by solving Eq. (6.34) as indicated above. The solid line corresponds to the stable DRCS and SD while the dotted line corresponds to unstable localized structures which have a shape similar to that of the stable DRCS. The threshold for existence of DRCS is marked in the diagram of Figure 6.18 as $E_{0,2}$. It may appear counterintuitive that DRCS lose their stability for increasing pump intensities where one would expect diffraction to be more effective on the local domain walls. The amplitude of the local oscillations at the tails of the domain walls, however, has a complex dependence on the parameters of the system and decreases for increasing input energies. Furthermore, it is clear from Fig. 6.18 that the coefficient γ grows with the pump; therefore the shrinking force due to front curvature becomes more important, overcoming the interaction of the

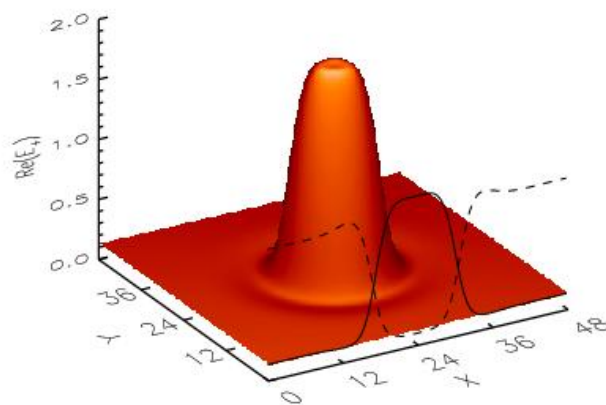


Figure 6.19: A DRCS of the vectorial Kerr resonator model for $E_0 = 1.6$ and the other parameters specified in the text. The vertical variable is the real part of the E_+ field. The dashed line represents the central section of the real part of the E_- field.

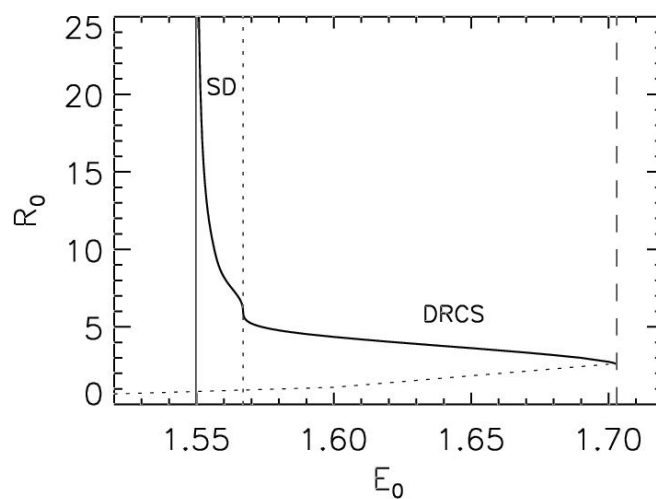


Figure 6.20: Radius of the cavity solitons as a function of the pump parameter E_0 for the VKR. Solid (dotted) lines correspond to stable (unstable) cavity solitons. The vertical solid line indicates $E_{0,1}$, the vertical dashed line indicates $E_{0,2}$ and the vertical dotted line indicates $E_{0,3}$, the transition from DRCS to SD (see text).

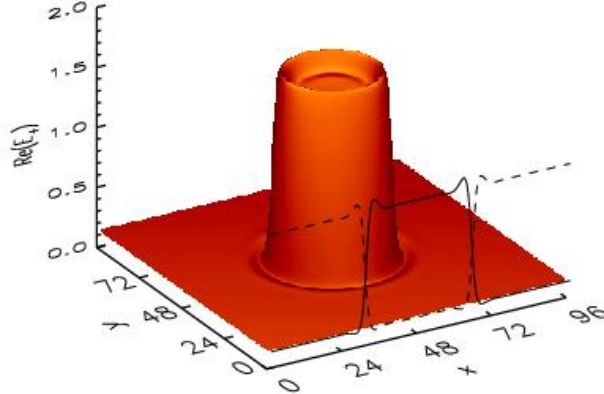


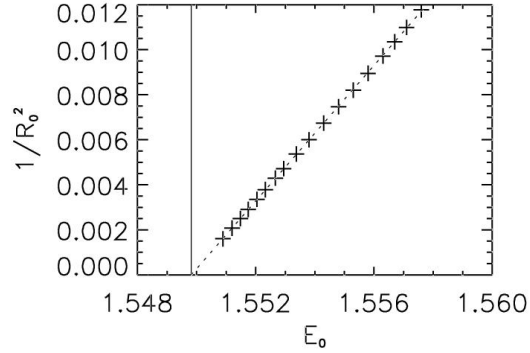
Figure 6.21: A stable droplet of the vectorial Kerr resonator model for $E_0 = 1.55238$ and the other parameters specified in the text. The vertical variable is the real part of the E_+ field. The dashed line represents the central section of the real part of the E_- field.

tails at $E_0 = E_{0,2}$. In terms of stationary solutions, this threshold corresponds to a saddle-node bifurcation where the stable and the unstable branches of the DRCS collide (Fig. 6.20). No cavity solitons are observed for pump values larger than $E_{0,2}$, indicating that this is the onset of domain coarsening.

We focus now on the region close to the modulational instability of the flat domain wall but for $E_0 > E_{0,1}$. In agreement with the theory of the previous section, close to the point $E_{0,1}$ where γ vanishes, nonlinear corrections to Eq. (6.9) must be considered. The derivation of the amplitude equation (6.21), carried out for a general system in the previous section, yields $c_1 = 0.591$ and $c_3 = -0.393$ for the case considered here. Since c_3 is negative we expect a region of stability of SD. These are indeed found in numerical simulations as Figures 6.20 and 6.21 clearly display. The SD are found exactly in the same way as the DRCS: namely, by solving (6.34) as indicated above. As expected, the radius of the SD quickly diverges to infinity the closer we move to $E_{0,1}$. In the vectorial Kerr resonator the SD is in fact an elliptically polarized domain embedded in a background with opposite elliptical polarization and therefore it constitutes a cavity polarization soliton.

We have checked that the SD cavity soliton found in the vectorial Kerr resonator model has the universal properties suggested in Section II. At the center of the SD, the field takes the value of one of the homogeneous solutions. Depending on the value of the pump, the radius of the SD can be extremely large. In fact, the radius diverges at $E_{0,1}$ as $R_0 \approx 1/\sqrt{E_0 - E_{0,1}}$. Figure 6.22 shows a comparison of $1/R_0^2$ between the theory of Eq. (6.26) (dotted line in Figure 6.22) and the numerical simulations (crosses) in the vicinity of $E_{0,1}$ (vertical solid line) where SD are large. The agreement is excellent thus demonstrating that the SD are a universal feature of systems with modulational instability of the flat front.

Figure 6.22: The linear dependence of $1/R_0^2$ with the control parameter E_0 for the SD in the vectorial Kerr resonator. The dotted line corresponds to Eq. (6.26) with $c_1 = 0.591$ and $c_3 = -0.393$, while the crosses are from the numerical determination of the SD as steady states of Eq. (6.32).



Moving now in the direction of increasing E_0 , we find that the SD stable branch has a change of behavior at $E_0 = E_{0,3}$ (see Fig. 6.20). This particular point corresponds to the value of the pump for which the interaction of the tails becomes of the same order as the nonlinear correction of Eq. (6.21). We note that the transition from DRCS to SD is continuous and that the SD nucleates out of the DRCS. Such a transition is, however, marked by a sudden change in the size of the cavity soliton. While the radius of the DRCS changes very little with decreasing control parameter E_0 , the radius of the SD changes rapidly with $(E_0 - E_{0,1})$ as shown in Eq. (6.26). For $E_{0,3} < E_0 < E_{0,2}$ the interaction of the oscillatory tails is dominant and the cavity soliton is a DRCS characterized by a larger intensity at the center than in the surrounding background (see Fig. 6.19). For $E_{0,1} < E_0 < E_{0,3}$ the nonlinear curvature effects (including the growth which leads to the SD) dominate over the interaction of the oscillatory tails and a stable stationary circular domain wall is formed. We note here that unlike the DOPO case discussed in the next section, the SD emerges directly from the single peak DRCS and that there is no bistability between any DRCS and SD.

6.3.2 Degenerate Optical Parametric Oscillator

The second nonlinear optical device that we consider is the phase matched DOPO where both pump A_0 and signal A_1 fields are resonant. The mean field equations are [178]:

$$\begin{aligned}\partial_t A_0 &= \Gamma[-A_0 + E_0 - A_1^2] + \frac{ia}{2}\nabla^2 A_0 \\ \partial_t A_1 &= -A_1 - i\Delta_1 A_1 + A_0 A_1^* + ia\nabla^2 A_1,\end{aligned}\quad (6.35)$$

where Γ is the ratio between the pump and signal cavity decay rates, E_0 is the amplitude of the external pump field (our control parameter), Δ_1 is the signal detuning and a is the diffraction parameter. In [179, 181] DRCS have been found for $\Delta_1 = 0$ (resonant case) and for $\Delta_1 > 0$. In order to find a modulational instability of the flat front we need, however, to turn our attention to negative signal detunings and we choose $\Delta_1 = -1$. Moreover, it is possible to show that the modulational instability of the flat front approaches the signal generation threshold from above

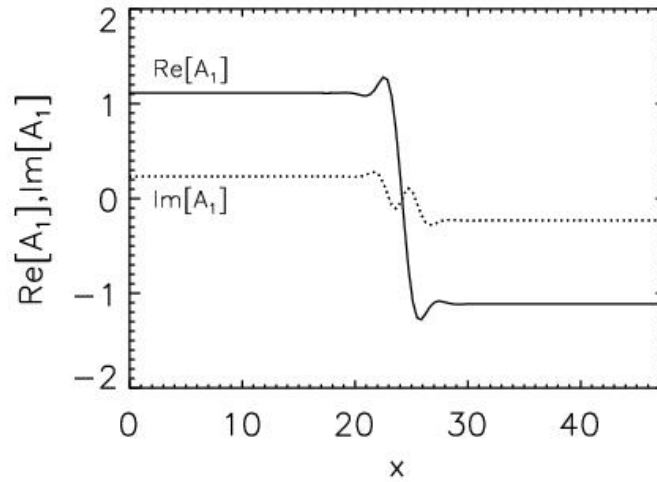


Figure 6.23: Profile of the one dimensional front connecting the two equivalent homogeneous solutions of the DOPO for $E_0 = 2.5$.

in the limit of high Γ in a way analogous to what is observed for the thresholds of DRCS and pattern formation for positive and zero signal detunings [181]. We then select $\Gamma = 6$ and $a = 0.5$ which allow for the analysis of the transition from DRCS to SD at parameter values which are experimentally accessible. For $0 < E_0 < 1$ the zero homogeneous solution is stable. Above the $E_0 = 1$ threshold a stripe intensity pattern is formed [178]. For pump values above a second threshold, $E_0 \approx 1.56$, there is multistability between two nonzero homogeneous solutions and several (regular or irregular) spatially modulated solutions. The latter cease to exist at the threshold of labyrinthine patterns, i.e. the modulational instability of the flat front connecting the two homogeneous solutions, which occurs at $E_{0,1} = 2.189$. The two homogeneous solutions have the same intensity and stability properties for all values of the control parameter. They only differ by a π phase shift in the signal field A_1 . The profile of a $d = 1$ front connecting these two homogeneous solutions is shown in Fig. 6.23. The front profile has been calculated solving numerically as before the $d = 1$ stationary form of Eq. (6.35),

$$\begin{aligned}
 0 &= \Gamma[-A_0(x) + E_0 - A_1^2(x)] + \frac{ia}{2}d_x^2 A_0(x) \\
 0 &= -A_1(x) - i\Delta_1 A_1(x) + A_0(x)A_1^*(x) + iad_x^2 A_1(x).
 \end{aligned} \tag{6.36}$$

Figure 6.24 shows the behavior of the growth rate for a circular domain $\gamma(E_0)$ for the DOPO calculated from the $d = 1$ front profile using Eq. 6.8. Again, three dynamical regimes can be identified. For $E_0 > E_{0,2}$ there is a regime of domain coarsening and no cavity solitons. For $E_{0,1} < E < E_{0,2}$ asymptotic cavity solitons exist, either DRCS or SD. Finally, for $E_0 < E_{0,1}$ labyrinthine patterns appear. We note here a difference with the case of the vectorial Kerr resonator. In this region the

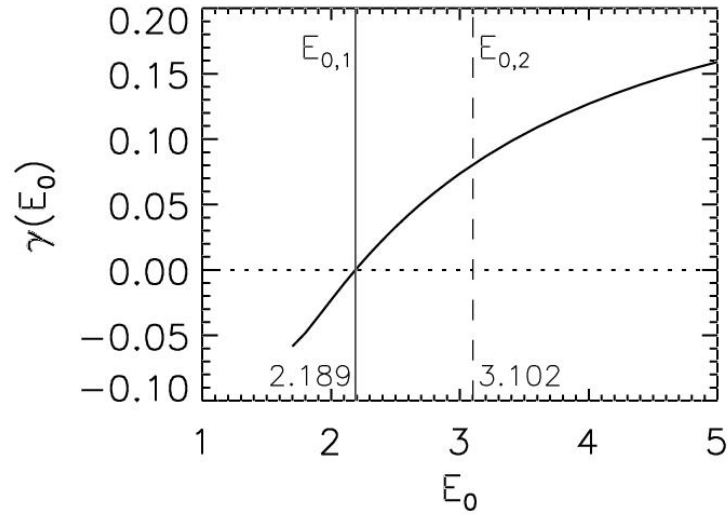


Figure 6.24: Growth rate γ for the DOPO equations (6.35). Vertical solid line indicates $E_{0,1}$ and vertical dashed line indicates $E_{0,2}$.

interaction of the tails of the domain walls between the stable homogeneous solutions is still strong enough to stabilize a single peak (primary) DRCS corresponding to the locking of the first maxima of the oscillatory tails. This is clearly visible in Fig. 6.25 where one branch of the DRCS extends well below the modulational instability threshold at $E_{0,1}$ where labyrinthine patterns exist. Note that the $d = 2$ cavity soliton (of the SD or DRCS type) and their stability have been calculated by solving the stationary radial equations

$$\begin{aligned}
 0 &= \Gamma[-A_0(x) + E_0 - A_1^2(x)] + \frac{ia}{2} \left(d_r^2 + \frac{1}{r} d_r \right) A_0(x) \\
 0 &= -A_1(x) - i\Delta_1 A_1(x) + A_0(x) A_1^*(x) + ia \left(d_r^2 + \frac{1}{r} d_r \right) A_1(x) \quad (6.37)
 \end{aligned}$$

with the numerical methods described in Sec. 6.2.2 [181].

Since the SD are always on the side opposite to the labyrinths, SD for the DOPO with these parameters cannot nucleate out of the single peak DRCS. It has been shown in Ref. [181] that the single peak DRCS, corresponding to the locking of the first maxima, is just one of several solitons whose stability is due to the interactions of the tails of the domain walls. For example a secondary DRCS with a central trough, corresponding to the locking of the first minima is also stable at resonance. We have also located such secondary DRCS structures in the vicinity of the modulational instability of the flat front. The uppermost solid line on the right side of $E_{0,3}$ in Fig. 6.25 gives the radius of the stable DRCS displayed in Fig. 6.26. Unlike the DOPO at resonance ($\Delta_1 = 0$) considered in Ref. [179, 181], the unstable branch of the secondary ('trough') DRCS merges with the stable branch of the primary ('single peak') DRCS at around $E_0 \sim 2.126$. We explain this fact by noting that

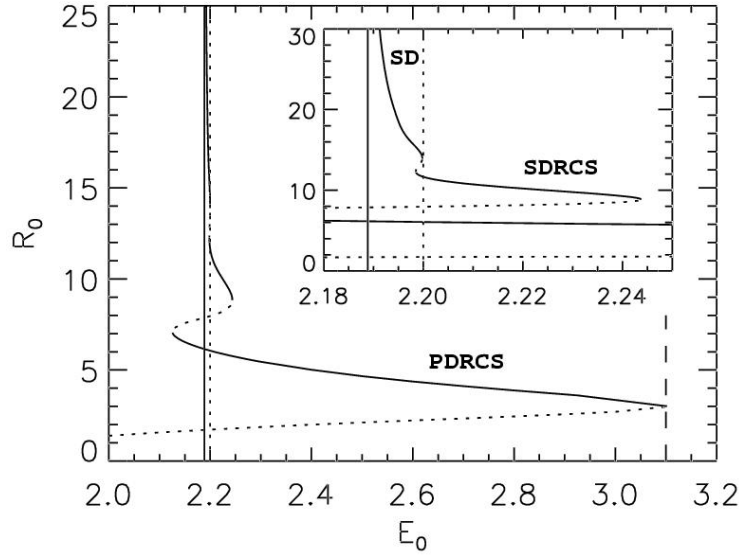


Figure 6.25: Radius of the cavity solitons as a function of the pump parameter E_0 for the DOPO. Solid (dotted) lines correspond to stable (unstable) cavity solitons. Primary (secondary) DRCS are labelled as PDRCS (SDRCS). The vertical solid line indicates $E_{0,1}$, the vertical dashed line indicates $E_{0,2}$ and the vertical dotted line indicates $E_{0,3}$, the transition from DRCS to SD. The inset shows a close up of this transition.

$\gamma(E_0)$ of Eq. (6.9) increases with E_0 in the case described here (see Fig. 6.25) and instead decreases with E_0 at resonance.

The secondary DRCS loses stability just after the $E_{0,3}$ line of Fig. 6.25 when decreasing E_0 . The unstable branch of this saddle-node bifurcation is then linked to the stable branch of the SD which start to inflate at $E_{0,3}$. Again, one observes a sudden change in the radius of the CS when switching from DRCS to SD. The radius of the SD then quickly grows with the parameter E_0 approaching the modulation instability of the stable front as clearly displayed in Fig. 6.25. As shown in Fig. 6.27, SD in the DOPO again satisfy the general Eq. (6.26) with $c_1 = 0.115$ and $c_3 = -0.244$, where the value of these coefficients is obtained from the derivation of the amplitude equation (6.21) following the procedure indicated in section 6.2. One important aspect of the SD in the DOPO system is that SD are now bichromatic since they are visible in both pump and signal fields.

In the entire regime of existence of SD in the DOPO we observe bistability of SD and primary ('single peak') DRCS (see Fig. 6.25). We show in Fig. 6.28 an interesting composite cavity soliton which is a natural consequence of this bistability. A primary ('single peak') DRCS is stable at the center of a large SD at $E_0 = 2.19015$.

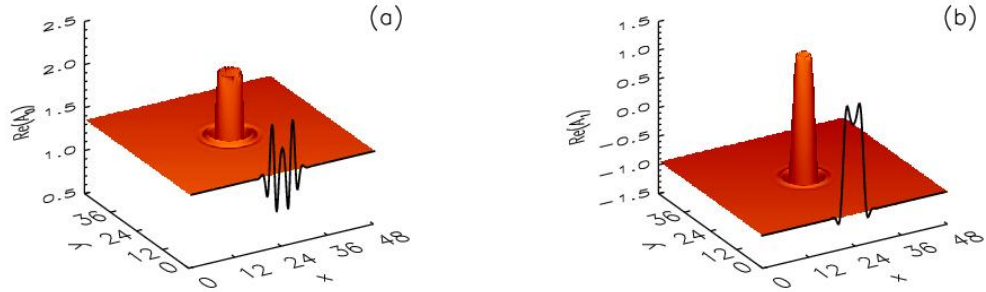


Figure 6.26: The real part of the pump (a) and signal (b) fields of a secondary ('trough') DRCS for the DOPO at $E_0 = 2.21$. The solid lines are the central sections of the 3D plots.

Figure 6.27: The linear dependence of $1/R_0^2$ with the control parameter E_0 for the SD in DOPO. The dotted line corresponds to Eq. (6.26) with $c_1 = 0.115$ and $c_3 = -0.244$, while the crosses are from the numerical determination of the SD as steady states of Eq. (6.35).

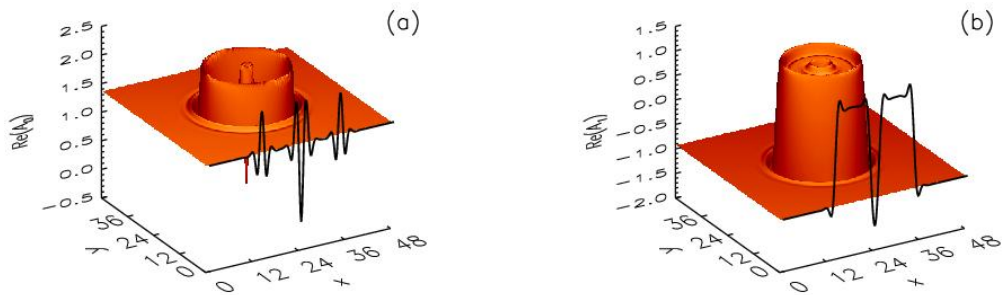
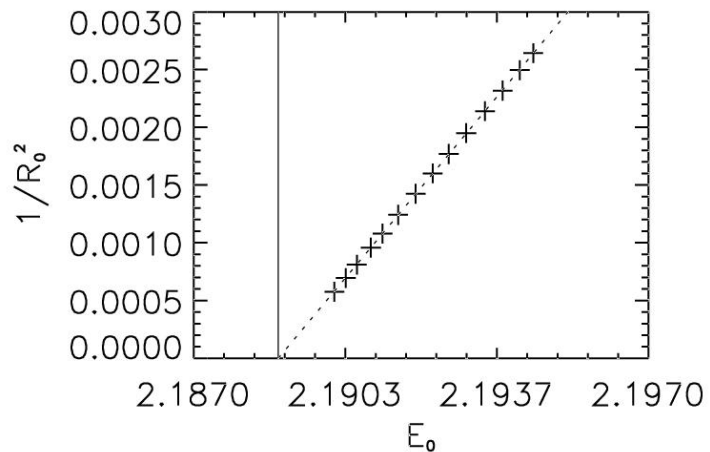


Figure 6.28: A primary ('single peak') DRCS at the center of a SD for the DOPO at $E_0 = 2.1915$. Both cavity solitons taken separately are stable in this parameter region. Real part of the pump field (a) and real part of the signal field (b). The solid lines are the central sections of the 3D plots.

6.4 Conclusions

In this chapter we have analyzed a generic situation of domain wall motion driven by curvature effects in which the proportionality coefficient γ between wall velocity and curvature changes sign at a bifurcation point leading to a transition from a coarsening regime (γ positive and large) to labyrinthine pattern formation ($\gamma < 0$). In the regime of coarsening the growth of domains is given by the Allen-Cahn $t^{1/2}$ power law. For γ positive but small, localized structures can be formed as a consequence of the interactions of the tails of the fronts. In this regime there is no self-similar evolution. The amplitude equation for the curvature in the vicinity of the bifurcation point predicts just above the bifurcation the existence of stable nonlinear solutions which are droplets of one phase embedded in a background of the second equivalent phase. Nonlinear dynamics of the curvature leads to growth laws different from the Allen-Cahn $t^{1/2}$ power law. The existence of a large characteristic length given by the radius of the stable droplet destroys the possibility of self-similar evolution. At the bifurcation point a $t^{1/4}$ growth law is obtained.

The determination of growth laws allows to establish from both theoretical and experimental data the mechanism that governs the dynamics of interfaces. We have explained different growth process in a framework which allow to include many nonpotential systems, for which interface dynamics is, in general, quite poorly understood. Our results come from a rigorous analysis which allow us to show in which regions of the parameter space a growth law $t^{1/2}$ or $t^{1/4}$ can be found and in which regions the growth rate of a domain does not follow a power law. Growth laws of the form $t^{1/3}$ do not appear in these systems. This result was obtained numerically [229, 136], probably because the measurement was done in transient regimes where the asymptotic growth rate was not yet reached. Furthermore, we have demonstrated the existence of a novel kind of localized structures, the stable droplets, which owe their stability to the interplay between curvature and nonlinear effects, and therefore do not exist in 1d systems.

Our results are universal in that any 2d system with a modulational instability of a flat front connecting two equivalent homogeneous states displays similar droplets and dynamics independently of the nature of the coexisting phases. Such systems can be found in fields as diverse as hydrodynamics, chemical reactions, material science and nonlinear optics. Transitions from coarsening to labyrinthine regimes has been observed experimentally in reaction diffusion [189] and optical [224] systems. Particularly relevant is the field of nonlinear optics, where the criterion for the modulational instability of a domain wall can be easily reached due to the diffractive coupling between real and imaginary parts of the complex field amplitude. We have applied our results to a model for a self-defocusing vectorial Kerr cavity with linearly polarized input field and to a model for a optical parametric oscillator. We have demonstrated that in both cases there exist stable circular domains. For the vectorial Kerr resonator these domains are in fact polarization domains, cavity polarization solitons, while for the optical parametric oscillator they are domains of opposite phase. This offers two different possibilities for addressing and manipulating cavity

solitons. We have also shown that stable droplets nucleate out of dark ring cavity solitons but can coexist with dark ring cavity solitons in the parameter space. This fact may be exploited in increasing the information capacity of these devices by using the stable droplets and dark ring cavity solitons to encode separate information.

Chapter 7

Conclusions and Outlook

In this work numerical techniques from dynamical systems theory have been applied to study the dynamics of spatial structures in extended systems. In order to properly describe the infinite number of spatial degrees of freedom specific numerical techniques have been used and developed. The result has been a much deeper understanding of the dynamics of spatial structures that would have been possible using only numerical simulations. These semi-analytic techniques have allowed us a further understanding in the study of spatial structures than analytic methods or numerical simulations taken separately.

We have first studied the dynamics of extended patterns in two microscopic models for two different optical systems, a self-focusing Kerr cavity and a sodium vapor cell with a feedback-mirror. In both cases we first have solved the stationary equations seeking for stationary solutions in the form of hexagonal patterns. This is done solving the stationary equations for the Fourier coefficients of the hexagonal patterns by means of Newton method. This approach is extremely accurate and much faster than numerical simulations. The whole range of existence of stationary hexagonal solutions can be easily explored by means of continuation techniques. Moreover, with this method, the wavenumber of a hexagonal pattern is treated as parameter and therefore we find hexagonal patterns with all possible wavenumbers. We have also performed the stability analysis of these stationary solutions finding the region of stability in the parameter space and the modes that are relevant in the instabilities.

In the Kerr cavity case, hexagonal patterns with somehow large wavenumber have oscillatory instabilities, both homogeneous and at a finite wavenumber, while hexagons with smaller wavenumbers become unstable against long-wavelength perturbations or undergo homogeneous stationary instabilities. The oscillatory instabilities of hexagonal patterns in this system can be understood as a collective behavior of coupled oscillators, since each peak separately can be considered as an independent dynamical system close to a Hopf bifurcation. The underlying mechanism leading to the oscillation of the peaks is related to the collapse phenomenon in the 2d nonlinear Schrödinger equation which is avoided by the cavity losses. There is, how-

ever, an important difference, the isolated peaks (Kerr cavity solitons) never become chaotic while hexagonal patterns show a richer behavior. Therefore, the coupling between nearby peaks, which comes through diffraction, plays a crucial role. For low couplings, i.e. low wavenumbers, the pattern oscillated homogeneously, while for larger couplings a finite wavelength instability lead to a splitting of the hexagonal pattern in three superlattices oscillating periodically in antiphase. In this case we have also analyzed further instabilities until a regime of optical turbulence is reached. We have properly characterized a Neimark-Sacker bifurcation of the oscillating superlattices showing how the system becomes simultaneously spatial and temporally more complicated. The temporal behavior would fit in a Ruelle-Takens scenario while the breaking of the spatial synchrony would rather be a generalization of spatial period doubling. A subsequent long-wavelength instability, which is present only in spatially extended systems, leads to chaotically oscillating peaks which are still located on a hexagonal lattices. The lose of spatial order entering in a regime of optical turbulence takes place, probably, through a crisis.

The model for the sodium vapor cell with a feedback-mirror shows, in general, very different instabilities. At difference with the Kerr cavity, this system displays negative hexagons, and the self-focusing collapse leading to the oscillatory behavior of the peaks is not present in the system. The long-wavelength instability of hexagonal patterns is, however, common to both systems. This is a very general instability associated to the dynamics of the phase of the patterns associated to the breaking of the translational invariance. All the other instabilities of a hexagonal pattern in the sodium vapor with a single feedback mirror are stationary finite wavelength instabilities. In some cases the instability leads to hexagonal pattern with a stable wavenumber, and in others to a periodic pattern with twelve wavevectors, a superlattice. Most of the instabilities are sub-critical and this leads to a large variety of structures coexisting for the same values of the pump intensity. This multistability is observed in the experimental system and plays a very important role when the noise is present, as it is always the case in the experiment. Some of the observed superlattices correspond with the patterns arising from the secondary instabilities of hexagons in the model.

We have also studied the effects of noise in a hexagonal pattern in the model for the self-focusing Kerr cavity. We have performed semi-analytical and numerical calculations taking into account a large number of harmonics, thus avoiding the limitations of few modes approximations. This is particularly important for hexagonal patterns since they are generally subcritical, so that even close to threshold a large number of harmonics have a significant amplitude. We have seen that the modes responsible for the fluctuations in the near field, namely the Goldstone and soft modes, at first order in the noise intensity do not contribute to the fluctuations of the far-field intensity peaks. The structure of the fluctuations in the far-field is given by the structure of more damped eigenmodes, leading to a strong correlation between the different modes of the patterns and their harmonics, and a strong anticorrelation between the off-axis modes and the homogeneous. The strongest correlation between the six fundamental harmonics of the hexagonal pattern pat-

terns is for those forming 120° . While the anticorrelation of the homogeneous mode with the off-axis wavevectors can be understood in terms of energy conservation, the common microscopic interpretation of the far-field intensity correlations in terms of emission of twin photons would naively suggest that the strongest correlation is between the wavevectors forming a 180° angle. In fact, the total transverse momentum conservation involve always at least four modes simultaneously and give some hints about how the correlations should be, but does not identifies the pairs with stronger correlations.

In the second part of the thesis we have studied the dynamical properties of two different types of localized structures. Numerical techniques similar to those used to study extended structures in the first part have been used. The main difference is that, while the Fourier modes constitute a natural basis to describe periodic patterns, localized structures are most suitable described by a discrete radial equation. The number of effective variables is similar in both cases. Localized structures, associated to the coexistence of a sub-critical cellular pattern and a homogeneous solution, has been studied in the self-focusing Kerr cavity model. We have definitively proved a region of stability of the stationary Kerr cavity soliton in the parameter space. This region is bounded by two azimuthal instabilities for low values of the detuning and for a Hopf instability for larger values. Very generally, azimuthal instabilities impose an upper limit for the stability of localized structures in presence of a modulation instability. In our case a very interesting instability with azimuthal number $m = 5$ leads to a expanding pattern with five fold symmetry. The Hopf instability leads to a oscillating Kerr cavity soliton. This oscillation does not prevent the potential application of this structures as bit in optical memories, since, in average, the intensity of the oscillating cavity solitons can be clearly distinguished from the situation of no cavity soliton. A very interesting tertiary bifurcation of the oscillating cavity soliton, namely a saddle-loop bifurcation, have been rigorously characterized. This is a global bifurcation associated to the collision of a saddle fix point with a limit cycle and which we can not detect performing an stability analysis. However, the semi-analytical techniques are still useful to determine the eigenvalues of the saddle and together with numerical simulations it is possible to characterize the bifurcation rigorously. The saddle-loop bifurcation leads to a novel regime of excitability never reported before in the context of localized structures. In this case the local dynamics of the system is no excitable but the projection on the phase sub-space determined by the localized modes is. This is an example of the richness of the partial differential equations to display very different dynamical regimes through their coherent structures.

Finally, we have studied the second type of localized structures, i.e., those associated to the coexistence of two homogeneous solutions. The formation and stability of these structures is strongly related to the problem of domain growth and front motion. We have develop by means of semianalytical techniques a general theory of domain wall dynamics for a very general class of system including models of nonlinear optical cavities and chemical reactions. Our result have resolved a long standing controversy about the power laws for domain growth in nonlinear optical cavities.

This disagreement had its origin in ambiguous results obtained from numerical simulations without verifying that the asymptotic regime has been reached and that scaling properties exist. Our results rigorously establish in which regions of the parameter space a growth law $t^{1/2}$ or $t^{1/4}$ can be found and in which regions the growth rate of a domain does not follow a power law. Furthermore we also predict a new kind of localized structures whose stability is based on nonlinear curvature effects. These structures, at difference with localized structures stabilized by oscillatory tails interaction, have no 1-dimensional counterparts. As a particular case we have shown the existence of this new structures in models for a vectorial Kerr cavity and degenerate OPO. These structures have not been yet experimentally demonstrated but, experiments in an oscillatory chemical reaction forced at twice its natural frequency are being done in this direction by the group of Dr. Anna Lin in Durham University (USA).

In this work we have answered several important questions about the dynamics of both extended and localized structures, but there are still many problems to be solved. We hope this work will contribute to the basis for a new way to tackle dynamics of patterns and localized structures.

Appendix A

Linear stability analysis of stationary periodic patterns

In this appendix we explain the procedure we have used in chapters 2, 3 and 4 to perform the linear stability analysis of stationary periodic patterns of a partial differential equation. Here we consider a single two dimensional complex partial differential equation, however, the analysis can be easily generalized to any number of dimensions and coupled equations.

Let us consider partial differential equations of the form

$$\partial_t E(\vec{x}, t) = W(\nabla^{(2n)}, E(\vec{x}, t)), \quad (\text{A.1})$$

where $E(\vec{x}, t)$ is a two dimensional complex field, $\nabla^{(2n)}$ ($n = 1, \dots$) are even powers of the two dimensional Laplacian and W is a homogeneous nonlinear operator. Let $E_h(\vec{x})$ be a stationary spatially periodic solution ($W(\nabla^{(2n)}, E_h(\vec{x})) = 0$), for example a hexagonal pattern.

Linearizing Eq. (A.1) around the stationary solution (A.8) the following equation for the fluctuations $\delta E(\vec{x}, t) = E(\vec{x}, t) - E_h(\vec{x})$ is obtained

$$\partial_t \delta E = \alpha(\nabla^{2n}, E_h(\vec{x}))\delta E + \beta(\nabla^{2n}, E_h(\vec{x}))\delta E^*, \quad (\text{A.2})$$

where $\alpha = \delta_E W|_{E_h}$ is the functional derivative of W with respect to E evaluated at E_h . Equivalently $\beta = \delta_{E^*} W|_{E_h}$. α and β depend nonlinearly on $E_h(\vec{x})$ and $\nabla^{(2n)} E_h(\vec{x})$ but do not depend on δE . Therefore, they are space dependent with the same periodicity than the stationary solution $E_h(\vec{x})$. For the Kerr cavity discussed in chapter 2 (Sec. 2.4) $\alpha = -(1 + i\theta) + i\nabla^2 + i4|E_h|^2$ and $\beta = i2E_h^2$. Eq. (A.2) involve δE and δE^* that must be considered as independent variables. By considering $\delta \vec{E} = (\delta E, \delta E^*)^T$, we have from Eq. (A.2)

$$\partial_t \delta \vec{E} = L(E_h) \delta \vec{E}, \quad (\text{A.3})$$

where

$$L(E_h) = \begin{pmatrix} \delta_E W|_{E_h} & \delta_{E^*} W|_{E_h} \\ \delta_E W^*|_{E_h} & \delta_{E^*} W^*|_{E_h} \end{pmatrix} = \begin{pmatrix} \alpha & \beta \\ \beta^* & \alpha^* \end{pmatrix}. \quad (\text{A.4})$$

The stability of E_h is determined by the eigenvalues λ of L

$$L(E_h)\vec{\psi} = \lambda\vec{\psi}, \quad (\text{A.5})$$

where $\vec{\psi}$ is the eigenvector associated to the eigenvalue λ . If any of the eigenvalues is positive the pattern will be unstable. Furthermore, the eigenvector associated to this positive eigenvalue indicates the spatial profile of the growing perturbation. As the coefficients of L are periodic, we can use the Bloch's theorem to find its eigenvectors and eigenvalues [13]. The eigenvectors $\vec{\psi}$ have the form of a plane wave times a function with the same periodicity than the pattern E_h :

$$\vec{\psi}(\vec{x}, \vec{q}) = \begin{pmatrix} e^{i\vec{q}\vec{x}} A(\vec{x}, \vec{q}) \\ e^{-i\vec{q}\vec{x}} A^*(\vec{x}, -\vec{q}) \end{pmatrix}, \quad (\text{A.6})$$

where

$$A(\vec{x} + \vec{R}, \vec{q}) = A(\vec{x}, \vec{q}), \quad (\text{A.7})$$

being \vec{R} any vector of the lattice defined by the pattern.

We can write the stationary pattern as

$$E_h(\vec{x}) = \sum_{m=0}^{N-1} a_m e^{i\vec{k}_m^0 \vec{x}}, \quad (\text{A.8})$$

where \vec{k}_n^0 are the wavevectors of the pattern, a_n are complex coefficients and N is the number of Fourier modes considered in the analysis. \vec{k}_0^0 is the homogeneous mode and \vec{k}_n^0 for $n = 1, N - 1$ are the off-axis wavevectors of the pattern containing the fundamental wavevectors with modulus k ($n = 1, 6$ for a hexagonal pattern) and their harmonics. The accuracy of the method increases with the number of modes considered in the analysis. The amplitude of the last harmonics in the truncation is an indicator of the error. $A(\vec{x}, \vec{q})$ can be, therefore, written as

$$A(\vec{x}, \vec{q}) = \sum_{m=0}^{N-1} \delta a_m(\vec{q}) e^{i\vec{k}_m^0 \vec{x}}. \quad (\text{A.9})$$

From (A.9), (A.6) and (A.5) we have

$$\begin{aligned} & \alpha(\nabla^{2n}, E_h(\vec{x})) \sum_{m=0}^{N-1} \delta a_m(\vec{q}) e^{i(\vec{k}_m^0 + \vec{q})\vec{x}} \\ & + \beta(\nabla^{2n}, E_h(\vec{x})) \sum_{m=0}^{N-1} \delta a_m^*(-\vec{q}) e^{-i(\vec{k}_m^0 + \vec{q})\vec{x}} = \lambda \sum_{m=0}^{N-1} \delta a_m(\vec{q}) e^{i(\vec{k}_m^0 + \vec{q})\vec{x}} \end{aligned} \quad (\text{A.10})$$

$$\begin{aligned} & \beta^*(\nabla^{2n}, E_h(\vec{x})) \sum_{m=0}^{N-1} \delta a_m(\vec{q}) e^{i(\vec{k}_m^0 + \vec{q})\vec{x}} \\ & + \alpha^*(\nabla^{2n}, E_h(\vec{x})) \sum_{m=0}^{N-1} \delta a_m^*(-\vec{q}) e^{-i(\vec{k}_m^0 + \vec{q})\vec{x}} = \lambda \sum_{m=0}^{N-1} \delta a_m^*(-\vec{q}) e^{-i(\vec{k}_m^0 + \vec{q})\vec{x}}. \end{aligned} \quad (\text{A.11})$$

For example, for the Kerr cavity one obtains

$$\begin{aligned}
 & - (1 + i(\theta + |\vec{k}_m^0 + \vec{q}|^2)) \sum_{m=0}^{N-1} \delta a_m(\vec{q}) e^{i(\vec{k}_m^0 + \vec{q})\vec{x}} \\
 & + i4 \sum_{l=0}^{N-1} \sum_{m=0}^{N-1} \sum_{n=0}^{N-1} a_l a_m^* \delta a_n(\vec{q}) e^{i(\vec{k}_l^0 - \vec{k}_m^0 + \vec{k}_n^0 + \vec{q})\vec{x}} \\
 & + i2 \sum_{l=0}^{N-1} \sum_{m=0}^{N-1} \sum_{n=0}^{N-1} a_l a_m \delta a_n^*(-\vec{q}) e^{i(\vec{k}_l^0 + \vec{k}_m^0 - \vec{k}_n^0 - \vec{q})\vec{x}} \\
 & = \lambda \sum_{m=0}^{N-1} \delta a_m(\vec{q}) e^{i(\vec{k}_m^0 + \vec{q})\vec{x}} \tag{A.12}
 \end{aligned}$$

$$\begin{aligned}
 & - i2 \sum_{l=0}^{N-1} \sum_{m=0}^{N-1} \sum_{n=0}^{N-1} a_l^* a_m^* \delta a_n(\vec{q}) e^{-i(\vec{k}_l^0 + \vec{k}_m^0 - \vec{k}_n^0 - \vec{q})\vec{x}} \\
 & - (1 - i(\theta + |\vec{k}_m^0 + \vec{q}|^2)) \sum_{m=0}^{N-1} \delta a_m^*(-\vec{q}) e^{-i(\vec{k}_m^0 + \vec{q})\vec{x}} \\
 & - i4 \sum_{l=0}^{N-1} \sum_{m=0}^{N-1} \sum_{n=0}^{N-1} a_l^* a_m \delta a_n^*(-\vec{q}) e^{-i(\vec{k}_l^0 - \vec{k}_m^0 + \vec{k}_n^0 + \vec{q})\vec{x}} \\
 & = \lambda \sum_{m=0}^{N-1} \delta a_m^*(-\vec{q}) e^{-i(\vec{k}_m^0 + \vec{q})\vec{x}}, \tag{A.13}
 \end{aligned}$$

and grouping the terms with the same exponential argument

$$\begin{aligned}
 & \left[-(1 + i\theta) - i|\vec{k}_n^0 \pm \vec{q}|^2 \right] \delta a_n(\pm\vec{q}) + i4 \left[\sum_{l=0}^{N-1} \sum_{m=0}^{N-1} a_l a_m^* \delta a_{n-l+m}(\pm\vec{q}) \right] \\
 & + i2 \left[\sum_{l=0}^{N-1} \sum_{m=0}^{N-1} a_l a_m \delta a_{-n+l+m}^*(\mp\vec{q}) \right] = \lambda \delta a_n(\vec{q}, t), \tag{A.14}
 \end{aligned}$$

where $\delta a_{n-l+m}(\pm\vec{q}) = \delta a_j(\pm\vec{q})$ with $\vec{k}_j^0 = \vec{k}_n^0 - \vec{k}_l^0 + \vec{k}_m^0$.

In general one obtains

$$M(a_m, \vec{q}) \vec{\Sigma}(\vec{q}, t) = \lambda(\vec{q}) \vec{\Sigma}(\vec{q}), \tag{A.15}$$

where $\vec{\Sigma}_n(\vec{q}) \equiv (\delta a_0(\vec{q}), \dots, \delta a_{N-1}(\vec{q}), \delta a_0^*(-\vec{q}), \dots, \delta a_{N-1}^*(-\vec{q}))^T$.

Bloch theorem basically tells us that perturbations can be written as a superposition of Bloch waves (A.6), and that each Bloch wave with different \vec{q} is independent of the others, except those with \vec{q} and $-\vec{q}$ due to the coupling between δE and δE^* in Eq. (A.2). If such a coupling is not present, as for example in real equations, $\vec{\Sigma}_n(\vec{q})$ contains only the coefficients with \vec{q} and not those with $-\vec{q}$.

The stability of $E_h(\vec{x})$ reduces, then, to finding the $2N$ eigenvalues $\lambda_n(\vec{q})$ of the matrix $M(a_m, \vec{q})$ for each value of the vector \vec{q} . The eigenvalues for a given \vec{q} determine the stability of the pattern against perturbations containing any set of wavevectors $\vec{k}_n^0 \pm \vec{q}$. To know the stability of the solution against any possible perturbation it is sufficient to consider only vectors \vec{q} inside the first Brillouin zone of the lattice defined by the wavevectors \vec{k}_n^0 of the pattern (Fig. 2.6). Any perturbation with a vector \vec{q}' outside the first Brillouin zone is equivalent to another with a vector $\vec{q} = \vec{q}' + \vec{k}_n^0$ inside. In solid state physics this representation is described as a *reduced zone scheme* [13]. Moreover only half of the first Brillouin zone has to be explored since vectors \vec{q} and $-\vec{q}$ are simultaneously contained in $\vec{\Sigma}(\vec{q})$. In fact, due to the symmetry of the pattern, only a fraction of the first Brillouin zone, for example 1/6 for a hexagonal pattern, has to be considered.

To illustrate the power of this method in front of the naive “brute-force” approach, let us consider that the pattern is contained in a 256×256 spatial grid, a size quite typical in our numerical simulations. The Jacobian matrix of such pattern has a size of $(256 \times 256) \times (256 \times 256) = 2^{32}$. If each element of the grid is a double-precision complex number, the storage of the full Jacobian requires 16×2^{32} byte = 64 Gbytes of memory, far beyond the RAM memory of any computer used in this thesis. Not to mention the time it would take to diagonalize a matrix of such size. Furthermore, only perturbations with wavevector \vec{q} included in the reciprocal lattice of the 256×256 pattern are considered, therefore $|\vec{q}_m \text{ in}| \sim 2\pi/L$, where L is the system size. If one wants to explore instabilities at smaller wavenumbers, it is required to increase the systems size, but the Jacobian matrix grows as L^4 . The problem with the brute-force approach is that attempts to solve the stability analysis for all \vec{q} simultaneously. With the approach considered here, each values of \vec{q} is solved separately, so that the matrices to diagonalize have a much smaller size: $2N \times 2N$, where $N = 91$ typically is more than enough for the patterns considered. Furthermore all \vec{q} perturbations are possible no matter how small $|\vec{q}|$ is, without any need to increase the computational complexity.

Appendix B

1d fronts between two equivalent homogeneous states

In this appendix we attempt to classify the 1d fronts between equivalent homogeneous states considering two independent properties of their profiles: the symmetries and the shape of the tails.

B.1 Front symmetries

We consider fronts in systems having translational ($\mathcal{T} : \vec{x} \rightarrow \vec{x} + \vec{x}'$) and parity ($\mathcal{P} : \vec{x} \rightarrow -\vec{x}$) invariance. We need also the system to have a discrete symmetry \mathcal{Z} that allows for the existence of two equivalent solutions \vec{A}_1 and \vec{A}_2 . These two solutions are transformed into each other on applying \mathcal{Z} ($\mathcal{Z}\vec{A}_1 = \vec{A}_2$ and $\mathcal{Z}\vec{A}_2 = \vec{A}_1$). Due to the parity invariance, for each front $\vec{A}(x)$ connecting from left to right \vec{A}_1 with \vec{A}_2 , the opposite one connecting \vec{A}_2 with \vec{A}_1 in the same direction also exist, and they are transformed into each other on applying \mathcal{Z} . This symmetry allows us to define the center x_0 of a front $\vec{A}(x)$ as the point where $\vec{A}(x_0) = \mathcal{Z}\vec{A}(x_0)$.

Considering all these symmetry properties, following [170], we can classify the fronts connecting the two equivalent homogeneous solutions depending on the result of applying the transformation $\mathcal{S} = \mathcal{Z}\mathcal{P}_0$, where the subscript $_0$ means that the reference frame for the spatial inversion is chosen at the center of the wall x_0 . Note that $\mathcal{S}\mathcal{S} = I$, with I the identity matrix. There is, then, two types of fronts (Fig. B.1):

- **Ising walls.** A front $\vec{A}(x)$ is called a Ising wall if it is invariant with respect to \mathcal{S} , i.e. $\mathcal{S}\vec{A}(x) = \vec{A}(x)$. We say, then, that an Ising wall is symmetric with respect to \mathcal{S} . Due to the symmetry, an Ising wall is always stationary.
- **Bloch walls.** In some systems, a transition from a symmetric (Ising) to two asymmetric fronts associated with a breaking of the \mathcal{S} invariance occurs. Then, a couple of new asymmetric fronts $\vec{A}_+(x)$ and $\vec{A}_-(x)$ appear as solutions connecting the two homogeneous states. The symmetry operator \mathcal{S} transform

the two fronts into each other ($\mathcal{S}\vec{A}_+(x) = \vec{A}_-(x)$). We call these fronts Bloch walls and the \mathcal{S} symmetry breaking bifurcation Ising-Bloch transition. The main feature of a Bloch wall is its asymmetry with respect to \mathcal{S} . The chirality is a measure of the departure of a Bloch wall from the invariance with respect to \mathcal{S} . A vectorial chiral order parameter $\vec{\chi}$ can be defined for a front $\vec{A}_+(x)$ as $\vec{\chi}(\vec{A}_+) = \vec{A}_+(x_0) - \vec{A}(x_0)$ where $\vec{A}(x)$ is the Ising front for the same values of the parameters. It is said that $\vec{A}_+(x)$ and $\vec{A}_-(x)$ are Bloch walls with opposite chirality since $\vec{\chi}(\vec{A}_+) = -\vec{\chi}(\vec{A}_-)$. In nonpotential systems, despite the fact of connecting equivalent states, Bloch walls usually move due to nonpotential effects. Bloch walls with opposite chirality move in opposite directions.

The definition of Ising and Bloch walls given above is a generalization of the common definition given in the literature [34], for which the order parameter vanishes at the core of a Ising wall, but not at the core of a Bloch wall.

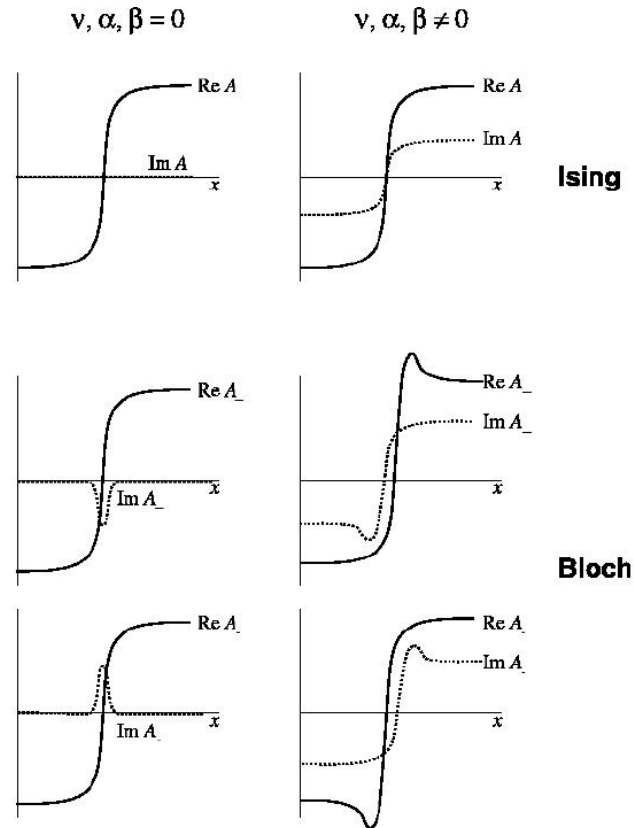


Figure B.1: Diagram of the Ising and Bloch fronts for the parametrically driven complex Ginzburg-Landau equation Eq. (6.1). For this equation $\mathcal{Z} : \vec{A} \rightarrow -\vec{A}$. Notice the breaking of the \mathcal{S} symmetry in the Bloch solution.

B.2 Front tails

It is convenient to distinguish between fronts that approach monotonically the asymptotic states and fronts whose profiles show damped oscillatory tails. The

shape of the tails plays an important role in the interaction between two walls. When the front has monotonic tails the interaction between two walls is attractive, however, when the profile shows spatial oscillations, it is known that the interaction can involve both attractive and repulsive forces [32].

The existence of oscillatory tails can be determined by means of a spatial linear stability analysis of the homogeneous asymptotic solutions. A non vanishing imaginary part of any of the resulting eigenvalues reveals the existence of oscillatory tails in the front profiles. The real part has to do with the damping rate of the oscillations. Let us see a couple of examples. The Ginzburg-Landau equation (GLE)

$$\partial_t \psi = \partial_{xx} \psi + \psi - \psi^3, \quad (\text{B.1})$$

gives the dynamical evolution of a system described by a nonconserved scalar order parameter. The stationary solutions satisfy

$$\partial_{xx} \psi + \psi - \psi^3 = 0. \quad (\text{B.2})$$

Let us call ψ_1 and ψ_2 the two homogeneous solutions of Eq. (B.2). Writing $\psi = \psi_i + \epsilon e^{\lambda x}$, we get, upon insertion into (B.2),

$$\lambda^2 = -1 + 3\psi_i^2, \quad i = 1, 2. \quad (\text{B.3})$$

Since the $\psi_i^2 = 1$ the eigenvalues λ given by (B.3) are real. Therefore, the fronts are monotonic such as the one of Fig. B.2 (a).

Let us consider now the Swift-Hohenberg equation (SHE)

$$\partial_t \psi = \psi - (\partial_{xx} + k_0^2)^2 \psi - \psi^3. \quad (\text{B.4})$$

This is the simplest model equation describing a Turing instability [238] in systems with a real order parameter $\psi(\vec{x}, t)$. First derived as an order parameter equation for Rayleigh-Benard convection [223], it finds also application for the description of various pattern forming systems including nonlinear optical systems such as the nascent bistability [162], or degenerate optical parametric oscillators and degenerate four wave mixing [43]. The stationary solutions satisfy

$$-\partial_{xxxx} \psi - 2k_0^2 \partial_{xx} \psi + (1 - k_0^4) \psi - \psi^3 = 0, \quad (\text{B.5})$$

The same analysis as before yields to the following four order polynomial for the eigenvalues

$$\lambda^4 + 2k_0^2 \lambda^2 + 2(1 - k_0^4) = 0. \quad (\text{B.6})$$

For $k_0^2 < \sqrt{2/3}$ there are four complex spatial eigenvalues, so that the fronts have oscillatory tails such as the one of Fig. B.2 (b).

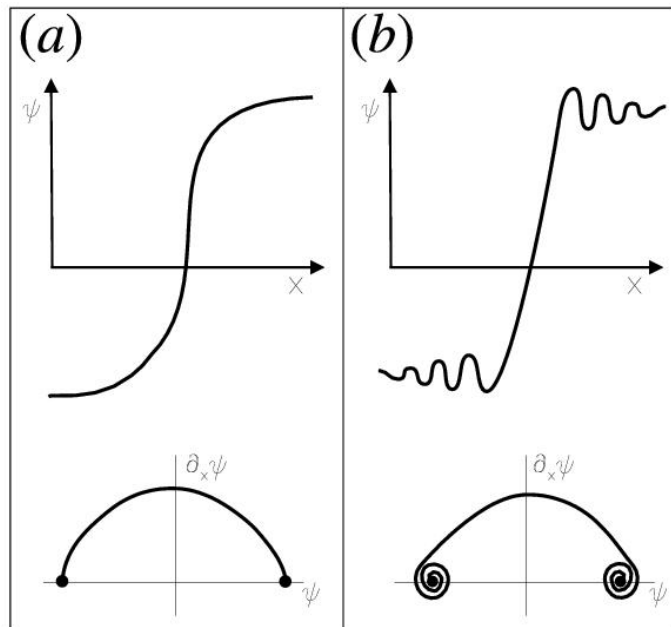


Figure B.2: Profile of a front connecting to equivalent homogeneous states and its corresponding heteroclinic orbit in phase space for the case of a monotonic front (a) and a front showing spatial oscillations (b).

Appendix C

Moving reference frame

To track the motion of a front it is useful to make a change of coordinates to an orthogonal coordinate system (u, s) that moves with the front itself [69, 240]. In the vicinity of the interface, the change of coordinates is defined by (see Fig. C.1):

$$\mathbf{r}(u, s, t) = \mathbf{R}(s, t) + u \hat{\mathbf{n}}(s, t), \quad (\text{C.1})$$

where $\mathbf{r}(u, s, t)$ is the position vector in the laboratory reference frame and $\mathbf{R}(s, t) = (X(s, t), Y(s, t))$ is the position vector of the line front in the laboratory reference frame. The coordinate s is the arclength of the line front while u is the normal coordinate to the front. The vector $\hat{\mathbf{n}}(s, t) = Y_s \hat{\mathbf{x}} - X_s \hat{\mathbf{y}}$ is the unit normal vector to the curve, being $\hat{\mathbf{x}}$ and $\hat{\mathbf{y}}$ normal unitary vectors along the x and y axis. The subscripts indicate partial derivatives. The Jacobian matrix of the transformation

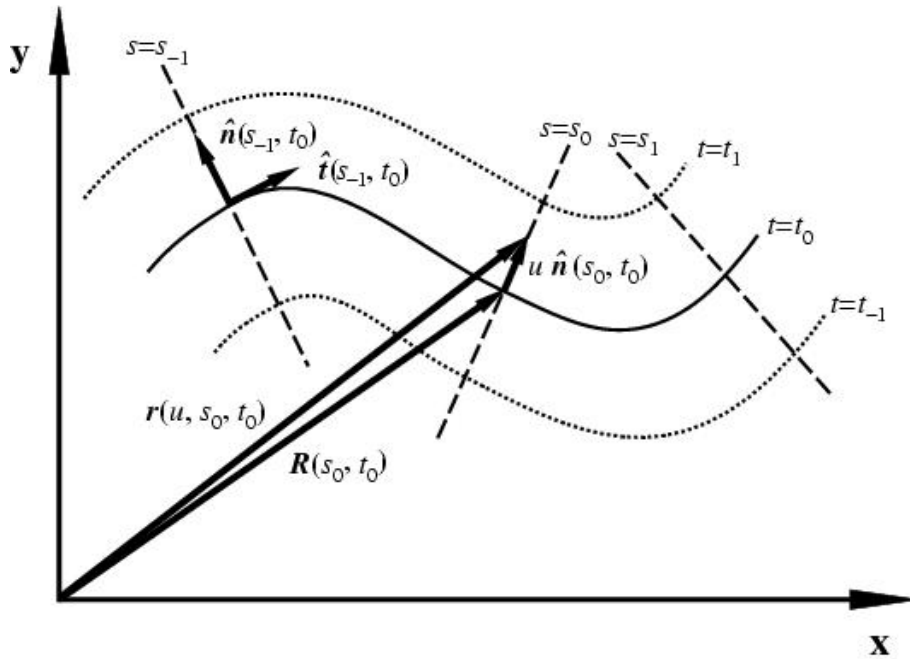


Figure C.1: Schematic of the change of coordinates defined by Eq. (C.1).

is given by:

$$M(u, s, t) \equiv \frac{\partial \mathbf{r}(u, s, t)}{\partial(u, s)} = \begin{pmatrix} Y_s & X_s + uY_{ss} \\ -X_s & Y_s - uX_{ss} \end{pmatrix}. \quad (\text{C.2})$$

The matrix of the metric defined by the change of coordinates is now easily obtained:

$$G(u, s, t) \equiv M^\dagger M = \begin{pmatrix} 1 & 0 \\ 0 & (1 + u\kappa)^2 \end{pmatrix}. \quad (\text{C.3})$$

Here $\kappa(s, t)$ is the local curvature of the front line and we have used the identities:

$$\kappa(s, t) = X_s Y_{ss} - Y_s X_{ss} = \sqrt{X_{ss}^2 + Y_{ss}^2}, \quad (\text{C.4})$$

$$X_s^2 + Y_s^2 = 1. \quad (\text{C.5})$$

The Laplacian and the temporal derivative are transformed according to the relations:

$$\nabla_{u,s}^2 = \frac{1}{G_{11}G_{22}} \left[\frac{\partial}{\partial u} \left(\sqrt{\frac{G_{22}}{G_{11}}} \frac{\partial}{\partial u} \right) + \frac{\partial}{\partial s} \left(\sqrt{\frac{G_{11}}{G_{22}}} \frac{\partial}{\partial s} \right) \right] \quad (\text{C.6})$$

$$= \frac{\kappa}{1 + u\kappa} \frac{\partial}{\partial u} + \frac{\partial^2}{\partial u^2} - \frac{u\kappa_s}{(1 + u\kappa)^3} \frac{\partial}{\partial s} + \frac{1}{(1 + u\kappa)^2} \frac{\partial^2}{\partial s^2}, \quad (\text{C.7})$$

$$\frac{\partial}{\partial t} = -v_n \frac{\partial}{\partial u} - \frac{1}{1 + u\kappa} \mathbf{r}_t \cdot \hat{\mathbf{t}} \frac{\partial}{\partial s} + \frac{\partial}{\partial t'}, \quad (\text{C.8})$$

where $v_n = -\mathbf{r}_t \cdot \hat{\mathbf{n}}$ is the normal velocity, $\hat{\mathbf{t}} = X_s \hat{\mathbf{x}} + Y_s \hat{\mathbf{y}}$ is a unit vector tangent to the front line and t' is the time in the moving reference frame, which is taken equal to the time t in the laboratory reference frame. Usually one assumes that the front tangent velocity term can be neglected.

Bibliography

- [1] M.J. Ablowitz, D.J. Kaup, A.C. Newell, H. Segur, Phys. Rev. Lett. **31**, 125 (1973).
- [2] T. Ackemann, T. Scholz, Ch. Vorgerd, J. Nalik, L.M. Hoffer and G.L. Lippi, Opt. Commun. **147**, 411 (1998).
- [3] T. Ackemann, S. Barland, M. Giudici, J. Tredicce, S. Balle, R. Jaeger, M. Grabherr, M. Miller, and K.J. Ebeling, Phys. Stat. Sol. B **221**, 133 (2000).
- [4] T. Ackemann and W. Lange, Appl. Phys. B **72**, 21 (2001).
- [5] T. Ackemann, A. Aumann, E. Grosse Westhoff, Y.A. Logvin and W. Lange, J. Opt. B: Quantum Semiclass. Opt. **3**, S124 (2001).
- [6] T. Ackemann, E. Grosse Westhoff, M. Pesch, D. Rudolph, and W. Lange, Proc. SPIE. **4751**, 370 (2002).
- [7] M. Aguado, R.F. Rodriguez, and M.San Miguel, Phys. Rev. A **39**, 5686 (1989).
- [8] J.S. Aitchison, A.M. Weiner, Y. Silberberg, M.K. Oliver, J.L. Jackel, D.E. Leaird, E.M. Vogel and P.W.E. Smith, Opt. Lett. **15**, 471 (1990).
- [9] N.N. Akhmediev and A. Ankiwicz , “Solitons: Nonlinear Pulses and Beams” (Chapman and Hall, London, 1997).
- [10] S.M. Allen and J.W. Cahn, Acta Metall. **27**, 1085 (1979).
- [11] R.E. Amritkar and P.M. Gade, Phys. Rev. Lett. **70**, 3408 (1993).
- [12] F.T. Arecchi, S. Boccaletti and P.L. Ramazza, Phys. Rep. **318**, 1-83 (1999).
- [13] N.W. Ashcroft and N.D. Mermin, *Solid State Physics* (Holt, Rinehart and Winston, New York; London, 1976).
- [14] A. Aumann, E. Büthe, Y.A. Logvin, T. Ackemann and W. Lange, Phys. Rev. A **56**, R1709 (1997).
- [15] A. Aumann, E. Grosse Westhoff, R. Herrero, T. Ackemann and W. Lange, J. Opt. B: Quantum Semiclass. Opt. **1**, 166 (1999).

-
- [16] S. Barland, J. R. Tredicce, M. Brambilla, L.A. Lugiato, S. Balle, M. Giudici, T. Maggipinto, L. Spinelli, G. Tissoni, T. Knödl, M. Miller & R. Jäger, *Nature* **419**, 699 (2002).
- [17] A. Barthelemy, S. Maneuf and C. Froehly, *Opt. Commun.* **55**, 201 (1985).
- [18] P. Berge, Y. Pomeau and C. Vidal, *Order within Chaos* (John Wiley & Sons, New York, 1984).
- [19] M. Bestehorn, *Phys. Rev. E* **48**, 3622 (1993).
- [20] R.S. Bennink, V. Wong, A.M. Marino, D.L. Aronstein, R.W. Boyd, C.R. Stroud, Jr., and S. Lukishova, *Phys. Rev. Lett.* **88**, 113901 (2002).
- [21] R.W. Boyd, *Nonlinear optics* (Academic Press, Boston, 1992).
- [22] M. Brambilla, L. A. Lugiato, F. Prati, L. Spinelli and W. J. Firth, "Spatial Soliton Pixels in Semiconductor Devices", *Phys. Rev. Lett.* **79**, 2042-2045 (1997).
- [23] F.H. Busse, *Rep. Prog. Phys.* **41**, 1929 (1978).
- [24] D. Cai, D.W. McLaughlin, and K. T.-R. McLaughlin, *Handbook of Dynamical Systems* **2**, 599 (2002).
- [25] S.-K. Chan, *J. Chem. Phys.* **67**, 5755 (1977).
- [26] J.H.E. Cartwright, E. Hernández-García and O. Piro, *Phys. Rev. Lett.* **79**, 527 (1997).
- [27] F. Castelli and L.A. Lugiato, *J. Mod. Opt.* **44**, 765 (1997).
- [28] S.-K. Chan, *J. Chem. Phys.* **67**, 5755 (1977).
- [29] R. Chang, W.J. Firth, R. Indik, J.V. Moloney and E.M. Wright, *Opt. Commun.* **88** 167 (1992).
- [30] S. Chi, Q. Guo, *Opt. Lett.* **20**, 1598 (1995).
- [31] S. Ciliberto, E. Pampaloni, and C. Pérez-García, *Phys. Rev. Lett.* **61**, 1198 (1988).
- [32] P. Coulet, C. Elphick, and D. Repaux, *Phys. Rev. Lett.* **58**, 431 (1987).
- [33] P. Coulet, and G. Iooss, *Phys. Rev. Lett.* **64**, 8 (1990).
- [34] P. Coulet, J. Lega, B. Houchmanzadeh and J. Lajzerowicz, *Phys. Rev. Lett.* **65**, 1352 (1990).
- [35] P. Coulet and K. Emilsson, *Physica D*, **61**, 119 (1992).
- [36] P. Coulet, C. Riera and C. Tresser, *Phys. Rev. Lett.* **84**, 3069 (2000).

- [37] P. Couillet, *Int. J. Bif. Chaos* **12**, 2445 (2002).
- [38] J.Y. Courtois and G. Grynberg, *Opt. Commun.* **87**, 186 (1992).
- [39] M.C. Cross and P.C. Hohenberg, *Rev. Mod. Phys.* **65**, 851 (1993).
- [40] M.C. Cross and D.I. Meiron, *Phys. Rev. Lett.* **75**, 2152 (1995).
- [41] G. D'Alessandro and W.J. Firth, *Phys. Rev. Lett.* **66**, 2597 (1991).
- [42] G. D'Alessandro and W.J. Firth, *Phys. Rev. A* **46**, 537 (1992).
- [43] G.J. de Valcárcel, K. Staliunas, E. Roldán and V.J. Sánchez-Morcillo, *Phys. Rev. A* **54**, 1609 (1996).
- [44] O. Descalzi and R. Graham, *Phys. Lett. A* **170**, 84 (1992).
- [45] O. Descalzi and R. Graham, *Z. Phys. B* **93**, 509 (1994).
- [46] B. Dionne and M. Golubitsky, *Z. angew. Math. Phys.* **43**, 36 (1992).
- [47] B. Dionne, M. Silber, and A.C. Skeldon, *Nonlinearity* **10**, 321 (1997).
- [48] P.D. Drummond, K.J. McNeil, and D.F. Walls, *Opt. Acta* **27**, 321 (1980).
- [49] S. Dyachenko, A.C. Newell, A. Pushkarev, V.E. Zakharov, *Physica D* **57**, 96 (1992).
- [50] B. Echebarria and C. Pérez-García, *Europhys. Lett.* **43**, 35 (1998).
- [51] C. Etrich, U. Peschel, and F. Lederer, *Phys. Rev. E* **56**, 4803 (1997).
- [52] C. Etrich, U. Peschel and F. Lederer, *Phys. Rev. Lett.* **79**, 2454 (1997).
- [53] S. Fauve and O. Thual, *J. Phys. France* **49**, 1829 (1988).
- [54] W.J. Firth and C. Parè, *Opt. Lett.* **13**, 1096 (1988).
- [55] W.J. Firth, *J. Mod. Opt.* **37**, 151 (1990).
- [56] W.J. Firth, A.J. Scroggie, G.S. McDonald and L.A. Lugiato, *Phys. Rev. A* **46**, R3609 (1992).
- [57] W.J. Firth and A.J. Scroggie, *Europhys. Lett.* **26**, 521 (1994).
- [58] W.J. Firth and A. Lord, *Journal of Mod. Opt.* **43**, 1071 (1996).
- [59] W. J. Firth, A. Lord, & A. J. Scroggie, *Phys. Scripta*, **T67**, 12 (1996).
- [60] W.J. Firth and A.J. Scroggie, *Phys. Rev. Lett.* **76** 1623, (1996).
- [61] W.J. Firth and G.K. Harkness, *Asian J. Phys.* **7**, 665 (1998).

- [62] W.J. Firth and G.K. Harkness, A. Lord, J. McSloy, D. Gomila and P. Colet, J. Opt. Soc. Am. B **19**, 747 (2002).
- [63] W.J. Firth and C.O. Weis, Opt. Photon. News **13**, 55 (2002).
- [64] D. Foster, *Hydrodynamic Fluctuations, Broken Symmetry and Correlation Fluctuations* (Addison Wesley, Redwood City, CA, 1983).
- [65] R.A. Fuerst, D.-M. Baboiu, B. Lawrence, W.E. Torruellas, G.I. Stegeman, S. Trillo, and S. Wabnitz, Phys. Rev. Lett. **78**, 2756 (1997).
- [66] A. Gahl, T. Ackemann, W. Grosse-Nobis, G.L. Lippi, L.M. Hoffer, M. Moller and W. Lange, Phys. Rev. A **57**, 4026 (1998).
- [67] R. Gallego, M. San Miguel and R. Toral, Phys. Rev. E **58**, 3125 (1998).
- [68] R. Gallego, M. San Miguel and R. Toral, Phys. Rev. E **61**, 2241 (2000).
- [69] R. Gallego, Ph.D. Thesis (2000).
- [70] C.W. Gardiner, *Handbook of Stochastic Methods* (Springer-Verlag, Berlin Heidelberg 1983 and 1985).
- [71] A. Gatti and L.A. Lugiato, P, Phys. Rev. A **52**, 1675 (1995).
- [72] A. Gatti, H. Wiedemann, L.A. Lugiato, I. Marzoli, G.-L. Oppo and S.M. Barnett, Phys. Rev. A **56**, 877 (1997).
- [73] A. Gatti, L.A. Lugiato, G.-L. Oppo, R. Martin, P. Di Trapani and A. Berzanskis, Opt. Expr. **1**, 21 (1997).
- [74] A. Gatti and S. Mancini, Phys. Rev. A, **65**, 013816 (2001).
- [75] J.B. Geddes, J.V. Moloney, E.M. Wright and W.J. Firth, Opt. Commun. **111**, 623 (1994).
- [76] J.B. Geddes, R.A. Indik, J.V. Moloney and W.J. Firth, Phys. Rev. A **50**, 3471 (1994).
- [77] H.M. Gibbs, P. Mandel, N. Peyghambarian, S.D. Smith (Eds.), *Optical Bistability III*, Springer, Berlin (1986).
- [78] L. Gil, Physica D **147**, 300 (2000).
- [79] G. Giusfredi, J.F. Valley, r. Pon, G. Khitrova and H.M. Gibbs, J. Opt. Soc. Am. B **5**, 1181 (1998).
- [80] L.Y. Glebsky and L.M. Lerman, Chaos **5**, 424 (1995).
- [81] P. Glendinning, *Stability, instability and chaos* (Cambridge University Press, 1994).

-
- [82] M.V. Goldman, K. Rypdal, and B. Hafzi, *Phys. Fluids* **23**, 945 (1980).
- [83] R.E. Goldstein, D.J. Muraki and D.M. Petrich, *Phys. Rev. E* **53**, 3933 (1996).
- [84] J.P. Gollub and J.S. Langer, *Rev. Mod. Phys.* **71**, S396 (1999).
- [85] D. Gomila, P. Colet, G.-L. Oppo and M. San Miguel, *Phys. Rev. Lett.* **87**, 194101 (2001).
- [86] D. Gomila and P. Colet, *Phys. Rev. E* **66**, 046223 (2002).
- [87] D. Gomila, P. Colet, M. San Miguel, A.J. Scroggie and G.-L. Oppo, *IEEE J. Quantum Electron.* **39**, 238 (2003).
- [88] D. Gomila and P. Colet, submitted (2003).
- [89] K.A. Gorshkov, L.N. Korzinov, M.I. Rabinovich, and L.S. Tsimring, *J. Stat. Phys.* **74**, 1033 (1994).
- [90] R. Graham and T. Tél, *Phys. Rev. A* **42**, 4661 (1990).
- [91] R. Graham in *Instabilities and Nonequilibrium Structures III*, E. Tirapegui and W. Zeller, eds. Reidel, Dordrecht (1991).
- [92] R. Graham in *Instabilities and Nonequilibrium Structures*, E. Tirapegui and D. Villarroel, eds. Reidel, Dordrecht (1993).
- [93] R. Graham in *25 years of Nonequilibrium Statistical Mechanics*, J. Brey, J. Marro, J.M. Rubi and M. San Miguel, eds. Springer Verlag (1995).
- [94] E. Große Westhoff, R. Herrero, T. Ackemann, and W. Lange, unpublished (2002).
- [95] E. Große Westhoff, Phd thesis, Westfälische Wilhelms-Universität Münster (2002).
- [96] G. Grynberg, E. Le Bihan, P. Verkerk, P. Simoneau, J.R.R. Leite, D. Bloch, S. Le Boiteux and M. Ducloy, *Opt. Commun.* **67**, 363 (1988).
- [97] G. Grynberg and L.A. Lugiato, *Opt. Commun.* **101**, 69 (1993).
- [98] J. Guckenheimer and P. Holmes, *Nonlinear Oscillations, Dynamical Systems and Bifurcations of Vector Fields*, Springer-Verlag (1983).
- [99] J.D. Gunton, M. San Miguel and P. Sahni in *Phase Transitions and Critical Phenomena*, edited by C. Domb and J.L. Lebowitz (Academic Press, Ney York, 1983), Vol. **8**, p. 269.
- [100] M. Haelterman and A.P. Sheppard, *Chaos Solitons and Fractals* **4**, 1731 (1994).

-
- [101] H. Haken, *Synergetics: an introduction to nonequilibrium phase transitions and self-organization in physics, chemistry and biology* (Springer, Berlin, 1983).
- [102] G. Harkness, G.-L. Oppo, R. Martin, A.J. Scroggie, and W.J. Firth, Phys. Rev. A **58**, 2577 (1998).
- [103] G. Harkness, W.J. Firth, G.-L. Oppo, and J.M. McSloy, Phys. Rev. E **66**, 046605 (2002).
- [104] K. He, Phys. Rev. Lett. **84**, 3290 (2000).
- [105] E. Hernández-García, J. Viñals, R. Toral and M. San Miguel, Phys. Rev. Lett. **70**, 3576 (1993).
- [106] R. Herrero, E. Grosse Westhoff, A. Aumann, T. Ackemann, Yu.A. Logvin, and W. Lange, Phys. Rev. Lett. **82**, 4627 (1999).
- [107] R. Horak, J. Bajer, M. Bertolotti, and C. Sibilía, Phys. Rev. E **52**, 4421 (1995).
- [108] M. Hoyuelos, P. Colet, M. San Miguel. Phys. Rev. E **58**, 74 (1997).
- [109] M. Hoyuelos, P. Colet, M. San Miguel, and D. Walgraef, Phys. Rev. E, **58**, 2292 (1998).
- [110] M. Hoyuelos, A. Sinatra, P. Colet, L. Lugiato, and M. San Miguel. Phys. Rev. A **59**, 1622 (1998).
- [111] M.D. Iturbe Castillo, J.J.Sanchez-Mondragon, S.I. Stepanov, M.B. Klein and B.A. Wechsler, Opt. Commun. **118**, 515 (1995).
- [112] P.K. Jacobsen, R.A. indik, J.V. Moloney, A.C. Newell, H.G. Winful and L. Raman, J. Opt. Soc. Am. B **8**, 1674 (1991).
- [113] C. Josserand and S. Rica, Phys. Rev. Lett. **69**, 1215 (1997).
- [114] S.L. Judd and M. Silber, Physica D **136**, 45 (2000).
- [115] A. Kastler, J. Opt. Soc. Am. **47**, 460 (1957).
- [116] D.J. Kaup, A.C. Newell, Proc. R. Soc. London A **361**, 413 (1978).
- [117] K. Kawasaki and T. Ohta, Physica A **116**, 573 (1982).
- [118] Y.S. Kivshar and X. Yang, Chaos Solitons and Fractals **4**, 174 (1994)
- [119] Y.S. Kivshar, B. Luther-Davies, Phys. Rep. **298**, 81 (1998).
- [120] L. Kramer, Z. Phys. B **41**, 357 (1981); *Ibíd.* **45**, 167 (1981).
- [121] A. Kudrolli, B. Pier, and J.P. Gollub, Physica D **123**, 99 (1998).

-
- [122] Y.A. Kuznetsov, *Elements of Applied Bifurcation Theory* (Springer-Verlag New York, 1995).
- [123] E.A. Kusnetsov, A.M. Rebenchik, V.E. Zakharov, Phys. Rep. **142**, 103 (1986).
- [124] P. La Penna, G. Giusfredi, Phys. Rev. A **48**, 2299 (1993).
- [125] A.M. Lacasta, A. Hernández-Machado, J.M. Sancho and R. Toral, Phys. Rev. B **45**, 5276 (1992).
- [126] W. Lange, F. Mitschke, R. Deserno and J. Mlynek, Philos. Trans. R. Soc. London, Ser. A **313**, 421 (1984).
- [127] W. Lange, Y.A. Logvin and T. Ackemann, Physica D **96**, 230 (1996).
- [128] W. Lange and T. Ackemann, Asian J. Phys. **7**, 439 (1998).
- [129] W. Lange, T. Ackemann, A. Aumann, E. Bütthe and Y.A. Logvin, Chaos Solitons & Fractals **10**, 617 (1999).
- [130] J. Langer, Rev. Mod. Phys. **52**, 1 (1980).
- [131] J. Lauzeral, D. Metens, and D. Walgraef, Europhys. Lett. **24**, 707 (1993).
- [132] C.T. Law and G.A. Swartzlander Jr., Chaos Solitons and Fractals **4**, 1759 (1994).
- [133] M. Le Berre, A.S. Patrascu, E. Ressayre, and A. Tallet, Phys. Rev. A **56**, 3150 (1997).
- [134] M. Le Berre, E. Ressayre and A. Tallet, J. Opt. B **1**, 107 (1999).
- [135] M. Le Berre, D. Leduc, E. Ressayre and A. Tallet, J. Opt. B **1**, 153 (1999).
- [136] M. Le Berre, E. Ressayre, and A. Tallet, J. Opt. B **2**, 347 (2000).
- [137] I. Lifshitz and V.V. Slyozov, J. Phys. Chem. Solids **19**, 35 (1961).
- [138] I.M. Lifshitz Sov. Phys. JETP **15**, 939 (1962).
- [139] G.L. Lippi, T. Ackemann, L.M. Hoffer, A. Gahl and W. Lange, Phys. Rev. A **48**, R4043 (1993).
- [140] G.L. Lippi, T. Ackemann, L.M. Hoffer and W. Lange, Chaos Solitons and Fractals **4**, 1409 (1994).
- [141] G.L. Lippi, T. Ackemann, L.M. Hoffer and W. Lange, Chaos Solitons and Fractals **4**, 1433 (1994)
- [142] P. Lodahl and M. Saffman, Phys. Rev. A **60**, 3251 (1999).

- [143] P. Lodahl and M. Saffman, *Opt. Commun.* **27**, 110 (2002).
- [144] S. Longhi, *J. Mod. Opt.* **43** 1089 (1996); *ibid.* **43** 1569 (1996).
- [145] S. Longhi, *Phys. Rev. A* **53**, 4488 (1996).
- [146] S. Longhi and A. Geraci, *Phys. Rev. A* **54**, 4581 (1996).
- [147] S. Longhi, *Phys. Scripta* **56**, 611 (1997).
- [148] S. Longhi, *Opt. Commun.* **149**, 335 (1998).
- [149] S. Longhi, G.-L. Oppo and W.J. Firth, unpublished.
- [150] L.A. Lugiato and R. Lefever, *Phys. Rev. Lett.* **58**, 2209 (1987).
- [151] L.A. Lugiato and C. Oldano, *Phys. Rev. A* **37**, 3896 (1988).
- [152] L.A. Lugiato and F. Castelli, *Phys. Rev. Lett.* **68**, 3284 (1992).
- [153] L. A. Lugiato (editor), Special issue on “Nonlinear Optical Structures, Patterns, Chaos”, *Chaos, Solitons & Fractals*, **4**, Numbers 8/9 (1994).
- [154] L.A. Lugiato, W. Kaige, N.B. Abraham, *Phys. Rev. A* **49**, 2049 (1994).
- [155] L.A. Lugiato and G. Grynberg, *Europhys. Lett.* **29**, 675 (1995).
- [156] L.A. Lugiato and I. Marzoli, *Phys. Rev. A* **52**, 4886 (1995).
- [157] L. A. Lugiato, M. Brambilla, and A. Gatti, *Adv. Atom. Mol. Opt. Phys.* **40**, 229 (1999).
- [158] S.K. Ma, *Statistical Mechanics* (World Scientific, Singapore, 1985).
- [159] T. Maggipinto, M. Brambilla, G.K. Harkness and W.J.Firth, *Phys. Rev. E* **62**, 8726 (2000).
- [160] A.V. Mamaev and M. Saffman, *Phys. Rev. Lett.* **80**, 3499 (1998).
- [161] P. Mandel and T. Erneux, *Opt. Commun.* **44**, 5 (1982).
- [162] P. Mandel, M. Georgiou and T. Erneux, *Phys. Rev. A* **47**, 4277 (1993)
- [163] S. Maneuf, R. Desailly and C. Froehly, *Opt. Commun.* **65**, 193 (1988).
- [164] S. Maneuf and F. Reynaud, *Opt. Commun.* **66**, 325 (1988).
- [165] P. Manneville, *Dissipative Structures and Weak Turbulence* (Academic Press, Inc. 1990).
- [166] G. S. McDonald and W. J. Firth, *J Opt Soc Am B*, **7**, 1328 (1990).

- [167] J.M. McSloy, W.J. Firth, G.K. Harkness, and G.-L. Oppo, Phys. Rev. E **66**, 046606 (2002).
- [168] E. Meron, Phys. Rep. **218**, 1 (1992).
- [169] D. Michaelis, U. Peschel, and F. Lederer, Opt. Lett. **23**, 1814 (1998).
- [170] D. Michaelis, U. Peschel, F. Lederer, D.V. Skryabin, and W.J. Firth, Phys. Rev. E **63**, 066602 (2001).
- [171] F. Mitschke, R. Deserno, W. Lange, and J. Mlynek, Phys. Rev. A **33**, 3219 (1986).
- [172] R. Montagne, E. Hernández-García, and M. San Miguel, Physica D **96**, 47 (1996).
- [173] J. Nalik, L.M. Hoffer, G.L. Lippi, Ch. Vorgerd, W. Lange, Phys. Rev. A **45**, R4237 (1992).
- [174] A.C. Newell, "Solitons in Mathematics & Physics", SIAM, Philadelphia, 1987.
- [175] A.C. Newell, D.A. Rand and D. Russell, Physics Lett. A **132**, 112 (1988).
- [176] A.C. Newell and J. Moloney, *Nonlinear optics* (Addison-Wesley, Redwood City, 1992).
- [177] G.-L. Oppo, M. Brambilla, D. Camesasca, A. Gatti, and L.A. Lugiato, J. Mod. Opt. **41**, 1151 (1994).
- [178] G.-L. Oppo, M. Brambilla and L.A. Lugiato, Phys. Rev. A **49**, 2028 (1994).
- [179] G.-L. Oppo, A.J. Scroggie and W. Firth, J. Opt. B **1**, 133 (1999).
- [180] G.-L. Oppo, A.J. Scroggie, S. Sinclair, and M. Brambilla, J. Mod. Opt. **47**, 2005 (2000).
- [181] G.-L. Oppo, A.J. Scroggie and W. Firth, Phys. Rev. E **63**, 066209 (2001).
- [182] K. Otsuka, Phys. Rev. Lett. **65**, 329 (1990).
- [183] E. Ott, *Chaos in dynamical systems* (Cambridge University Press 1993).
- [184] K. Ouchi and H. Fujisaka, Phys. Rev. E **54**, 3895 (1996).
- [185] E. Pampaloni, S. Soria, and F.T. Arecchi, Phys. Rev. Lett. **78**, 1042 (1997).
- [186] J. Pender and L. Hesselink, J. Opt. Soc. Am. B **7**, 1361 (1990).
- [187] U. Peschel, D. Michaelis, C. Etrich, and F. Lederer, Phys. Rev. E **58**, R2745 (1998).

-
- [188] A. Petrossian, M. Pinard, A. Maitre, J.-Y. Courtois, and G. Grynberg, *Europhys. Lett* **18**, 689 (1992).
- [189] V. Petrov, Q. Ouyang and H.L. Swinney, *Nature* **388**, 655 (1997).
- [190] H.-J. Pi, S. Park, J. Lee, and K. Lee, *Phys. Rev. Lett.* **84**, 5316 (2000).
- [191] C. Pirat and L. Gil, unpublished (2003).
- [192] Y. Pomeau, *Physica (Amsterdam)* **23D**, 3 (1986).
- [193] P.L. Ramazza, S. Ducci, S. Boccaletti and F.T. Arecchi, *J. Opt. B* **2**, 399 (2000).
- [194] J.J. Rasmussen, K. Rypdal, *Phys. Scr.* **33**, 481 (1986).
- [195] S. Residori, A. Petrossian, and L. Gil, *Phys. Rev. Lett.* **88**, 233901 (2002).
- [196] F. Reynaud and A. Barthelemy, *Europhys. Lett.* **12**, 401 (1990).
- [197] P.A. Robinson, *Rev. Mod. Phys.* **69**, 507 (1997).
- [198] J.L. Rogers, M.F. Schatz, O. Brausch, and W. Pesch, *Phys. Rev. Lett.* **85**, 4281 (2000).
- [199] N.N. Rosanov, *Proc. SPIE* **1840**, 130 (1991).
- [200] N.N. Rosanov, V.A. Smirnov and N.V. Vyssotina, *Chaos Solitons and Fractals* **4**, 1767 (1994).
- [201] N.N. Rosanov in *Progress in Optics*, vol. 35 (Elsevier, Amsterdam, 1996).
- [202] K. Rypdal, and J.J. Rasmussen, *Phys. Scr.* **33**, 498 (1986).
- [203] M. San Miguel in *Growth Patterns in Physical Sciences and Biology*, Ed. J.M. García-Ruíz et. al. (Plenum Press, New York, 1993).
- [204] M. San Miguel and R. Toral, in *Stochastic Effects in Physical Systems, Instabilities and Nonequilibrium Structures VI*, Ed. E. Tirapegui and W. Zeller, Kluwer Academic, 1999.
- [205] San Miguel and R. Toral, in *Instabilities and Nonlinear Equilibrium Structures*, ed. by E. Tirapegui, J. Martinez and R. Tiemann, (Kluwer, 2000).
- [206] V.J. Sánchez-Morcillo and G.J. de Valcárcel, *Quantum Semiclass. Opt.* **8**, 919 (1996).
- [207] V.J. Sánchez-Morcillo, I. Pérez-Arjona, F. Silva, G.J. de Valcárcel, and E. Roldán, *Optics Lett.* **25**, 957 (2000).
- [208] J. Satsuma, N. Yajima, *Suppl. of Progr. Theor. Phys.* **55**, 284 (1974).

- [209] B. Schäpers, M. Feldmann, T. Ackemann and W. Lange, Phys. Rev. Lett. **85**, 748-751 (2000); B. Schäpers, T. Ackemann and W. Lange, Proc. SPIE, 4271, 130 (2001).
- [210] A. Schreiber, B. Thüering, M. Kreuzer and T. Tschudi, Optics Commun. **136**, 415 (1997).
- [211] A.J. Scroggie, W.J. Firth, G.S. McDonald, M. Tlidi, R. Lefever and L.A. Lugiato, Chaos, Solitons & Fractals **4**, 1323 (1994).
- [212] D. V. Skryabin, "Energy of the soliton internal modes and broken symmetries in nonlinear optics", J. Opt. Soc. Am. B **19**, 529 (2002).
- [213] M. Silber and M.R.E. Proctor, Phys. Rev. Lett. **81**, 2450 (1998).
- [214] R. Smoluchowski, Phys. Rev. **83**, 69 (1951)
- [215] J.M. Soto-Crespo, N.N. Akhmediev, Opt. Commun. **101** 223 (1993).
- [216] K. Staliunas, J. Mod. Opt. **42**, 1261 (1995).
- [217] K. Staliunas and V. J. Sánchez-Morcillo, Opt. Commun. **139**, 306 (1997).
- [218] K. Staliunas and V.J. Sánchez-Morcillo, Phys. Rev. A, **57**, 1454-1457 (1998).
- [219] K. Staliunas and V.J. Sánchez-Morcillo, Phys. Lett. A **241**, 28 (1998); V.J. Sánchez-Morcillo and K. Staliunas Phys. Rev. E **60**, 6153 (1999).
- [220] S.H. Strogatz, *Nonlinear Dynamics and Chaos* (Perseus Books Publishing, 1994).
- [221] C. Sulem and P.-L. Sulem, *The nonlinear Schrödinger equation: self-focusing and wave collapse* (Springer-Verlag, New York, 1999).
- [222] M.M. Sushchik and L.S. Tsimring, Physica D **74**, 90 (1994).
- [223] J. Swift and P.C. Hohenberg, Phys. Rev. A **15**, 319 (1977).
- [224] V.B. Taranenko, K. Staliunas, and C.O. Weiss, Phys. Rev. Lett. **81**, 2236 (1998).
- [225] V. B. Taranenko, I. Ganne, R. J. Kuszelewicz and C. O. Weiss, Phys. Rev. A **61**, 063818 (2000).
- [226] M. Tlidi, M. Georgiou and P. Mandel, Phys. Rev. A **48**, 4605 (1993).
- [227] M. Tlidi, P. Mandel, and R. Lefever, Phys. Rev. Lett. **73**, 640 (1994).
- [228] M. Tlidi, R. Lefever and P. Mandel, Quantum Semiclass. Opt. **8** 931 (1996).

- [229] M. Tlidi, P. Mandel and R. Lefever, Phys. Rev. Lett. **81**, 979 (1998); M. Tlidi, P. Mandel, M. Le Berre, E. Ressayre, A. Tallet and L. Di Menza, Optics Lett. **25**, 487 (2000); M. Tlidi and P. Mandel, Europhys. Lett. **44**, 449 (1998).
- [230] M. Tlidi and P. Mandel, Phys. Rev. A **59**, R2575 (1999).
- [231] R. Toral and A. Chakrabarti, Compute Physics Communications **74**, 327 (1993).
- [232] L. Torner in *Beam shaping and control with nonlinear optics*, ed. by F. Kajzar and R. Reinisch (Plenum Press, New York, 1998).
- [233] L. Torner and A.P. Sukhorukov, Opt. Photon. News **13**, 43 (2002).
- [234] W.E. Torruellas, Z. Wang, D.J. Hagan, E.W. VanStryland, G.I. Stegeman, L. Torner, and C.R. Menyuk, Phys. Rev. Lett. **74**, 5036 (1995).
- [235] S. Trillo, M. Haelterman, and A. Sheppard, Opt. Lett., **22**, 970 (1997).
- [236] D.P. Tse, A.M. Rucklidge, R.B. Hoyle, and M. Silber, Physica D **146**, 367 (2000).
- [237] L.S. Tsimring and I. Aronson, Phys. Rev. Lett. **79**, 213 (1997).
- [238] A. Turing, Philos. Trans. R. Soc. London B **237**, 37 (1952).
- [239] D. Turnbull, Trans. Metall. Soc. AIME **191**, 661 (1951).
- [240] H. Tutu, Phys. Rev. E **56**, 5036 (1997).
- [241] M. Vaupel, A. Maitre, and C. Fabre, Phys. Rev. Lett. **83**, 5278 (1999).
- [242] J. Viñals, E. Hernández-García, M. San Miguel, and R. Toral, Phys. Rev. A **44**, 1123 (1991).
- [243] C. Wagner, H.W. Müller, and K. Knorr, Phys. Rev. Lett. **83**, 308 (1999).
- [244] C. Wagner, H.W. Müller, and K. Knorr, Phys. Rev. E **62**, R33 (2000).
- [245] D. Walgraef, *Spatio-Temporal Pattern Formation*, (Springer-Verlag, 1997).
- [246] S.S. Wang and H.G. Winful, Appl. Phys. Lett. **52**, 1774 (1998).
- [247] K. Wiesenfeld, J. Stat. Phys. **38**, 1071 (1985).
- [248] V.E. Zakharov, A.B. Shabat, Sov. Phys. JETP **34**, 62 (1972).
- [249] V.E. Zakharov, A.B. Shabat, Sov. Phys. JETP **37**, 823 (1973).
- [250] R. Zambrini, M. Hoyuelos, A. Gatti, P. Colet, L.A. Lugiato and M. San Miguel, Phys. Rev. A, **62**, 063801 (2000).

Curriculum Vitae

• PERSONAL DATA

Name: Damià Gomila Villalonga

Date of birth: 22th June 1976

Sex: Male

Place of birth: Maó, Balearic Islands, Spain

Nationality: Spanish

Place of work: Institut Mediterrani d'Estudis Avançats

Campus Universitat Illes Balears

E-07122, Palma de Mallorca, Balears, Spain.

Tel: +34-971-171314; Fax: +34-971-173248

E-mail: gomila@imedea.uib.es

URL: <http://www.imedea.uib.es/~gomila>

• EDUCATION AND FELLOWSHIPS

Master degree in Physics (June 1998) Universitat de Barcelona, Spain.

PhD in Physics (March 2003) Universitat de les Illes Balears, Palma de Mallorca, Spain.

PhD Thesis: *Dynamics of Spatial Structures in Nonlinear Optics*.

Supervisor: Pere Colet.

Spoken languages: Catalan, Spanish, English and Italian.

Fellowships (1994-2002)

1. Scholarship of the Spanish Government, Universitat de Barcelona (1994-1998).
2. PhD fellowship of the Spanish Government, Universitat de les Illes Balears (1999-2002).

• PUBLICATIONS

- D. Gomila, P. Colet, G.-L. Oppo and M. San Miguel, “Growth laws and stable droplets close to the modulational instability of a domain wall”, *Phys. Rev. Lett.* **87**, 194101 (2001).
- W. Firth, G.K. Harkness, A. Lord, J. McSloy, D. Gomila and P. Colet, “Dynamical properties of 2D Kerr cavity solitons”, *J. Opt. Soc. Am. B* **19**, 747 (2002).
- D. Gomila and P. Colet, “Fluctuations and correlations in hexagonal optical patterns”, *Phys. Rev. E* **66**, 046223 (2002).
- D. Gomila, P. Colet, M. San Miguel, A.J. Scroggie and G.-L. Oppo, “Stable Droplets and Dark Ring Cavity Solitons in Nonlinear Optical Devices”, *IEEE J. Quantum Electron.* **39**, 238 (2003).
- D. Gomila, T. Ackemann, E. Grosse, P. Colet, and W. Lange, “Secondary bifurcations of hexagonal patterns in a nonlinear optical system: alkali metal vapor in a single-mirror arrangement”, submitted (2003).
- D. Gomila and P. Colet, “Transition from hexagons to spatiotemporal chaos”, submitted (2003).

• SCHOOLS ATTENDED

- “Nonlinearity: Patterns and Defects, Solitons, Chaos and Turbulence”. Summer courses of the “Fundación General de la Universidad Complutense”, El Escorial, Spain (19-23 July, 1999).
- “Space Time Chaos: Characterization Control and Synchronization”. International School of the “Universidad de Navarra”, Pamplona, Spain (19-23 June 2000). Poster presentation: D. Gomila, M. Santagiustina, P. Colet, M. San Miguel, and M. Hoyuelos, “From Hexagons to Optical Turbulence”.
- “Topics in nonlinear dynamics”. International School of the Venice International University, Venice, Italy (January 30 - February 1, 2002).
- “School and Conference on Spatiotemporal chaos”. The Abdus Salam international center for theoretical physics, Trieste, Italy (8-19 July 2002). Talk: D. Gomila, P. Colet and M. San Miguel, “From Hexagons to Spatiotemporal chaos”.

• CONFERENCE COMMUNICATIONS

- D. Gomila, P. Colet, “Hexagonal pattern correlations in a Kerr cavity” (poster). “Quantum Optics X”, conference of the European Science Foundation, Cala Vinyes, Mallorca, Spain (2-7 October, 1999)
- D. Gomila, P. Colet, M. Hoyuelos, M. San Miguel and M. Zimmermann, “From hexagons to optical turbulence” (poster). “Quantum Optics X”, conference of the European Science Foundation, Cala Vinyes, Mallorca, Spain (2-7 October, 1999)
- D. Gomila, P. Colet, M. Hoyuelos, M. San Miguel, M. Santagiustina and M. Zimmermann, “Pattern dynamics in nonlinear Kerr resonators” (poster). “Control of Complex Behaviour in Optical Systems and Applications” (COCOS), Münster, Germany (7-10 October, 1999).
- D. Gomila and P. Colet, “Hexagonal Pattern Correlations in a Kerr Cavity” (talk). QSTRUCT’00 Meeting (European TMR network, Training and Mobility of Researchers). Les Houches, France (15-19 March, 2000).
- D. Gomila, M. Santagiustina, P. Colet, M. San Miguel, and M. Hoyuelos, “From Hexagons to Optical Turbulence” (poster). “Coherent Structures in Classical Systems”, XVII Conference on Statistical Mechanics, Sitges, Barcelona, Spain (5-9 June, 2000).
- D. Gomila, M. Santagiustina, P. Colet, M. San Miguel, and M. Hoyuelos, “From Hexagons to Optical Turbulence” (talk). “CLEO/Europe International Quantum Electronics Conference 2000”, Nice, France (10-15 September, 2000)
- D. Gomila and P. Colet, “Hexagonal Pattern Correlations in a Kerr Cavity. “CLEO/Europe International Quantum Electronics Conference 2000”, Nice, France (10-15 September, 2000).
- D. Gomila, M. Santagiustina, P. Colet and M. San Miguel, “Transition from hexagons to turbulence in a Kerr cavity (talk). First workshop of the network “Phase Domains and Spatial Solitons in Nonlinear Optics” (PHASE) of the European Science Foundation, Crete, Greece (22-27 September, 2000).
- D. Gomila, P. Colet, G.-L. Oppo and M. San Miguel, “Localized structures in the Parametrically forced CGLE” (invited talk). “The complex Ginzburg-Landau equation: theoretical and experimental relevance for the dynamics of extended systems”, Florence, Italy (21-23 May, 2001).
- D. Gomila, P. Colet, G.-L. Oppo and M. San Miguel. “Growth laws and circular domain walls in nonlinear optics” (talk). Meeting of the network “Phase Domains and Spatial Solitons in Nonlinear Optics” (PHASE) of the European Science Foundation, Gif sur Yvette, France (5-8 June, 2001).

-
- D. Gomila, P. Colet, G.-L. Oppo and M. San Miguel, “Growth Laws and Circular Domain Walls in Nonlinear Optics” (poster). “CLEO/Europe-EQEC”, Munich, Germany (18-22 June 2001).
 - D. Gomila, P. Colet, G.-L. Oppo and M. San Miguel, “Growth laws and stable droplets in nonlinear optics” (poster). “Quantum Electronics and Photonics 15” (QEP-15), Glasgow, United Kingdom (3-6 September, 2001).
 - D. Gomila, P. Colet, G.-L. Oppo and M. San Miguel, “Growth laws and stable droplets close to the modulational instability of a domain wall” (talk). “II Jornades de la Xarxa Temàtica *Dinàmiques no lineals d’autoorganització espaciotemporal*”, Barcelona, Spain (6-8 February 2002).
 - D. Gomila, P. Colet, G.-L. Oppo and M. San Miguel, “Growth Laws and Stable Droplets close to the Modulational instability of a domain wall” (talk). “XI Congreso de Física Estadística (FISES 2002)”, Tarragona, Spain (23-25 May 2002).
 - D. Gomila, P. Colet, G.-L. Oppo and M. San Miguel, “Dark ring cavity solitons and stable droplets in nonlinear optical cavities” (talk). “2nd International Workshop on Dynamics of Nonlinear Optical Systems (PICS), Platja d’Aro, Spain (2-6 September, 2002).
 - D. Gomila, T. Ackemann, E. Grosse Westhoff, P. Colet and W. Lange, “Secondary bifurcation of hexagonal patterns in a nonlinear optical system: alkali metal vapor in a single-mirror arrangement” (invited talk). Meeting of the network “Phase Domains and Spatial Solitons in Nonlinear Optics” (PHASE) of the European Science Foundation, Venice, Italy (16-18 October, 2002).

• SEMINARS

- “Hexagonal pattern correlations in a Kerr Cavity”, Mediterranean Institute for Advanced Studies, Palma de Mallorca, Spain (october 1999).
- “From hexagons to optical turbulence”, Department of Physics and Applied Physics, Strathclyde University, Glasgow, UK (november 1999).
- “Transition to turbulence”, Institut Mediterrani d’Estudis Avançats, Palma de Mallorca, Spain (setember 2000).
- “Growth laws and Stable droplets in Nonlinear Optics”, “Institut für Angewandte Physik”, “Westfälische Wilhelms-Universität, Münster, Germany (october 2001).
- “Growth laws and Stable droplets in Nonlinear Optics”, “Institut für Festkörpertheorie und Theoretische Optik”, “Friedrich-Schiller Universität”, Jena, Germany (october 2001).

-
- “Localized Structures in Nonlinear Optical Cavities: Cavity Solitons”, “Istituto Nazionale di Fisica della Materia (INFN), Dipartimento di Elettronica e Informatica, Università di Padova”, Padova, Italy (january 2002).
 - “Localized Structures in Nonlinear Optical Cavities: Cavity Solitons”, Institut Mediterrani d’Estudis Avançats, Palma de Mallorca, Spain (february 2002).
 - “Secondary bifurcations of hexagonal patterns in a nonlinear optical system: alkali metal vapor in a single-feedback mirror arrangement, Institut Mediterrani d’Estudis Avançats, Palma de Mallorca, Spain (december 2002).

• VISITS TO OTHER INSTITUTIONS

- November 6 - December 4, 1999, with the “Computational Nonlinear and Quantum Optics group” of the “Department of Physics and Applied Physics” of the Strathclyde University, Glasgow, Scotland (UK).
- June 24 - August 19, 2000, with the “Computational nonlinear and quantum optics group” of the “Department of Physics and Applied Physics” of the Strathclyde University, Glasgow, Scotland (UK).
- 15 - 21 October, 2001, with the group “Nonlinear Optics and Pattern Formation” of the “Institut für Angewandte Physikla” of the “Westfälische Wilhelms-Universität”, Münster, Germany.
- 22 - 24 October, 2001, at the “Institut für Festkörpertheorie und Theoretische Optik” of the “Friedrich-Schiller Universität”, Jena, Germany.
- January 23 - February 2, 2002 at the “Istituto Nazionale di Fisica della Materia” (INFN), “Dipartimento di Elettronica e Informatica”, Università di Padova, Padova, Italy.
- 21-26 July, 2002, with the group “Nonlinear Optics and Pattern Formation” of the “Institut für Angewandte Physikla” of the “Westfälische Wilhelms-Universität”, Münster, Germany.
- 12-16 February, 2003, with the “Computational Nonlinear and Quantum Optics group” of the “Department of Physics and Applied Physics” of the Strathclyde University, Glasgow, Scotland (UK).
- 23-28 February, 2003, with the group “Nonlinear Optics and Pattern Formation” of the “Institut für Angewandte Physikla” of the “Westfälische Wilhelms-Universität”, Münster, Germany.